RADAR REMOTE SENSING DATA FOR APPLICATIONS IN FORESTRY

Promotoren: dr.ir. M. Molenaar,
hoogleraar landmeetkunde en teledetectie

ir. L. Krul,
hoogleraar microgolftechniek
aan de Technische Universiteit Delft

Dirk Herman Hoekman

RADAR REMOTE SENSING DATA FOR APPLICATIONS IN FORESTRY

Proefschrift
ter verkrijging van de graad van
doctor in de landbouw– en milieuwetenschappen,
op gezag van de rector magnificus,
dr. H.C. van der Plas,
in het openbaar te verdedigen
op woensdag 17 oktober 1990
des namiddags te vier uur in de Aula
van de Landbouwuniversiteit te Wageningen

STELLINGEN

1. Aangezien de autocorrelatiefunctie van de ruimtelijke structuur van bossen op een directe en eenvoudige manier met radar kan worden gemeten, verdient het aanbeveling om de bruikbaarheid van deze maat voor de beschrijving van bosstructuur en bosontwikkeling te onderzoeken.
(Dit proefschrift, hoofdstuk 6.5)

2. Voor deze autocorrelatiemetingen biedt een (nieuw) type radar met een hoge range resolutie en een gedistribueerde antenne, met een Gaussisch stralingspatroon in azimut, de beste mogelijkheden.

3. Het "speckle probleem" kan op verschillende wijzen worden benaderd. Vermindering van de storende invloed van speckle, zonder gebruik van (topografische) voorkennis, kan bereikt worden middels (1) het opnamesysteem (bandbreedte en keuze golfparameters) en/of (2) beeldbewerking. Aangezien de laatste methode onvoorspelbare radiometrische en geometrische vervormingen kan introduceren verdient de eerste methode de voorkeur.
(Dit proefschrift, hoofdstuk 6.2)

4. Transmissiviteitsmetingen met behulp van in een bos geplaatste cornerreflectoren kunnen behalve met SLAR ook met scatterometers zoals Dutscat worden uitgevoerd. Vanwege de smalle bundelbreedtes zijn de operationele problemen groter. De doel-achtergrond signaalsterkteverhouding is bij scatterometers echter iets gunstiger.

5. Indien men denkt aan het volgen van processen aan het aardoppervlak vanuit satellieten dan is de kwalificatie "monitoringsinstrument" vrijwel uitsluitend van toepassing voor systemen uitgerust met microgolfsensoren.

6. Indien men uitspraken wil doen over bepaalde met remote sensing methoden geobserveerde objecten, bijvoorbeeld klassificatieresultaten of toestandsbeschrijvingen, dient men te bedenken dat nieuwe perceptiemogelijkheden nieuwe en/of andere definitiemogelijkheden voor de kenmerken van deze objecten met zich mee brengen.

7. Zowel de remote sensing als de GIS zijn sterk gebaat bij de ontwikkeling van methodieken voor de integratie van deze technieken. Enerzijds zal voorkennis ingebracht door GIS de interpretatiemogelijkheden van remote sensing data sterk vergroten, anderzijds biedt de remote sensing unieke methoden om op snelle en synoptische wijze relevante data voor GIS te verwerven.

8. Aangezien de beeldvorming bij SLAR systemen relatief eenvoudig is zal de mogelijkheid onderzoek uit te voeren met een polarimetrische SLAR een welkome aanvulling betekenen op het onderzoek met polarimetrische SAR.

9. Het bepalen van de ruimtelijke schaal waarop elektromagnetische interactiemodellen hun geldigheid bezitten en de verenigbaarheid van deze schaal met de schaal waarop de waarnemingen worden verricht zijn twee problemen waar in de remote sensing niet altijd de vereiste aandacht aan wordt besteed.

10. Een van de grootste uitdagingen van het Earth Observing System (EOS) ligt in de enorme omvang van de hoeveelheid gegenereerde data. In dit licht gezien, en dit geldt met name voor monitoringstoepassingen, is het opmerkelijk dat de aandacht die momenteel wordt geschonken aan (1) een snelle en sterk geautomatiseerde verwerking van remote sensing beelden en (2) de telecommunicatie aspecten ten behoeve van de benodigde snelle en omvangrijke datadistributie, nog steeds gering is.

11. De grote inspanningen die nodig blijken te zijn voor het verkrijgen van goed gecalibreerde radardatasets, met de bijbehorende gestandaardiseerde objectgegevens, maken intensievere samenwerking van Europese onderzoeksgroepen noodzakelijk.

12. De discussie over de voordelen van optische remote sensing ten opzichte van microgolf remote sensing is een zinloze discussie die veel overeenkomsten vertoont met de discussie over de voordelen van vector gestructureerde GIS ten opzichte van raster gestructureerde GIS.

13. Met het remote sensing onderzoek van tropisch regenwoud zou niet alleen het beoogde doel: een beter beheer en/of duurzaam gebruik, verwezenlijkt kunnen worden. Indien de politieke wil en/of de beheersmogelijkheden niet voldoende aanwezig zijn, zou het regionaal ook kunnen leiden tot het tegenovergestelde: een versnelde, destructieve, exploitatie.

14. Een ieder die tracht informatie te verwerven middels het "bekijken" van ruimtelijke afbeeldingen van radardata zou moeten bedenken dat er een manier bestaat om aanvullende informatie te verkrijgen middels het "luisteren" naar deze radardata.

(Dit proefschrift, appendix II)

Stellingen behorende bij het proefschrift van D.H. Hoekman:
Radar remote sensing data for applications in forestry.
Wageningen, 17 oktober 1990.

Preface

My interest in microwave remote developed while I was with the Microwave Laboratory of the Department of Electrical Engineering of the Delft University of Technology. Here, professor ir. L. Krul and ir. E.P.W. Attema introduced me to the work of ROVE, some of the unique capabilities of radar and the prospects of radar for remote sensing applications.

After spending a period of practical training at Queen's University, Kingston, Ontario, in 1980, where I worked on the development of a subsurface guided radar system, I continued my work at Delft's Microwave Laboratory. Using ground–based scatterometer data collected by the ROVE team, I carried out a thesis research on the backscatter modelling of agricultural crops.

Dr.ir. A.R.P. Janse and ir. H.J. Buiten invited me to continue this type of research at the Department of Land Surveying and Remote Sensing (then headed by prof.ir. G.A. van Wely) of the Wageningen Agricultural University (WAU). Meanwhile, the Coordination Board on Remote Sensing Education and Research (OOT) of WAU proposed to start forestry related research, in close cooperation with the ROVE team. With the development of Dutscat at the Microwave Laboratory in Delft, in addition to the availability of an accurate SLAR, it seemed technically well feasible to explore this new field of application.

A special fund for the stimulation of remote sensing of the Ministry of Science and Education enabled me to prepare a feasibility study on "radar remote sensing for forest inventory" in 1982 and 1983. Additional BCRS funding was used for a series of SLAR flights and for data processing. In the meantime, the ROVE–Forestry working group was set up to support this study.

The results of this first ROVE–Forestry project led to the definition of a follow–on study in which Dutscat, in addition to SLAR, would play an important role. This research was carried out as a Ph.D. study funded by WAU for a nominal period of three years, starting in 1984. Again, BCRS provided additional funding for flights and data preprocessing.

Though these flights were executed successfully in 1984 and 1985, data preprocessing took substantially more time than expected. For the SLAR data, this was indirectly caused by an upgrading of the system. To capitalize on the improved capabilities, the preprocessing software had to be adapted by NLR, which eventually caused a substantial delay in data delivery. When preprocessing the Dutscat data, it was recognized that, because of the thickness of forest canopies, the approach adopted at the Delft's Microwave Laboratory could lead to erroneous results for forests. Therefore a new preprocessing approach (and software package) had to be developed for Dutscat data. As a result of these difficulties, it

took until early 1987 before all data were available for analysis.

During these years, the prospects for radar remote sensing applications grew vigourously: ESA developed the ERS–1 satellite; NASA worked towards realization of the Earth observing system (Eos). Though the importance of these developments was recognized and the research had been very successful, funds for continuation of radar remote sensing research were not provided by the university. These delays therefore obliged me to simultaneously carry out other research projects (funded by ESA and BCRS). In 1986, I joined the ESA/INPE Amazonian expedition to acquire Dutscat data of tropical rainforests in Brazil. In 1987 and 1988, I participated in the ESA/JRC Agriscatt campaign as science coordinator for ESA. In 1989, I participated in the ESA/JRC Maestro–1 campaign as coordinating investigator of the Dutch test site.

These projects took substantial amounts of time and interfered with the completion of the forestry research. Participation in the international research projects, however, was a very worthwhile experience. In addition to the scientific achievements, it acquainted me with the people, the work and organization of many European research groups and the (remote sensing of) tropical rainforests.

Here, I wish to take the opportunity to express my gratitude to all who contributed to this work.

The ROVE–Forestry working group was established in 1982 to supervise the forest radar experiments (until 1986) and, at the same time, to act as a board of advisors for my research. I am grateful to the members of this group: ir. H.J. Buiten, ir. P.J. Faber, Dr.ir. A.R.P. Janse, ir. J.J. Jansen, Prof.ir. L. Krul, Prof.Dr.ir. M. Molenaar and ir. G. Sicco Smit for their many useful suggestions, evaluations and comments. I am especially grateful to Prof. Krul and Prof. Molenaar who continued their supervision of my work (after 1986) and supported me in the preparation of this thesis.

I want to acknowledge the cooperation and fruitful discussions I had with other investigators. I am particularly grateful to ir. P. Snoeij (Dutscat), ir. H.C. Peters (speckle analysis), ir. P. Hoogeboom (SLAR and calibration) and Dr.ir. J.J. Gerbrands (image processing).

I also want to acknowledge NLR for their cooperation and support. I especially want to thank ir. G.L. Lamers for his excellent coordination and execution of the radar flights, and Dr.ir. N.J.J. Bunnik, who headed the NLR's remote sensing department before joining The Netherlands Remote Sensing Board (BCRS) as director of the Programme Board. I also want to thank Dr. Bunnik for the cooperation in the latter period and BCRS, in general,

for funding the radar flights and preprocessing.

Finally, I would like to express my gratitude to the members of the Department of Land Surveying and Remote Sensing of WAU and those students who were somehow involved in this research, the State Forest Service and the IJsselmeerpolders Development Authority, for their technical support and cooperation. I want to acknowledge Mrs. Ann Stewart for editing and correcting the English manuscript.

Abstract

Hoekman, D.H., 1990. Radar remote sensing data for applications in forestry. Ph.D. Thesis, Wageningen Agricultural University, The Netherlands. 279 pp., 78 figs, 39 tables, 5 appendices.

This thesis describes an investigation into the applications of radar remote sensing in forestry. During a four–year period (1982–1985), an extensive set of radar data was acquired at four test sites with forest plantations in The Netherlands: the Roggebotzand and Horsterwold sites at Flevoland and the Speulderbos and Kootwijk sites at The Veluwe. Two systems were deployed: a digital X–band SLAR and the multiband airborne scatterometer Dutscat. The thesis includes a description of these systems and the radar signal properties. Results of radar signature, transmissivity and canopy probing measurements are described. After discussing the physical properties of the radar data, the use of spatial analysis techniques is evaluated and the potential applications of radar data for classification and biophysical parameter estimation are elaborated. The thesis concludes with a conceptual elaboration of processing and data interpretation strategies.

Keywords: radar, remote sensing, forestry, Dutscat

RADAR REMOTE SENSING DATA FOR APPLICATIONS IN FORESTRY

CONTENTS

List of symbols [1,2]

Symbol	Unit	Description
A	m^2	antenna aperture
A_e	m^2	effective antenna aperture
A_i	–	contribution of scatter plane i to γ
A_{ill}	m^2	illuminated area
A_{proj}	m^2	area of resolution cell projected in beam direction
A_{res}	m^2	resolution cell area
B	Hz	spectral width of frequency uncertainty in speckle power density spectrum
c	$m \cdot s^{-1}$	speed of light
d	m	distance
$d_{\parallel}$	m	spatial resolution in azimuth direction
$d_{\perp}$	m	spatial resolution in range direction
$E()$	–	expectation value
$g_\theta(\theta)$	–	directivity function in elevation direction
$g_\varphi(\varphi)$	–	directivity function in azimuth direction
G, $G(\theta,\varphi)$	–	antenna gain (directional pattern)
G_0	–	maximum of antenna gain
h	m	height
h_c	m	height of canopy
h_i	m	height of sensor above scatter plane i
$I_i(t)$	s^{-2}	return signal shape factor for level i
J_{eff}	s^{-1}	effective time–integrated return signal shape factor
k	–	number of independent realisations of the radar return signal
k	$W \cdot s^2$	polarization and band dependent constant in radar equation
l	m	length of corner reflector edge
L_x	m	effective antenna length
N	m^{-3}	number of particles per unit volume
$N(\mu,\sigma)$	–	Gausian distribution
$p()$	–	probability density function
$p(i,j)$	–	GLCO–matrix [3]
$p(t)$	–	normalized pulse shape
P_r, $P_r(t)$	W	received power
$P_{rf}(t)$	W	power received from forest

P_t, $P_t(t)$	W	transmitted power
P_{tm}	W	maximum value of transmitted power
Q	m^2	attenuation cross section of a particle
r	–	correlation coefficient
r	m	distance
r_0	m	distance of sensor to collection of scatterers
$s_{n,u}$	–	standard deviation of γ of object n in image u
S	$W \cdot m^{-2}$	power density
S_{is}	$W \cdot m^{-2}$	power density of isotropic radiator
$S_{<speckle>}(f)$	$W^2 \cdot Hz^{-1}$	speckle power density spectrum
t	s	time
t_j	–	date of flight
T	s	time delay
$v(i)$	–	GLD–vector [3]
v_0	$m \cdot s^{-1}$	velocity of aircraft
x_s	m	tree row spacing
γ	–	radar cross section per unit projected area
γ_d, $\gamma_d(\theta_i,t_j,\omega_n)$	–	deterministic part of radar signature
γ_f	–	hypothetical γ for a forest area tilted in such a way that the upper canopy surface is parallel to the horizontal plane
γ_i	–	radar cross section per unit projected area for canopy layer i
γ_s, $\gamma_s(\theta_i,t_j,\omega_n)$	–	synthesized radar signature
γ_{soil}	–	contribution to γ of the soil
γ_{total}	–	total γ of soil plus vegetation ($\equiv \gamma$)
γ_{veg}	–	contribution to γ of the vegetation layer
δ_r	m	relative displacement of hypothetical column of scatterers in forest canopy
Δf_{min}	Hz	frequency uncertainty in speckle power density spectrum
ϵ	–	stochastic part of radar signature
η_0	ohm	impedance of free space
θ	rad	elevation angle
θ_B	rad	effective beam width in elevation direction
θ_i, θ_{inc}	rad	angle of incidence
θ_{gr}	rad	grazing angle

θ_t	rad	antenna tilt angle
λ	m	wave length
ρ	–	correlation coefficient
σ	m^2	radar cross section
σ^0	–	differential radar cross section
σ_b	m^2	radar cross section of background
σ_b^0	–	differential radar cross section of background
σ_{b+c}	m^2	radar cross section corner reflector plus background
σ_{b+ca}	m^2	radar cross section forest area plus corner reflector under forest canopy
σ_c	m^2	maximum of radar cross section of corner reflector in free space
σ_c'	m^2	σ_c corrected for actual sensor aspect angle
σ_{ca}	m^2	$\equiv \tau_e \cdot \sigma_c$
σ_{max}	m^2	maximum radar cross section observable by system
$\sigma(x)$	m^2	radar cross section function in azimuth direction
$\sigma_i(x_i)$	m^2	discrete radar cross section function in azimuth direction
τ	s	pulse duration
τ, τ_t	–	(two–way) transmissivity
τ_e	–	equivalent (two–way) transmissivity
τ_i	–	(two–way) transmissivity for canopy layer i
φ	rad	azimuth angle
φ_B	rad	effective beam width in azimuth direction
$\phi_{11}(x)$	m^4	autocorrelation function of $\sigma(x)$
ω_n	–	forest class n
Ω	sr	solid angle

---

1) This list does not cover all symbols used in Appendices I, II and III.

2) Symbols used for tree and stand parameters are listed in table 4.1.

3) Symbols used for textural features are listed in table 6.6.

1. INTRODUCTION

1.1 Radar remote sensing and forestry: a review

Compared with optical systems, the use of microwave systems in remote sensing is fairly new. The application of "side–looking radar" [1] dates back to the 1960s, when the first results of its use appeared in the literature. Notably through the results of a survey project executed in Panama, the special capabilities of this new technique became widely known. Darien province in Panama, in the easternmost part of the country, comprises impregnable swamplands and mountainous jungle terrain. The area became known as the "Darien gap", as it stood as an impassable barrier to the completion of the Pan American Highway. This name was very appropriate, since the nearly perpetual cloud cover prohibited the use of aerial photography for topographic mapping. Over a period of nearly 20 years (since 1947) all attempts to fill this "photographic gap" failed. In 1965 the RAMP project (radar mapping of Panama) was initiated to demonstrate the capabilities of a novel device designed to acquire high–resolution images: the Ka–band [2] AN/APQ–97 side–looking radar system developed by Westinghouse Electric Corporation. Four hours of flying time were needed to collect images covering the 17,000 km^2 area. Unimpeded by the presence of clouds, the system was well capable of providing data from which topographic maps at a scale of 1:250,000 could be derived (Crandell, 1969; Hockeborn, 1971).

Many different side–looking radar (SLR) systems, including the type now known as "synthetic aperture radar" (SAR), were developed during the 1950s (Sherwin et al., 1962). The first unclassified papers describing these new devices appeared in 1961 (Cutrona et al., 1961, 1962). Civil applications emerged only after the declassification of images produced by the "real aperture" Westinghouse system in 1964. After the success of project RAMP, imaging radar was deployed to acquire data over vast tracts of previously unmapped areas, much of it covered by woodland.

These early radar images clearly showed geomorphic features and surface drainage patterns and were appreciated not only for their use in cartography but also as a tool in such disciplines as geology, hydrology and soil science. Though geological survey usually was the prime motive for radar flights, it became apparent in an early stage that radar images could be used for vegetation mapping as well. From their study of the Darien images,

---

[1] Radar is an acronym for radio detection and ranging

[2] The frequency band ranges and nomenclature are given in table 2.1.

Viksne et al. (1970) concluded that it was possible to deliniate 11 broad vegetation classes (the major forest types present, wetlands, grasslands and clearings) at a scale of 1:250,000. The specific grey tones and textures could be interpreted on the basis of local knowledge of the vegetation associations in the various geographic zones of the study area. In high–relief areas and transition zones, delineation was found to be troublesome. Sicco Smit (1974, 1975, 1976) studied the use of radar images for forestry applications in Colombia. From terrain physiography, which was well perceivable, the occurrence of specific vegetation classes could be deduced. Using additional information from aerial photographs, groundtruth and knowledge of existing vegetation characteristics, a significant improvement in the deliniation and differentiation of vegetation types was possible.

The Darien project and similar projects covering the forested coastal zone of Columbia in 1968 and 1969 and a forested area in Nicaragua in 1971 (Francis, 1976), all executed with the Westinghouse system, were followed by another radar survey project, which is still the largest and most impressive of its type to date. This project, known as RADAM (projeto radar Amazon), aimed at mapping the natural resources of the Brazilian Amazon basin (Azevedo, 1971). In the early 1970s, a total area of 8.5 million km^2 was surveyed using the newly–available X–band synthetic aperture radar GEMS (Goodyear electronic mapping system) operated by Aero Services. Radar mosaics at a scale of 1:250,000 were constructed (van Roessel, 1974). Using additional information (some large– and small–scale aerial photographs and groundtruth), thematic maps at a scale of 1:1,000,000 of geomorphology, geology, soils and vegetation were produced (RADAM reports, 1973–1978; Correa, 1980). In the same period, the same system was used to survey adjacent parts of the Amazon rainforest in Colombia (see also Koopmans, 1974; Leberl, 1974), Peru and Venezuela, covering another 1.8 million km^2. In subsequent years, forested areas in South–East Asia were imaged (Froidevaux, 1980). In Africa, Nigeria (Parry and Trevett, 1979) and Togo (Dellwig, 1980) were surveyed using another system, an X–band "real aperture" radar system operated by Motorola (MARS) Ltd.

The notion that a multidisciplinary approach can support each single element of the interpretation was increasingly being recognized. It was known, for example, that there are certain relationships among vegetation, edaphic factors and terrain drainage. Knowledge of such relationships could considerably support the interpretation. Additional terrain information (ground truth, some large–scale aerial photographs) was still found to be necessary. Because of the presence of the radar images, however, this additional information could be collected efficiently and the amount of fieldwork could be kept at an acceptably low level.

Commercial radar surveys, aiming at small–scale mapping, continue. The unique capability to penetrate clouds, and hence its potential use for (fast and systematic) forest surveys in

areas of persistent or severe cloud cover, such as all tropical rainforests and also boreal forests (in Canada, Scandinavia, USSR), is highly regarded. Interpretation of radar images (of forests), however, is still not considered to be without difficulties. For example, the tonal and textural variations were not always found to be related to differences in vegetation, and gross differences in vegetation were not always reflected in the tone or texture. In a case study of the mahogany forest region in the state of Goiás, Brazil, Sicco Smit (1978) found that forest and non–forest areas could be accurately delineated on the RADAM radar images, but the mahogany forest types could not be differentiated from the non–mahogany types by tone/texture or physiographic location. On the other hand, it is the experience of the author that reinterpretion of RADAM radar images (performed for specific areas and objectives) using new insights and newly–acquired additional terrain information can improve previous interpretations.

Of course, it is unrealistic to assume that radar alone can provide *all* information relevant to all types of surveys. Some of these "difficulties" may be inherent to the radar systems used, however, and could be overcome in principle. The selection of wave parameters (i.e. frequency, polarization, incidence angle, etc.) for radar systems was not directed to vegetation studies. On the one hand, this was caused by technical limitations; on the other hand, it was simply not known which wave parameters (or combination of wave parameters) were appropriate. The first systems deployed for civil applications all used a single and relatively short wavelength. Later, more elaborate systems became available for research.

Research

Most of the early research efforts were based on the Westinghouse Ka–band SLAR, which was capable of collecting HH and HV polarized data. In their study of the Horsefly Mountain site in Oregon, Morain and Simonett (1966,1967) found it was possible to distinguish such classes as pine forest, white fir forest, hardwood forest, juniper woodlands, sagebrush and grasslands, and that multipolarization data were imperative to make some of these distinctions.

Daus and Lauer (1971) emphasized the increased complexity of interpretation for terrain with steep slopes. From their study of mixed coniferous forests in the Sierra Nevada mountains in California, they concluded that there were clear relationships between tone and vegetation type only if slopes were less than ≈20%. Classification in relatively flat areas was regarded to be considerably easier and, for classification, texture was found to be more important than tone. They also stated that it was not possible to assess timber quality or stand volume.

The separability of vegetation classes was also found to depend on incidence angle. Hardy et al. (1971), using the same Westinghouse system, concluded from their research in Yellowstone Park that some vegetation communities could be differentiated best (or exclusively) at steep angles (i.e. in the "near range" of the strip imaged), others at more shallow angles (or "far range"). This held true for differentiations based on tone as well as texture. To increase classification potential, Hardy et al. recommended covering areas in near, middle *and* far ranges.

This notion was corroborated by MacDonald and Waite (1971). They found that bare deciduous trees exhibited a "backscatter" level that was fairly independent of incidence angle, whereas bare soils showed a (moisture–dependent) relatively steep decrease of backscatter level with increasing incidence angle. Moreover, in their study site in the Mississippi River delta, they found that at steep incidence angles a qualitative estimate of soil moisture in (bare deciduous) forests was possible.

In the early 1970s, the Environmental Research Institute of Michigan (ERIM) developed a high–resolution dual–frequency airborne SAR. This device was capable of acquiring data in four channels simultaneously: X–band and L–band, each with HH and HV polarization (Shuchman et al., 1975). Since 1973, more than 20 experimental flights have been carried out. Shuchman et al. (1978) studied data acquired over a forest plantation in Michigan with deciduous and coniferous species. It was found that all four channels were valuable for making the discriminations and hence could contribute to the overall classification result. The difference in wavelength, however, was considered to have a larger impact than the difference in polarization. Texture, in these high–resolution images (3 m), was found to be as important a classifier as tone.

Hardy (1981) emphasized that visual interpretation of radar images is tedious and requires a certain expertise in radar image interpretation as well as forestry. An interpretation experiment using X–band SAR (Goodyear) images acquired over forest regrowth sites in Oregon was conducted by 10 experienced aerial photo interpreters. They were able to distinguish different textures in the radar images, but were often unable to associate these textures with different vegetation structures, though a simple interpretation key was available. Clearcut zones and selective cutting areas were often not recognized as such because of the different stages of regrowth. Also the effects of incidence angle–dependence, the different meanings of shadow and parallax and the lower resolution were found to confuse the photo interpreters. Subtle differences in vegetation structure, if perceivable from the images, were recognized only by skilled "forest radar image" interpreters.

Francis (1976) studied images (from the Ka–band Westinghouse system) obtained over pine stands (*Pinus caribeae*) in Nicaragua. He stated that it was possible to distinguish

three density classes in these pine stands. Other researchers at other sites, using images acquired by the same system, did not clearly reveal such a capability or even concluded that it was impossible to derive biophysical characteristics such as stand volume. The notion grew that longer wavelengths penetrate the forest canopy farther and therefore might yield new information in this respect. Wedler et al. (1980), using the ERIM system, found L–band (23 cm wavelength) to be superior to X–band (3.2 cm wavelength) in forest regeneration assessment surveys. Using an L–band SAR with HH and HV polarization developed by JPL (Jet Propulsion Laboratory, Pasadena), Riom and Le Toan (1980) and Shahin (1980) were able to delineate two density classes of maritime pine (*Pinus pinaster*) at their study site in southern France. Moreover, three age groups (0–4 years, 4–10 years and >10 years) could be distinguished.

Recent developments

Despite all these research efforts, no consensus could be reached on the most appropriate choice of wave parameters for vegetation studies. It became apparent, however, that the information contained in the radar signals received depends on the choice of the wave parameters. Many of the wave parameter combinations (frequency, polarization,..) studied seemed to be useful in the sense that their deployment could contribute to the success of classification and delineation of vegetation types. Moreover, some indications were obtained that assessment of certain (yet to be defined more precisely) biophysical characteristics, relevant in the description of forest (re)growth and forest development, might be possible, thus suggesting that radar, with its so–called "all–weather capability", in addition to being a useful survey instrument, might also be useful as a monitoring instrument.

One might say the radar surveys of the 1960s and '70s were a result of a "technology push". New technologic developments, notably in the areas of radar technology, digital electronics and space technology, opened new perspectives for the application of radar for vegetation studies.

Rapid developments in digital electronics made it possible to sample, store and process ("SAR processing") radar signals in a digital form, to handle larger data streams and to analyse images by computer. The latter possibility opened ways to quantify tones and textures, to develop objective interpretation tools and hence to automate the analysis and handle large data volumes within a reasonable time.

Developments in space technology have had an impact of comparable importance. The availability of spaceborne platforms for remote sensing devices opened the possibility of covering any area of the earth frequently (this applies especially to radar with its

all–weather and day–night capability) and hence to monitor processes over vast and remote areas. The feasibility of spaceborne imaging radar was shown by the SEASAT satellite in 1978 (Ford et al., 1980), and the SIR–A (Ford et al., 1983) and SIR–B (Cimino et al., 1988) systems deployed from space shuttles Columbia and Challenger in 1981 and 1984, respectively.

New radar techniques such as "polarimetry" or "interferometry" are increasingly recognized as being useful for civil applications. (Imaging) radar polarimeters are capable of assessing the "full polarimetric signature" of an object (Huynen, 1970). Radar interferometric systems produce conventional radar images, but are capable of providing extra information, for example height (Graham, 1974). In addition to airborne surveys, the use of these techniques is envisaged for future space missions (Elachi, 1986).

ESA's [1] "Land Applications Working Group" (ESA, 1987) anticipates an important role for spaceborne radar remote sensing in European forestry. As woodlands comprise 31% of Europe's area (the USSR excluded), a general role in surveying and monitoring is expected, in particular for rapid damage assessment (in southern Europe forest fires destroy vast areas each year) and disease detection (in relation to a severe acidification stress in some areas).

NASA [2] envisages spaceborne radar monitoring of forests to become a vital element in the global environment research programmes (NASA 1987, 1988). On a global scale, as they comprise 90% of the terrestrial biomass, forests play an important role in all hydrologic, climatic and biochemical cycles.

The potential relevance of airborne radar surveys and future spaceborne monitoring missions is generally acknowledged. At the same time, however, it is recognized that there is still a general lack of knowledge of the interaction of microwaves with vegetation. Though this knowledge is expected to support the application of radar for vegetation studies in general, it might be of crucial importance for some of these anticipated applications.

---

[1] European Space Agency

[2] National Aeronautics and Space Administration

1.2 Aim of this study

Radar images, notably those collected during the 1960s and '70s, were often treated as if they were aerial photographs. The shades of grey, textures and patterns perceived in hard copies (data prints on film or paper, usually uncalibrated) were interpreted using techniques very simular to the traditional and well–established aerial photo interpretation techniques. This was a very dangerous approach, since other physical principles underlie radar imaging. In contrast to photography, radar imaging is *active* (meaning the terrain is illuminated by the sensor), utilizing *coherent* waves in a totally *different spectral range*. Moreover, radar imaging is based on a different geometric principle, i.e., the projection of range differences instead of the projection of angular differences.

For human beings used to the perception of the world through the naked eye or (conventional) photographs, the perception of the world through "radar eyes" is therefore confusing. To be able to assess the true nature of the phenomena observed, we should *consciously* apply a thorough knowledge of how the image is formed, including a sufficient amount of physical knowledge.

To gather this physical knowledge, a mere experimental approach is not likely to suffice because of the wide diversity of forest types, environmental conditions and ecologic variation. Another difficulty is the fact that the empirical results obtained to date seem to be inconsistent. For example, from published results it can be deduced that the possibilities of differentiation of specific vegetation classes, even when the same wave parameters are used, may differ significantly from case to case. For these reasons, and to be able to generalize empirical findings, *modelling* should effectively complement the experimental approach.

In this study, a systematic experimental approach (within specific technical and logistic limits) was pursued, the interpretation of the results being based on basic physical descriptions of the radar return signal.

There is ample experience in The Netherlands in the field of radar remote sensing of soils and vegetation, notably crops. Research activities started in 1968, utilizing side–looking radar data collected over The Netherlands (de Loor, 1969). A few years later, an interdisciplinary working group, the Dutch ROVE team (radar observation of vegetation), was formed to investigate the possibilities of radar remote sensing in agriculture (de Loor et al., 1982). An extensive ground–based "scatterometry" measurement programme was carried out on agricultural test farms in the period 1975–1980. For the airborne verification, an EMI X–band SLAR was deployed in the period 1974–1978. In 1979, a new, accurate X–band SLAR with digital recording facilities was designed and built.

Although ROVE research in agriculture was successful, research in the field of forest vegetation was still lacking. Also at the international level, forest research had got little attention compared with other fields of application. Until the early 1980s no major systematic studies were carried out at all. Though a fair number of individual studies were subsequently carried out, their (empirical) results are difficult to compare. The great diversity of vegetation appearances among the different studies, the lack of a proper description of this vegetation, the variety of sensors used (and wave parameters!), and the general lack of calibration prevent a proper generalization of these results.

In 1982, ROVE decided to start systematic forestry–related radar research in The Netherlands. Suitable forest test sites, large forest plantations in the Veluwe and Flevoland comprising a fair range of species and conditions, were present. The availability of the accurate digital SLAR and the anticipated availability of an accurate airborne scatterometer system called Dutscat [1] were considered as a good basis to explore this field of application.

Research activities started with a multitemporal SLAR data–acquisition campaign (1982–1983) to get a general impression of the feasibility of inventory, the temporal and spatial variations and basic backscatter properties. During a second stage of research (1984–1985), an upgrading of the SLAR and the availability of Dutscat were expected to permit new (types of) experiments.

In an early stage of this research, it was recognized, on the basis of theoretical descriptions of the radar return signal, that forest signals have some properties distinct from those of agricultural crops, caused by differences in plant geometry. The large dimensions of trees, compared with agricultural crops, allow the execution of some specific experiments which, to a certain extent, reveal the nature of forest backscatter. Moreover, it was recognized that under these conditions, "speckle" (a strong fluctuation of the return signal caused by wave interference), usually regarded as a noise–like inconvenient feature of radar images, contains information related to forest structure.

In addition to using the research instruments (SLAR and Dutscat) in a "conventional" way, it therefore seemed advantageous to put a major effort into the development of methods to fully utilize the specific capabilities these instruments offer to forest research.

---

[1] Dutscat is an acronym for Delft University of Technology Scatterometer.

The long–term objective of the forestry research is the assessment of radar's (full) potential and the development of generally applicable concepts in information extraction from forest radar data. A basic physical understanding of forest backscatter (to be deduced from experimental results on the basis of theoretical considerations) and the empirical findings themselves may indicate the type(s) of information radar signals, in principle, contain. To assess the type(s) of information that can be provided through the practical use of radar it is necessary to evaluate promising *information extraction strategies*. Techniques such as image processing, texture quantification and the use of additional data and knowledge are envisaged to be useful elements in such strategies.

1.3 Thesis organization

Chapter 2 provides an introduction to the basic principles of radar and its use for remote sensing measurements. The basic concept of radar and relevant concepts such as antenna gain, radar cross section and spatial resolution are introduced. The theoretical "Rayleigh fading" model, describing the "speckle" properties of most distributed land target types, including forests, are described. Some relevant mathematical aspects of the speckle description are elaborated in Appendix I. After indicating some characteristic properties of radar system types commonly used in remote sensing, i.e., of the scatterometer, SLAR and SAR, two experimental radar systems used in this research, the "Netherlands digital X–band SLAR" and the airborne "multiband scatterometer Dutscat", are described.

Chapter 3 contains a basic description of the radar backscatter signals for homogeneous vegetation canopies. The expectation of the backscatter signal level is described using the "cloud model". The description of the signal statistics, i.e. the speckle, is extended. It will be shown that for (incoherent) radar systems utilizing the side–looking radar configuration, speckle statistics contain information on features at the subresolution cell level. A full theoretical description is included in Appendix II. The "probing" capability of the Dutscat scatterometer for forests is elucidated. The antenna beam of Dutscat, a so–called "pencil beam", is relatively narrow. As a result, because of the large height of forest vegetation relative to flight altitude, backscatter signal components originating from different height levels in the forest canopy are detected separately in time to a certain extent. The "multilevel" model is introduced to describe properly the backscatter signal of such "thick" vegetation canopies. Through inversion of the proposed multilevel model, backscatter components from a number of forest "layers" can be computed. Moreover, an alternative and simpler signal processing technique to compute the backscatter coefficient is indicated. It will be shown that the use of this newly–developed processing technique for Dutscat data is imperative to avoid gross errors in the computation of the backscatter coefficient of forests (i.e. "thick" vegetation layers). Within this research, an experiment was conducted

to determine canopy transmissivity. The return signal of calibration targets placed at the forest floor, attenuated by the forest canopy, is described and the procedures to estimate the transmissivity are indicated.

In chapter 4, the four forest test sites selected (the Roggebotzand, the Horsterwold, the Speulderbos and the Kootwijk forest) are described using examples of X–band images covering these sites. Maps of the test sites are included in Appendix IV. Next, ground data collection and radar data collection are discussed. Radar measurement geometries and (ground and radar) data collection strategies will be related to experiment objectives for the various SLAR and Dutscat campaigns conducted throughout the research period (1982–1985). Chapter 4 concludes with some notes on radar data quality and on the "intercalibration" and determination of radar signatures from the 1982–1983 X–band SLAR images. The mathematical background of these points is described in Appendix III.

Experimentally obtained X–, C– and L–band forest radar data are discussed in chapter 5. From the X–band SLAR images, a large number of (forest stand) radar signatures could be assessed covering many species, all four test sites and several times of observation. The properties of these radar signatures will be described systematically and related to several types of object characteristics, such as species type, morphologic features, stand parameters and tree parameters. The speckle properties (i.e., the ensemble statistics) are described using the "Rayleigh fading" model introduced in chapter 2. X–band transmissivity data covering a variety of forest stands are presented and related to forest characteristics. C– and L–band data could be obtained through the Dutscat system. The properties of C– and L–band signatures are described systematically and compared with the X–band signatures. Moreover, results from canopy "probing" measurements, utilizing the "multilevel" model introduced in chapter 3, are discussed. After providing an overview of the basic results, the nature of the (microwave) interaction with forests is described in more depth. Notably, the presumed effects of leaf orientation and needle loss (at X– and C–bands) and the presumed fundamental differences between the L–band ("large" wavelength) and X– and C–band (i.e., "small" wavelengths) are discussed. The results are then related to recently published results of other authors. Chapter 5 concludes with an evaluation of all results. In particular, the appropriateness of the "multilayer cloud model" (introduced in chapter 3) to describe forest backscatter is discussed. A selection of the experimentally obtained data, especially the most recent data, is included in Appendix V. Since radar data of forests (still) are relatively scarce, it might serve as a useful reference for future studies.

The application potentials of radar data are elaborated in chapter 6. Based on the previously derived models for the radar signature and the interaction mechanism (chapter 5), a classification algorithm is proposed. Classification potentials were studied on the basis of empirically established forest radar data. The impact of image processing tools and the

relevance of these tools compared with other factors (such as a radar data collection strategy or radar system design) were investigated. The extraction of spatial parameters and the use of spatial relationships in imaging radar data in data extraction are discussed next. On the basis of the previously obtained insights into the interaction mechanism, a simple geometric model to compute the influence of relief in homogeneous forest areas is derived. Smaller spatial features can be assessed through analysis of image texture and speckle. The use of image texture, notably for classification purposes, will be elucidated. Through the theoretical speckle description derived for (incoherent) radar systems using the side–looking radar configuration (Appendix II), and based on a simple geometric model for the forest canopy structure, the feasibility of a technique to derive spatial features at the sub–resolution cell level will be demonstrated experimentally. Chapter 6 concludes with an overview, as suggested by the results of this research, of the type and nature of (forest) characteristics that can be assessed through the use of radar remote sensing.

On the basis of results described in chapters 5 and 6, a tentative overview of anticipated types and areas of application in forestry will be given in chapter 7. To achieve the full potential benefits of radar remote sensing, appropriate "strategies" (i.e. for system design, mission planning, signal processing and data interpretation) should be developed for (future) operational systems, and these strategies should be directed towards certain applications. To facilitate this discussion, several types of application, related processing techniques and related (types of) physical models (or physical knowledge) will be considered. Radar is expected to play a major role in remote sensing, especially in monitoring systems. Since these (future) systems will generate large quantities of data, and, considering the types of application foreseen, two general approaches in radar data interpretation seem to become of particular importance. Both approaches will be discussed briefly. The first relates to the use of backscatter models for physical parameter estimation. The status of (forest) backscatter modelling will be reviewed and the inherent limitions of its practical use will be indicated. The second approach relates to the integration of radar data with other types of data (such as topographic data, other remote sensing data, etc.). An integrated approach that incorporates spatial, semantical and temporal aspects is suggested.

The main results and conclusions will be summarized in chapter 8.

2. RADAR BASICS

For an in–depth study of the elementary concepts and specific aspects of radar, the reader is referred to the handbooks of Colwell (1983), Skolnik (1980) and Ulaby, Moore and Fung (1981, 1982 and 1986). For more profound technical descriptions on system design and data processing, the reader is referred to the papers of Hoogeboom (1982) and Hoogeboom et al. (1984) for the SLAR and of Attema and Snoeij (1985) and Snoeij and Swart (1987) for Dutscat.

2.1 Principles of radar remote sensing measurements

2.1.1 Basic concept

Radar was originally developed to detect isolated targets such as ships or aircraft and to determine their position and/or velocity. The basic concept is straightforward. The radar emits an electromagnetic wave signal within a pointed beam. If a target is present within this beam, a part of the signal is reflected back (the "radar echo" or "backscatter"). If the received power is above a certain threshold, the target is said to be "detected". The position of the target follows from the fact that the target is located in the beam (thus the direction follows) at a distance or "range" that follows from the speed of light and the time elapsed between emission and reception of the signal.

In radar remote sensing, the Earth's surface backscatter is of interest. To this aim, special imaging radar systems have been developed to measure the backscatter properties of so–called "distributed targets". The basic radar concept, however, is still the same. Remote sensing radar systems use primarily the 1 to 40 GHz band, the lower part of the so–called "microwave region" of the electromagnetic spectrum. The microwave band is subdivided into several specific frequency bands. The nomenclature for these bands is given in table 2.1. Specific locations within these bands are designated for radar applications and within the radar bands specific locations are designated for Earth observation. Thus interference with other types of application, such as telecommunications or air traffic control, is avoided.

Table 2.1. Standard radar frequency letter–band nomenclature. The commonly used (old) nomenclature as well as the more recently introduced (NATO) nomenclature are shown. The frequency ranges shown are based on the 1979 International Telecommunications Union (ITU) assignment.

Old band designation	Nominal frequency range	NATO band designation	Nominal frequency range
UHF	0.3 – 1 GHz	B	0.25 – 0.5 GHz
		C	0.5 – 1 GHz
L	1 – 2 GHz	D	1 – 2 GHz
S	2 – 4 GHz	E	2 – 3 GHz
		F	3 – 4 GHz
C	4 – 8 GHz	G	4 – 6 GHz
		H	6 – 8 GHz
X	8 – 12 GHz	I	8 – 10 GHz
Ku (or J)	12 – 18 GHz	J	10 – 20 GHz
K	18 – 27 GHz	K	20 – 40 GHz
Ka (or Q)	27 – 40 GHz		

Specific radio location (radar) bands	Allocations for Earth observation	
0.420 – 0.450		UHF
0.890 – 0.942		UHF
1.215 – 1.4	1.215 – 1.3	L
2.3 – 2.5		S
2.7 – 3.7	3.1 – 3.3	S
5.25 – 5.925	5.25 – 5.35	C
8.5 – 10.68	8.55 – 8.65	X
	9.50 – 9.80	X
13.4 – 14.0	13.4 – 14.0	Ku
15.7 – 17.7	17.2 – 17.3	Ku
24.05 – 24.25	24.05 – 24.25	K
33.4 – 36.0	35.5 – 35.6	Ka

2.1.2 Basic principles

Antenna gain

Reception and emission of electromagnetic waves by an antenna can be described through the "antenna gain function". The definition of antenna gain in the microwave region is based on the concept of an "isotropic radiator". This hypothetical antenna radiates the power P_t equally in all directions. On the surface of a sphere with radius d described with the radiator as a centre, the power density (power per unit area) therefore equals

$$S_{is} = P_t/(4\pi d^2). \tag{2.1}$$

When, for the moment, an ideal antenna is assumed, which radiates power uniformly over

the solid angle Ω (figure 2.1), the power density at the sphere's surface within this solid angle equals

$$S = P_t/(\Omega d^2) \tag{2.2}$$

and equals zero outside this solid angle. Since $S > S_{is}$, a "gain" G can be defined as

$$G = S/S_{is} = 4\pi/\Omega. \tag{2.3}$$

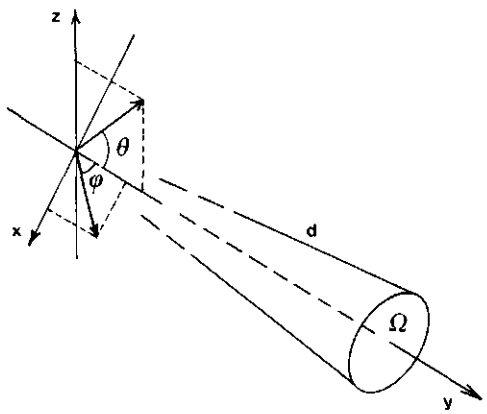

Figure 2.1. Hypothetical antenna radiating power uniformly over the solid angle Ω. Look direction is defined through an azimuth angle φ and an elevation angle θ.

Real antennas radiate non–uniformly and antenna gain should therefore be specified for each direction. The gain is usually defined as a function of azimuth angle φ and elevation angle θ as

$$G = G(\theta,\varphi). \tag{2.4}$$

The gain function may often be separated into components in the θ and φ directions and is written as

$$G(\theta,\varphi) = G_0 \cdot g_\theta(\theta) \cdot g_\varphi(\varphi) \tag{2.5}$$

where $g_\theta(\theta)$ and $g_\varphi(\varphi)$ are directivity functions with maximum value unity and G_0 is the maximum gain.

Directivity functions are often idealized. This means that all power is assumed to be radiated uniformly within an "effective beam width". In many practical cases, the effective

width is assumed to be equal to the so–called "half–power beam width", which is defined as the angular range between the angles at which the power density is equal to half of the maximum power density (figure 2.2). For a rectangular radiating area (the "aperture") with dimensions a and b (figure 2.3), the effective beam widths follow as approximately $\theta_B \approx \lambda/b$ radians in "elevation" direction and as $\varphi_B \approx \lambda/a$ radians in "azimuth" direction. Directivity functions, as well as the gain G, are physically related to antenna geometry and wavelength λ. For an idealized antenna with a rectangular aperture with dimensions a and b, the area A of the aperture is $a \cdot b$ and the related solid angle Ω of the transmitted beam is $\approx \lambda/a \cdot \lambda/b$. Using the law of reciprocity, antenna theory (Silver, 1949) gives the relationship between the transmitting gain and the receiving effective area A_e of an antenna as

$$G = 4\pi \cdot A_e/\lambda^2. \tag{2.6}$$

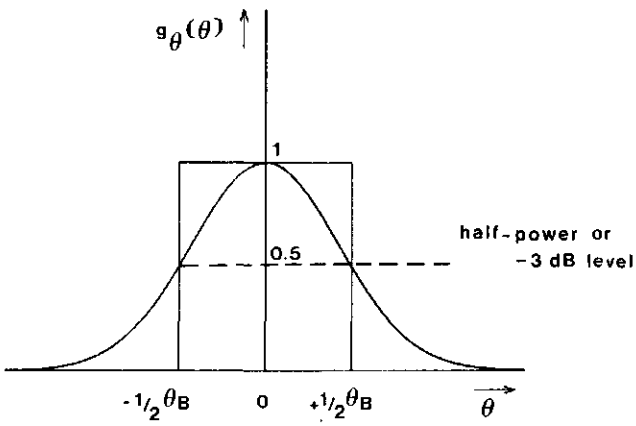

Figure 2.2. Idealized directivity function $g_0(\theta)$. For many antennas and many practical purposes, all power is often assumed to be radiated uniformly within the half–power or –3 dB beam width.

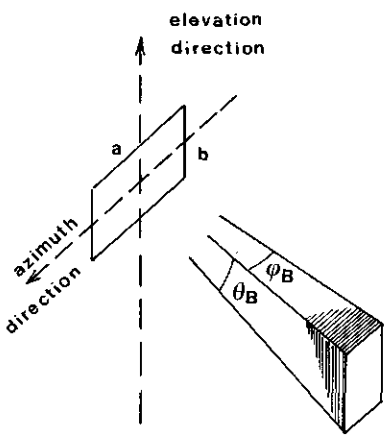

Figure 2.3. Rectangular antenna aperture with dimension a in elevation (the vertical direction) and dimension b in azimuth (the flight direction) is shown with an idealized antenna beam with a width θ_B in elevation and φ_B in azimuth.

Radar cross section

The "radar cross section" is a measure to express the backscatter properties of a target. The radar cross section σ is defined by the "radar equation" which can be derived as follows. For an antenna with gain G, radiating the power P_t, the power density at a distance d is $GP_t/(4\pi d^2)$. A target at distance d with radar cross section σ is assumed to have a fictitious area of σ m^2, intercepting a fraction $\sigma GP_t/(4\pi d^2)$ of the radiated power. The next assumption is that the intercepted power is re–radiated completely and isotropically (eq. 2.1). The antenna, with an effective aperture A_e, and now acting as a receiving antenna, intercepts a fraction $A_e/(4\pi d^2)$ of this re–radiated power. Thus the received power P_r follows as

$$P_r = \frac{G \cdot P_t}{4\pi d^2} \cdot \sigma \cdot \frac{A_e}{4\pi d^2} \tag{2.7a}$$

and using eq. 2.6,

$$P_r = \frac{G^2 \lambda^2 \cdot P_t}{(4\pi)^3 \cdot d^4} \cdot \sigma. \tag{2.7b}$$

Herewith σ is defined and becomes computable, since G, λ and P_t are known system constants and d follows from a measurement of elapsed time between emission and reception:

$$\sigma = \frac{P_r \cdot (4\pi)^3 \cdot d^4}{P_t \cdot G^2 \cdot \lambda^2} \quad [m^2]. \tag{2.8}$$

σ has a physical meaning for isolated targets . For distributed targets, σ will depend on the size of the resolution cell. For a surface with homogeneous scattering properties, the larger the resolution cell area A_{res} (that part of the Earth's surface located within the beam and pulse), the larger the number of "scatter elements" and the larger the power intercepted. On average (see discussion on fading, section 2.1.4), the backscattered power detected and thus σ will be larger. In order to define the backscatter strength of homogeneous distributed targets unambigiously and to become independent of the size of the instantaneously illuminated area, another backscatter parameter is used. This dimensionless measure, the "differential radar cross section" denoted σ^0, is defined as the expectation of the radar cross section σ per unit area:

$$\sigma^0 = <\sigma> / A_{res} \quad [m^2/m^2]. \tag{2.9}$$

In addition to σ^0, the measure γ is commonly used for distributed targets. γ is defined as

the radar cross section per unit projected area (figure 2.4):

$$\gamma = <\sigma>/(A_{res} \cdot \sin(\theta_{gr})) \quad [m^2/m^2]. \tag{2.10}$$

γ is simply related to σ^o as

$$\gamma = \sigma^o/\sin(\theta_{gr}). \tag{2.11}$$

In this research, the use of the measure γ was adopted since it has a stronger relationship with physical scattering mechanisms at the land surface. γ, for example, shows a flat angular response for idealised targets such as the "rough surface scatterer" or the "isotropic volume scatterer" and thus direct comparison of actual responses with theoretical responses of some major classes of land targets is achieved.

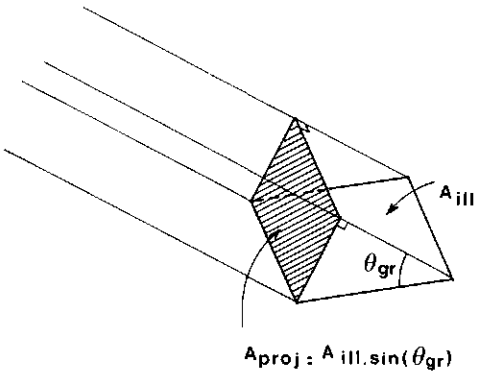

Figure 2.4. The parameter σ^o is defined as radar cross section per unit illuminated area (A_{ill}). Note that the plane of the illuminated area is assumed to have horizontal orientation. θ_{gr} is the grazing angle. The parameter γ is defined as radar cross section per unit projected area (A_{proj}). The plane of the hypothetical projected area is oriented perpendicular to the direction of the incidence beam.

Spatial resolution

For remote sensing radar, it is practical to define the two–dimensional spatial resolution on the (Earth's) surface as the width in θ and φ directions of the (instantaneously illuminated) area where incident power density does not drop more than 3 dB below the maximum value of power density on that surface. The spatial resolution of a radar system depends on several factors. For so–called "beam–limited" system types, spatial resolution is determined by the antenna beam width and the sensor–target distance (figure 2.5). For a system looking sideways with respect to the direction of displacement, the spatial resolution in range direction (i.e. the direction the beam points), and denoted as $d_\perp$, is

$$d_{\perp} = \theta_B \cdot d/\sin(\theta_{gr}) \quad [\mathrm{m}] \tag{2.12a}$$

and in azimuth direction (i.e. the direction of displacement or flight for an airborne system) the spatial resolution, denoted $d\|$, is

$$d\| = \varphi_B \cdot d \quad [\mathrm{m}]. \tag{2.12b}$$

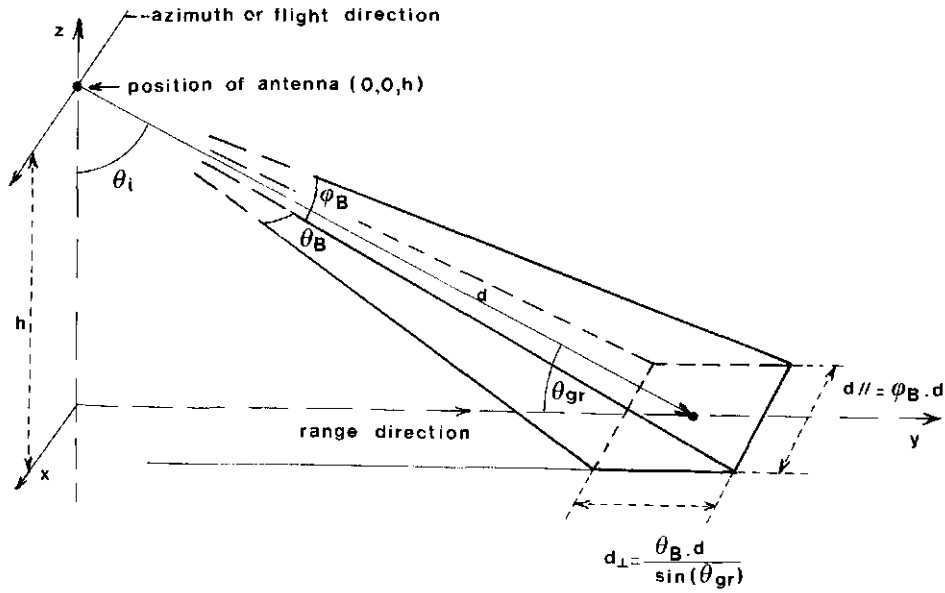

Figure 2.5. Scatterometer measurement geometry. In a beam–limited system, the resolutions in range ($d_\perp$) and azimuth ($d\|$) depend on distance (d).

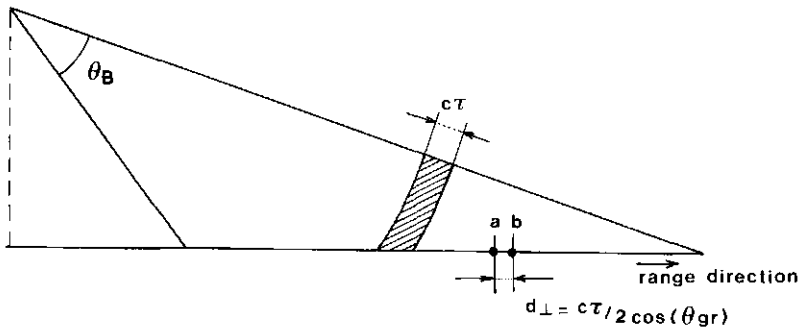

Figure 2.6. Dependence of range resolution ($d_\perp$) on pulse length ($c\tau$) and grazing angle (θ_{gr}).

Spatial resolution can be increased in several fundamental ways. By modulation of the transmitted radar wave in frequency and/or amplitude resolution in range direction can be increased. Pulse radars, for example, achieve a good range resolution by transmitting short pulses with duration τ and length $c\tau$ (figure 2.6). Since two points (a and b) within the illuminated area give echos separated in time if the distance sensor – point b – sensor is at least a length $c\tau$ larger then the distance sensor – point a – sensor, a range resolution of $c\tau/2$ follows. At the ground surface (or in ground range), the spatial resolution then becomes

$$d_{\perp} = c\tau/(2.\cos(\theta_{gr})) \quad [\text{m}]. \tag{2.13}$$

The ground range resolution increases with decreasing grazing angle and hence is worst at steep angles. It is noted that if the beam width in elevation direction is sufficiently small and/or the pulse length is sufficiently large, the spatial resolution in range deteriorates to that of the beam–limited case.

An increase in azimuth resolution can be "synthesized" by processing a series of return signals from the target area, each return signal recorded (in amplitude and phase) for a slight displacement of the antenna in azimuth direction. This principle is utilized in so–called "synthetic aperture radar" (SAR) systems. Theoretically, the best achievable azimuth resolution that can be synthesized is independent of distance and is equal to a half antenna length:

$$d_{\parallel} = L_x/2 \quad [\text{m}]. \tag{2.14}$$

2.1.3 Radar system types

Scatterometers

Scatterometer systems are used for accurate measurements of γ. A good radiometric resolution, which is defined here as the ratio of the standard deviation of γ and the expectation of γ at the logarithmic dB–scale, is achieved by a high signal–to–noise ratio (the S/N ratio is the ratio of signal level and the noise added by the system) and by averaging a large number of independent samples to reduce the effect of speckle (section 2.1.4). A good overall radiometric performance may be achieved by accurate absolute calibration. An imaging capability is usually not pursued. Beam–limited systems are often used and, consequently, spatial resolution is quite small at large distances (eqs. 2.12a–b). Scatterometers can be operated on the ground (ground–based), from aircraft (airborne) or from satellites (spaceborne). Because of their poor spatial resolution, spaceborne

scatterometers are used mainly for sea applications. For research applications, scatterometers are operated at short distances, from either the ground or low–flying aircraft.

SLR configuration

Imaging radar systems are designed to combine good radiometric performance with good geometric performance. Imaging systems are always operated in the side–looking radar (SLR) configuration. An oblong antenna with the long axis parallel to the line of flight directs a "fan–beam" sidewards (figure 2.7). The azimuth beam width φ_B is small and the beam width θ_B in range direction is fairly large.

Side–looking airborne radar (SLAR) achieves a good range resolution by modulating the amplitude of the transmitted wave signal with short pulses. Imaging with a SLAR results from sampling the returned power level of a transmitted pulse in subsequent "range cells". Thus a strip perpendicular to the line of flight is scanned. With the next pulse, a (partly overlapping) adjacent strip is sampled. The SLAR's range resolution (eq. 2.13) is typically in the order of several meters or a few tens of meters and is independent of distance. The SLAR's azimuthal resolution, however, depends on distance and beam width (eq. 2.12b), the latter depending on antenna length and wavelength. Even with a fairly long antenna (e.g. 4 m) and short wavelength (e.g. 8 mm) and, consequently, a relatively small beam width (in this example ≈2 mrad follows), the azimuth resolution at a distance of 1000 km (typical for a spaceborne radar) will be approximately 2 km. This is far less than the achievable range resolution. For an airborne radar operating at a distance of 10 km, the

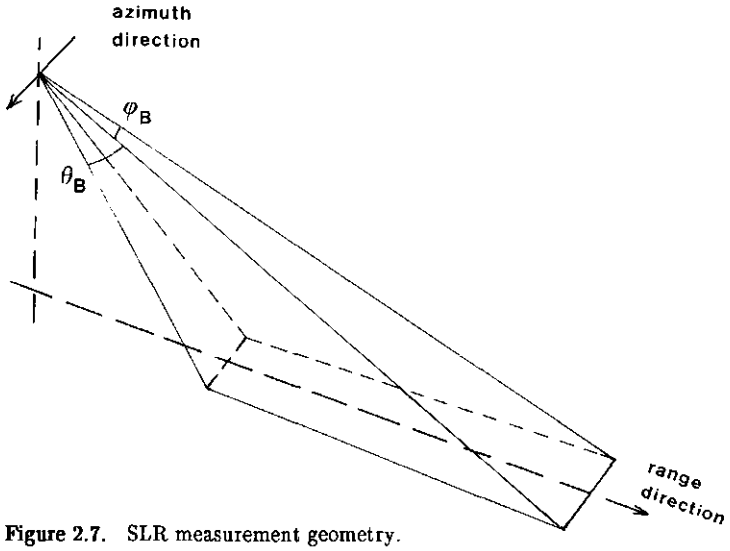

Figure 2.7. SLR measurement geometry.

azimuth resolution in this example follows as 20 m, which may be acceptable. Because of the bad azimuth resolution of SLAR systems at large distances, these systems, however, are unfit for space applications.

A technical solution is offered by synthetic aperture radar (SAR). SAR, like SLAR, utilizes the side–looking radar (SLR) configuration and the same principle to increase range resolution. A good azimuthal resolution is synthesized by processing the detected signals afterwards (SAR processing). In theory, images with an azimuth resolution of a half–antenna length, independent of distance, might be achieved (eq. 2.14).

2.1.4 Speckle

Radar images have a "grainy" or "speckled" appearance as an inherent feature. Notably in presumably homogeneous areas, these stochastic fluctuations show up clearly, even for systems with a high S/N ratio. It can be shown that this behaviour is fundamental to any active system using coherent waves (radars, lasers) and is caused by interference (or "fading") of waves returned from an ensemble of independent scatterers. Both systems used in this research, the Dutscat and the X–band SLAR (to be discussed in the next section), have a high S/N ratio (typically in the order of 30 to 50 dB) and the contribution of thermal noise to the signal fluctuations may therefore be assumed to be negligible in most practical cases.

These interference fluctations may be described with the theoretical "Rayleigh fading" model, commonly assumed to be applicable to a wide range of distributed land target types. In this model, the overall (or compound) radar return signal is assumed to be composed of contributions from a large number of (independent) discrete scatterers. In a vegetated area, for example, individual leaves might be imagined as being the scatterers.

In figure 2.8a, the amplitudes of the individual signal components are shown as vectors (phasors) in the (complex) x,y–plane. The amplitude r of the sum signal simply follows as the length of the sum vector. If the same ensemble of scatterers is observed at another time, and the relative positions in space of the scatterers are somewhat different (this might be caused by wind affecting vegetation, or when the ensemble is viewed from a slightly different aspect), the amplitudes might remain the same, but the relative phase differences may be completely different. In that instance, a new and "independent" realisation of the sum signal is obtained (figure 2.8b). If the number of scatterers n is effectively large (effectively large in this context meaning that the signal is not dominated by a few strong scatterers), then it follows from the central limit theorem that both the x and y components of the (complex) amplitude are approximately normally distributed with

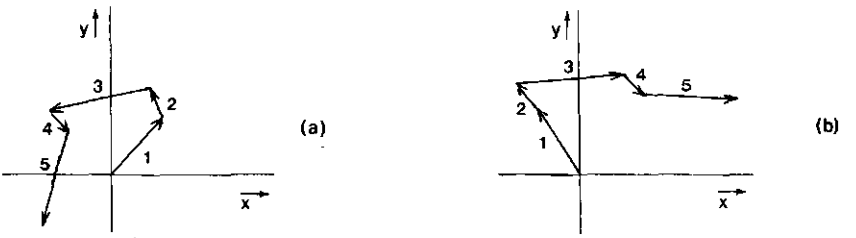

Figure 2.8. (a) A single realisation of the sum of amplitudes (vectors in the complex x–, y–plane) of five independent scatterers. (b) The individual amplitudes are the same, but the phases are completely re–arranged or decorrelated, and as a result the amplitude of the sum has changed.

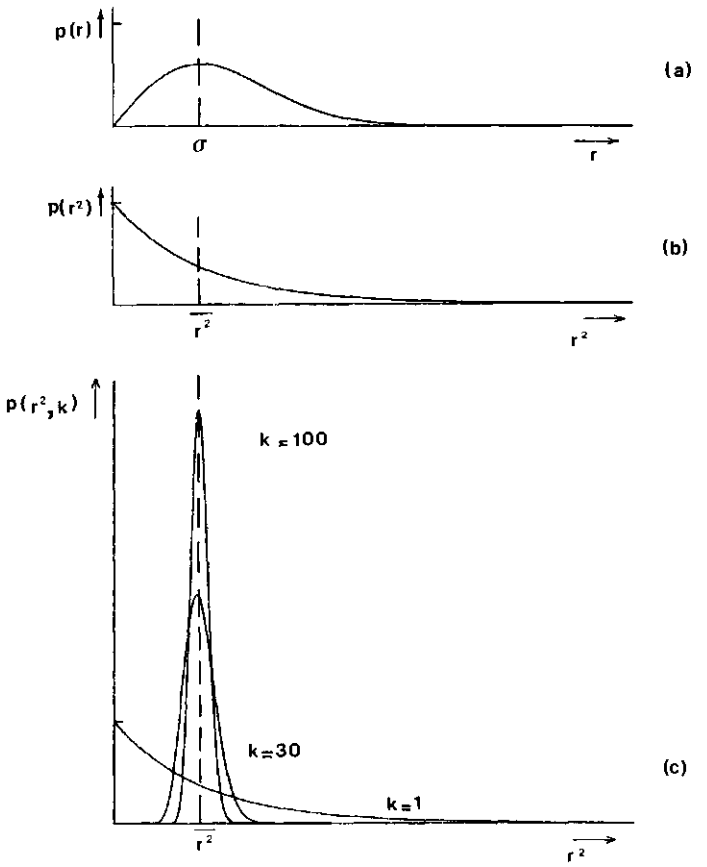

Figure 2.9. (a) The amplitude of the sum (the detected field strength r) follows the Rayleigh distribution. (b) The square of the amplitude of the sum (the detected power r^2) follows the negative exponential distribution. (c) Distributions of averaged power samples. Distributions are shown for averaging 1, 30 and 100 independent samples.

mean zero and standard deviation a:

$$p(x,y) = \frac{1}{2\pi a^2} \cdot \exp(-(x^2+y^2)/2a^2)). \tag{2.15}$$

The distribution of the amplitude r, $r=(x^2+y^2)^{\frac{1}{2}}$ and the phase φ, $\varphi = \arctan(y/x)$ of the sum signal follows from a transformation from the Cartesian coordinate system (x,y) to the polar coordinate system (r,φ):

$$p(r,\varphi) = p(r)\cdot p(\varphi) \text{ and} \tag{2.16}$$

$$p(r) = (r/\sigma^2)\cdot\exp(-r^2/(2\sigma^2)),$$

with $(\pi/2)\sigma^2 = (\bar{r})^2$

and $\bar{r}$ is the mean of the distribution,

and $p(\varphi) = 1/(2\pi)$.

Thus it follows that the phase of the sum signal is uniformly distributed and the amplitude of the sum signal is Rayleigh–distributed (figure 2.9a). Hence the name "Rayleigh fading" is used. Norton et al. (1955) indicated that 10 independent scatterers were sufficient for a reasonable approximation of this distribution.

Many radar systems do not detect the amplitude but the square of the amplitude (or power) of the return signal. The distribution of r^2, which directly follows from eq. 2.16,

$$p(r^2) = 1/(2\sigma^2)\cdot\exp(-r^2/(2\sigma^2)), \tag{2. 17}$$

with $2\sigma^2 = \overline{r^2}$

and $\overline{r^2}$ as the mean of this distribution,

is known as the exponential distribution (figure 2.9b).

Both the Rayleigh (eq. 2.16) and exponential distributions (eq. 2.17) are single parameter distributions. This means that when the mean amplitude $\bar{r}$ or the mean power $\overline{r^2}$ is known, the related distribution follows directly. It also implies that all information from Rayleigh fading objects is contained in a single parameter. Radar measurements are therefore directed to make accurate estimations of this parameter. This is done mathematically by linear averaging over a large number (k) of independent realisations of the return signal. (How this is achieved technically is discussed in a subsequent section.) The resulting averaged signal value (amplitude or power) is an unbiased estimation of the mean value. The distribution of averaged values depends on the number k. The larger the k, the

narrower the distributions of the averaged signal values and thus the more accurate the estimation of the mean. Figure 2.9c shows the distribution $p(r^2,k)$ for several values of k. The Rayleigh fading statistics of averaged power data and, moreover, the statistics of logarithmically scaled power data (as is the usual form of presentation) are elaborated in Appendix I.

Averaging reduces the magnitude of the stochastic fluctations and is therefore sometimes called "speckle reduction". As may have become evident, relevant averaging is obtained only when done over (statistically) independent realisations of the sum signal. In this context, the terms "independent samples" or "signal decorrelation" are also frequently used. Technically, speckle reduction can be achieved in a number of fundamentally different ways, which will be indicated briefly (for a thorough explanation the reader is referred to the handbooks). A radar at a fixed position and observing a fixed area can measure a new independent realisation of the sum signal when

(1) the phases (and/or strength) of the individual return signals are sufficiently rearranged (e.g. under certain conditions, wind is known to have such an effect on vegetation) or

(2) when the frequency of the transmitted microwaves is changed by a certain amount. (This point will not be elaborated. Technically, it can be achieved by so–called "frequency–modulated continuous–wave (FM–CW) scatterometer systems" which can take tens of independent samples almost instantaneously.)

When the radar system is moved, the number of ways to decorrelate the return signal increases:

(3) The same ensemble of scatterers is viewed from a (sufficiently) different aspect.

(4) Another area with identical (statistical) properties, as part of a larger area, can be observed (e.g. adjacent spatial resolution cells in a homogeneous agricultural field).

(5) It can be shown that the return signal observed by a radar operating in the SLR configuration is decorrelated when the antenna is moved (in flight direction) over a half–antenna length.

Both the airborne scatterometer Dutscat and the Dutch SLAR use the last two methods for speckle reduction.

2.2 Sensor description

2.2.1 The X–band SLAR system

Specifications

The Dutch digital SLAR is a joint development of the Delft University of Technology (TU Delft), the Physics and Electronics Laboratory TNO (FEL–TNO) and the National Aerospace Laboratory (NLR). It is installed in the NLR Metro II laboratory aircraft and operated by the NLR. The main system specifications are listed in table 2.2. The SLAR has digital recording facilities for radar and flight data. Recently (1985), an internal calibration circuit was added and the antenna support construction was changed. The latter modification enables the user to select between two predefined mechanical settings of the antenna elevation angle.

The pulse repetition frequency (PRF) is selectable within a wide range, but for this research it was fixed at 200 Hz. Decorrelation of the backscatter signal in azimuth (or flight) direction theoretically occurs at approximately 1.0 m intervals (the effective half–antenna length). The nominal speed of flight (relative to the ground) is fixed at 180 knots (92.6 m/s). With a PRF of 200 Hz, a displacement length in azimuth direction of slightly less then 0.5 m between two successive lines follows. Since sampling in azimuth is ample within the decorrelation length, averaging of samples can be considered to be done effectively over the theoretical maximum number of independent samples (i.e. ≈1 per m).

Table 2.2. Specifications of Dutch digital SLAR (1984/1985).

Frequency	9.4 GHz
Antenna	2.5 m slotted wave guide
Effective antenna length	2.0 m
Transmitted power	25 kW
Operating range	12 km maximum
Pulse length	50 ns
PRF	200 Hz
Polarization	HH
(Two–way) antenna beamwidth	10 mrad
Sample frequency	50 MHz (3 m) ,12 bits
Receiver bandwidth	20 MHz
Dynamic range	80 dB
Spatial resolution	
in range	7.5 m
in azimuth	10 m/km
Pixel size	7.5 m x 7.5 m
Independent samples	≈15 per pixel

The spatial resolution in range direction is ≈7.5 m (corresponding to a system band width of 20 MHz). It can be shown (using the sampling theorem) that a maximum of two independent samples per range resolution length (≈7.5 m) can be obtained when the range signal is adequately sampled. The sampling frequency of 50 MHz, every 3 m in range, is ample to obtain, effectively, the theoretical maximum number of independent samples in range (≈2 per 7.5 m).

During data processing, the samples corresponding to a 7.5 m square area are averaged to form a (slant range) pixel. The number of independent samples per (slant range) pixel thus becomes ≈15 (≈7.5 in azimuth times ≈2 in slant range). Averaging 15 independent samples theoretically results in a standard deviation of 1.14 dB for the speckle at the logarithmic dB scale for Rayleigh fading homogeneous objects (eq. I.26, Appendix I).

The system transmits horizontally polarized waves and receives the horizontally polarized component of the backscattered signal; hence the system is called HH polarized. Other radar systems may use other combinations for transmitted and received polarization; the most common are the so–called "like–polarizations" (HH and VV) or "cross–polarizations" (HV and VH).

Finally, a remark has to be made concerning radiometric performance. One of the most difficult elements in radiometric correction procedures for SLR imaging systems is the correction for antenna gain function in range direction. The antenna gain function $G(\theta,\varphi)$ was measured in the laboratory of the TU Delft. In figure 2.10, the square of this antenna gain function integrated over the azimuthal angular range

$$G^2(\theta) = \int_{-\pi}^{\pi} G^2(\theta,\varphi)\, d\varphi \qquad (2.18)$$

is shown as the solid line. (The factor $G^2(\theta)$ is an element of the radar equation used in the radiometric correction algorithm; eq. 2.8.) The aircraft, however, notably the wing, is likely to distort the antenna gain function to some extent. To avoid this problem, the gain function should be determined for the complete system (i.e. antenna mounted under the aircraft). This was done by FEL–TNO using sugar beet fields with known radar signatures as distributed calibration targets. The broken curve in figure 2.10 resulted. The NLR took a different approach. A large number of scenes were averaged and the antenna gain function was shaped in such a way that a flat angular response for γ resulted. The result is shown in figure 2.10 as dots. The three approaches yielded results similar within a few dB. The latter result was implemented in the PARES (preprocessing of airborne remote sensing data) algorithm and used for all images in this research. The experimental results in section 5.2 (figure 5.13) show that all backscatter signatures for individual tree classes show local

maxima at ≈35° and ≈57° grazing angles and a local minimum at ≈45° grazing angle. These are probably artefacts, caused by the unknown difference between the assumed best approximation of the antenna gain function, used for radiometric corrections, and the actual antenna gain function. If one of the other two functions had been applied, however, these local maxima and minima would not disappear. They would remain as pronounced (± 1 dB) and shift to other angles. It might be concluded that the assumption of an unknown (and presumably fixed) angular modulation of backscatter signatures within a few dB is realistic.

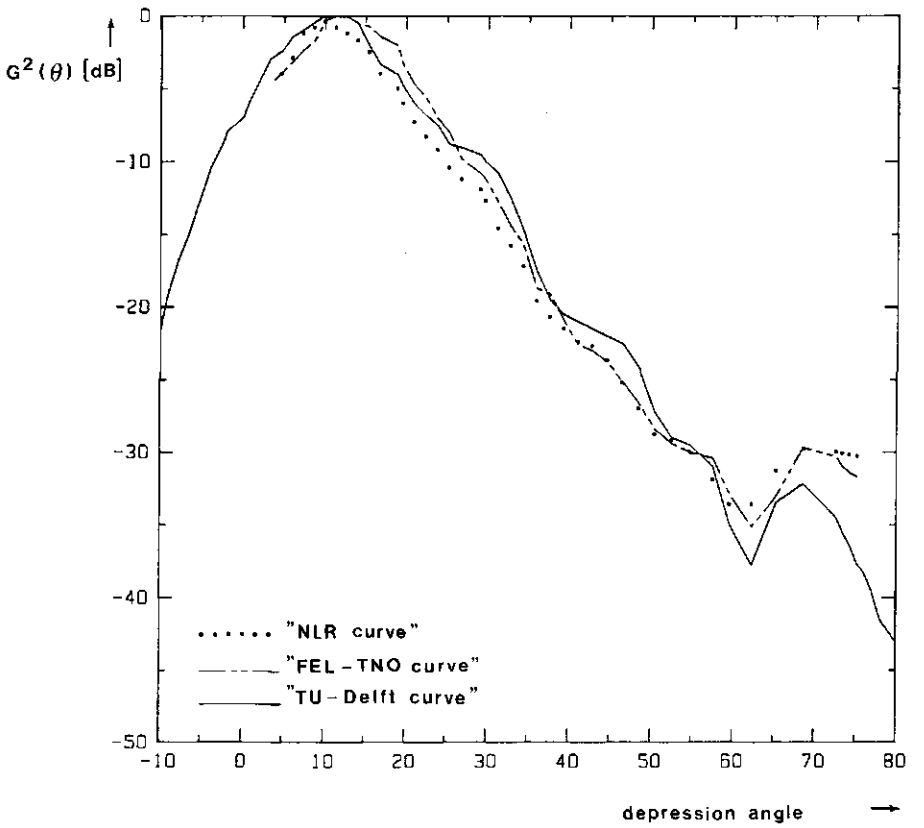

Figure 2.10. Integrated antenna gain function $G^2(\theta)$ of the SLAR in dB.

SLAR system modifications overview

Because the SLAR was modified three times during the research period, the measurement flights can be differentiated into three groups: (1) the 1982 and 1983 measurements, (2) the 1984 measurements and (3) the 1985 measurements.

The specifications in table 2.2 show the current status, which applies to the 1984 and 1985 measurements. In 1982 and 1983, however, the sample frequency of the SLAR was 20 MHz instead of 50 MHz. A 50 MHz sampling frequency is more appropriate considering the receiver band width of 20 MHz and transmitted pulse length of 50 ns. The range resolution of the SLAR improved from 15 to 7.5 m and, as a consequence, the number of independent samples per unit area was doubled.

In the period between the 1984 and 1985 measurements, an internal calibration circuit was added (Snoeij, 1985; Pouwels, 1986; Hoogeboom, 1986). The internal calibration signal is a small and constant fraction of the transmitted signal. Variations in the transmitted power level are measured by sampling this signal. By incorporating these data in the radiometric correction procedures, the backscatter values resulting from different scan lines and different recordings are linked with a fixed arbitrarily–chosen level. In addition, external calibration (with calibration targets such as corner reflectors) is needed to establish the absolute value of that level. This work was started by FEL–TNO in 1986, but it was not satisfactorily completed in time to be included in the results presented here. A limited absolute calibration experiment was executed in the framework of this research, however, as discussed in section 3.3. From the internal calibration signal, the stability of the transmitted power can be derived and, in retrospect, some conclusions could be made regarding the quality of earlier measurements. This point is elaborated in section 4.2.4.

The second modification in 1985 was related to the antenna tilt angle. With a new mechanical antenna support construction, one of two predefined settings of the antenna could be selected. It became possible to keep the antenna in the usual position or to tilt it 17.5° to nadir. (The curves in figure 2.10 apply to the old option.) With the second option, good image quality was obtained up to ≈65° grazing angle. This is a significant improvement over the 1982 and 1983 images which yielded useful data up to only ≈40°. The total increase of ≈25° resulted from a combined effect of improved range resolution (in 1984) and the antenna tilt to nadir (in 1985). It may have become evident that these modifications had a major impact on the experiment design and research objectives. (This point is elucidated in section 4.2.3.)

Data types and data processing

Basically, two types of SLAR radar data products were made available for this research: raw data and (pre)processed data. The first type represents power samples organized in recordings representing single scanlines. Each scanline contains 4096 power samples corresponding to a 12 km range (sampling is done every 3 m in range). The internal calibration signal is contained in the beginning of each recording. The power samples are presented at a dB scale in 256 steps of 0.3 dB. The second type represents γ values and is contained in geometrically corrected images. The PARES data processing software package was developed to accurately correct the raw radar data both geometrically and radiometrically using the digitally recorded radar and flight data (Hoogeboom et al., 1984). The maximum positional deviation caused by system distortions and aircraft position and attitude changes of the resulting PARES images is claimed to be 15 m in range and azimuth directions for the whole scene. It indicates relative gamma values at the logarithmic dB scale in 256 steps of 0.2 dB.

For data collected before the year 1984, pixels correspond to 15 m square scene elements. To take advantage of the increased range resolution of the system (since 1984), the SLAR preprocessing software was adapted to include an option to generate pixels corresponding to 7.5 m square scene elements. Pixels generated from the 1982 and 1983 data were based on 30 independent samples (per 15 m square area) and a "speckle level" of 0.80 dB follows (eq. I.26). Since 1984, pixels may be based on 15 independent samples (per 7.5 m square area); this results in a speckle level of 1.14 dB. Cubic convolution is applied to convert data from slant range (pixels) to ground range (pixels). This technique, which may be considered as a type of image filtering process, has a slight smoothening effect and, consequently, also slightly reduces the speckle level.

An image analysis system is indispensable for further processing of the corrected images as well as the raw data. At a display unit, objects or areas of interest can be recognized and indicated by a cursor or by drawing polygons or frames. Pixel values and coordinates can be retained for analysis in other computer systems or processed directly. In the corrected images, the nadir–line, the vertical projection of the actual line–of–flight, is indicated as a white line (see figures 4.2a–d). The nadir–line was computed from the first ground echo and the flight data. From the location of the nadir–line, together with the height of flight, the grazing angle can be derived for any pixel in the image.

2.2.2 The DUTSCAT system

Specifications

Dutscat was jointly developed by the TU Delft and the NLR. It is installed in the NLR Beechcraft Queen Air laboratory aircraft and operated by the NLR. The airborne multiband scatterometer is side–looking and of the coherent–pulse type, i.e. the transmitted microwaves are coherent from pulse to pulse. The main system specifications are listed in table 2.3. Its 0.9 m parabolic dish antenna is manually adjustable during flight and can be pointed between 0° and 80° incidence angle. The beam width depends on the frequency band and varies from 1.0° for the 17.25 GHz band to 13.0° for the 1.2 GHz band. The range resolution is 15 m for all bands; hence the system may be called beam–limited in some instances (notably for high frequencies and/or short distances) or may provide a certain imaging capability in others (notably for low frequencies and/or longer distances). For forests, even for the beam–limited case, another type of "imaging" is feasible. Because of the relatively large height of forest vegetation, responses from treetops may arrive somewhat earlier than the responses of lower parts or the ground. This technique, called probing, is discussed in section 3.2. A video camera attached to the supporting structure of the antenna registers the measured objects. The video images as well as the digital radar and flight data are time–tagged to link objects of interest and radar and flight data.

The period in which the Dutscat system was developed at the Technical University of Delft largely coincided with the period in which this forest research project was executed. The "final" multiband system, which is capable of making measurements in six bands simultaneously, was not completed until 1987. During the development stage, however, a number of measurement flights could be executed with single–band (C– and L–bands)

Table 2.3. Specifications of Dutscat (1984/1985).

Type	Coherent–pulse scatterometer
Frequencies multiband (1987)	1.2, 3.2, 5.3, 9.65, 13.7 and 17.25 GHz
Frequencies prototypes	1.2 and 5.3 GHz
Antenna	0.9 m parabolic dish
Transmitted power	250 mW
Operating range	50 – 1920 m
Pulse length	100 ns
PRF	78.125 kHz
Polarization	HH and VV
Sample frequency	20 MHz (7.5 m), 8 bits I and Q
Range resolution	15 m
Output	A–scan; 5 A–scans per second and per frequency

partially calibrated (only internal calibration) prototypes. Both the final multiband system and the prototypes can measure one polarization at a time (HH or VV), selected by simply setting a mechanical switch.

The effective antenna aperture length is approximately 60 to 70 cm, somewhat dependent on frequency. Thus, theoretically, the azimuth backscatter signal sufficiently decorrelates in 30 to 35 cm and ≈30 independent samples might effectively be obtained within a 10 m displacement. The system operates at the high pulse repetition frequency (PRF) of 78.125 kHz. Since the system is coherent, the high PRF can be used to improve the signal–to–noise ratio. This is achieved by coherent integration, thus calculating power signals. These power signals are subsequently accumulated 256 times. This is all done by hardware and only the result, the 64 times 256 times averaged signal, the so–called "A–scan", is stored on tape. A–scans are obtained once every 210 ms (78.125 kHz means a pulse every 12.8 μs and 64 x 256 x 12.8 μs is 210 ms); since the speed of flight is fixed at 55 m/s, this means one A–scan is collected roughly every 10 m. The speckle level (at the logarithmic dB scale) for 30 independent samples, obtained within a ≈10 m displacement, can be calculated as 0.8 dB (eq. I.26).

Data types and data processing

Only raw data were obtained from Dutscat. At the time of this research, the pre)processing software to calculate the quantity γ was not yet sufficiently developed at TU Delft. The raw data, delivered by TU Delft in suitable format, include:

(1) radar data recordings (series of time–tagged A–scans containing averaged power samples of the backscatter signal),
(2) calibration recordings (series of time–tagged A–scans containing averaged power samples of the internal calibration signal),
(3) files with auxiliary data (attenuator and polarization settings, nominal incidence angle, etc.) and
(4) files with flight data (height, roll, pitch, heading).

In retrospect, the absence of (pre)processing software was irrelevant. The software for Dutscat, as implemented now at the TU Delft, is based on the same principle used for SLR imaging systems. For forest data, however, this approach appears inappropriate (section 3.2). Dedicated software for forests has been developed by the author in the context of this research to calculate γ as well as to quantify relative contributions to γ of scatterers located at different height levels.

3. SIGNAL DESCRIPTION

3.1 Basic signal description for vegetation canopies

3.1.1 Some aspects of the backscatter signal

The radar backscatter signal relates to system as well as target (or object) parameters. Only one type of target, the homogeneous vegetation canopies, will be discussed in this chapter. The condition of homogeneity means that dimensions of structural elements (in the horizontal plane) of the physical canopy do not exceed the system's spatial resolution.

The radar backscatter signal description has several aspects. Relevant information is contained in (1) the mean signal level, (2) the polarization and phase properties of the signal and (3) the signal statistics. The first is common to all types of remote sensing signals (e.g. radar backscatter, thermal emission or reflected sunlight). The expectation of signal level may be expressed as a function of object and system parameters.

The other aspects typically apply to systems that illuminate the target area by (polarized) coherent waves (such as radar). The signal's polarization and phase properties are usually described by the scatter matrix or Stokes matrix and are also a function of object and system parameters (Huynen, 1970; van Zijl et al., 1987). Complete measurement of this information requires so–called "polarimetric systems". In the microwave region, these systems are called "radar polarimeters". The third aspect relates to the large fluctuations of the signal, which are intrinsic to the use of coherent waves. These fluctuations, called speckle, are not entirely stochastic but are known to relate to the spatial distribution of scatterers (Weissman and Johnson, 1979; Hoekman, 1988a and 1989a).

The properties of polarimetric signals are not discussed in this thesis. It suffices to depart from very simple and basic assumptions to describe the properties of the mean and statistics of the signal. The target, a homogeneous vegetation canopy, is presented as a homogeneous layer consisting of a large number of discrete and identical scatterers with a certain spatial distribution. Further, it is assumed that only single scattering is present and also that the theoretical Rayleigh fading concept introduced in section 2.1.4 is applicable. On the basis of these assumptions, the mean radar backscatter signal (section 3.1.2) and the statistics or speckle properties of the signal are described (section 3.1.3).

3.1.2 Mean backscatter signal

The well–known cloud model can be used to describe the mean radar backscatter signal. The basic concept of the cloud model was formulated by Attema and Ulaby (1978). It is based on the assumptions that a vegetation layer can be adequatly modelled as a low–density cloud of small identical (spherical) particles with a uniform random spatial distribution and that only single scattering is present. The backscatter contribution γ_{veg} of a vegetation layer modelled as such a cloud can be calculated as

$$\gamma_{veg} = \sigma/2Q \cdot [1-\exp(-2NQh/\cos(\theta_i))] \tag{3.1}$$

where N = the number of particles per unit volume,
h = the height of the vegetation layer,
σ = the radar cross section of a particle,
Q = the attenuation cross section of a particle and
θ_i = the angle of incidence.

The variable N (in the original concept) is directly related to the amount of plant water per unit volume and is therefore also related to the more commonly used object parameters, biomass and water content. The product $2 \cdot N \cdot Q$ and the ratio $\sigma/2Q$ are variables relating to plant morphology and must be determined empirically. Since Q, σ and N do not need to be known explicitly, the assumption that particles are identical appears to be irrelevant for this basic form of the cloud model.

Assuming the soil backscattering to add incoherently to the vegetation scattering, the (total) gamma value becomes

$$\gamma_{total} = \gamma_{veg} + \exp(-2NQh/\cos(\theta_i)) \cdot \gamma_{soil}. \tag{3.2}$$

With

$$\tau = \exp(-2NQh/\cos(\theta_i)) \tag{3.3}$$

this equation is simplified to

$$\gamma_{total} = \sigma/2Q \cdot [1-\tau] + \tau \cdot \gamma_{soil}. \tag{3.4}$$

If τ is small, and thus $\gamma_{veg} >> \tau \cdot \gamma_{soil}$ and γ_{veg} is close to $\sigma/2Q$, the layer is said to be "opaque". If τ is close to unity, the layer is said to be "transparent".

To account adequately for more complex structures and to improve accuracy, many

modifications of the original concept have been suggested (section 7.2). The variables σ and Q, for example, can be assumed to depend on the angle of incidence, and other types of scatterers can be added (as is done in the multiconstituent and multilayer approaches). Even more elaborate modifications may be needed to describe vegetation backscatter properly for a wide range of sensor and object parameters (section 7.2).

It is not likely that a forest canopy return signal can be described adequately by a single layer with identical scatterers. By assuming the forest canopy to be composed of n discrete layers with different types of scatterers, the basic cloud model equation can be extended simply (figure 3.1). It follows from induction that

$$\gamma_{veg} = \gamma_1 + \tau_1\gamma_2 + \tau_1\tau_2\gamma_3 + \ldots + \tau_1\tau_2\ldots\tau_{n-1}\gamma_n \tag{3.5a}$$

where index 1 stands for the top layer,

$$\gamma_i = \sigma_i/2Q_i\cdot[1-\tau_i] \tag{3.5b}$$

and

$$\tau_i = \exp(-2N_iQ_ih_i/\cos\theta). \tag{3.5c}$$

With

$$\tau_t = \tau_1\tau_2\tau_3\ldots\tau_n \tag{3.6}$$

it follows that

$$\gamma_{total} = \gamma_{veg} + \tau_t\cdot\gamma_{soil}. \tag{3.7}$$

The parameters τ (eq. 3.3) or τ_t (eq. 3.6) are known as the two–way (canopy) transmissivity.

3.1.3 Speckle

The speckle phenomenon is caused by interference between scatterers illuminated by coherent waves (radar, laser). The backscattered signal from an ensemble of scatterers at fixed random positions illuminated by a beam of coherent microwaves can be seen as a single realisation of a stochastic process. New (independent) realisations of the process can be obtained by an adequate spatial rearrangement of the scatterers in the ensemble (under some conditions wind can provide sufficient decorrelation), by observing the same ensemble from a (sufficiently) different aspect or observing an adjacent area of the scene with the same statistical properties.

In section 2.1.4, the statistics of the ensemble of a large number of small scatterers at fixed

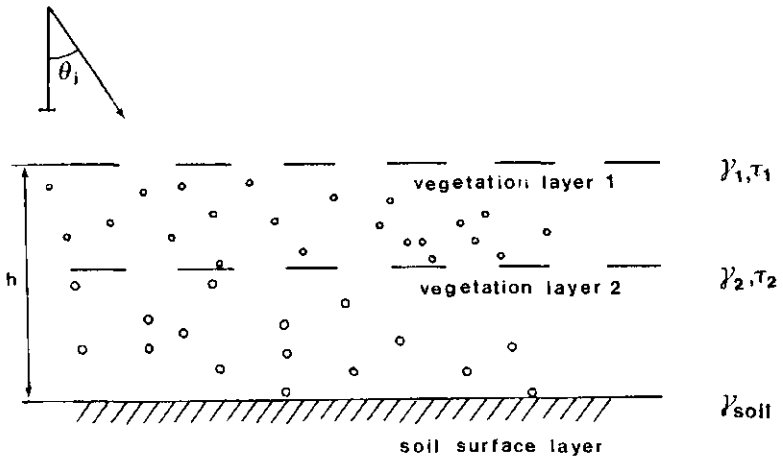

Figure 3.1. Two–layer cloud model.

random positions were described. It was shown that the average (the mean backscatter value) contains all information on the target and can be estimated accurately only after averaging over an adequate number of independent realisations.

For airborne radar systems, averaging can also be achieved in a somewhat different way. As was noted in section 2.1.4, the backscattered signal decorrelates in azimuth direction when the sensor is moved about one half–antenna length in flight direction. Since the resolution cell is usually much wider than this half–antenna length, almost the same ensemble is observed but, as can be shown, a sufficient decorrelation is achieved because the ensemble is viewed from a slightly different aspect.

When the conditions for ergodicity do not hold for this process, however, the statistics of the ensemble are not necessarily identical to the statistics of the time signal as observed by a system operated in the SLR configuration. In fact, theory predicts that the time signal of the speckle in azimuth, as contrasted with the ensemble statistics, contains information on not only the mean backscatter level but also the geometric arrangement of scatterers at subresolution cell level. Those details of arrangement, which are not directly perceivable from either the image or the raw data, however, can be revealed to some extent through an analysis of the speckle.

Weissman and Johnson (1979) conducted a theoretical study on the measurements of sea wave spectra employing incoherent radar, e.g. an incoherent SLAR or an incoherent airborne scatterometer. (Incoherent in this context means that the transmitted microwaves

are not coherent from pulse to pulse.) Their study indicates that the backscattered signal (in azimuth), when the sea surface is assumed to be effectively "frozen" in time, may contain information on very small spatial backscatter features of the sea surface, i.e. at the subresolution cell level. Experiments conducted at sea, however, have not yielded clear results (Peters, 1985; Pellemans, 1986). This is believed to be caused by the specific backscatter properties of the sea surface and the wave motions.

The author (Hoekman, 1989) recently elaborated on this theory for applications in forestry. Experimental evidence (discussed in section 6.5) is very compelling and demonstrates the feasibility of speckle analysis techniques for forests. The theoretical development is explained in Appendix II.

Theory shows that spatial information at the subresolution cell level is contained, in a statistical sense, in the power density spectrum of the azimuth signal of a system operating in the SLR configuration. This information takes the form of the autocorrelation function of the backscatter signature in azimuth and can be retrieved from the power density spectrum in a straightforward way (eq. II.14c, Appendix II). The author (Hoekman, 1989) showed that, if the antenna's azimuth directivity function can be assumed to have a Gaussian shape, the properties of the power density spectrum can be described in a relatively simple and easily comprehensible way (eq. II.27a). The statistics of the power density spectrum were also described by Hoekman (eq. II.34). On the basis of this statistical description (of speckle power density spectra), the accuracy of estimation of the autocorrelation function was assessed. Theory further indicates that spatial details, as expressed by the autocorrelation function, as large as the half–antenna length (a fundamental limit) can be resolved from speckle power density spectra (eq. II.31).

3.2 The effect of canopy height

3.2.1 The probing capability of Dutscat

Both the Dutscat scatterometer and the X–band SLAR are used to measure γ. There are some elementary differences, however. As noted above, the SLAR is an imaging system operating at a single frequency and a single polarization, whereas Dutscat is non–imaging and functions at six frequencies simultaneously in a selectable polarization combination (HH or VV).

Another difference between SLAR and the scatterometer (the multiband scatterometer as well as the prototypes) is not immediately apparent. It follows from differences in measurement geometry. The SLAR is usually operated from higher altitudes and the beam

width in range direction is considerably larger, making the illuminated spot width in the order of several kilometers, whereas it is in the order of several tens of meters for the scatterometer. As a result, contributions of scatterers from different horizontal layers in the forest will, in the case of a narrow–beam scatterometer, arrive somewhat separated in time at the receiver, as illustrated in figure 3.2.

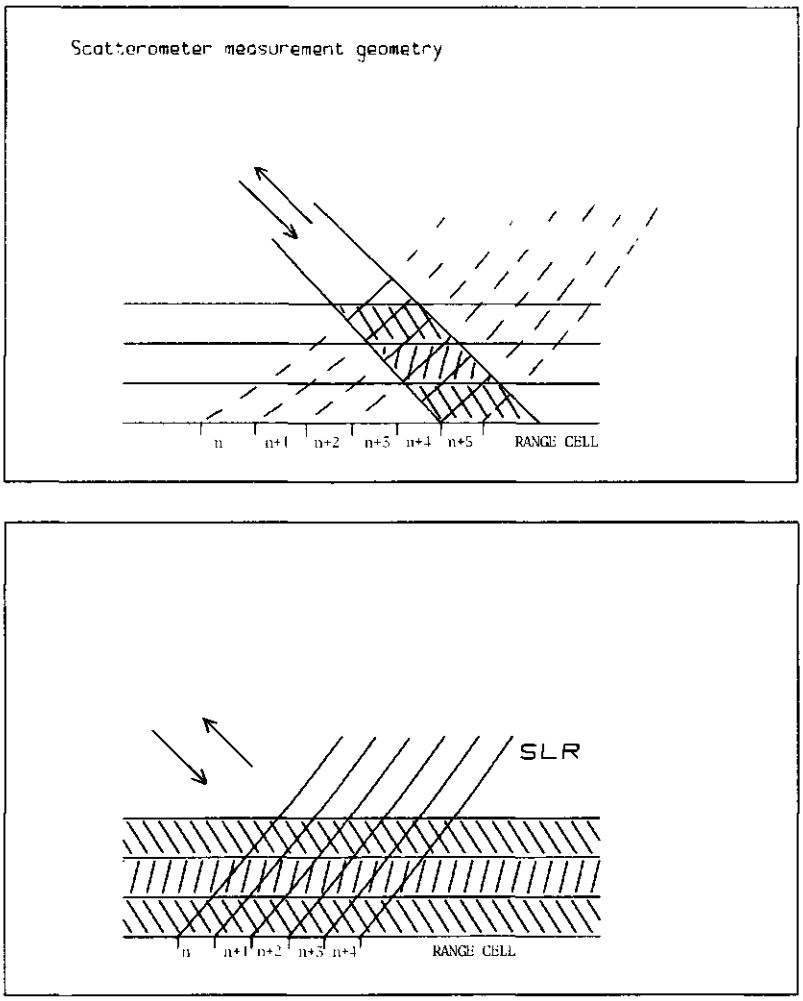

Figure 3.2 (a–b). Because of the relatively small beam width and low height of flight of the scatterometer (Dutscat), contributions of scatterers from different horizontal layers in the forest are measured in different range cells. For the SLAR system, all forest layers are (equally) represented in every range cell.

It turns out that the system can acquire information on the vertical distribution of backscattering. Through inversion of a multilevel model, introduced in section 3.2.2, γ can be divided into contributions of a number (typically three or four) of arbitrarily chosen forest layers. Hence the system is said to have a so–called "probing" capability. Results are shown in section 5.8. The possibility of distinguishing between sources of scattering can be used advantageously as it supports the model–making effort considerably (section 3.4).

On the other hand, this property makes the usual method of signal processing of Dutscat data of non–forested areas questionable for Dutscat data of forests. Simulations based on the same multilevel model will make this point clear. A simple and accurate new approach for the computation of γ for forests (or other thick vegetation covers) from scatterometer data is given in section 3.2.3. Experimental results are compared with results obtained from the (less appropriate) processing used for other types of targets (section 3.2.4).

3.2.2 The analysis of forest scatterometer data using a multilevel model.

When solving the radar equation for airborne radar data, backscattering is assumed to originate from a certain plane or surface. Because of relevant height differences of scatterers in a forest volume, this assumption is easily violated. When operating at relatively low altitudes and with small beam widths in range direction, as with Dutscat, height differences of scatterers in a forest have to be taken into account to avoid major errors. This phenomenon can be studied by assuming that scattering takes place at a number of homogeneous isotropically–scattering flat surfaces. As a first step, the actual pulse shape and delay time of the radar return are calculated for a single surface and the effect of flight altitude deviations is analysed.

For a transmitted pulse with shape $P_t(t)$ and antenna pattern with shape $G(\theta,\varphi)$, the equation for the received pulse follows from the radar equation and integration over the illuminated area (Ulaby et al., 1982, p.573):

$$P_r(t) = \iint_{\substack{\text{illuminated}\\ \text{area}}} \frac{P_t(t-T)\cdot G^2(\theta,\varphi)\cdot \lambda^2 \sigma^\circ}{(4\pi)^3 r^4}\, dxdy \qquad (3.8)$$

where T is the delay time, t is the time, θ is the cross–track (or range) direction, φ is the along–track (or azimuth) direction, λ is the wavelength and r is the distance. The antenna gain may be separated into components in the θ and φ directions:

$$G(\theta,\varphi) = G_0 \cdot g_\theta(\theta)\cdot g_\varphi(\varphi) \qquad (3.9a)$$

where $g_\theta(\theta)$ and $g_\varphi(\varphi)$ are directivity functions with maximum value unity and G_0 is the maximum gain. For the Dutscat, it can be shown that, as a result of the narrow beams for all six frequencies, the along–track differential distance dx can be approximated by

$$dx = r d\varphi. \tag{3.9b}$$

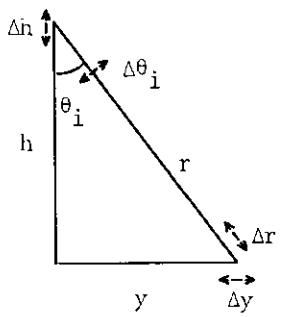

Figure 3.3. Dutscat measurement geometry with height of flight (h), distance sensor–target (r), ground range distance (y) and angle of incidence (θ_i).

With $r = \frac{1}{2}cT$ and $y = (r^2 - h^2)^{\frac{1}{2}}$ (figure 3.3), the cross–track differential distance dy can be written as

$$dy = dT \frac{c}{2\sin\theta_{\text{inc}}}. \tag{3.9c}$$

Here

$$\sigma^0 = \gamma \cdot \cos\theta_{\text{inc}} \tag{3.9d}$$

(γ is the modified differential scattering cross section per unit projected area),

$$P_t(t) = P_{tm} \cdot p(t), \tag{3.9e}$$

where P_{tm} is the maximum value of the transmitted power and $p(t)$ has a maximum value of unity, and

$$\theta_{\text{inc}} = \theta_{\text{inc}}(T) = \arccos(\frac{h}{r}) = \arccos(\frac{2h}{cT}). \tag{3.9f}$$

On substituting equations 3.9a–f, equation 3.8 can be rewritten as

$$P_r(t) = \frac{\lambda^2}{16c^2\pi^3} P_{tm} G_0^2 \int g_\varphi^2(\varphi) d\varphi \int \frac{p(t-T) \cdot g_\theta^2(\theta(T)) \cdot \gamma(\theta_{\text{inc}})}{T^3 \tan\theta_{\text{inc}}(T)} dT \tag{3.10}$$

The factors before the second integral are constants for each band and polarization. The factors in the second integral (a convolution) determine the actual shape of the radar return signal. For the Dutscat, the factor $p(t)$ may be approximated by the Gaussian function

$$p(t) = \exp\left[-\ln(2)\,\frac{t^2}{(\frac{1}{2}\tau)^2}\right] \tag{3.11a}$$

whereas the factor $g_\theta^2(\theta)$ may be approximated for the Dutscat by the Gaussian function

$$g_\theta^2(\theta) = \exp\left[-\ln(2)\,\frac{(\theta_{\rm inc}-\theta_{\rm t})^2}{(\frac{1}{2}\theta_{\rm B})^2}\right] \tag{3.11b}$$

where the pulse length τ is 100 ns, $\theta_{\rm t}$ is the antenna tilt angle ($\theta=\theta_{\rm inc}-\theta_{\rm t}$) and $\theta_{\rm B}$ is the two–way cross–track beam width, which is 2.4° in the C–band with HH polarization and 13.0° in the L–band with HH polarization.

With small beam widths $\theta_{\rm B}$ in the range direction, the factor γ, which is a function of $\theta_{\rm inc}$, may be approximated as a constant value. Especially for the C–band and higher frequencies, this seems to be a fair assumption. Equation 3.10 can thus be written in a concise notation as

$$P_{\rm r}(t) = \gamma k I_0(t) \tag{3.12}$$

with

$$k = \frac{\lambda^2}{16 c^2 \pi^3}\, P_{\rm tm} G_0^2 \int g_\varphi^2(\varphi)\, d\varphi$$

(k is a constant for each band and polarization) and

$$I_0(t) = \int \frac{p(t-T)\cdot g_\theta^2(\theta(T))}{T^3 \tan\theta_{\rm inc}(T)}\, dT$$

For a homogeneous isotropically–scattering surface, the shape of the return signal, $I_0(t)$, is shown as a function of range distance in figure 3.4a (for L–band and HH polarization). The large arrow indicates the position of the centre of the beam, the small arrows the ± 3° and ± 6° beside centre points. The differences in distance to the radar within the illuminated spot cause the strongest returns from an area just before the position of the centre of the beam on the surface.

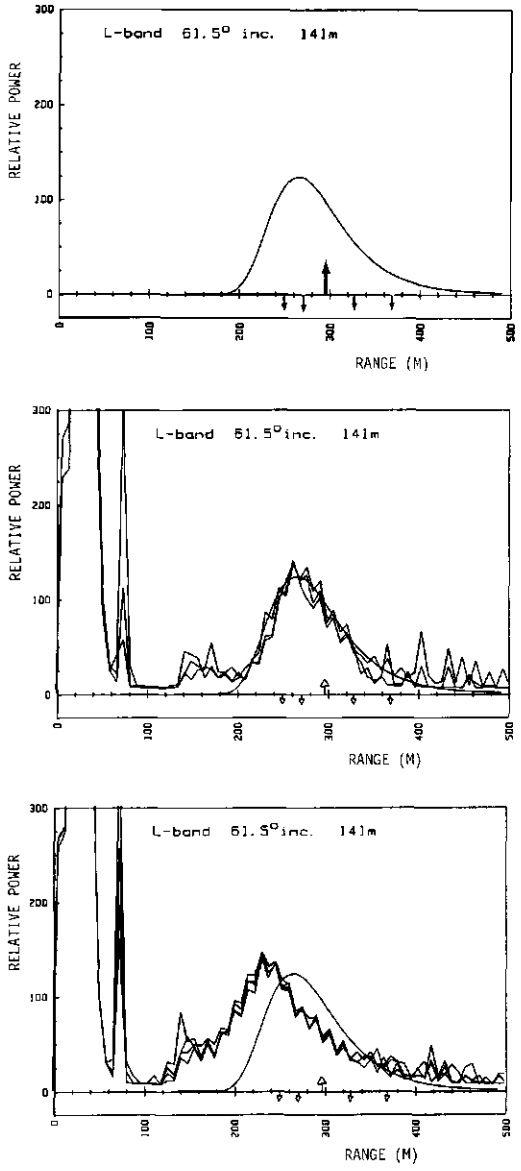

Figure 3.4. **(a)** Simulated radar return signal (expressed as relative power at a linear scale) as a function of range from a homogeneous isotropically–scattering flat surface in L–band at 61.5° angle of incidence and a 141 m altitude.

(b) Measured returns from a grass field are drawn together with the simulated return of (a). The strong signal at the left is the calibration signal which is a part of the transmitted pulse fed directly back to the receiver through a delay line. The signal between 140 and 160 m range distance is caused by the first hit on the ground. The grass field return between 200 and ≈350 m closely matches the simulated return. The signal peaks at range distances exceeding 350 m are artefacts introduced by the receiver.

(c) Measured returns from a poplar field are drawn together with the simulated return of (a). Note that also in this case the first hit on the ground is visible.

Actual measurements of a grass field approximate the simulated return very well (figure 3.4b). A stand of poplars next to the grass field, measured in the same run at the same incidence angle and altitude, yielded a significantly different return. The received signal was wider and delay time was less, as is apparant from figure 3.4c. (All signals are scaled to the same level.)

Unlike the situation for most other types of targets, scatterers of a forest canopy, with a significant height with respect to aircraft altitude, cannot be assumed to be concentrated on a horizontal plane without introducing gross errors in the radar equation. To describe the return of a forest stand more accurately, a simple model is therefore introduced. Figure 3.5 shows how a stand of poplars with a tree height of 27 m is modelled as a collection of four scatter planes at 9 m intervals. All scatterers are assumed to be located on one of the four planes.

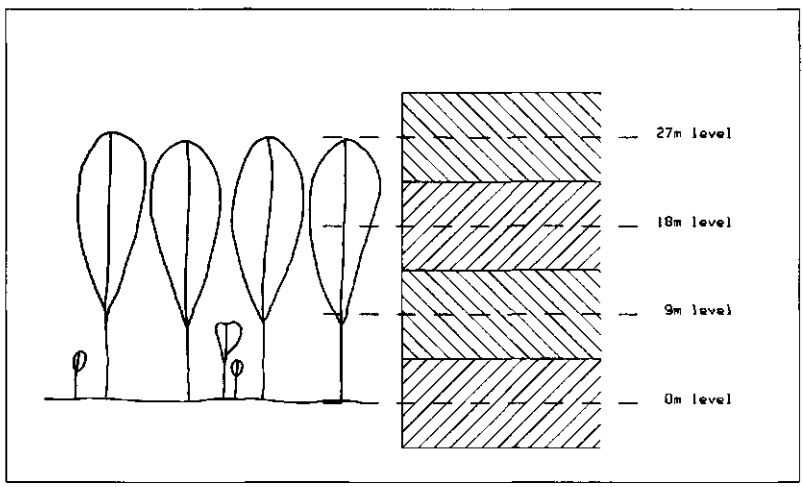

Figure 3.5. In the multilevel model, all scatterers within a certain layer of the forest canopy are assumed to be located on a single plane. In the four–level 9 m spacing model, all scatterers between 27 ± 4.5 m are assumed to be located on the 27 m level, the scatterers of the 18 ± 4.5 m layer on the 18 m level, etc.

In general, the return $P_{rf}(t)$ for a forest modelled as a collection of n equidistant scatter planes is thus formulated as

$$P_{rf}(t) = \sum_{i=0}^{n-1} A_i k I_i(t) \tag{3.13a}$$

with the coefficients A_i representing the contribution of each scatter plane to γ:

$$\gamma = \sum_{i=0}^{n-1} A_i \tag{3.13b}$$

and in the integrals

$$I_i(t) = \int \frac{p(t-T) \cdot g_\theta^2(\theta(T))}{T^3 \tan\theta_{inc}(T)} \, dT \tag{3.14}$$

with $\theta_{inc}(T) = \arccos(2h_i/cT)$, h_i represents the altitude of the sensor above the corresponding scatter plane.

For a homogeneous isotropically–scattering surface, the shape of the return signal, $I_0(t)$ (for L–band and HH polarization), is shown as a function of range in figure 3.6a as level 0 (the ground). Again, the large arrow indicates the position of the centre of the beam, the small arrows the ± 3° and ± 6° beside centre points. In figure 3.6a, the individual radar returns from each of the other three planes of figure 3.5 are also shown. The return signal of level 3 (tree tops), or $I_3(t)$, which is closest to the radar, is the strongest, the narrowest and has the shortest delay time. The return from level 0, or $I_0(t)$, is the weakest, the widest and has the longest delay time. In figure 3.6b, simulated returns for the same levels are drawn for a different frequency (C–band) and a different incidence angle (16.5°).

In figure 3.7a, the same simulated returns are drawn and compared with the actual returns of the grass field (figure 3.7b) and the poplar stand (figure 3.7c). As expected, the return of the grass field closely matches the return of level 0 from the model. The poplar return shows a second peak matching the level 2 return from the model. Apparently there are contributions from the ground as well as from scatterers near the 18 m level. Near the 27 m and 9 m levels, the returns are clearly weaker. In this instance, contributions of scatterers from several layers can be separated at first glance. This is not true, however, of the example given in figure 3.4c (i.e. the L–band at a large incidence angle).

An objective way to separate returns from distinct arbitrary levels in actual measurements

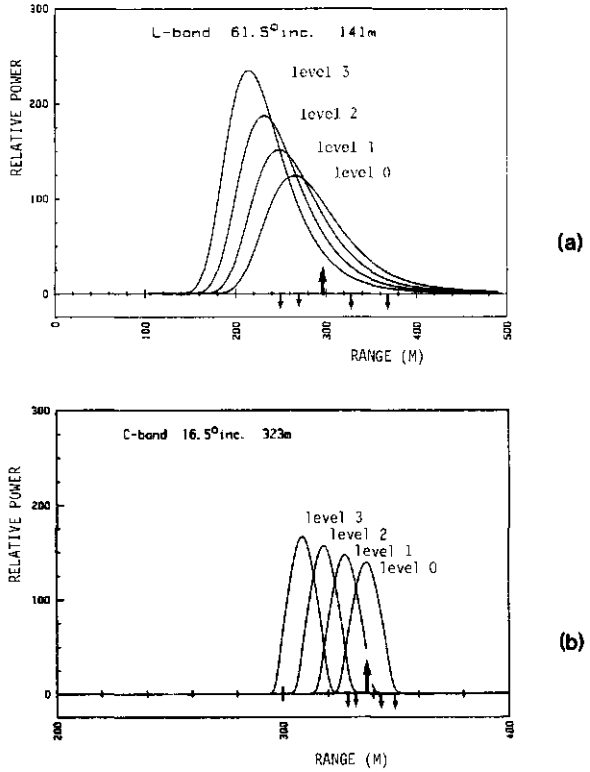

Figure 3.6. **(a)** Simulated radar return signals (relative power at linear scale) as a function of range for identical homogeneous isotropically–scattering flat surfaces in L–band at 61.5° angle of incidence. The height of flight is 141 m above level 0, 132 (=141–9) m above level 1, 123 (=141–18) m above level 2 and 114 (=141–27) m above level 3. The large arrow at a range of 295 m indicates the position of the centre of the beam, the small arrows the ± 3° and ± 6° beside–centre points.

(b) As in (a), but in the C–band at 16.5° angle of incidence. The height of flight is 323 m above level 0, 314 m above level 1, 305 m above level 2 and 296 m above level 3.

Table 3.1. Correlation matrices of estimates for L–band , HH polarization, 14.5° angle of incidence and 250 m flying height.

CORRELATIONS OF ESTIMATES

(a) four–level 9 m spacing model

0	1.00			
1	–0.78	1.00		
2	0.52	–0.80	1.00	
3	–0.31	0.51	–0.78	1.00

(b) three–level 12.5 m spacing model

0	1.00		
1	–0.52	1.00	
2	0.23	–0.51	1.00

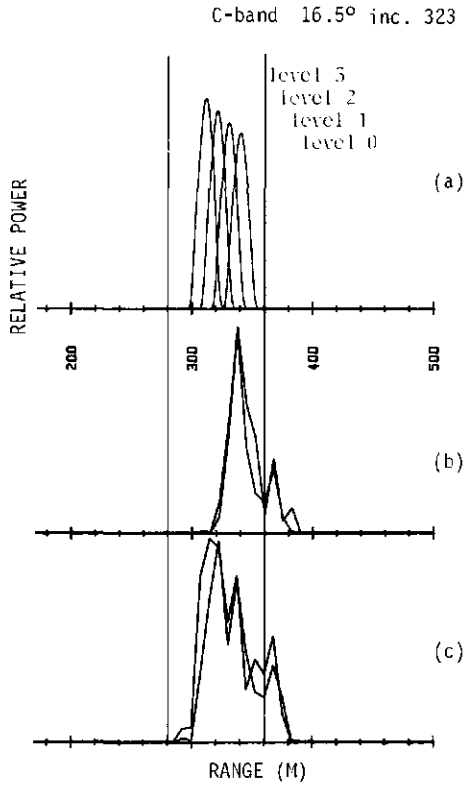

Figure 3.7. **(a)** Simulated radar return signals (relative power at linear scale) originating from four equally distanced identical planes in C–band at 16.5° incidence angle. The height of flight is 323 m above level 0, 323–9 m above level 1, etc.

(b) Measured returns from a grass field. The largest signal peak closely matches the simulated return of level 0. The signal part exceeding a range distance of 360 m is an artefact introduced by the receiver.

(c) Measured returns from a poplar field. Two peaks are visible. The first matches level 2; the second one level 0. Again the signal part exceeding a range distance of 360 m is an artefact.

is through inversion of the multilevel model. Since the n–level model equation (eq. 3.13a) contains n unknown coefficients A_i, at least n independent samples of the return signal are needed to solve these coefficients from the model. The calculation of the coefficients together with their confidence intervals is most effectively done by applying linear regression analysis techniques.

The choice of the number of levels and level spacing (the scatter planes do not necessarily have to be equidistant) in the multilevel model for a specific case depends on several factors (flight geometry, height of forest, confidence level, etc). When returns from the scatter planes are highly correlated, as in figure 3.6a, it is difficult to estimate the individual returns following the model prediction. A strong correlation in the individual returns results in a strong correlation between the estimates of the coefficients A_i. The correlation matrix for the estimates for this case is shown in table 3.1a. The estimates are negatively correlated in pairs. This means that, for example, an overestimation of A_0 is easily compensated by an underestimation of A_1 (r=–0.78), which in turn can be compensated by an overestimation of A_2 (r=–0.80), etc. When using a three–level model with 12.5 m spacing, the correlation matrix for the estimates, in table 3.1b, shows lower correlations and correspondingly higher significances for the estimates.

The correlation matrix of the estimates of A_i (or the covariance matrix of the model returns), together with the number of samples and speckle level, can serve as a measure to indicate the minimum level spacing allowed when a certain accuracy is specified. Since the correlation of the returns, as well as the number of relevant samples, are influenced by flight geometry, the degree of separability of the radar return in contributions of individual forest layers is an element of experiment design.

Some experimental results for several poplar stands measured in L– and C–bands with HH polarization at 60° and 15° incidence angle are discussed in section 5.8. These results should be interpretated with care, however, since there are some limitations inherent to inversion techniques of this type. The multilevel model is a simple scatter model designed to make an inversion of the received signal possible without additional data and to obtain a more elaborate geometric correction in the radar equation. But distinguishing between contributions of multiple scattering and contributions of single scattering, for example, is hardly possible.

3.2.3 Accurate computation of gamma

The computation of γ (according to eq. 3.13b) is a tedious task since contributions of a number of horizontal layers have to be determined first. On the other hand, the "standard" processing procedures can be followed, in which γ is directly related via the radar equation (eq. 3.10) to the returned power signal. The term "standard" applies to all data processing methods based on the usual form of the radar equation (eq. 3.8), which is limited to cases where all scatterers may be assumed to be located on a single surface. This procedure is far less complicated, but does not account properly for forest height. This raises the question of under which circumstances standard processing is allowed for forests.

The importance of this question can be illustrated by the following simulation based on the multilevel model. The relative contributions, the coefficients A_i, of a poplar stand 'Robusta' at C–band, 16.5° incidence and HH polarization have been established experimentally (figure 5.21a). These are: level 0 =43%, level 1 =7%, level 2 =48% and level 3 =2%. When these numbers are used in equation 3.13a for the four–level case, this equation can serve as a model for simulation purposes. In figure 3.8a, the return signal is simulated for a 9 m level spacing at a flight altitude of 323 m (compare with figure 3.7c). Figure 3.8b shows the return signal when the level spacing is ignored. Since for the C–band the maximum level of power can be related directly to γ, according to standard preprocessing models, it is clear from this example that the γ value will be underestimated by approximately 2.4 dB. In figure 3.8c, the simulated return signal for the 9 m level spacing at a flight altitude of 1800 m is shown. This is the maximum altitude at this angle of measurement for the specified maximum range of operation. Figure 3.8d shows the simulated return signal at this flight altitude when the level spacing is ignored. The underestimation of γ is 1.3 dB. Although the error decreased as a result of the increased flight altitude, it still cannot be ignored.

In general, the error made when height differences between relevant scatterers are not accounted for is difficult to predict. The error becomes negligible when all contributions originate from a thin layer. This situation might occur when (1) the forest is very low or (2) the forest has a closed and smooth canopy and attenuation is very strong (at the higher frequencies). When the canopy is not closed, has a rough surface (emergent trees), or the attenuation is not strong (lower frequencies), however, the effect is far from predictable.

It will be shown that when a different approach is followed, however, a significant improvement in accuracy can be achieved in a simple way. In this approach, γ is no longer related to the backscattered power (via the radar equation) but to the backscattered energy. Integration in the time domain of equation 3.13a results in

$$\int P_{rf}(t)dt = \sum_{i=0}^{n-1} A_i k \int I_i(t)dt. \tag{3.15}$$

If the (mathematical) condition

$$\int I_0(t)dt \simeq \int I_1(t)dt \simeq \cdots \simeq \int I_{n-1}(t)dt \simeq J_{eff} \tag{3.16}$$

holds, then

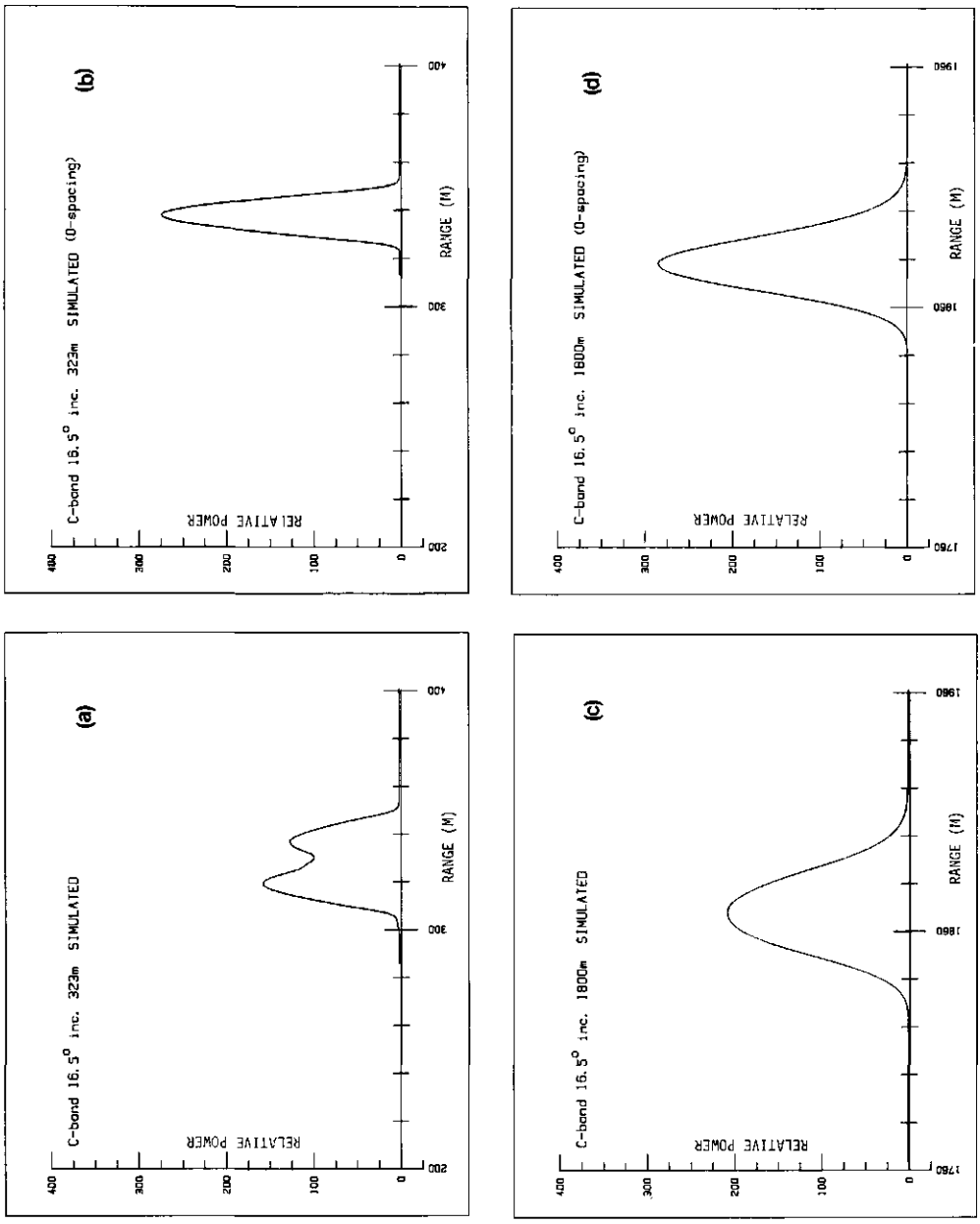

Figure 3.8 (a–d). Simulated radar returns (relative power at linear scale) from a poplar 'Robusta' stand based on the multilevel model shown as a function of range distance. In (a) and (b) the returns are compared for the C–band, 16.5° incidence angle and an altitude of 323 m where, respectively, the level spacing is kept at 9 m and in the second the level spacing is ignored. In (c) and (d) the simulation is repeated for an altitude of 1800 m.

$$\gamma = \sum_{i=0}^{n-1} A_i \simeq \frac{\int P_{rf}(t)dt}{kJ_{eff}}. \tag{3.17}$$

This is actually a more general form of the radar equation. It can be shown that when level spacing is reduced to zero, the usual form of the radar equation (eq. 3.10) follows as a special case.

At this point, it is already possible to indicate qualitatively why this approach is more accurate (see figure 3.6b). The condition in equation 3.16 means that the areas under the four curves shown have to be approximately equal to get an accurate result. But when the standard approach is followed, the values of the four curves at a specific point (distance) have to be approximately equal to get a good result, and this is clearly not the case here. The accuracy of the new approach can be quantified by examining the condition in equation 3.16. With

$$a = \frac{\ln 2}{(\frac{1}{2}\tau)^2}, \quad b = \frac{\ln 2}{(\frac{1}{2}\theta_B)^2} \tag{3.18a,b}$$

the integrals of equation 3.16 can be written as

$$\int I_i(t)dt = \iint \frac{\exp[-a(t-T)^2]\cdot\exp[-b(\theta_{inc}(T)-\theta_t)^2]}{T^3\tan\theta_{inc}(T)}\, dTdt. \tag{3.19}$$

With $\cos\theta_{inc} = 2h_i/cT$, T can be written as

$$T = 2h_i/(c\cdot\cos\theta_{inc}) \tag{3.20a}$$

and dT as

$$dT = \frac{2h_i\cdot\sin\theta_{inc}}{c\cdot\cos^2\theta_{inc}}\, d\theta_{inc}. \tag{3.20b}$$

It follows that

$$\int I_i(t)dt = \frac{c^2}{4h_i^2}\left[\frac{\pi}{a}\right]^{\frac{1}{2}} \int_{-\pi/2}^{\pi/2} \exp[-b(\theta_{inc}-\theta_t)^2]\cos^2\theta_{inc}d\theta_{inc}. \tag{3.21}$$

No exact analytical expression can be given for this integral. When b is large and the antenna tilt–angle θ_t is not very small, however, a very good approximation is given by

$$\int_{-\pi/2}^{\pi/2} \exp[-b(\theta_{\rm inc}-\theta_{\rm t})^2]\cos^2\theta_{\rm inc} d\theta_{\rm inc} \simeq$$

$$\cos^2\theta_{\rm t} \int_{-\pi/2}^{\pi/2} \exp(-b\theta_{\rm inc}^2) d\theta = \left[\frac{\pi}{b}\right]^{\frac{1}{2}} \cos^2\theta_{\rm t}. \qquad (3.22)$$

Therefore, for actual measurements in the C–band and higher–frequency bands, a very good approximation for the integrals of equation 3.16 follows as

$$\int I_{\rm i}(t)dt \simeq \frac{c^2 \pi \cdot \tau \cdot \theta_{\rm B}}{16\ \ln 2 \cdot h_{\rm i}^2} \cos^2\theta_{\rm t}. \qquad (3.23)$$

It is clear from this equation (together with eqs. 3.16 and 3.17) that the only important design factor is $1/h_{\rm i}^2$. For Dutscat, angle of incidence or beam width (C–band and higher) does not influence the accuracy! Equation 3.23 allows the experimenter to predict the maximum error when this new approach is followed. This will be illustrated with the next example.

Suppose the radar signature has to be determined of an area with tropical rainforest with emerging trees up to 40 m tall. The flight altitude is 900 m. In the worst case, one assumes (for some reason) that all backscatter originates from a layer at 20 m, but actually all backscatter originates from a layer at 40 m. The factor $J_{\rm eff}$ in equation 3.17 that should therefore be used corresponds to an $h_{\rm i}$ of 860 m, but instead an $h_{\rm i}$ of 880 m is used. The error in $J_{\rm eff}$, and therefore also in γ, is only a factor $(880/860)^2$ or 0.20 dB. This is far less than the maximum error one can expect when standard preprocessing is applied. This is shown experimentally below.

3.2.4 Experimental results of gamma computations

Some of the results of a Dutscat C–band scatterometer flight are shown in figure V.11 (App. V). In these figures, γ values computed with the standard processing technique are compared with values computed with the new (and more appropriate) approach.

In figures V.11a and V.11b, results are shown for a stand with a mixture of beech (*Fagus sylvatica*) and oak (*Quercus robur*) and a stand of Norway spruce (*Picea abies*). These stands have a low height, less than 10 m, and both approaches therefore yield accurate results. The differences are small. In figures V.11e and V.11n, for example, differences are clearly visible. These poplar stands, with a height of 27 m, have non–negligible height

differences between relevant scatterers.

The differences in figure V.11e can be elucidated from figures 3.7c, 5.21a and 5.21e, since these figures are based on the same measurements (it is the same stand). At an angle of incidence of 16.5°, the return signal of this poplar stand clearly shows two peaks (figure 3.7c), and, according to the multilevel model assumptions, almost half of the backscatter originates near the ground level and the other half originates near the 18 m level (figure 5.21a). The standard procedure cannot handle this situation and makes an underestimation of almost 2 dB (figure V.11e). At 30° the error is the same, but at 45° and higher the error is small. The reason is that at these angles the vertical penetration depth is less (figure 5.21e), and the height differences between relevant scatterers are therefore much smaller. Note that the angular dependence of γ may differ significantly between the two approaches.

3.3 The effect of canopy attenuation

3.3.1 Transmissivity measurements

Experiments with large corner reflectors placed on the forest ground surface were conducted in an effort to gain more insight into the attenuating properties of the forest canopy. The experiments were carried out with the SLAR for several tree species. The measurement set–up, the experiment design and data analysis are discussed below. The parameter estimated with this technique, the (equivalent) two–way canopy transmissivity τ_e, is important in most backscatter models. Direct assessment of this parameter may support the model–making effort considerably (section 3.4). To elucidate the general set–up of these experiments, the measurement geometry of the first experiment performed at 14 August 1984 (see section 4.2) is outlined in section 3.3.2 as an example. The major considerations and restraints with respect to experiment design, the backscatter signal description and the procedure adopted for estimation of the parameter τ_e are discussed in subsequent sections. The experimental results are discussed in section 5.4.

3.3.2 Corner reflectors and measurement set–up

Three "45 dBm^2" and three "38 dBm^2" corner reflectors were manufactured especially for this experiment. They were made of 3 mm thick aluminum plates, with triangular sides and rectangular bottom plates. The lengths l of the edges of the plates were 1.425 m and 0.930 m, respectively. The maximum of the radar cross section (main direction) in free space of such corner reflectors is given by the equation

$$\sigma_c = 0.691 \cdot l^4 \cdot 4\pi/\lambda^2 \quad [m^2]. \tag{3.24}$$

σ_c is usually expressed at the logarithmic dB scale. (Since the dimension of the radar cross section is m^2, the dB value is denoted as dBm^2.) It follows that σ_c = 45.4 dBm^2 for the three 1.425 m reflectors and σ_c = 38.0 dBm^2 for the three 0.930 m reflectors. Angular patterns for this type of corner reflector were derived by Keen (1983). Construction tolerances can be found in the report of Barnes (1981). For corner reflectors of this size, it is difficult to satisfy the required tolerances and maintain them during transport and operation. For this reason, the reflectors were disassembled for transport. They had to be reassembled in situ and adjusted until flatness and orthogonality of the constituent plates were within the required limits.

The SLAR experiment was carried out four times. The general set–up was the same for all corner reflector measurements. The only variable during the course of these experiments was the flight altitude. Since the SLAR was not absolutely calibrated, the measurements had to be combined with an external calibration measurement. The set–up of the calibration corner reflectors and the large forest corner reflectors is depicted schematically in figure 3.9. The height of flight was 600 m. The angle of the incident beam at the reflectors was 45° grazing angle. The calibration corner reflectors (with radar cross sections of 25 dBm^2 and 31 dBm^2) were placed on a short–cut grassland. Three corner reflectors (of 45 dBm^2) were placed on the forest floor in a stand of poplar. The other three large corner reflectors (of 38 dBm^2) were placed in a stand of oak.

3.3.3 Experiment design

The design of the measuring set–up was not a straightforward one since conflicting constraints had to be met. These can be indicated by means of the well–known radar equation:

$$P_r = \frac{P_t \cdot \lambda^2 \cdot G^2}{(4\pi)^3 \cdot d^4}\,\sigma, \tag{3.25}$$

in which the expectation of σ of a uniformly distributed target is the product of the differential radar cross section σ^0 and the resolution cell area A_{res}:

$$\langle\sigma\rangle = \sigma^0 \cdot A_{res} \tag{3.26}$$

with (see section 2.1)

$$A_{res} = \theta_B \cdot d \cdot c\tau/(2 \cdot \cos\theta_{gr}). \tag{3.27}$$

For the Dutch X–band SLAR, $\theta_B = 10$ mrad (two–way antenna beam width) and $c\tau/2 = 7.5$ m (the range resolution).

The constraints to be met were:

(1) A precise calibration measurement demands the radar cross section of the reflector to be substantially higher than the radar cross section σ_b of the background (i.e. of background resolution cell). Since $\sigma_b = \sigma_b^0 \cdot A_{res}$, this can be achieved by choosing a background target with a low value of σ_b^0 (e.g. short–cut grassland) and/or making A_{res} small by choosing a short distance d. Basically, the same is true for the attenuation measurement, but then the attenuated signal from the reflector has to be significantly stronger than the background signal (i.e. the signal of the forest stand of interest). The radar cross section of the background may not always be low, however, and in the design phase the attenuation factor is unknown.

(2) The precision can be increased by averaging independent samples. The longer the distance d, the more independent samples can be obtained.

(3) According to the link budget of the SLAR (Hooijmans, 1984), the received power P_r has to be kept below –30 dBm to avoid distortion of the received signal.

(4) The design of flight geometry has to include desired incidence angles and spatial resolutions for the objects of interest.

As a result, the most critical element in the design is the size of the corner reflectors. Another critical element is the sensor–target distance d, which affects the ratio between reflector signal level and background signal level, but also the number of independent samples. One has to optimize here and consider the link budget. For calibration measurements, preferably, a background area with a low σ_b^0 must be selected. For attenuation measurements, a basic expectation of the possible range of transmissivity is desirable. As became evident in retrospect, on the basis of the experimental results obtained, the chosen corner reflector sizes were fairly appropriate.

3.3.4 Corner reflector signal

The received power P_r, by definition, is related to the radar cross section σ through the radar equation (eq. 3.25). For a fixed measurement set–up, P_r is therefore a constant times σ. The radar measures power. A comparison of measured power with the (theoretical) strength of the return signal of a corner reflector has to be made on a common basis. This

may be done either on a power basis, by expressing the radar cross sections of the reflectors as a power level (via the radar equation), or vice versa, by expressing all power samples as σ values (via the same radar equation). The latter approach was chosen.

In the following parts of this section, σ values thus relate to single power samples and not to averaged power or to the expectation of power, as usually is the case.

With

σ_c as the radar cross section of the corner reflector,

σ_b as radar cross section (related to a single sample of the received power) of the background, $p(\sigma_b)$ is assumed to be Rayleigh distributed and

σ_{b+c} as the radar cross section (related to a single sample of the received power) of the background plus reflector, the backscatter signal of a "calibration" reflector on a Rayleigh fading background may be described as follows.

The electromagnetic field strength, near the receiver, is the sum of a component with a constant amplitude (from the reflector) and a component with a Rayleigh distributed amplitude (from the background). The phase difference between these components is random. The compound signal, as detected by an envelope detector, is known to be Rician distributed (Rice, 1945). The probability distribution of the received power P_r (and thus σ_{b+c}), as measured with the square law detector of the SLAR, can be calculated from the Rician distribution as

$$P(\sigma_{b+c}) = \frac{1}{\bar{\sigma}_b} \exp\left[-\frac{\sigma_{b+c} + \sigma_c}{\bar{\sigma}_b}\right] \cdot I_0\left[\frac{2\sqrt{\sigma_{b+c} \cdot \sigma_c}}{\bar{\sigma}_b}\right], \tag{3.28}$$

where $I_0()$ is the modified Bessel function of order zero. It can be shown that

$$\sigma_{b+c} \neq \sigma_b + \sigma_c \quad \text{and} \quad E(\sigma_{b+c}) = E(\sigma_b) + \sigma_c. \tag{3.29}$$

The distribution of the average of n independent samples of σ_{b+c} can be calculated through numerical analysis, but is cumbersome.

To describe the backscatter signal of a forest reflector, the following quantities are defined.

τ_e is the equivalent (two–way) transmissivity for this measurement set–up,

σ_{ca} $= \tau_e \cdot \sigma_c$ is the hypothetical radar cross section of a corner reflector in free space multiplied by the factor τ_e and

σ_{b+ca} is the radar cross section (related to a single sample of the received power) of a corner reflector under an attenuating forest canopy.

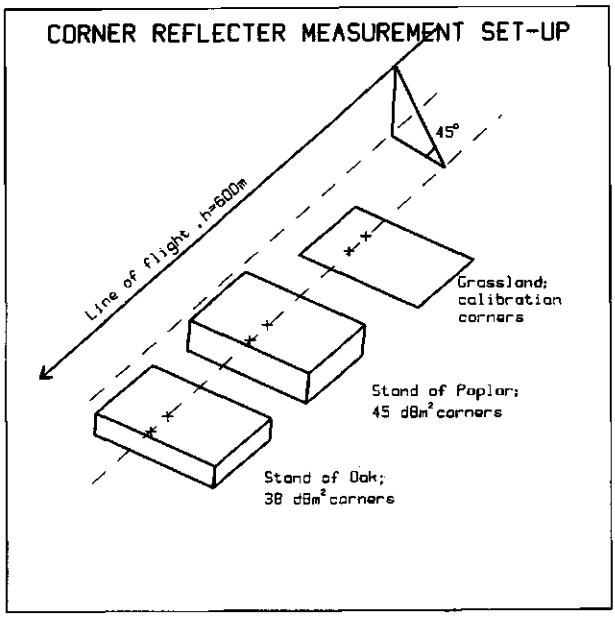

Figure 3.9. Measurement set–up for the 1984 corner reflector experiment. Absolute values of radar cross section have been determined by means of a set of calibration corner reflectors. Forest canopy transmissivity has been calculated from the responses received from large corner reflectors on the forest ground surface.

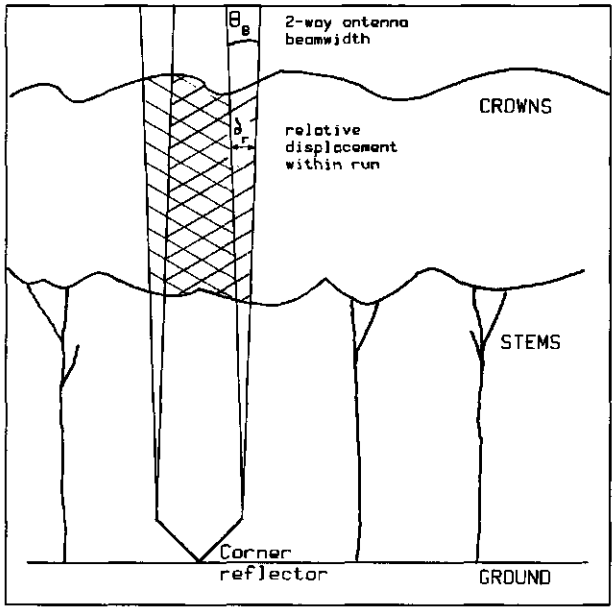

Figure 3.10. The relative displacement δ_r, within one run, of a hypothetical column of particles located between corner reflector surface and sensor.

Since the physical mechanism of canopy transmissivity is still largely unknown, the distribution of σ_{b+ca}, unlike the distribution of σ_{b+c} (eq. 3.28), is unknown.

Before describing the estimation of τ_e, it is useful to consider the measurement geometry and, in particular, the effect of the small changes in measurement geometry related to successive samples of the backscatter signal within one recording. The raw SLAR data were used in the analysis. It is noted that the shape of the response in azimuth direction (flight direction) of a point–like object, such as a corner reflector, is determined by the antenna pattern. Since sampling in azimuth direction is done every 0.5 m, and the (–3 dB, two–way) width of the illuminated spot typically is in the order of 10 to 30 m, the antenna pattern, notably the main lobe, may be obtained from the raw data.

Two typical examples of azimuth signals are shown in figure 3.11. The upper curve in this figure shows a measurement of a reflector placed within a poplar stand at the Roggebotzand site (14 August 1984, recording Rbz16). Since the (two–way) antenna beam width of the SLAR is 10 mrad and the distance target–sensor is 1000 m, there is a –3 dB width of the reflector response (in azimuth direction) of 10 m. The lower curve in figure 3.11 shows a measurement of a reflector placed within a pine stand at the Kootwijk site (11 July 1985, recording Kw3). Since the distance target–sensor is larger (3000 m), the response is wider (30 m) and the level lower (in both cases the 45 dBm^2 reflectors were used).

A simple analysis of the azimuth signals yielded the following results. The standard deviation of the (attenuated) reflector response plus background, relative to a fit of the known antenna pattern and within the –3 dB width of the expected reflector response, ranges from ≈1 to ≈4 dB. The smaller values were found when the reflector response was relatively strong compared with the background. The standard deviation of the Rayleigh fading background was found to be ≈5.6 dB (and in agreement with theory; see Appendix I). When the influence of the background signal is taken into account, the standard deviation of the signal component originating from the reflector is relatively low. It may therefore be concluded that effects of fading between the signal component originating directly from the reflector surface and (hypothetical) signal components originating from object–reflector interactions are small.

In addition to effects of fading, the attenuated reflector response is influenced by changes in (the expectation of) τ_e. These changes result from changes of sensor aspect, as may be explained as follows. The particles determining the factor τ_e are localized in a small volume, smaller than the volume of the "three–dimensional resolution cell" (the volume determined by beam width and pulse length). This hypothetical volume of particles can be imagined as a column between the reflector's surface and the sensor. Changes in sensor

aspect may result in a change of the (statistical) properties of particles within this (relatively small) hypothetical volume. Even for a forest stand that is homogeneous at the scale of the resolution cell, the factor τ_e, as measured with this set–up, may depend locally on the relative position of the reflector with respect to the position of trunks, crowns and gaps in the canopy and on the direction of measurement. During a SLAR recording, a series of independent measurements is made through slightly different paths. Depending on canopy height and antenna beam width, as depicted in figure 3.10, the relative displacement of the hypothetical column of particles, denoted as δ_r, can be expressed as

$$\delta_r = \theta_B \cdot h_c / \sin\theta_{gr},$$

$$\text{with } h_c = \text{canopy height.} \tag{3.30}$$

For the SLAR, dependent on canopy height, δ_r ranges from 15 to 40 cm. This is small compared with the width of the corner reflector (or the hypothetical column of particles). Since the composition of the attenuating particles and their relative orientations are not expected to vary much (in a statistical sense) within one recording, the (expectation of the) factor τ_e is not anticipated to vary much either.

The combined effect of fading and (statistical) changes of τ_e, within one recording, was small. As discussed above, the standard deviation of the attenuated reflector signal ranged from ≈1 to ≈4 dB. Since many independent samples were taken (typically in the range of 10 to 30), and applying the central limit theorem, the average of the attenuated signal (expressed as $\bar{\sigma}_{b+ca}$) could be estimated accurately. The typical accuracy was found to be within ± 1 dB limits, depending on the ratio of reflector and background signal levels and the number of independent samples.

A new SLAR recording covering the same track, however, may yield more relevant changes in orientation of the sensor with respect to gaps and crowns in the canopy. Differences in elevation angle of the sensor and heading of the aircraft can be in the order of a few degrees, which is much more than θ_B (which is 10 mrad or 0.57°). The relative displacement of the attenuating (hypothetical) volume between runs may thus be in the order of five times as large as the within–run displacement. Especially when large trees are measured, different results for different runs may therefore be obtained.

This view is consistent with the experimental results discussed in section 5.4. Significant between–run variations of the estimated parameter τ_e appeared, which could be explained qualitatively from a change of sensor aspect angle and canopy features.

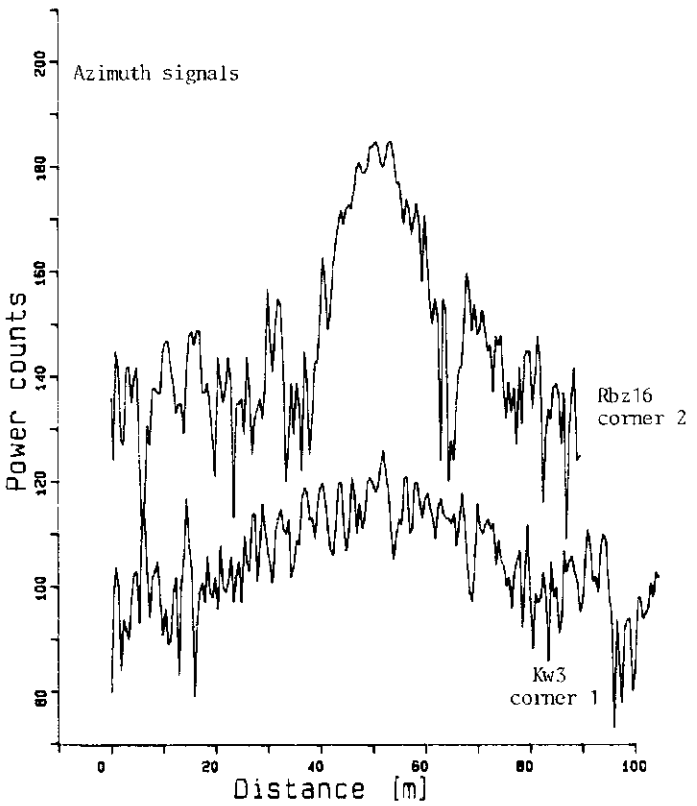

Figure 3.11. Azimuth signals of forest stands with corner reflectors. The upper signal is a measurement of a 45 dBm^2 reflector placed on the ground in a stand of poplars in the Roggebotzand site. The lower signal is a measurement of a 45 dBm^2 reflector placed in a stand of Scots pine in the Kootwijk site. The Kootwijk measurement took place at a larger distance d (Kootwijk d=3000 m; Roggebotzand d=1000 m) and therefore the signal level is lower and the reflector response wider. One power count in the raw data (logarithmic scale) equals 0.3 dB.

3.3.5 Estimation of transmissivity

The external calibration procedure will not be discussed here. It is assumed that from estimations of σ_b and σ_{b+c}, and using equation 3.29, the SLAR can be accurately calibrated for the grazing angle at which the reflectors are observed (45°, see figure 3.9). As a result, absolute values can be determined for σ_b and σ_{b+ca} and the maximum radar cross section, denoted σ_{max}, that can be measured according to the link budget.

The mean level of the background signal (denoted as $\bar{\sigma}_b$ in this section) can be estimated very accurately (averaging is done over thousands of independent samples obtained from the forest stand). If the azimuthal response resulting from attenuated reflector signals is clearly perceivable because of a relatively low background level, a fairly good estimate of the mean value of σ_{b+ca} (denoted as $\bar{\sigma}_{b+ca}$ in this section) can be made by fitting this pattern with the expected azimuth antenna pattern (as discussed above).

The parameter τ_e can be estimated very simply if $\bar{\sigma}_{b+ca}$ is much larger than the background value $\bar{\sigma}_b$. Then, following the definition given above, $\bar{\sigma}_{b+ca} \simeq \sigma_{ca} = \tau_e \cdot \sigma_c$ and the estimation of τ_e follows directly as

$$\tau_e \simeq \bar{\sigma}_{b+ca}/\sigma_c. \tag{3.31a}$$

In most instances, $\bar{\sigma}_{b+ca}$ is not significantly larger than $\bar{\sigma}_b$ and this simple solution is thus not generally applicable. A general solution proceeds as follows. It may be assumed that the variation of the compound signal resulting from background fading (which is assumed to be Rayleigh fading) is independent of the variation resulting from changes in τ_e. Using these assumptions and the central limit theorem, it can then be shown that (however, the exact distribution of the compound signal is unknown):

$$E(\sigma_{b+ca}) = \sigma_c \cdot E(\tau_e) + E(\sigma_b) \tag{3.31b}$$

and an estimation of τ_e follows as

$$\tau_e = \frac{\bar{\sigma}_{b+ca} - \bar{\sigma}_b}{\sigma_c}. \tag{3.31c}$$

If the attenuated reflector signal response is not perceivable, or not clearly perceivable to such an extent that an accurate estimation of $\bar{\sigma}_{b+ca}$ is possible, upper limits for τ_e may be established. Using radar target detection theory (Meyer and Mayer, 1973), perception limits can be established mathematically for targets (using mathematical fluctuation models) in a Rayleigh fading background. This point was indicated by Hoekman (1986a) but will not be discussed here. The following rule has been adopted for this analysis: If a reflector response is not (clearly) perceivable, the level of $\bar{\sigma}_{b+ca}$ is assumed to be less than 3 dB above the background level, or, $\bar{\sigma}_{b+ca} \leq 2 \cdot \bar{\sigma}_b$. Using this assumption, the upper limit for τ_e can be estimated as

$$\tau_e < \bar{\sigma}_b/\sigma_c. \tag{3.31d}$$

The empirically established values of τ_e are listed and discussed in section 5.4.

3.4 Concluding remarks

The parameter τ_e, the equivalent two–way canopy transmissivity, as estimated according the procedure discussed in section 3.3, is related to the parameter τ (or τ_t) of the cloud model. If the cloud model assumptions are acceptable, i.e. only single scattering is present and mutual electromagnetic coupling between scatterers (e.g. between reflector and trunks) can be neglected, the parameters τ and τ_e have the same physical meaning.

When more experience is gained with the cloud model (which has been introduced as a first step in the quantitative description of forest backscatter), these assumptions may appear to be too rough. In that case, other measurement methods (e.g. too avoid coupling) and or other (more elaborate) models may be utilized. Other, more elaborate models, for example as described by Eom and Fung (1984) or Engheta and Elachi (1982), describe the interaction in a somewhat different way (section 7.2).

Also the multilevel model introduced in section 3.2 is compatible with the cloud model. Like the cloud model, the multilevel model cannot properly distinguish between contributions of multiple scattering and single scattering. If multiple scattering can be ignored, however, the backscatter contributions of forest layers in the multilevel model have the same physical meaning as the backscatter contributions of layers in a corresponding multilayered cloud model.

For example, for a three–level model, γ is the sum of the coefficients A_i (eq. 3.13b):

$$\gamma_{\text{total}} = A_2 + A_1 + A_0. \tag{3.32}$$

This subdivision of gamma (according to the assumptions of the multilevel model and cloud model) can be related directly to the subdivision made in a two–layer cloud model.

$$\gamma_{\text{total}} = \gamma_1 + \tau_1\gamma_2 + \tau_1\tau_2\gamma_{\text{soil}}. \tag{3.33}$$

When the coefficient A_0 is assumed to correspond to the ground surface contribution, then

$$\gamma_1 = A_2, \tag{3.34a}$$
$$\tau_1\gamma_2 = A_1, \tag{3.34b}$$
$$\tau_1\tau_2\gamma_{\text{soil}} = A_0, \tag{3.34c}$$

and (as noted above)

$$\tau_t = \tau_1\tau_2 = \tau_e. \tag{3.34d}$$

The levels in the multilevel model do not necessarily have to be equidistant and may be adapted to the object's geometry.

According to cloud model assumptions, measurements of forest backscatter, estimations of forest layer backscatter contributions and estimations of transmissivity may thus be connected and may provide a first step in the quantitative description of the forest backscatter interaction mechanism.

4. MEASUREMENT CAMPAIGN AND DATABASE

4.1 The test sites

The forest sites selected for this research are in the central part of The Netherlands. Two test sites were selected in Flevoland and two in The Veluwe (figure 4.1). The province of Flevoland comprises two polders reclaimed from the IJsselmeer. This freshwater lake was formed in 1932 when the Zuyder Zee, a large bay containing brackish to salt water, was enclosed. The topsoil of Flevoland originates from marine sediments. The Veluwe region is in the province of Gelderland and features the largest forested region in The Netherlands. The soils are developed in coarse and fine Pleistocene sands.

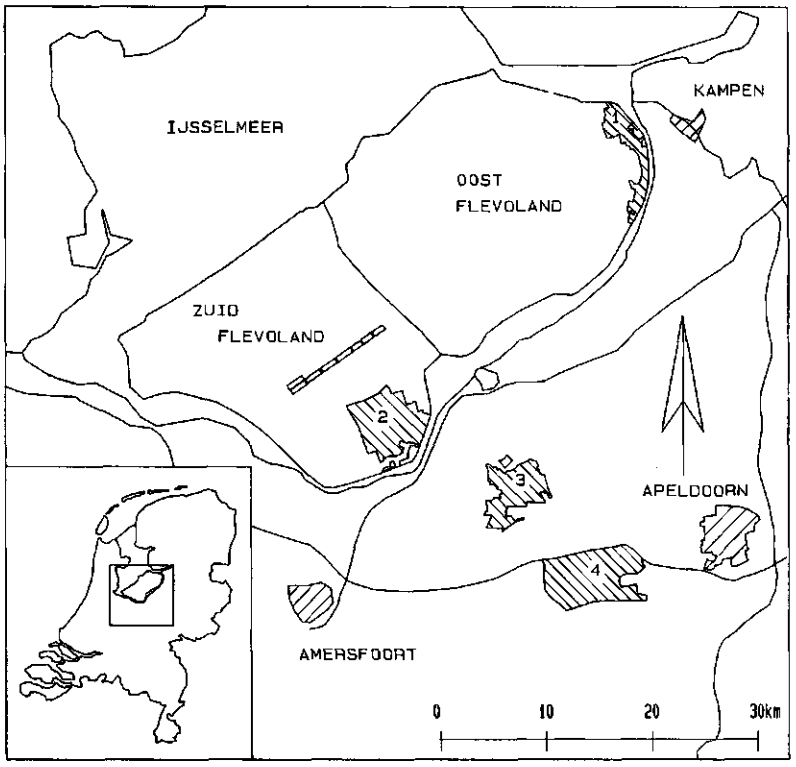

Figure 4.1. Location of forest test sites: (1) Roggebotzand, (2) Horsterwold, (3) Speulderbos and (4) Kootwijk. Maps of the test sites are included in Appendix IV.

The Roggebotzand site

The eastern Flevoland polder, reclaimed in 1957, comprises two forest districts managed by the State Forest Service: the "Roggebotzand" and the "Reve/Abbert" (figure IV.1, Appendix IV). These forests were planted in the period 1958–1962 and contain mainly poplar, pine and spruce stands. Other deciduous species are present, but they account for a small fraction of the total area. The soil consists of calcareous fine loamy sand from a Holocene sediment and can be classified as a Calcaric Fluvisol (World Soil Map). The soil profile is homogeneous and physically ripened. The ground water level varies in depth between 40 cm (winter) and 110 cm (summer) during the year. Since research at this site focused on the Roggebotzand part, this site, throughout the thesis, is referred to as "the Roggebotzand site".

The Horsterwold site

The other forest test site in Flevoland, the Horsterwold, is in the southern Flevoland polder, reclaimed in 1966 (figure IV.2). The forest is still managed by the IJsselmeerpolders Development Authority. Planting started in 1973. When completed, the forest will cover 4000 ha and will be the largest deciduous forest in the country. The site comprises large numbers of poplar stands and stands of other deciduous species such as willow, elm, beech, oak, alder, maple and ash. A small number of spruce and pine stands are present. The soil consists of fine loamy sand that originates from reworked Pleistocene sands. It can be classified as a Calcaric Fluvisol (World Soil Map). The ground water level varies in depth between 80 cm (winter) and 180 cm (summer) during the year. The construction of ditches and canals changed the original local profile by bringing up fine to coarse sands. The thickness of this layer varies (between 0 and 20 cm).

The Speulderbos site

The Speulder and Sprielderbos forest district in The Veluwe is managed by the State Forest Service (figure IV.3). Its area is 2390 ha and it contains many species in many age classes. Scots pine, Douglas fir, Japanese larch, beech and oak stands prevail. Corsican pine, European larch, Norway spruce and grand fir stands occur less frequently. Within the Speulderbos, there are some large old beech forests with a total area of 345 ha. These forests have been managed for hundreds of years. The structure in some parts of the old beech forests resembles to some extent that of natural forests. There are heathlands north and east of the forest district. The forest district comprises areas with loamy fine sands and areas with coarse sands. The sands belong mainly to preglacial fluviatile sediments shaped into low hills by the Saale ice sheet (ice–pushed ridge of Garderen). Soil classification (World Soil Map) distinguishes in this district a Leptic Podzol and Humic Podzol. The

depth of the ground water is in excess of 2 to 3 m. Since research in this forest district focused on the Speulderbos part, this site is referred to as "the Speulderbos site".

The Kootwijk site

The Kootwijk forest district, managed by the State Forest Service, covers 3070 ha and is also in The Veluwe (figure IV.4). The forest district comprises some large areas of heathland and bare inland dunes. The research was carried out at the western part of the forest district, the "Loobosch". The Loobosch contains principally Scots pine stands planted in the period 1929–1933. The Loobosch comprises a region of forested inland dunes in a moderately undulating region with fine sands. The soil may be classified as Arenosols (World Soil Map). The level of the ground water is mostly deep, in excess of several meters.

These four test sites together comprise a large range of species, age classes, soils and various environmental conditions. Stand areas typically range from one to several hectares, which is quite small but normal for large parts of Europe. The Roggebotzand and Horsterwold sites are representative for Flevoland, the Speulderbos site for The Veluwe. The soil of the Kootwijk area is unique, and trees in this area do not exhibit vigourous growth. Moreover, the Loobosch forest appears to be in relatively bad condition lately. One of the presumed causes may be an excessive ammonia deposit originating from intensive cattle farming in the area west of the Loobosch.

One image for each test site is briefly described below. The images are shown in figures 4.2 (a–d) and correspond to the maps of the test sites (App. IV). All images are displayed in such a way that the near range is at the top and the far range is at the bottom.

SLAR image Roggebotzand

An X–band SLAR image of the Roggebotzand, collected on 14 August 1984, is shown in figure 4.2a. The white line at the top is the nadir–line corresponding to track number 6 (see figure IV.1). The eastern part of the eastern Flevoland polder, with the Roggebotzand, Revebos and De Abbert forests and an agricultural area, is clearly shown. The black areas bordering the polder are open water bodies. The image shows the Ketelmeer, Vossemeer and Drontermeer lakes and the IJssel river–mouth. Grasslands south of Kampen appear in relatively dark tones. Within the forested areas, poplar stands can be differentiated by their relatively light tones. As a result of their height, poplar stands in this image are often associated with radar shadow (black strips behind the stands) and noticable effects of foreshortening (the stand borders viewed by the radar show a relatively light tone). Spruces and pines have a relatively dark tone.

SLAR image Speulderbos

On the same date, 14 August 1984, the SLAR image of the Speulderbos site (figure 4.2b) was obtained. The two large dark areas in the top left and middle bottom are heathlands. There is an agricultural area at the left. Isolated rows of trees, notably in the far range (the bottom of the image), show up clearly because of the effects of radar shadow and foreshortening. Within the forest, an area of oak stands has relatively light tones. The small black vertical stripes in the far range are artefacts introduced in the processing and caused by rapid changes in aircraft attitude (pitch, roll and yaw).

SLAR image Kootwijk

The SLAR image of the Kootwijk site (figure 4.2c) was also obtained on 14 August 1984. The Loobosch is in the centre of the image. The major roads through the forest are clearly visible. In the top right, a highway (two parallel black lines) and railway (a white line parallel to the highway) can be seen. Some heathlands along the railway and bare sands in the bottom right appear in dark tones. The white spots within the bare sand area are isolated groups of Scots pine trees. The pylons of a power line are visible in the midle. The area in the left is agricultural and is used for intensive cattle farming.

SLAR image Horsterwold

The SLAR image of the Horsterwold site (figure 4.2d) was obtained on 11 July 1985. The pattern of forest stands is clearly visible. The dark areas are the Nuldernauw and Wolderwijd lakes. Some other salient features are the city and harbour of Zeewolde (right), a holiday camp (the very bright area at the right border of the forest) and locks and a bridge (upper left).

Figure 4.2a. SLAR image of the Roggebotzand (image Rbz14; track 6; 14 August 1984). For description see text.

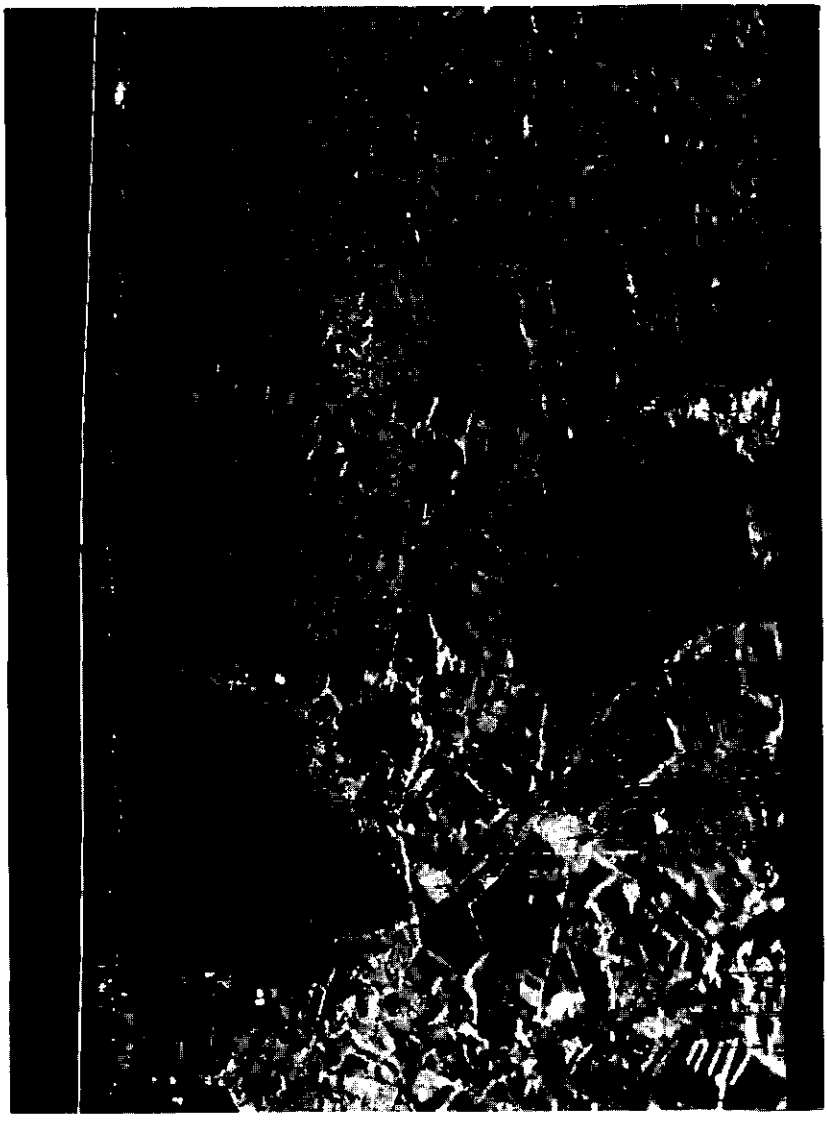

Figure 4.2b. SLAR image of the Speulderbos site (image Sp14; track 6; 14 August 1984). For description see text.

Figure 4.2c. SLAR image of the Kootwijk site (image Kwi: track 8; 14 August 1984). For description see text.

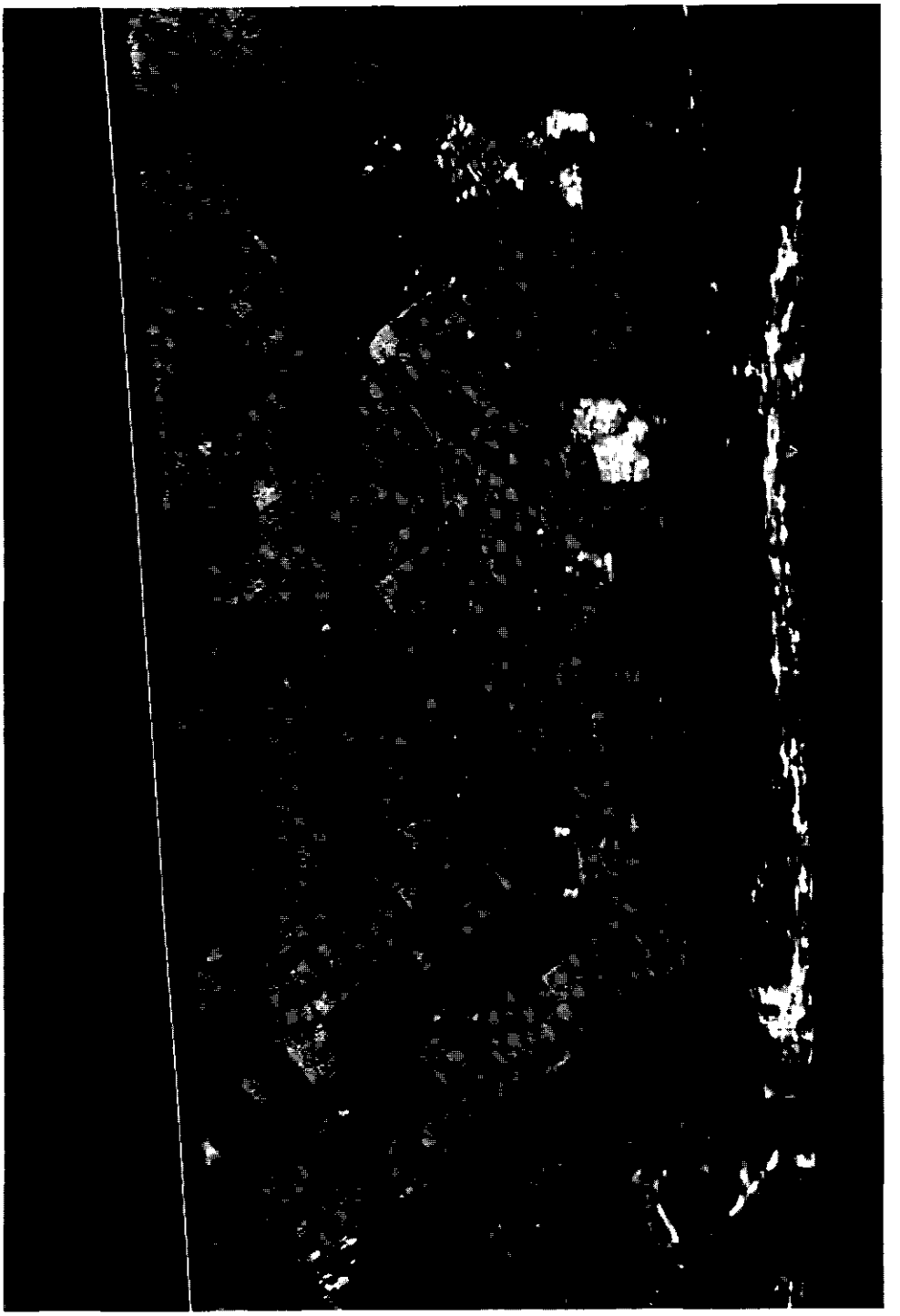

Figure 4.2d. SLAR image of the Horsterwold site (image Hw1; track 3; 11 July 1985). For description see text.

4.2 Data collection

4.2.1 Ground data collection approach

Studies conducted over the last 20 years have indicated that many (sensor and object) characteristics might affect the radar backscatter level of vegetation (Ulaby et al., 1986, Cihlar et al, 1987). Basically, the object should be described through its electromagnetic material properties and the spatial structure of its components (such as branches, leaves, the upper soil layer) and their spatial arangement. The effects of wind and water droplets, resulting from rain or dew deposition, might also cause noticable changes and therefore cannot be ignored in modelling studies.

Because of the potential complexity, it is still not clear which object characteristics, generally, are of (major) importance in vegetation backscatter models, how this depends on the characteristics of the sensor used and how they should be defined. Some insight has been developed on the basis of studies of agricultural crops. The scattering processes for forests, because of the presence of trunks and branches, are potentially far more complicated and have not been studied well. To date, the determining characteristics and mechanisms of forest backscatter are not clearly established. Another complicating factor in this area of research is the fact that many tree parameters are difficult to measure because of the large heights of trees. Furthermore, the large dimensions and complicated structure of trees, compared with for example agricultural crops, make measurements tedious and time consuming. At this stage of research, many object parameters were of potential interest. Because of the great difficulties involved in actual measurements or even the definition of many of the object parameters, a compromise with the practically feasible had to be made.

The only pragmatic way to proceed was to focus on the assessment of qualitative or empirical relationships between the microwave data and those object parameters that are relatively easy to assess. For future experiments, when a more profound basic understanding of the interaction mechanism is developed (one of the objectives of this project), the requirements for ground data collection can be defined better.

4.2.2 Reference data and meteorologic constraints

Since manpower was very limited in this project, an intensive ground data collection programme could not be carried out. Only those data that were relatively easy to assess or were already available in some form (maps, stand registers) were collected. A list of stand and tree parameters used is given in table 4.1.

Table 4.1. Object parameters and units

stand parameters:		
Age	number of years after planting	[year]
V	volume (of woody material)	[$m^3 \cdot ha^{-1}$]
I_m	mean annual increment (of woody volume)	[$m^3 \cdot ha^{-1} \cdot year^{-1}$]
N	number of trees	[ha^{-1}]
G	basal area	[$m^2 \cdot ha^{-1}$]
N_{cr}	number of crowns in upper canopy	[ha^{-1}]
R_{ct}	ratio N_{cr}/N	
tree parameters:		
h_{dom}	dominant height (expectation of maximum tree height on are)	[m]
dbh	diameter at breast height (1.30 m)	[cm]
cd	crown depth	[m]
cc	crown cover	
d_{cr}	diameter of crowns in upper canopy	[m]
nn	number of years of green needles	

Maps

Forest maps (1:10,000), topographic maps (1:25,000) and soil maps were collected for all four sites. These maps show the locations, dimensions and numbers of compartments and subcompartments, and provide data on tree species, varieties and the year of planting. Additional information can be found for forest stands with a mixed species composition (usually the species are identified and the degree of mixing is indicated) or a different type of management (e.g nature reserve areas).

Stereo aerial photographs

Substantial information could be obtained from stereo aerial photographs through visual interpretation and by simple photogrammetric techniques. Sets of recent aerial photographs were made available by the State Forest Service, the forest districts and the Agricultural University. To complement the existing data, additional sets of aerial photographs were obtained, as listed in table 4.2. Aerial photographs can be used to determine the actual dimensions of stands and to assess the current situation. Recent cutting activities and new plantings, which are usually not indicated on the most recent forest map, can be detected. The degree of homogeneity of the structure of the forest canopy can also be determined. Stands with major irregularities (large gaps or local differences in structure) can thus be recognized and discarded (or partially discarded) from further analysis. Many structure–related characteristics of the canopy can be quantified, such as the mean dimensions of crowns (d_{cr}) or the number of crowns in the upper canopy (N_{cr}).

Table 4.2. Overview of aerial photograph sets collected for this project. The Speulderbos site is encoded as Sp, the Roggebotzand site as Rbz and the Kootwijk site as Kw.

date	site	scale	type
1982 July 8	Sp	1:30.000	70 mm panchromatic with extended red
1982 July 9	Sp	1:30.000	70 mm infrared black & white
1982 July 14	Rbz	1:8.000	9 inch true color transparent
1984 July 8	Rbz and Sp	1:5.000	70 mm panchromatic with extended red
1984 August 14	Sp	1:5.000	70 mm panchromatic with extended red
1985 July 24	Kw	1:16.000	70 mm panchromatic with extended red and 70 mm black & white infrared

Stand registers

The forest districts' stand registers include many potentially relevant stand and tree data, but registers differ somewhat between the districts. The stand registers usually supply data for every subcompartment on the year of stand planting, timber volume (V), mean annual increment of this volume (I_m), the number of trees (N), basal area (G), tree height (h_{dom}), trunk diameter at breast height (dbh) and information on management, selective cuttings, diagnostics, etc. These data are not updated very frequently. In the worst instance, they were ten years old. Thus many stands were remeasured in the Speulderbos and Kootwijk sites, but many of the Roggebotzand site data were current.

In situ measurements

The Japanese larch at the Speulderbos site (table V.3), the Scots pine at the Kootwijk site (table V.5a), the Scots pine at the Speulderbos site (table V.5b) and the poplar clones 'Robusta' and 'Heidemij' at the Roggebotzand site (table V.1) were selected for empirical model studies (section 5.3). Only these species at these sites were represented by a fair number of (large and homogeneous) stands with a significant variation in age and/or a number of stand and tree parameters. Potentially relevant stand characteristics at the Speulderbos site were either measured (or remeasured) in situ or extracted from the stand registers; for the Kootwijk site, all data were acquired in situ; for the Roggebotzand site, no measurements were required since up–to–date data for all 'Heidemij' and 'Robusta' stands were available from the forest district.

For the study of radar image texture (section 6.4), forest structure had to be assessed to select areas with clear differences in spatial structure. To this aim, transect drawings were made of some selected areas in the "Drieersingels" beech forest complex at the Speulderbos

site. Large–scale aerial photographs of this area were also supportive in this respect. For the study of speckle spectra properties (section 6.5), mainly at the Horsterwold site, a description of the spatial characteristics of the forest structure was necessary; accurate row spacing measurements and transect drawings were made

Qualitative descriptions (and photographs) were made of the phenologic stage at all dates of radar measurements for all tree species of interest and for all sites. Some additional observations were made (along with literature study and consultation with experts) to arrive at a qualitative or quantitative assessment of some additional (morphologic) tree characteristics which might be of relevance. These included leaf and needle dimensions, leaf inclination angle distribution or tree architecture. Further, explicit observations were made of those stands with (unexpected) differing backscatter properties.

Meteorologic constraints

Factors such as wind or the presence of water droplets are potentially relevant. The possible effects on the radar backscatter are likely to be very small in general, but these factors, in principle, cannot be ignored. The strategy adopted was to eliminate their possible effects as much as feasible. Thus the need to introduce extra parameters in describing the physical structure is avoided and the results become, in a way, more comparable and are interpretable with less ambiguity.

Especially when results from different dates are to be compared, as in the series of (multitemporal) observations in the 1982–1983 campaign (section 5.1), it is important to make measurements under comparable conditions. For all flights executed in the framework of this research programme, special attention was given to the meteorologic conditions. The long standby period of the aircraft, typically one or two weeks, made it feasible to select appropriate meteorologic conditions to a certain extent. All flights were performed under the condition that (1) precipitation on previous days was not large, (2) no water droplets were present on the vegetation and (3) windspeed was low and not expected to decrease significantly in the standby period. The first two constraints were met on all occasions. Windspeeds were lower than or equal to 3 m/s for the measurements of the 1982–1983 campaign, except for the March measurement (but at that time deciduous trees were bare) when windspeeds up to 5.5 m/s were measured at the local meteorologic stations. For the 1984 and 1985 flights, windspeeds were measured in the range of 2 to 6 m/s, with the exception of the 28 August 1985 measurement. On that occasion a windspeed of 8 m/s was measured for Roggebotzand at the time of radar measurement, but the windspeed for Speulderbos at the time of radar measurement (one to three hours later) did not exceed 4 m/s.

4.2.3 Overview of SLAR and Dutscat measurements

SLAR 1982–1983

During the period June 1982 to May 1983, four SLAR flights were made over the Roggebotzand and Speulderbos sites. The main objective was to study radar's potential use for tree species classification. The dates were selected to cover different phenologic stages; the effect of seasonal changes on the radar backscatter could be established and, consequently, the impact of the observation time or combinations of observation times on the accuracy of (multitemporal) classification could be assessed (section 6.1).

Periods in which the vegetation structure of the tree species involved is relatively stable in time are of principal interest. These periods are winter, when deciduous trees and needle–shedding larch are bare, and summer, when deciduous trees and larch have a complete coverage of green leaves and needles. Of course, the lengths of these two periods vary with climatic conditions. Three flights were selected in these two periods with relatively stable vegetation structures. Two flights were made in summer: one at the beginning of this period (15 June 1982) and one at the end (9 September 1982). The other flight was made in the winter (3 March 1983).

It is likely that the radar backscatter properties related to vegetation structure in such "stable" periods are also stable and not subject to (species–dependent) rapid changes. The assessment of classification potential is therefore likely to be more representative and repeatable and not likely to be subject to accidental conditions.

In other periods (spring and autumn), the vegetation is subject to rapid structure changes, as during the fourth flight (17 May 1983). Careful state–of–growth observations were made in order to study some structure–related effects, especially with regard to the formation of new leaves and needles.

There are some experimental results suggesting an effect of leaf orientation on the radar backscatter in the C– and X–bands (see also section 5.9.3) and at higher frequencies. The special care taken with meteorologic conditions was expected to make physical interpretations easier by reducing differences in leaf orientation resulting from the effects of wind and water droplets.

The flight patterns for the first two flights were the same: four tracks were flown at two different altitudes and at two different headings. The track locations and headings are indicated on the maps (App.IV). The track numbers, corresponding altitudes and image codes and flight numbers are given in table 4.3. Tracks were selected so that most forest

stands were viewed four times and at different grazing angles. Since the SLAR's image quality degraded significantly at grazing angles larger then ± 45° (because of the antenna's radiation pattern and the antenna tilt angle) and the resolution degrades with distance, the total range of grazing angles that could be used in practice was limited to approximately 10° to 40°. The third and fourth flights in March 1983 and May 1983 were executed slightly differently. Since the amount of radar data appeared to be sufficient, these were limited to two tracks per site and the position of one of the tracks in the Roggebotzand site was changed.

SLAR 1984

Before the execution of the next flight, in August 1984, the sample frequency of the SLAR receiver was increased from 20 MHz to 50 MHz (section 2.2). As a consequence, the range resolution of the SLAR improved from 15 m to 7.5 m and the number of independent samples per unit area was doubled. This modification had a major impact on the design and objectives of the 1984 experiments. Both test areas of the 1982/1983 campaign were revisited but tracks were chosen differently (see table 4.3 and maps). By concentrating on parts of the forest areas and measuring from lower altitudes and shorter distances, the azimuth resolution could be kept high (9 to 15 m). The combined effect —of increased spatial resolution in range (because of system modifications) and azimuth (because of measurement geometry), the increased number of pixels to represent the same area and the increased radiometric resolution (per unit area)— strongly enhanced the perception of spatial detail in the 1984 images. As a result, many of the smaller stands, ranging in size from ≈0.3 to ≈1.0 ha, could also be included in the analysis. This was especially advantageous for the Speulderbos site where a substantial part of the total area is covered by stands of these sizes. A second merit of the increased spatial resolution was the possibility of perceiving clearly different spatial patterns or textures within homogeneous forest areas. Image texture can, to some extent, be related to spatial forest structures and might be a useful image feature to discriminate between forest types or development stages. The 1984 images of the Speulderbos site were used to study this point (section 5.4).

An experiment with corner reflectors was conducted at the Roggebotzand site to assess canopy transmissivity values. An array of four small corner reflectors was placed on a large grass field just outside the forest for an absolute calibration, and two arrays of three large corner reflectors were placed on the forest floor in two forest stands to study the transmissivity properties of the canopy. In track number 8, which was flown two times, these corner reflector arrays were viewed at a 45° angle of incidence.

A new test site, the Kootwijk forest, was included. This site comprises a considerable number of Scots pine stands with an age of ≈55 years. Other object parameters varied over

a wide range and this site was therefore considered interesting for model studies. Only one track was flown at this site in 1984.

SLAR 1985

Two more SLAR system modifications were to follow, and again these had an impact on the design and objectives of the new (1985) experiments. These modifications (internal calibration and antenna tilt angle change) were discussed in section 2.2.

The internal calibration radiometrically links all images collected from different sites and/or different dates. Until 1985, this was not possible. Intercalibration, applied to the 1982/1983 SLAR dataset, could link images but only those of the same scene and the same date (section 4.2.5). This technique could not be used to link data from different sites and/or different dates. Since the links could be established with the system's internal calibration, it was decided to measure all test sites again. As a result, radar signatures from different sites could be compared and, because of the changed antenna tilt angle, these radar signatures could cover a larger range of grazing angles, approximately 10° to 65°.

The raw data of the 1985 measurements (with the calibration signal included) were also very useful for an analysis of speckle. The first analysis of speckle spectra had used 1984 data from the Roggebotzand site. The set–up of the 1984 experiments, however, was not the most appropriate for this analysis; the azimuth resolution was in a sense too good and the row spacing of the poplar stands investigated too large. As could be anticipated, these first results were not very convincing, but they showed the feasibility of the technique and provided the incentive to proceed. It was for this reason that a new (fourth) test site was selected: the Horsterwold forest in southern Flevoland. This site comprises many large and homogeneous forest stands, but in contrast to the Roggebotzand in eastern Flevoland, tree row spacings in different stands vary considerably.

A fortunate circumstance was the presence of many different poplar clones and other, not yet measured, tree species. Three tracks were flown over this site, as indicated on the map. Only track number 2, in which the central study area was measured at approximately 35° to 45° grazing angle, was used for speckle analysis. The other two tracks yielded measurements of the same area at approximately 15° to 20° and 50° to 65°. Radar signatures of many tree species could thus be measured covering a wide range of grazing angles.

Since the 1984 transmissivity measurements had been successful, it was decided to repeat this experiment two times in 1985 and to select other tree species. For the 1984 experiment, stands of deciduous species (oak and poplar) were selected at the

Table 4.3. Overview of SLAR flights. Recordings (or images) of the Roggebotzand site are encoded as Rbz, the Speulderbos site as Sp, the Kootwijk site as Kw and the Horsterwold site as Hw.

date	recording	SLAR track	altitude [m]
1982 June 15	Rbz1	1	800
flight 202	Rbz2	2	800
	Rbz3	3	2000
	Rbz4	4	2000
	Sp1	1	800
	Sp2	2	800
	Sp3	3	1000
	Sp4	4	1000
1982 September 9	Rbz5	1	idem
flight 216	Rbz6	2	
	Rbz7	3	
	Rbz8	4	
	Sp5	1	
	Sp6	2	
	Sp7	3	
	Sp8	4	
1983 March 3	Rbz9	3	1000
	Rbz10	5	1000
	Sp9	3	1000
	Sp10	4	1000
1983 May 17	Rbz11	3	idem
	Rbz12	5	
	Sp11	3	
	Sp12	4	
1984 August 14	Rbz13	7	600
flight 323	Rbz14	6	600
	Rbz15	3	1000
	Rbz16	8	600
	Rbz17	8	600
	Sp13	5	700
	Sp14	6	700
	Sp15	7	700
	Kw1	8	700
1985 July 9	Rbz18,Rbz19	9	850
flight 392	Rbz20,Rbz21	9	850
	Rbz22	9	850
1985 July 11	Rbz23	6	2250
flight 393	Rbz24	7	2250
	Sp16	5	2250
	Sp17	6	2250
	Sp18	7	2250
	Kw2,Kw3	8	2250
	Hw1	3	800
	Hw2	2	1400
	Hw3	1	2250

Roggebotzand site. For the two following experiments, stands with coniferous species were selected at the Roggebotzand site (Austrian pine and Corsican pine) and at the Kootwijk site (Scots pine). At the Roggebotzand site, all six large corner refectors were used on 9 July 1985. They were viewed from track number 9, a newly chosen track. Since in total only six corner reflectors were constructed, and the use of all six at each site was planned, an extra flight was necessary to transport the corner reflectors for reassembly at the other site. On 11 July 1985, two days later, they were used again at the Kootwijk site.

Dutscat 1984–1985

For the Dutscat measurements over forests, seven tracks were selected at the Roggebotzand site and four at the Speulderbos site. To cover the whole range of incidence angles and possible polarization combinations, measurements were initially scheduled for 15°, 30°, 45°, 60° and 75° incidence angles at both HH and VV polarizations. Since no measurement programme had ever been executed with Dutscat over land before, the feasibility of such measurements was questioned. Problems were expected related to the relatively small size of forest stands (compared with study areas at sea), the flight performance (stability of the aircraft's attitude and navigation) or the repeatability of the gamma measurements. For this reason, it was decided, until more experience was gained, to limit the number of tracks and to omit VV polarization (except at 45°) and to make all measurements four times.

In retrospect, this set–up was adequate. The repeatability of the γ measurements was good. Because of the high demands made on navigation accuracy and the aircraft's roll movements, a substantial number of stand measurements, especially at large incidence angles, failed (section 4.2.4). Only because of the repetition of measurements was a useful dataset obtained.

Table 4.4. Overview of Dutscat flights. The Roggebotzand site is encoded as Rbz and the Speulderbos site as Sp. The geograpic locations of the tracks are not included in this thesis.

date	flight	band	site	scatterometer tracks
1984 July 6	FL1508 /FL1509	C–	Rbz	2, 3 and 6
1984 September 6	FL1522	C–	Rbz and Sp	7 1, 2 and 3
1985 July 18	FL1584 /FL1585	L–	Rbz	1, 2 and 3
1985 July 19	FL1587 /FL1588	L–	Sp	1 and 4
1985 August 28	FL1595	C–	Sp	1, 2 and 4
	FL1596	C–	Rbz	7

An overview of Dutscat flights is given in table 4.4. In all flights, measurements of selected stands were made at 15°, 30°, 45°, 60° and 75° with HH polarization and at 45° with VV polarization. The first flight was made on 6 July 1984 at the Roggebotzand with the C–band. A second C–band flight followed at 6 September 1984 over the Roggebotzand and Speulderbos sites. During the second Roggebotzand flight, only one very large and isolated stand of poplars was measured at 45° incidence with HH polarization only, but with six different look directions (section 5.6). Because of a technical failure, the video recordings of the second C–band flight were of very bad quality and the time intervals of the measurements of selected stands were scarcely discernable. Only the large Roggebotzand stand and some of the larger stands in the Speulderbos could be processed. It was decided to repeat this C–band flight at the Speulderbos in 1985 (28 August). On that same date, the (successful) measurement with six look directions at the Roggebotzand was repeated, but at 30°, 45° and 60° incidence angles. Again the Roggebotzand flight was successful and, again, the Speulderbos flight failed, this time because of a technical failure in one of the digitizing units.

No major difficulties were encountered with the L–band measurements made at the Roggebotzand (18 July 1985) and the Speulderbos (19 July 1985). Because of the larger beam width of the L–band, the flights were made at lower altitudes, the smaller stands were excluded and the selection of tracks was somewhat different.

4.2.4 Notes on radar data quality

SLAR

The internal calibration that radiometrically links all images collected from different sites and/or different dates was not available until the last year of research (1985). An "intercalibration" technique, discussed in section 4.2.5 and Appendix III, was developed and applied to the 1982/1983 images. With this technique, an overall image offset level was determined by minimizing differences in gamma level of stands present in different images and observed at the same grazing angle and date. Images of the same scene and the same date could thus be radiometrically linked. The intercalibration technique could not be used to link data from different sites and/or different dates.

The results of internal calibration (an optional PARES product since 1985) and intercalibration (table 4.6) are in agreement. Both techniques show the same range of power offset variation between recordings. These are of the order of a few dB. It therefore seems realistic to assume that the unknown variations between the 1982/1983 data of different sites and dates are of the same order.

The variations of transmitted power level within a recording are relatively small (a few tenths of a dB), as could be concluded by FEL–TNO (Hoogeboom, 1986) on the basis of an analysis of the internal calibration signal. To illustrate this, the NLR delivered one of the 1985 images (image Sp16) in two versions: one with and one without radiometric corrections for power variations. A simple experiment was performed. By substracting the two versions of the same image in an image analysis system, a histogram of the power variations within one recording was obtained directly (figure 4.3). A standard deviation of 0.77 grey levels or 0.15 dB followed in this example and may be an illustration of the transmitter's short–term stability. It seems realistic to assume that these small variations within recordings, corrected for from 1985 onwards, were also present in SLAR data collected before 1985.

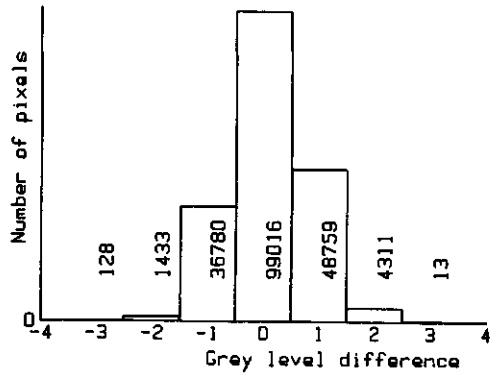

Figure 4.3. The transmitted power variations of the SLAR within one recording (Sp16) shown as a histogram of grey level differences between the uncorrected image (meaning no internal calibration applied) and the corrected image.

Dutscat

With Dutscat, the forest stands of interest were measured three or four times for each angle and/or polarization. For the relatively small stands and the high incidence angles, this repetition was found to be necessary. This can be explained as follows.

The distance r between sensor and object and the ground range distance y (figure 3.3) will fluctuate around planned nominal values. The effect of small roll movements and height variations of the platform can easily be quantified. Since $y = h \cdot \tan(\theta_i)$,

$$dy = \frac{h}{\cos^2 \theta_i} d\theta_i + \tan(\theta_i) \cdot dh. \tag{4.1}$$

Table 4.5. Illustration of repeatability. Typical example of dataset obtained from a single stand during one flight (stand: Robusta N44, flight: FL1584, L–band, Roggebotzand site). Measurements were repeated four times for six combinations of nominal incidence angle (15°, 30°, 45°, 60° and 75°) and polarization (VV for 45° only).

θ_i	n	γ [dB]	
75.1	24	–4.6	
75.0	23	–4.6	
76.1	23	–4.7	
74.6	24	–4.8	
61.3	24	–3.5	
60.3	24	–3.4	
61.8	27	–3.4	
61.1	27	–3.6	
46.7	25	–1.9	
46.5	25	–1.7	
47.0	25	–2.0	
45.6	27	–1.7	
31.4	24	–2.9	
			(target missed)
30.2	23	–2.8	
30.9	25	–2.8	
16.4	23	–1.5	
12.8	26	–1.8	
15.0	23	–2.4	
15.4	23	–1.0	
47.6	24	–2.6	(VV pol.)
46.5	26	–3.0	(VV pol.)
46.6	27	–3.1	(VV pol.)
47.2	26	–3.0	(VV pol.)

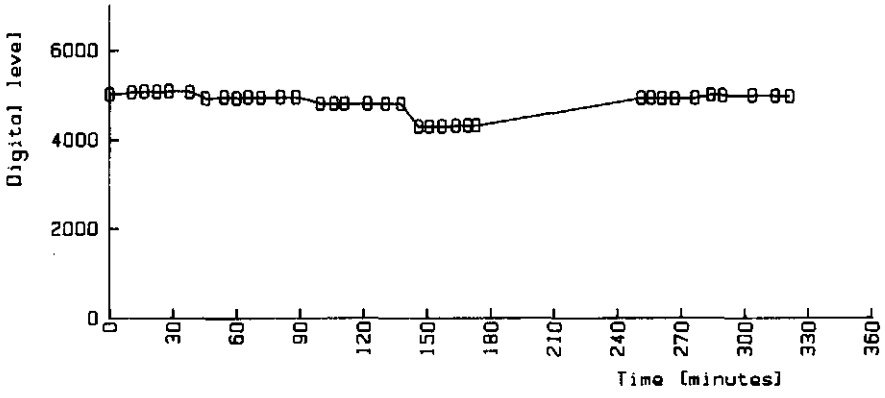

Figure 4.4. Variation of internal calibration signal level during one flight (FL1584).

This shows that, especially at high incidence angles, variations in dh and $d\theta_i$ will have a strong effect. This is illustrated by the following numeric example. Suppose the height of flight is 200 m and angle of incidence is 60°. Realistic values for height and roll variation are: $dh = +10$ m and $d\theta_i = +2°$. This results in

$$y = 346.4 \text{ m} \quad \text{and} \quad dy = +48.6 \text{ m}.$$

The variation in dy is troublesome when small stands have to be measured. If navigation is perfect, variations in height and roll angle will still cause the illuminated spot to sweep across the stand and occasionally cross borders. Only the largest forest stands (exceeding 200 m in ground range) were therefore selected for the Dutscat campaigns.

The γ values as well as the actual incidence angles show little variation between passes. This is illustrated in table 4.5 by a typical result obtained for a large poplar stand. Figure 4.4 shows a typical example of the power variations within a Dutscat measurement flight. These power data were obtained from the calibration recordings taken after every one or two data recordings. The calibration data results are related to those data recordings nearest in time. Since the transmitted power level appears to be very stable, radiometric corrections on the basis of the internal calibration signal may be assumed to be accurate.

4.2.5 Notes on determination of radar signatures from X–band SLAR images

Radar signatures can be assessed with both SLAR and Dutscat. With Dutscat, the procedure is rather straightforward. Selected stands can be measured for a series of incidence angle and polarization combinations. During a single Dutscat flight, a large number of tracks (more than 50) may be flown. For the SLAR, it is not feasible to take more than a few recordings (among other things because of the high costs of flight and processing). A single SLAR recording, however, covers hundreds of forest stands at a wide range of incidence angles. If a certain number of very similar forest stands are present (e.g. same species, same age, etc.), a signature for this "class" can be based on the combined data from these stands. Moreover, covering many similar (in certain aspects) forest stands offers the opportunity to adequately study variations within classes.

An extensive set of radar signatures of tree classes was calculated on the basis of data from the 1982 and 1983 SLAR images. Data used to determine radar signatures relate to forest stands (or parts of forest stands) with a homogeneous spatial structure. With the aid of an image analysis system, the following statistics were extracted for these objects: the stand–averaged mean, the standard deviation, the number of pixels and the mean grazing angle. To account for the sensor's spatial resolution and the effects of radar parallax,

foreshortening and radar shadow, not the entire stand area but an area amply within stand borders was selected. The smaller areas (less than an arbitrarily chosen number of 50 pixels) were excluded from this analysis.

Concerning the "stand–averaged mean", as measured with the SLAR, averaging was done at the dB scale. A small underestimation of 0.07 dB therefore results for the mean of Rayleigh fading objects (Appendix I). In addition to this offset being negligibly small, and in principle can be corrected for, knowledge of this offset is not very relevant since the system was not calibrated and only Rayleigh fading objects were studied. Major problems, however, arose from the fact that the antenna gain function was not exactly known (when mounted under the aircraft) and the absence of internal calibration (in 1982 and 1983). The first problem was discussed in section 2.2, and probably the only consequence is an unknown but fixed angular dependent offset common to all images and thus common to all calculated signatures. The second problem can be solved to some extent by so–called "intercalibration" techniques.

Since only four images per site per date were recorded in 1982 and only two in 1983, it was not feasible to calculate radar signatures for individual objects on the basis of these SLAR data. Instead radar signatures were calculated for tree classes. A tree class contains all objects belonging to a particular species or variety or group of varieties. Further differentiations, for example into age classes, were not made. For reasons which will become evident, this was an appropriate choice (for X–band). Since the internal calibration was not available, the 1982 and 1983 signatures had to be calculated separately for each site. The tracks were chosen in such a way that most forest stands were viewed four (or two) times at different viewing angles. The tracks were flown in two opposite directions and, as a consequence, the objects were viewed at two different look directions. Intercalibration is based on comparison of objects observed at the same grazing angle and the assumption that these observations give the same (stand–averaged) backscatter level. Since the radar backscatter of objects may also show look direction dependence, this assumption may be violated. The effect is to some extent species–dependent, however, and, since many different species are present, can be detected in principle. During the analysis, dedicated checks were made to detect any significant look direction dependencies of the (mean) radar backscatter signatures of tree classes.

Procedures for intercalibration and signature determination were developed in the framework of this research. It is beyond the scope of this thesis to give a complete mathematical derivation. (A fully elaborated derivation is contained in Hoekman, 1984.) Appendix III is confined to a mathematical definition of the problem and an indication of the main steps and considerations towards the adopted solutions. A complete overview of the results (intercalibration factors, signatures and signature confidence intervals) is

Table 4.6. Relative offset of γ between recordings of the same scene and date as determined by intercalibration.

Rbz1	reference	Rbz5	reference
Rbz2	+0.25 dB	Rbz6	+0.35 dB
Rbz3	–0.61 dB	Rbz7	–0.31 dB
Rbz4	+0.02 dB	Rbz8	+0.16 dB
Rbz9	reference	Rbz11	reference
Rbz10	+0.31 dB	Rbz12	+0.44 dB
Sp1	reference	Sp5	reference
Sp2	+0.85 dB	Sp6	+0.52 dB
Sp3	+0.61 dB	Sp7	+0.07 dB
Sp4	+1.30 dB	Sp8	+0.10 dB
Sp9	reference	Sp11	reference
Sp10	+0.45 dB	Sp12	+0.77 dB

contained in a separate data report (Hoekman, 1983).

The intercalibration, which in fact was only an intermediate step in the analysis, will not be discussed further. A brief overview of results is given in table 4.6. The procedure was used four times for a set of four images, the June and September 1982 measurements of the Roggebotzand (Rbz) and Speulderbos (Sp) areas, and four times for a set of two images, the March and May 1983 measurements of the same two areas. The offset, taken relative to the first image recorded at a particular site and date, was small and ranged from –0.6 dB to +1.3 dB. One major problem was encountered during processing. Routine quality checks, which are basic elements in the intercalibration software developed, indicated anomalous behaviour of the poplar stands. In contrast to all other tree classes, poplars showed a significant look direction dependence. This phenemenon was found only for the September and May measurements (a physical explanation is suggested in section 5.9.3). It was therefore decided to omit poplar stands in these samples (September and May) from the intercalibration processing and to determine two separate signatures for the poplars (one for each of the two look directions).

The maximum likelihood approach was used for the intercalibration (App. III). For the estimation of signatures, results of all three approaches were included in the data report (Hoekman, 1983). On the basis of theoretical considerations, the maximum likelihood approach is the most appropriate one (it fits in with maximum likelihood classification to be discussed later) but the differences with the weighted least–squares approach were very marginal. This can be explained from the fact that the variable $s_{n,u}$ (App. III) shows very little variation and, as a consequence, the maximum likelihood approach effectively degenerates to the weighted least–squares approach. Some typical examples (taken from the data report) of signatures and confidence intervals are shown in figure 4.5 (a–d).

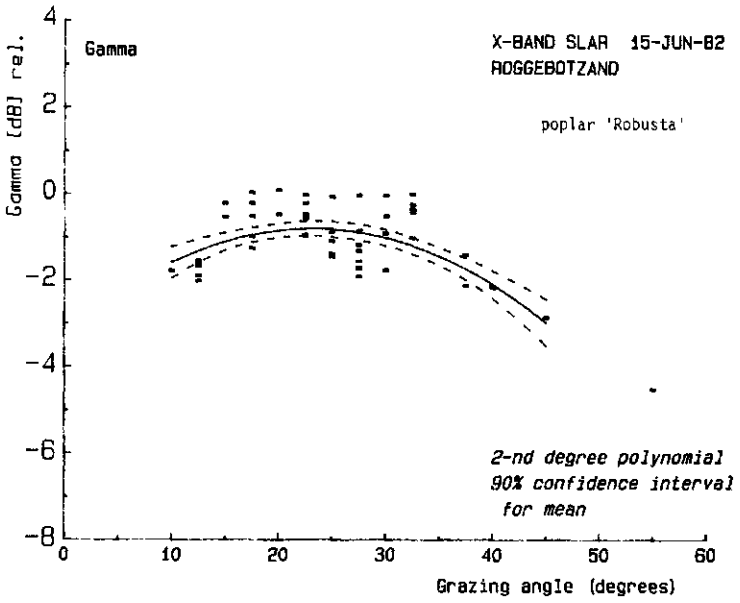
Gamma
X-BAND SLAR 15-JUN-82
ROGGEBOTZAND
poplar 'Robusta'
Gamma [dB] rel.
4
2
0
-2
-4
-6
-8
0
10
20
30
40
50
60
Grazing angle (degrees)
2-nd degree polynomial
90% confidence interval
for mean

(a)

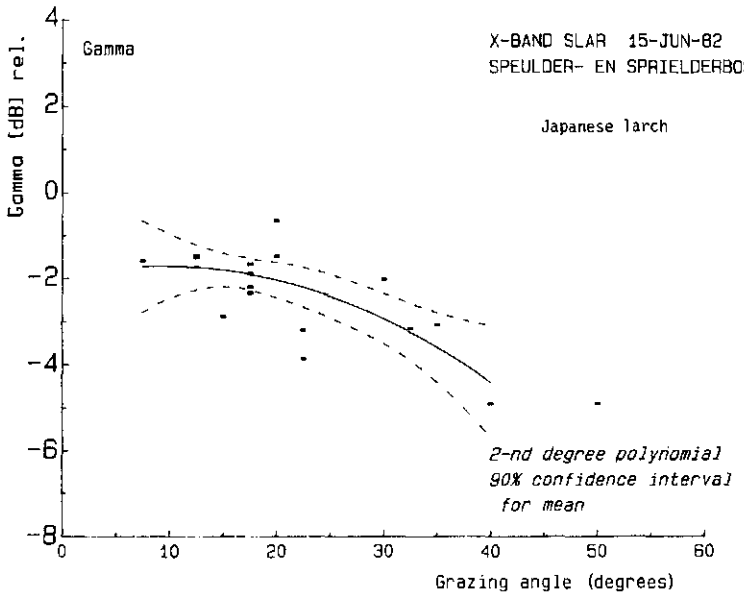
Gamma
X-BAND SLAR 15-JUN-82
SPEULDER- EN SPRIELDERBOS
Japanese larch
Gamma [dB] rel.
4
2
0
-2
-4
-6
-8
0
10
20
30
40
50
60
Grazing angle (degrees)
2-nd degree polynomial
90% confidence interval
for mean

(b)

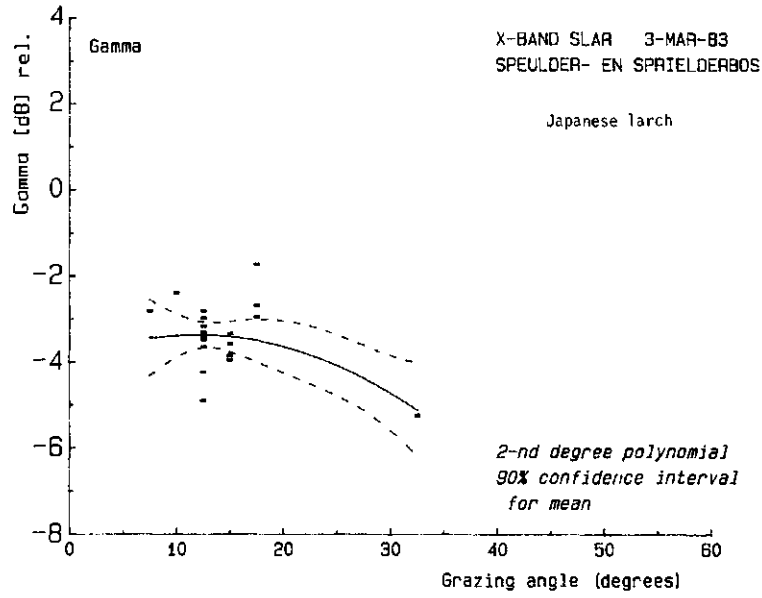

(c)

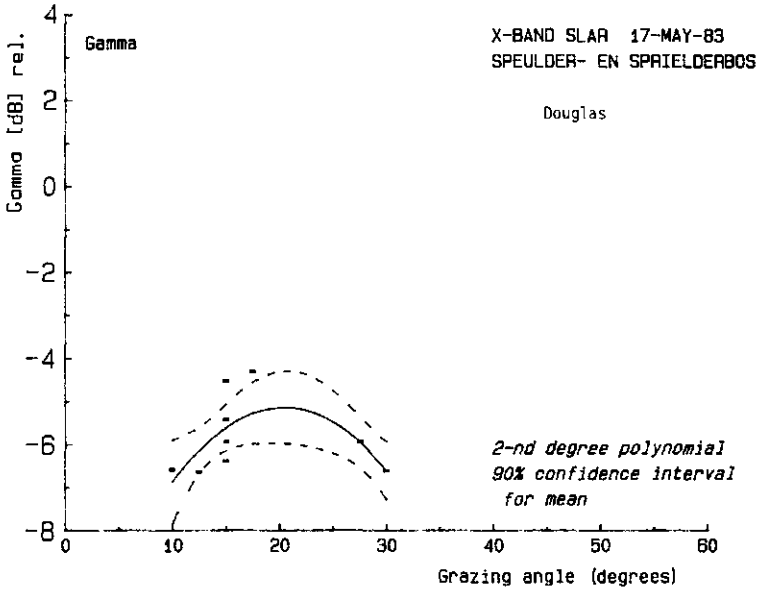

(d)

Figure 4.5 (a–d). Four examples of radar signatures and confidence intervals calculated on the basis of data obtained from four or two images of the same scene and date.

5. DISCUSSION OF EXPERIMENTAL DATA

5.1 The X–band multitemporal data set

The first series of SLAR measurements was made during the period June 1982 – May 1983 at the Roggebotzand and Speulderbos test sites. The emphasis in that period was placed on empirical assessment of X–band (HH polarized) radar backscatter properties of tree species and the temporal variation of these properties throughout the year. Four measurement flights, related to different phenologic stages, were made at times with comparable meteorologic conditions (section 4.2.2). Tree species represented by a sufficient number of large and homogeneous stands were selected for analysis. These species and their range of stand ages are shown in table 5.1.

An image analysis system was used to prepare histograms of stands of interest, with selected areas drawn as polygons on a videoscreen. The mean grey value, the standard deviation of grey values and the number of pixels for all stands of interest in all images were thus obtained. Radar signatures were calculated using the method described in section 4.2.5 for each of the 16 selected tree "classes" (table 5.1) for all four dates. This differentiation in classes was a tentative one, made to avoid grouping objects with different backscatter behaviour. A tree class in this context may be related to a particular species, clone or variety.

Table 5.1. Tree classes researched: common names, scientific names and tree ages.

Roggebotzand site:		
poplar 'Robusta'	*Populus spec.*	20–24 years
poplar 'Heidemij'	" "	" " "
willow	*Salix spec.*	12–21 "
ash	*Fraxinus excelsior*	12–23 "
oak	*Quercus robur*	21–22 "
beech	*Fagus sylvatica*	20–22 "
Norway spruce	*Picea abies*	21–24 "
Sitka spruce	*Picea sitchensis*	" " "
Scots pine	*Pinus sylvestris*	23–24 "
Corsican pine	*Pinus nigra* 'corsicana'	24 "
Austrian pine	*Pinus nigra* 'nigra'	24 "
Speulderbos site:		
old beech forest	*Fagus sylv.* mingled with *Quercus robur*	heterogeneous; ≈ 60–150 years
Scots pine	*Pinus sylvestris*	18–61 years
Japanese larch	*Larix kaempferi*	19–53 years
oak	*Quercus robur*	heterogeneous; 60–70 years
Douglas fir	*Pseudotsuga menziesii*	18–46 years

Because of a lack, at present, of knowledge of the physical radar backscatter properties of forests, polynomials were used, rather than physical models, to fit the data. For an old beech forest, for example, mean radar backscatter as a function of grazing angle was fitted by regression analysis with a third–degree polynomial (figure 5.1a). This figure also shows the 90% confidence interval (Brownlee, 1965) for the mean signature. It is clear from this figure that the mean signature is defined accurately in the range of 10^{o} to 40^{o} grazing angle. A 90% confidence interval for the individual stands, meaning that 90% of the stand–averaged mean values lie within this interval, is shown in figure 5.1b. An example of poplar 'Heidemij' is shown in figures 5.2a and 5.2b. More variation between the mean values of stands is present here, thus making both types of confidence interval larger. All data obtained from the images and all calculated signatures were reported separately in a data report (Hoekman, 1983). A synthesis of the most relevant results is presented below.

Speckle level

Table 5.2 shows the weighted (by stand area) mean of the standard deviation of γ values from individual stands for all tree classes and dates of flight. For the Roggebotzand site, on average, the mean value is 0.90 dB and, willow excluded, ranges from 0.72 to 1.03 dB. For the willow, and for most tree classes and dates of the Speulderbos site, these values are a little higher. The theoretical minimum (following from the Rayleigh fading model) of the speckle level, in this type of image with $\approx$30 independent samples per pixel, is expected to be approximately 0.8 dB (section 2.1).

In some instances, the standard deviation for spruces and pines at the Roggebotzand site is slightly less than the theoretical minimum for 30 independent samples. This is because during preprocessing, slant range data are transformed to ground range and resampled by cubic convolution, which has a slight smoothening effect (section 2.2). The standard deviations for the measurements of March and May are also slightly less; on these dates, only two of the four tracks were flown and, for these tracks, the grazing angles for the stands were, on average, smaller. The number of independent measurements per pixel, on average, was thus larger.

The theoretical minimum of speckle level applies to homogeneous forest stands with small structural elements compared with the system's spatial resolution. This is probably the case for the young spruce and pine stands at the Roggebotzand site and also for the ash and oak stands, which all have tree spacings of a few meters. Even for the poplar stands which have a considerably larger tree spacing (8 m to 10 m), this condition seems to apply. In the Roggebotzand forest, only for the willow, with a tree spacing of 16 m, is the standard deviation significantly larger, but still not very large in an absolute sense. Relatively large values are also found for many stands in the Speulderbos. These stands are older and

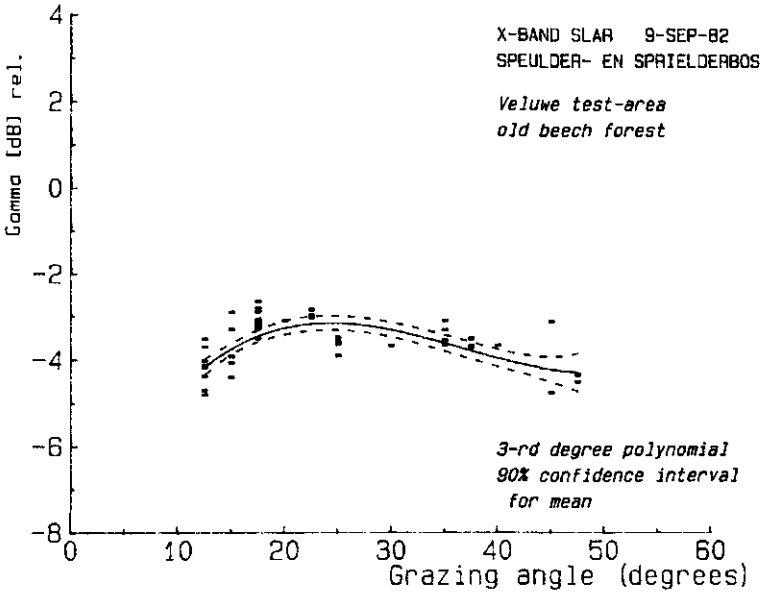

Figure 5.1a. Radar signature of old beech forests with a 90% confidence interval for overall radar return (X–band SLAR, 9 September 1982, Speulderbos site). The plotted squares indicate mean values of individual parcels.

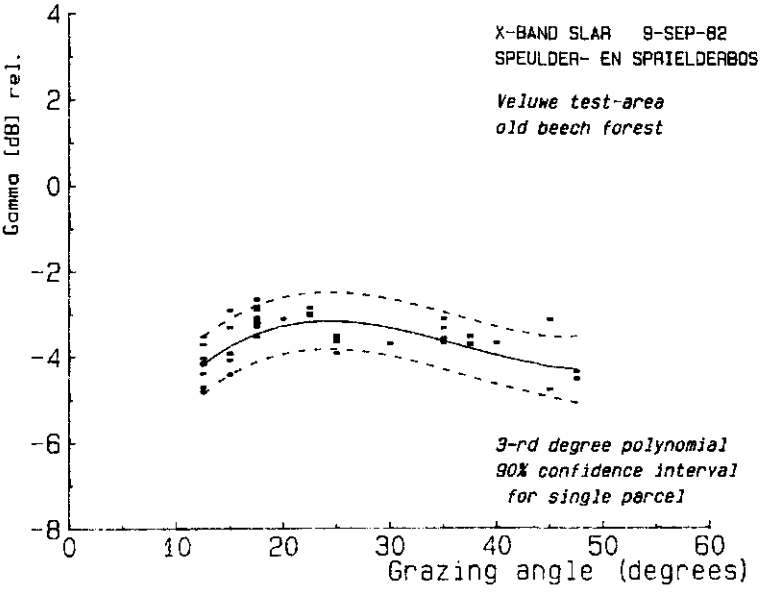

Figure 5.1b. Radar signature of old beech forests with a 90% confidence interval for mean radar returns of individual stands (X–band SLAR, 9 September 1982, Speulderbos site).

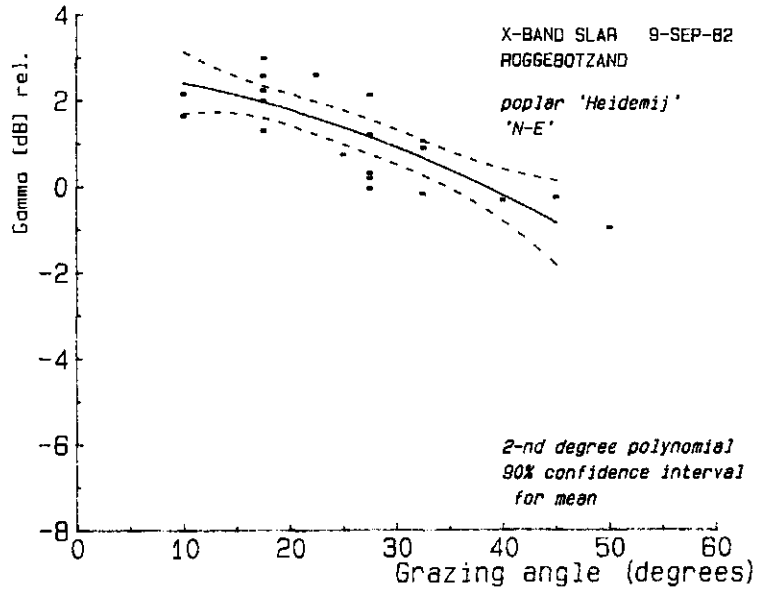

Figure 5.2a. Radar signature of poplar clone 'Heidemij' with a 90% confidence interval for overall radar return (X–band SLAR, 9 September 1982, Roggebotzand site).

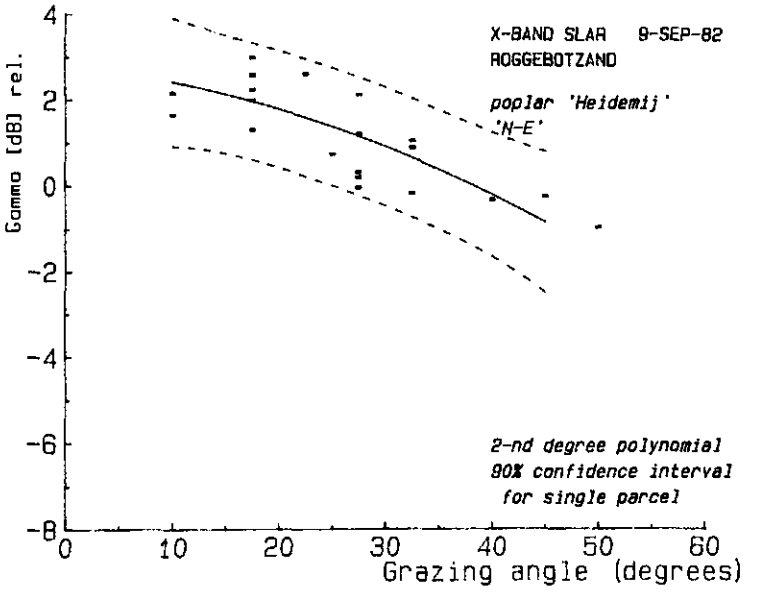

Figure 5.2b. Radar signature of poplar clone 'Heidemij' with a 90% confidence interval for mean radar returns of individual stands (X–band SLAR, 9 September 1982, Roggebotzand site).

Table 5.2. Mean standard deviation of γ values within stands for specific classes and dates of flight in the (a) Roggebotzand and (b) Speulderbos sites.

(a)	Jun'82	Sep'82	Mar'83	May'83	mean of species
poplar 'Robusta'	1.00	0.97	0.92	0.87	0.95
poplar 'Heidemij'	0.95	0.98	0.88	0.85	0.93
willow	1.06	1.20	1.12	1.15	1.13
ash	0.91	0.92	0.84	0.85	0.88
beech	0.83	0.95	1.03	0.94	0.95
Norway spruce	0.89	0.93	0.82	0.80	0.87
Sitka spruce	0.87	0.88	0.80	0.75	0.83
Scots pine	0.84	0.85	0.72	0.72	0.80
Corsican pine	0.96	0.80	0.74	0.86	0.86
Austrian pine	0.92	0.95	0.76	0.75	0.87
mean of dates	0.94	0.94	0.86	0.83	0.90

(b)	Jun'82	Sep'82	Mar'83	May'83	mean of species
old beech forest	1.30	1.31	1.14	1.11	1.26
Scots pine	1.34	1.13	0.89	0.84	1.14
Japanese larch	1.22	1.04	0.92	0.87	1.05
oak	1.91	1.25	0.96	0.92	1.48
Douglas fir	1.53	1.24	1.00	0.89	1.29
mean of dates	1.42	1.25	1.05	1.02	1.26

Table 5.3. Standard deviation (weighted by area) of stand–averaged γ values relative to the mean radar signatures for specific classes and dates of flight in the (a) Roggebotzand and (b) Speulderbos sites.

(a)	Jun'82	Sep'82	Mar'83	May'83	mean of species
poplar 'Robusta'	0.57	0.69	0.51	0.61	0.59
poplar 'Heidemij'	0.54	0.76	0.59	0.88	0.66
willow	0.46	1.03	0.61	0.24	0.63
ash	0.53	0.42	0.42	0.47	0.47
oak	0.77	0.43	0.35	0.45	0.54
beech	0.95	0.68	0.56	0.57	0.70
Norway spruce	0.40	0.55	0.37	0.40	0.45
Sitka spruce	0.63	0.89	0.43	0.42	0.64
Scots pine	0.35	0.52	0.22	0.83	0.50
Corsican pine	0.35	0.25	1.01	0.24	0.51
Austrian pine	0.55	0.50	0.17	0.20	0.43
overall mean					0.54

(b)	Jun'82	Sep'82	Mar'83	May'83	mean of species
old beech forest	0.62	0.42	0.44	0.42	0.51
Scots pine	0.55	0.50	0.54	0.47	0.52
Japanese larch	0.79	0.57	0.75	1.26	0.82
oak	0.44	0.45	0.31	0.37	0.42
Douglas fir	0.35	0.58	0.51	0.60	0.51
overall mean					0.52

consequently less homogeneous and have larger spatial structural elements. For example, the beech forests are heterogeneously mixed (at the level of the system's spatial resolution) with oak, and the oak stands have groups of emerging birch.

In summary, the standard deviation values found for homogeneous stands with spatial structural elements smaller than the system's spatial resolution are consistent with the theoretical expected minimum for Rayleigh fading. Only for homogeneous stands with large spatial structural elements are these values significantly higher.

The mean radar signature

Table 5.3 shows the (weighted by area) standard deviation of stand–averaged γ values, relative to the mean radar signature, for all tree classes and dates of flight. For both the Roggebotzand and Speulderbos sites, this figure, on average, is slightly more than 0.5 dB, and ranges for the mean of species (the Japanese larch excluded) between 0.42 and 0.70 dB. These figures are small compared with the overall range of (mean) γ values of the stands under research, which varies from $\approx$10 dB at the Roggebotzand in September to $\approx$4 dB at the Speulderbos in June. Almost all variation in the dataset (of stand–averaged γ values) seems to be explained by only two variables, namely the species type and the grazing angle. The remaining variation, in the order of 0.5 dB, is relatively small and does not vary much among the different tree classes. It might be explained by secondary effects such as variation in biophysical characteristics, ecologic factors or forest management systems or, on the other hand, might be partially explained by artefacts in the images (such as fringing or as a result of variations in the transmitted power). This is discussed in section 5.3. For the moment, it is sufficient to conclude that in the X–band with HH polarization and in the range of 10° to 40° grazing angle, the backscatter level generally seems to be determined by tree species type and grazing angle and that the effect of other variables of potential interest are marginal.

Temporal variation

Because the SLAR did not have internal calibration in the 1982–1983 period, the time dependence of the backscatter had to be presented relative to some arbitrarily chosen value. For the Roggebotzand, this was done relative to the mean signature of Norway spruce, which is very dense at that age and has no undergrowth. Its vegetation structure, compared with other species, is very stable during the whole year (with the exception of the period of forming new shoots) and is unlikely to give rise to strong backscatter fluctuations. For the same reason, the Douglas fir at the Speulderbos was selected as the most appropriate. The relative values were computed from the mean signatures for 15°, 25° and 35° grazing angles and are listed in table 5.4.

Table 5.4. Mean seasonal variations for tree classes, computed for 15°, 25° and 35° grazing angles, relative to Norway spruce (Roggebotzand) and Douglas fir (Speulderbos).

	June			September			March			May		
	15°	25°	35°	15°	25°	35°	15°	25°	35°	15°	25°	35°
(Roggebotzand site)												
pop. 'Robusta'	2.5	3.7	3.6	5.6	5.3	4.3	3.9	3.5	2.5	4.3	4.4	4.1
pop. 'Heidemij'	2.9	3.7	4.5	5.6	4.9	4.0	3.6	3.6	3.1	4.0	3.9	3.6
willow	0.9	2.1	2.9	2.5	2.3	2.5	3.4	4.0	3.9	1.9	1.9	2.2
ash	0.3	0.5	0.5	2.2	2.0	2.3	3.9	3.1	2.9	2.0	1.2	1.2
oak	−0.3	0.7	0.9	0.9	1.2	1.0	2.9	3.3	3.2	1.4	1.3	1.3
beech	0.4	0.4	1.9	1.6	0.9	1.1	2.8	3.4	3.4	1.2	2.2	2.9
Norway spruce	0.0	0.0	0.0	0.0	0.0	0.0	0.0	0.0	0.0	0.0	0.0	0.0
Sitka spruce	−0.9	−0.2	1.1	0.3	−0.3	−0.7	−0.1	0.0	0.2	−0.2	0.2	0.6
Scots pine	−0.3	−0.2	−0.1	−0.9	−1.1	−1.4	0.3	0.6	0.4	−0.6	−0.9	−0.9
Corsican pine	−1.3	−0.4	−0.4	−0.9	−1.2	−1.2	−0.7	−0.1	−0.1	−0.9	−0.7	−0.5
Austrian pine	−1.6	−1.3	−0.7	−2.3	−2.5	−2.5	−1.6	−1.1	−0.8	−2.0	−2.0	−1.6
(Speulderbos site)												
beech forest	−0.5	−0.3	0.5	−0.6	0.3	1.0	3.2	2.6	2.5	0.1	1.2	1.0
Scots pine	0.4	−0.1	0.2	−0.2	−0.1	−0.1	0.9	−0.2	−1.1	0.4	0.3	−0.4
Japanese larch	1.1	0.6	0.5	1.0	1.0	0.8	3.4	1.9	1.3	1.8	2.6	2.4
oak	1.0	0.5	1.3	1.3	1.5	1.6	3.9	3.6	3.5	1.9	2.2	1.5
Douglas fir	0.0	0.0	0.0	0.0	0.0	0.0	0.0	0.0	0.0	0.0	0.0	0.0

Figure 5.3 shows the (relative) seasonal variations for selected tree types at the Roggebotzand at 25° grazing angle. This graph shows some important features.

(1) In March there is a large differentiation between coniferous and deciduous tree types, which were fully defoliated at that time. Moreover, the different deciduous tree types show almost the same backscatter level. This is remarkable considering the large biophysical variations (such as tree dimensions or timber volume).

(2) Austrian pine can be differentiated very easily from other pine species. Actually, this is a striking phenomenon since physical structural differences between Austrian and Corsican pine (two varieties of *Pinus nigra*) are very small in this forest.

(3) For the poplar clones, which show a very high level of radar backscatter, directional differences during the May and September flights occurred between measurements from the north–east (tracks 2,4 and 5) and south–west (tracks 1 and 3). (This point is described below.)

Figure 5.4 shows the (relative) seasonal variations for selected tree types at the Speulderbos at 25° grazing angle. Here, also, a remarkable difference appears in winter between deciduous trees and the needle–shedding larch (high levels) and coniferous trees (low levels).

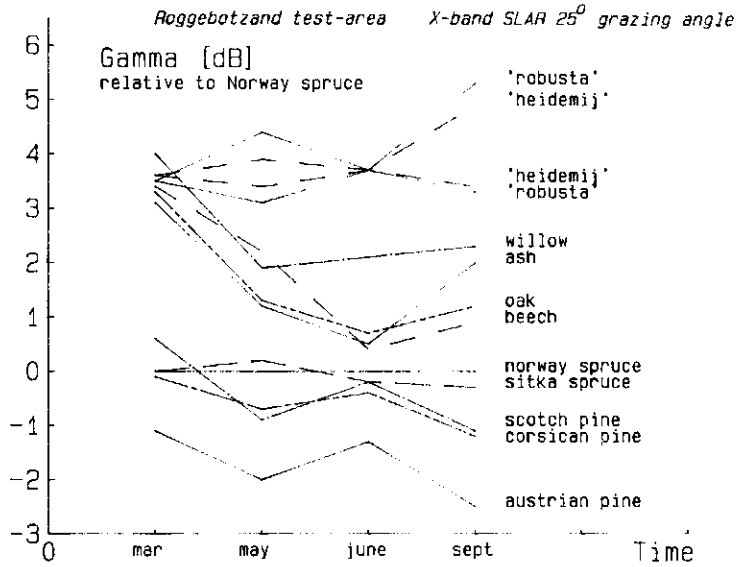

Figure 5.3. Seasonal variations in radar backscatter level for selected tree types in the Roggebotzand site (X–band SLAR, 25° grazing angle). For the poplar clones 'Robusta' and 'Heidemij', two figures are given for the May and September flights. The stronger radar returns correspond to observations from the north–east direction, the weaker radar returns correspond to observations from the south–west direction.

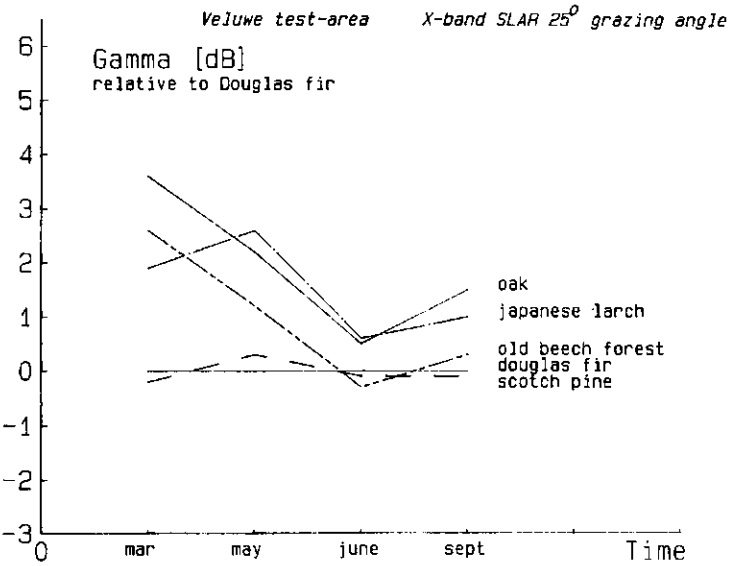

Figure 5.4. Seasonal variations in radar backscatter level for selected tree types at the Speulderbos site (X–band SLAR, 25° grazing angle).

Tree class differentiation

Figures 5.5 and 5.6 present the data in another way. In these figures, all stand–averaged γ values are shown for a particular site and date as a function of incidence angle. In figure 5.5, the differentiation between coniferous trees and the bare trees (deciduous species and larch) is obvious. In figure 5.6a, this differentiation shows up dramatically. An empty band with a width of ≈2 dB is present between the deciduous and coniferous species. Figure 5.6b shows the same stands in September; the situation has changed considerably. Relative to the coniferous species, the levels of poplar and willow have increased or remained the same. The other deciduous species show a relative decrease and get mixed up with the strongest levels of the coniferous species, in particular spruces. (This point is elaborated in section 6.1 where classification potentials are described.)

Directional dependence

In addition to seasonal and angular dependencies, a directional dependence of γ was noted at the Roggebotzand site for both poplar clones. The SLAR measurements were made in two opposite directions. The backscatter was measured from either the north–east (tracks 2, 4 and 5) or the south–west (tracks 1 and 3). Of all tree species under research, at both test sites, only the poplar clones (poplar 'Heidemij' and poplar 'Robusta') showed this behaviour and only in the May and September flights (figure 5.7a). The magnitude of this effect was in the order of 1 to 2 dB.

The data given in tables 5.2, 5.3 and 5.4 for the September and May measurements of these poplar clones relate to the measurements of tracks 2, 4 and 5 only. If the directional dependence were ignored, the figure 0.69 dB (the standard deviation of stand–averaged γ values) in table 5.3 for 'Robusta' in September, for example, would rise to 1.13 dB.

5.2 Comparison of X–band signatures from all four sites.

In 1985, the SLAR system was modified: an internal calibration circuit was added; an option was added to tilt the antenna towards steeper viewing angles; and the sampling frequency was increased from 20 MHz to 50 MHz. As a result, γ measurements of different sites could be compared directly, the range of viewing angles in which accurate measurements are possible was extended from $\approx$ 10°–40° to $\approx$ 10°–65° and, since the system's resolution was increased, smaller stands could be selected for the analysis. Furthermore, the use of corner reflectors for absolute calibration at grasslands just outside the Roggebotzand forest (section 3.3) yielded absolute values for the backscatter level at several incidence angles. As a result, the whole 1985 dataset is absolute within a few dB.

All four sites were visited (or revisited) in 1985 to compare backscatter signatures (for the extended range of viewing angles) of many different species, varieties, clones, etc. and to compare backscatter properties of the same species at different sites. In this respect, the Horsterwold made a significant contribution since many, mainly deciduous, species are present in fairly large and homogeneous stands (table 5.5a). The species selected at the other three sites are shown in tables 5.5b–d. All sites were surveyed in a single flight (11 July 1985) within a few hours and under comparable meteorologic conditions (section 4.2.2). At the Horsterwold site, three parallel tracks were flown at different altitudes. Thus an elongated strip parallel to the line of flight was viewed at three different and narrow ranges of viewing angle, centred at 20°, 40° and 60° grazing angle, at approximately the same distance in range. This strip contained ± 60 stands of interest. A total of 174 stand–averaged values could be obtained over a wide range of viewing angles. For the other three sites, the previously used tracks were reflown, but at a higher altitude, yielding, for these sites too, variation over a wide range of viewing angles. At these sites, 169 stand–averaged values were obtained.

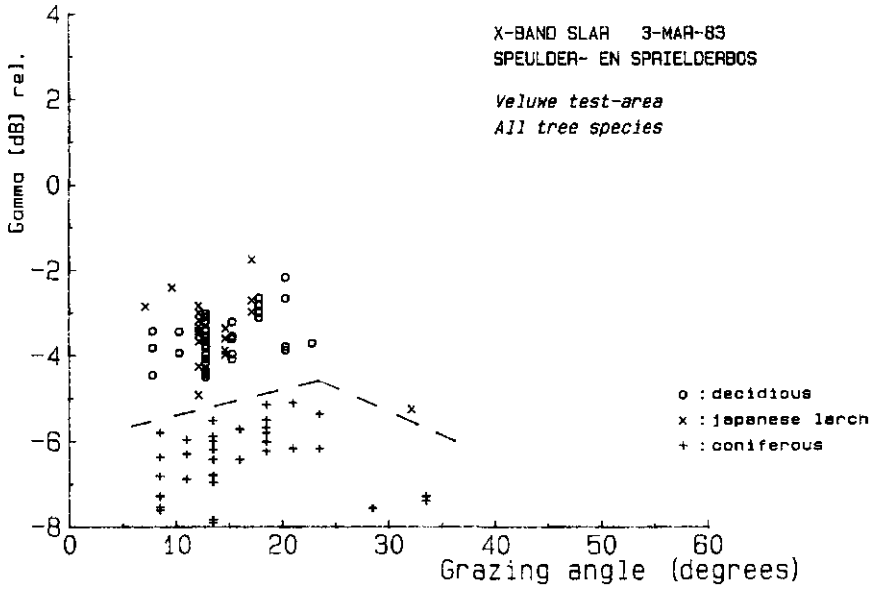

Figure 5.5. Mean radar backscatter levels of all stands in the Speulderbos site in winter (X–band SLAR, 3 March 1983). Three groups of tree types are shown: o, deciduous; x, the coniferous needle–shedding larch; +, other coniferous tree species.

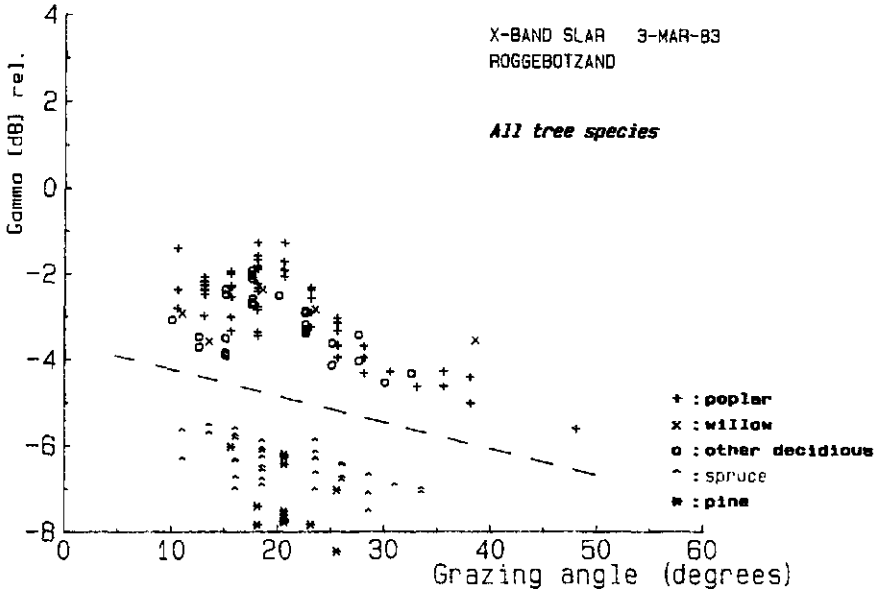

Figure 5.6a. Mean radar backscatter levels of all stands in the Roggebotzand site in winter (X–band SLAR, 3 March 1983). There is a marked difference in radar backscatter level between the deciduous tree species (+, poplar; x, willow; o, other decidious) and the coniferous types (^, spruce; *, pine).

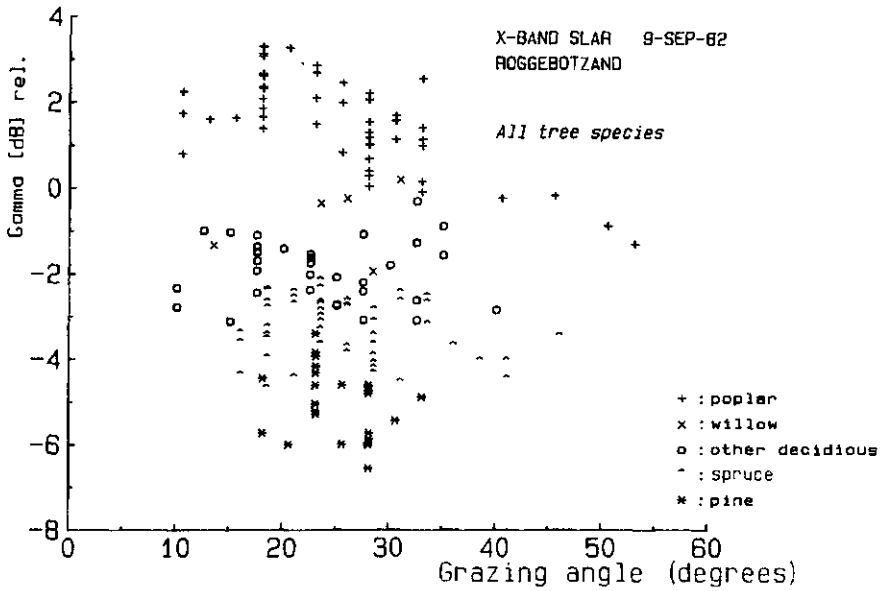

Figure 5.6b. Mean radar backscatter levels of all stands in the Roggebotzand site in summer (X–band SLAR, 9 September 1983). Key as in figure 5.6a.

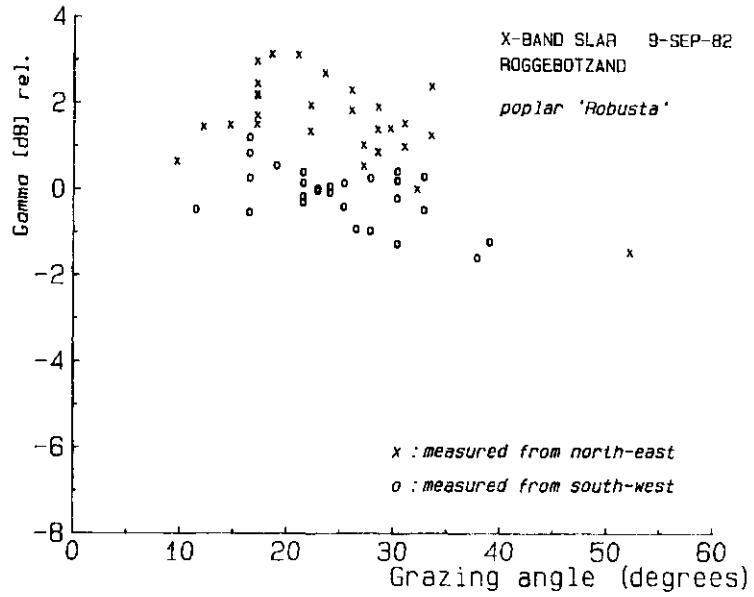

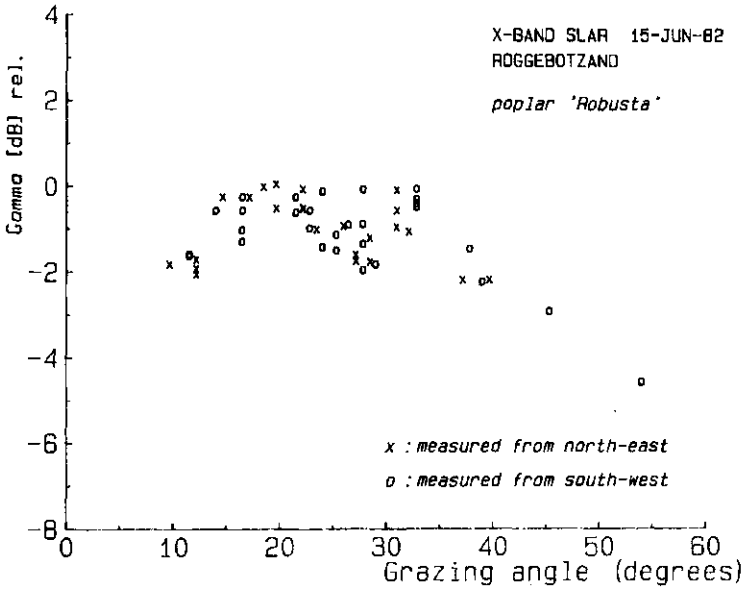

Figures 5.7 (a–b). Differences in mean radar backscatter levels of stands of the poplar clone 'Robusta' as a function of look direction were found for the (a) 9 September 1982 measurements but not for the (b) 15 June 1982 measurements. Measurements were made from the north–east (x) and the south–west (o).

Table 5.5a. Tree species in the Horsterwold site: common names and scientific names.

poplar (group I):		
Section Leuce (Albidae)		
	Pop. x *canescens*	'Witte van Haamstede'
	Pop. x *canescens*	'de Moffart'
poplar (group II):		
Section Aigeiros		
	Pop. x *euramericana*	'Robusta'
	" "	'Flevo'
	" "	'Zeeland'
	" "	'Dorskamp'
	" "	'Agathe F.'
	" "	'Florence Biondi'
poplar (group III):		
Section Tacamahaca		
	Pop. trichocarpa	'Fritzi Pauli'
	Pop. trichocarpa	'Heimburger'
poplar (group IV):		
Section Aigeiros x Tacamahaca		
	Pop.	'Geneva'
	Pop.	'Oxford'
	Pop.	'Rochester'
willow	*Salix spec.*	'Belders'
willow	*Salix spec.*	'Tinaarlo'
elm	*Ulmus* x *hollandica*	'Commelin'
beech	*Fagus sylvatica*	
oak	*Quercus robur*	
ash	*Fraxinus excelsior*	
maple	*Acer spec.*	
alder	*Alnus glutinosa*	
Norway spruce	*Picea Abies*	
Austrian pine	*Pinus nigra*	'nigra'

The year of planting for almost all stands researched is in the period 1973–1976. The few exceptions, planted in 1977, 1983 and 1984, are indicated in the text and figures explicitly.

The results are presented in figures V.1–10 (App. V) which show stand–averaged γ values (absolute within a few dB) as a function of grazing angle, per site and for groups of tree classes. The results are discussed mainly on the basis of figures 5.8–5.13 in which, for the ease of survey, the data from Appendix V are condensed as labeled clusters.

Poplar

The backscatter properties of the poplar clones 'Robusta' and 'Heidemij' at the Roggebotzand were very similar, despite the fact that tree and stand parameters varied over a considerable range. Two stands with other poplar clones, 'Oxford' and 'Geneva', belonging to another taxonomic group, showed a totally different behaviour. This also occurred in the 1985 data of the Horsterwold site, where many different poplar species and clones occur, often represented by a substantial number of stands. Here similar behaviour was found for all clones mentioned above; moreover, the variations in backscatter

Table 5.5b. Tree species in the Roggebotzand site: common names, scientific names and year of planting.

poplar 'Robusta'	*Populus spec.*	'58–'62
poplar 'Heidemij'	" "	" "
poplar 'Geneva'	" "	'61
ash	*Fraxinus excelsior*	'59–'60,'72
oak	*Quercus robur*	'60–'61
Norway spruce	*Picea abies*	'58–'61
Sitka spruce	*Picea sitchensis*	'58–'61
Scots pine	*Pinus sylvestris*	'58–'59
Corsican pine	*Pinus nigra* 'corsicana'	'58
Austrian pine	*Pinus nigra* 'nigra'	'58

Table 5.5c. Tree species in the Speulderbos site: common names, scientific names and ages.

old beech forest	*Fagus sylv.* mingled with *Quercus robur*	heterogeneous; mainly 60–150 years
Scots pine	*Pinus sylvestris*	22–93 years
Japanese larch	*Larix kaempferi*	22–55 years
oak	*Quercus robur*	heterogeneous; 60–70 years

Table 5.5d. Tree species in the Kootwijk site: common names, scientific names and year of planting.

Scots pine	*Pinus sylvestris*	'29–'33

properties for all clones of the Horsterwold were completely consistent with their taxonomic classification.

As shown in table 5.5a, the poplar clones can be divided into four taxonomic groups. Figure V.1 shows the γ values of the poplar stands of group IV, clones from the section *Aigeiros* x *Tacamahaca*. These clones, 'Oxford', 'Geneva' and 'Rochester', exhibit similar backscatter properties and a relatively steep increase in backscatter level as a function of grazing angle.

Figure V.2 shows clones from another taxonomic group, *Populus* x *euramericana*. Most selected stands at the Horsterwold were planted in the period 1973–1976; exceptions (younger stands) are explicitly indicated. With the exclusion of these younger stands, again, a small band of backscatter values appears for the clones of group II, each clone showing the same backscatter level and the same, rather gentle increase with the grazing angle.

The younger plantations show lower backscatter values, notably at large grazing angles. This effect is most clear for the 'Dorschkamp' stands. The older 'Dorschkamp' stands

(planted in 1973–1976) have tall (15 to 18 m) trees and fully closed canopies. Two young plantations from 1984 (one year old) and 1983 (two years old) have small trees (≈5 m) and open canopies. The 1983 stand has a greater degree of canopy closure than the 1984 stand. At all three ranges of viewing angle, the closed canopy gives the strongest return and the 1984 stand the weakest. The effect is the strongest for steep angles and the weakest for low grazing angles. At 20°, the difference between the older (closed) and the 1983 canopies even disappears. The backscatter level (relative to the backscatter level for the fully closed canopy) rises with the degree of canopy closure and with the angle of incidence. It might therefore be hypothesized that the lower returns are somehow caused by the absence of tree crown cover and the relatively small contributions of ground or undergrowth. If this is the correct interpretation, the degree of crown cover is a significant variable which might be obtained to a certain extent from radar images in monitoring applications.

Figure V.3 shows the measurements of clones belonging to two other taxonomic groups, *Populus* x *canescens* and *Populus trichocarpa*.

An overview, in the form of clusters, is shown in figure 5.8 for all four groups. Clearly, each group exhibits a characteristic behaviour. Group IV shows a steep increase with the grazing angle, starting with the lowest backscatter values and ending with the highest levels. Group II shows a very gentle increase, starting with the highest levels and ending with relatively low levels. The levels of group I are always relatively low, whereas the levels of group III are always relatively high.

Although there were differences in stand and tree characteristics, between stands of the same clone as well as between stands of different clones (as also occurred at Roggebotzand), only two (groups of) factors seem to affect the backscatter level. These are the taxonomic properties and the sensor parameters (i.e. grazing angle for the SLAR). For very young plantations, a third group of factors related to canopy closure and presumably ground and/or undergrowth has to be added.

Though a clear link with taxonomic properties might be evident, a causal link with relevant physical differences is not yet established. On the basis of these findings and on the basis of theoretical considerations (Eom and Fung, 1984, see also section 5.9.3), however, it is likely that leaf elevation angle is an important variable in this respect. The leaf angle distribution is planophile for group IV and erectophile for group II. The differences in angular behaviour of the backscatter might be explained to a certain extent from these different leaf angle distributions.

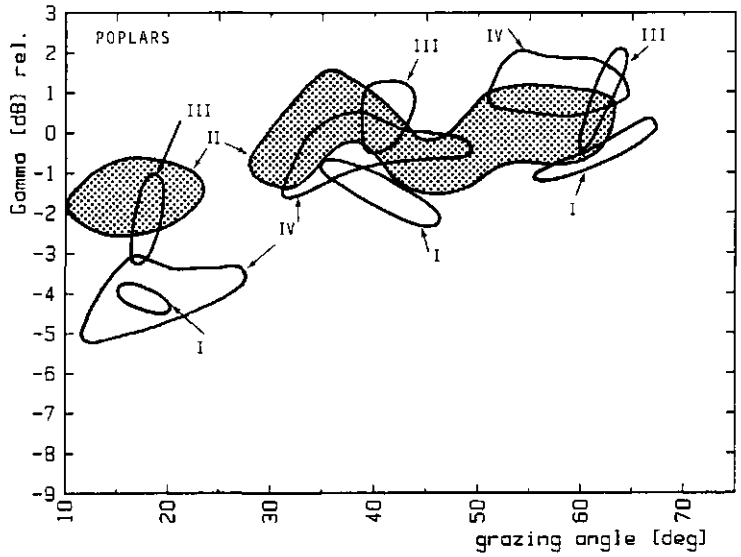

Figure 5.8. Clusters of mean γ values of selected stands as a function of grazing angle based on the data presented in figures V.1–3 and V.10. This figure shows the poplar clones of group I, II, III and IV (table 5.5) of the Horsterwold site and group II and IV of the Roggebotzand site.

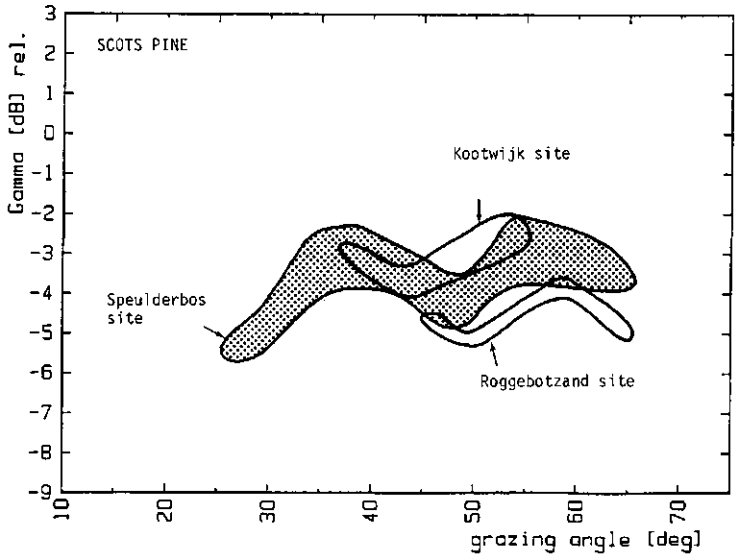

Figure 5.9. Clusters of mean γ values of selected stands as a function of grazing angle. This figure shows clusters of Scots pine at the Roggebotzand, Speulderbos and Kootwijk sites.

Scots pine

Figure 5.9 shows an overview of the results for Scots pine at three different sites: Kootwijk (figure V.7), Speulderbos (figure V.8) and Roggebotzand (figure V.10). A difference was observed between the backscatter levels of these sites. The Kootwijk site showed the highest levels, the Roggebotzand the lowest levels. The reason for this is not clear. It might be caused by differences in age: ≈25 years at the Roggebotzand, a range of 22 to 93 years at the Speulderbos and ≈55 years at the Kootwijk site. It might also be caused by ecologic or environmental factors. The younger stands at the Roggebotzand are healthy and dense. This contrasts with the stands at the Kootwijk site which have less favourable site factors and suffer from the effects of air pollution. The dimensions of individual trees are comparable for these two sites. This topic is elaborated in section 5.9.4.

Other coniferous species

An overview of the other coniferous species in the 1985 dataset is shown in figure 5.10. Austrian pine at the Roggebotzand (figure V.10) and Horsterwold (figure V.5), though measured at different viewing angles, have the same low level of backscatter. The levels of Norway and Sitka spruce at the Roggebotzand and Norway spruce at the Horsterwold are the same for the large grazing angles; for the small grazing angles, only stands at the Horsterwold were measured. The Japanese larch, measured at the Speulderbos (figure V.8), has a level only slightly higher than that of spruce. Corsican pine is clearly different from Austrian pine at the grazing angles shown. This also applies to small grazing angles, as noted in the preceding section.

Beech and oak

An overview of beech and oak stands from the Horsterwold (figure V.5), the Roggebotzand (figure V.10) and the Speulderbos (figure V.9) is shown in figure 5.11. Beech and oak show roughly the same backscatter properties for all three sites. Actually, this is quite remarkable. Many stand and tree characteristics, for both oak and beech, differ significantly between these sites. For example, the dimensions of the young beech trees at the Horsterwold (tree height ≈7 m, diameter at breast height ≈8 cm) clearly differ from the dimensions of trees in the old beech forests at the Speulderbos site (typical dimensions: tree height ≈25 m, dbh ≈60 cm). The backscatter levels, however, are the same.

Other deciduous species

The backscatter properties of the other deciduous species, measured at the Roggebotzand (figure V.10) and the Horsterwold (figures V.4 and V.6), can be divided into two distinct

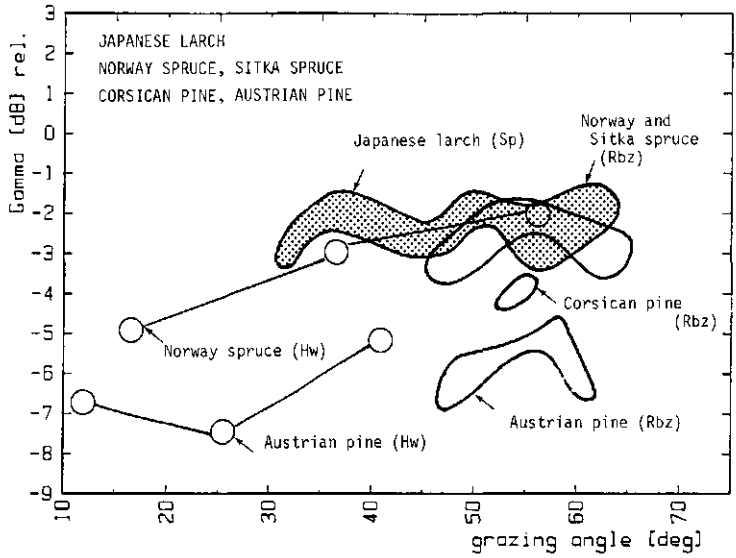

Figure 5.10. Clusters of mean γ values of selected stands as a function of grazing angle. This figure shows the other coniferous species: Austrian pine, Corsican pine, Norway plus Sitka spruce (Roggebotzand); Japanese larch (Speulderbos); Austrian pine and Norway spruce (Horsterwold).

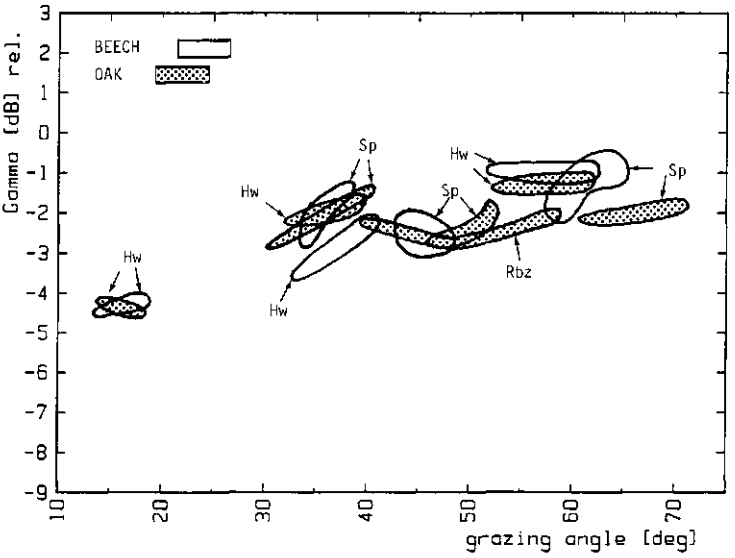

Figure 5.11. Clusters of mean γ values of selected stands as a function of grazing angle. Clusters of oak and beech stands at the Roggebotzand, Speulderbos and Horsterwold sites are shown.

groups (figure 5.12). Maple exhibits a relatively steep increase of the backscatter with grazing angle and clearly differs from all other tree species. Ash, alder, willow and elm seem to form a single group with very similar backscatter properties.

An ash stand planted in 1984 (one year old) is shown separately. This young plantation has small trees and an open canopy, in contrast to the older stands, and shows a completely different behaviour. As suggested for the new (one to two years old) poplar plantations, the difference might be attributed to the ground and/or undergrowth, which in these cases are poorly covered by a crown canopy.

All species

A generalized overview for all species is shown in figure 5.13. For most species, γ shows a flat response or gentle increase as a function of grazing angle. The only two exceptions are maple and the poplar clones of group IV, which show a relatively steep increase of γ with grazing angle.

Despite significant variations in the values of stand and tree parameters, the stand–averaged backscatter levels are confined to small (± 1 dB) bands for the tree classes researched. One exception is Scots pine. For the three individual sites, the values are confined to small bands. When these are compared, however, significant differences show up, which might be related to age and/or environmental factors.

Morphologic features, related to the taxonomic classification down to the level of varieties, seem to be the dominant factors. The two varieties of *Pinus nigra* (Austrian and Corsican pine) can be differentiated clearly. Also different (taxonomic) groups of poplar clones can be differentiated. On the other hand, different species might show comparable backscatter signatures. As far as can be concluded from this dataset, this may apply for beech and oak or Sitka and Norway spruce or ash, alder, willow and elm.

Finally, it should be remarked that all backscatter signatures for individual tree classes show local maxima at $\approx 35^{\circ}$ and $\approx 57^{\circ}$ grazing angles and a local minimum at $\approx 45^{\circ}$ grazing angle. These are probably artefacts, caused by the applied antenna gain function in the preprocessing algorithm. This function might deviate a little from the correct one (section 2.2).

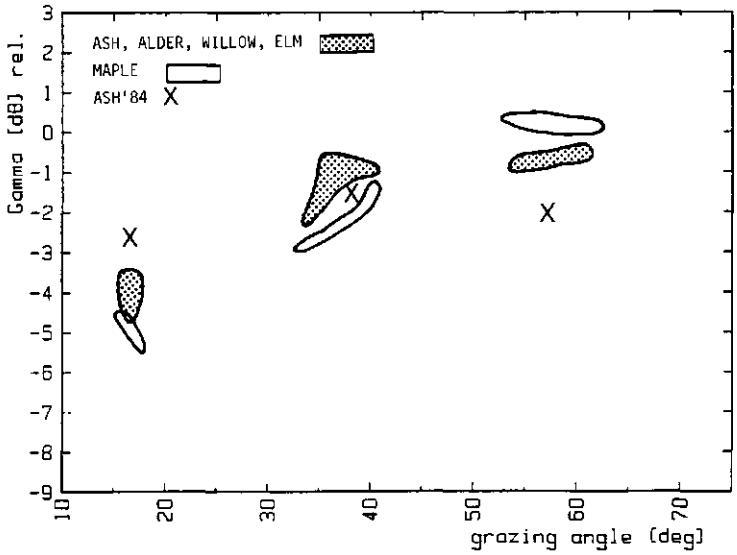

Figure 5.12. Clusters of mean γ values of selected stands as a function of grazing angle. This figure shows a cluster of maple and a cluster of ash planted in 1984 and a cluster of ash, alder, willow and elm (all data from Horsterwold site).

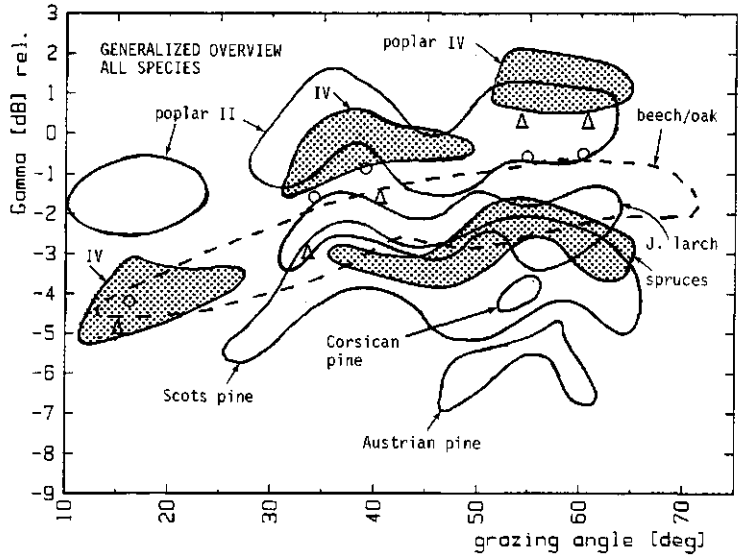

Figure 5.13. Generalized clusters of γ values of tree species and groups of tree species as a function of grazing angle (from figures 5.8–5.12). The triangles indicate maple, the circles indicate the group of ash, alder, willow and elm.

5.3 Empirical relationships of X–band data with tree and stand parameters

The results described in the two preceding sections bring out clearly the main factors which, directly or indirectly, determine the backscatter level of forest stands (at X–band frequencies with HH polarization). Tree classes (species, varieties or groups of species) could be described by a mean signature. Stand–averaged γ values, in general, are confined to a small band around this mean (typically the standard deviation is $\approx$0.5 dB). A physical relationship with morphological factors, somehow related to taxonomic factors and phenologic stage, appears to be the most plausible inference. In this section the relationship with stand and tree parameters will be investigated explicitly. This relationship, however, as may be inferred from the fact that the variation of stand–averaged means around a tree class dependent (mean) signature is small, can be expected to be a second–order effect.

The procedure adopted for this investigation was as follows. The selected tree classes were represented at a single site by a reasonable number of large and homogeneous stands, and with a significant variation in some stand and/or tree parameters (table 4.1). To reduce the effects of possibly disturbing factors, such as differences in site factors, environmental conditions or management, data from different forest test sites were not combined. Data of interest were obtained from stand registers or, when necessary, new measurements were made. Also additional data of potential interest were measured and qualitative descriptions (to incorporate characteristic stand features) of all selected stands were made.

Four tree classes were investigated in different studies: (1) Poplar clones 'Robusta' and 'Heidemij' at the Roggebotzand were studied on the basis of the multitemporal dataset obtained in 1982 and 1983 and the data available from the forest district. (2) The same was done for the Japanese larch at the Speulderbos. Because the number of stands was not very large and many more stands could be incorporated on the basis of images with higher resolution obtained in 1984 and 1985, this study was extended. Forest data, for the greater part, had to be remeasured and additional measurements were made (van der Sanden, 1985; Helfferich, 1987). Also Scots pine was studied on the basis of the 1984 and 1985 datasets for (3) the Speulderbos and (4) the Kootwijk site. The data for the Scots pine, for the greater part, also had to be remeasured and additional data were collected (Visser, 1986).

Since the backscatter level is also a function of the grazing angle and measurements vary over a certain range of angles, the object parameters were related to the stand–averaged backscatter level relative to the mean signature. The angular dependence may be an artefact caused by the applied correction for the antenna pattern (if this correction is not entirely correct, a 1 to 2 dB deviation is realistic) and/or may be caused by geometric properties of the object. In the latter case, the relationship with object parameters may be

grazing angle–dependent and only measurements related to a limited range of grazing angles can be compared objectively. Datasets covering a wide angular range were therefore split up.

To study the relationships within these datasets of relative γ values, limited in angular range and linked with a number of object parameters, correlation coefficients were calculated and figures were drawn (to visualize the dispersal of the data) for each object parameter. The correlation coefficients describe the statistical properties of the datasets and are useful to find the degree of association. Even if mathematical relationships are found that predict the backscatter level well, however, this does not necessarily imply causation. A physical explanation of any empirically derived and statistically significant relationship was therefore pursued.

The statistical significance of the correlation coefficient r,

$$r = \frac{cov(x,y)}{(var(x)\cdot var(y))^{\frac{1}{2}}}, \tag{5.1}$$

with x = the relative γ
and y = the object parameter,

is depicted in figure 5.14. Confidence intervals (Hoel, 1962) are shown for the null hypothesis ($\rho = 0$) as a function of the number of (independent) data points. Whenever an r–value is found outside an interval, the null hypothesis (meaning there is no correlation) is rejected at the indicated level of significance. Figure 5.14 also shows the intervals for the hypothesis $\rho = -0.5$. These intervals are used to evaluate the results.

Poplar

Table V.1 (App. V) shows the stand and tree parameters of 33 poplar stands, all planted in the period 1959 to 1962 with clones 'Robusta' and 'Heidemij', and the correlation coefficients for the relationships among these object parameters. The correlation coefficients for the relationships between radar and object parameters are shown in tables V.2a–e and relate to the radar data obtained from each single image from the 1982–1983 period. In table V.2a, the results are given for datasets including both 'Heidemij' and 'Robusta' in the range of 10° to 35° grazing angle. In tables V.2b–d, the results are shown for smaller datasets, limited either to 'Robusta' or 'Heidemij' or in angular range (10° to 20° or 20° to 30° grazing angle).

All results from the first four images (Rbz1–Rbz4, table 4.3) relate to the June flight, the

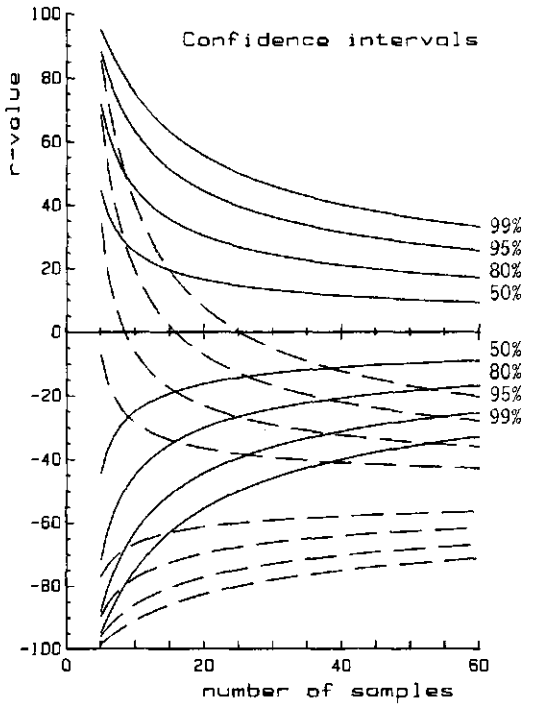

Figure 5.14. Confidence intervals for the correlation coefficient r for the hypothesis $\rho = 0$ and for the hypothesis $\rho = -0.5$ as a function of the number of independent samples for the 50%, 80%, 95% and 99% confidence levels.

next four relate to the September flight, images Rbz9 and Rbz10 relate to March and images Rbz11 and Rbz12 to May. Significant values were found for the parameters *dbh* and h_{dom} for the March and May flights. All other values are either small or inconsistent. For example, the value for *dbh* in image Rbz6 is 0.56, but since the other three figures for the same parameter and the same flight are 0.16, 0.00 and –0.27, respectively, this is probably the result of statistical fluctuation. A further check was made on the March and May data. Tables V.2b–e show the results for complementary subsets of the data. Also in these four cases —(7b) only 'Robusta' stands, (7c) only 'Heidemij' stands, (7d) 'Robusta' and 'Heidemij' but only the 10° to 20° range and (7e) only the 20° to 30° range— the figures remain significant, in almost all cases at the 95% confidence level, meaning the null hypothesis should be rejected. These results are shown in figure 5.15. Figure 5.16 shows the data points for the relationship between *dbh* and the radar data for Rbz12.

It can be concluded that the results show a significant positive relationship between the backscatter levels (relative to the mean signature) in March and May and the tree

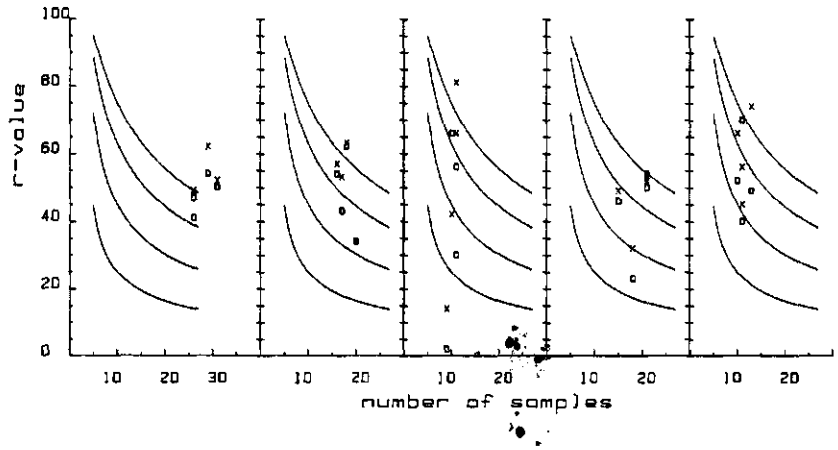

Figure 5.15. Graphical presentation of the significance of rejection of the null hypothesis for the results of table V.2 (a–e) of March and May for *dbh* (x) and h_{dom} (o).

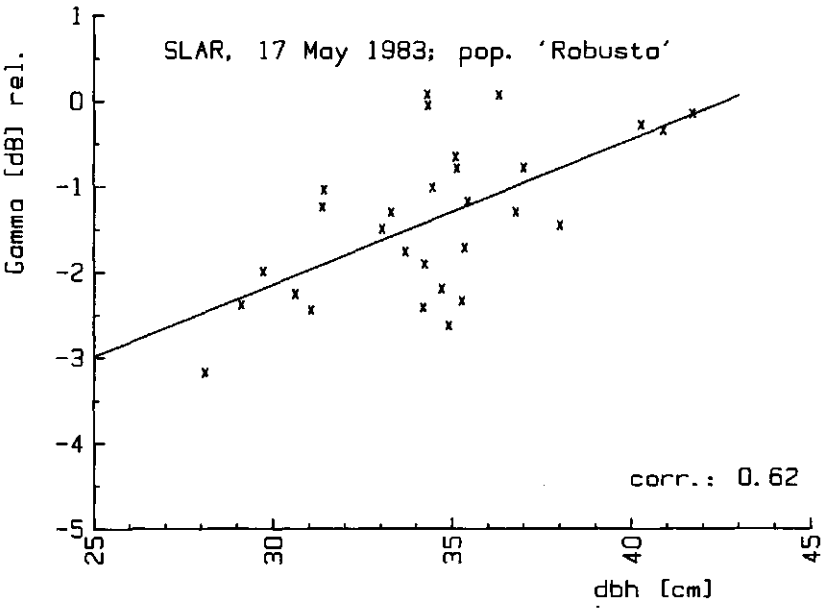

Figure 5.16. Relative radar backscatter level as a function of trunk diameter (at breast height) fitted by linear regression for poplar 'Robusta' and 'Heidemij' stands at the Roggebotzand site. The X–band SLAR measurements were taken on 17 May 1983 (image: Rbz12).

parameters *dbh* and h_{dom}. These two tree parameters are also significantly mutually correlated ($r = 0.70$, see table V.1). This suggests a possible causal relationship between backscatter and *dbh* or h_{dom} or both. On the one hand, it makes some sense that this relationship is found for the March observations (bare trees) and not for the fully foliated trees in June and September. On the other hand, in May, when the relationships seem to be even a little stronger, the poplars have just reached the stage of complete foliation. Moreover, a relationship in March with the trunk dimensions of the bare (poplar) tree contradicts the observation that all bare tree stands, regardless of species or age, have more or less the same, relatively strong, backscatter level (section 5.2). The empirical relationships found thus cannot be supported, as yet, by a plausible physical explanation.

Japanese larch

Table V.3 shows the stand and tree parameters of 21 Japanese larch stands, ranging in age from 22 to 55 years, and the correlation matrix of stand and tree parameters. The correlation coefficients for the relationship with the backscatter levels (relative to mean signature) are shown in table V.4a and relate to the data obtained for the four individual flights in the 1982–1983 period. Table V.4b includes one extra object parameter and relates to the August 1984 and the July 1985 flights. Since small stands (fewer than ≈70 pixels) were excluded from this analysis, the number of data points for flights in the 1982–1983 period is considerably less.

Because of the small number of data points for the 1982–1983 flights, almost none of the r–values differs significantly, at the 95% confidence level, from the null hypothesis. The only exception is the parameter N in September, which even differs significantly from the null hypothesis at the 99% confidence level. The results shown, though they are not very significant in general, are more or less consistent and do not seem implausible. In March when the trees are bare, the parameters G, *dbh* and h_{dom} describing the trunk, yield the highest r–values. For May, June and September, when needles are present, other parameters, notably N and N_{cr} and d_{cr} describing the crown canopy, seem more important.

In all cases, *Age* seems to be positively correlated with backscatter. Table V.3 shows the correlation between *Age* and the other object parameters. *Age* has no direct bearing on the physical structure of the objects, unless other conditions such as site factors and management (thinning regimes, initial planting) are taken into account; in general, it is therefore difficult to include *Age* in physical descriptions. In this analysis, however, a possible exception was encountered, which is described below.

Since the number of data points was small and no firm conclusions could be drawn, the analysis was extended over more data points, i.e. the smaller stands were included. The

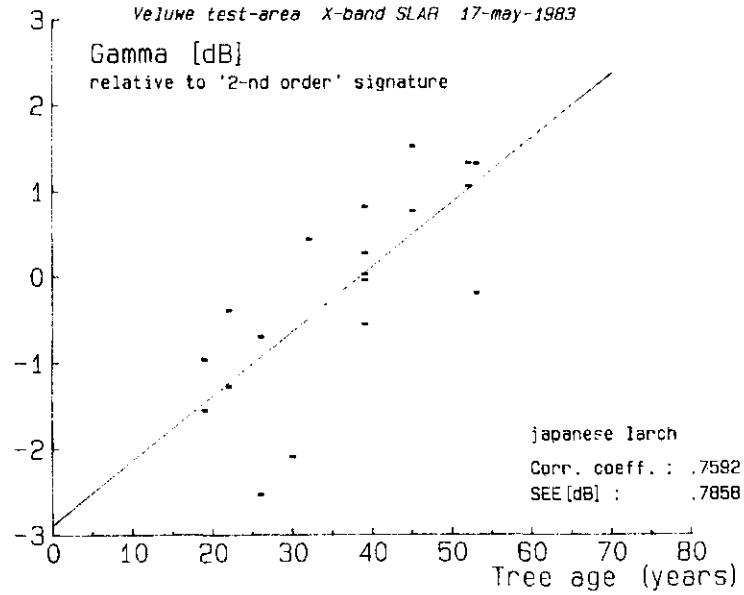

(a)

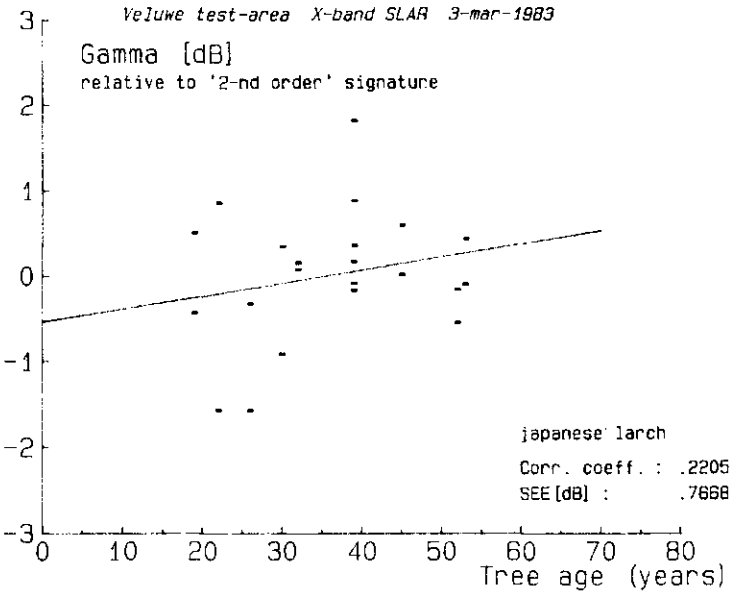

(b)

Figure 5.17 (a–b). Relative radar backscatter level as a function of tree age fitted by linear regression for Japanese larch stands at the Speulderbos site. The X–band SLAR measurements were taken on (**a**) 17 May 1983 and (b) 3 March 1983. The radar backscatter level is taken relative to the mean radar signature of the larch to account for angular dependence.

results remained more or less the same, however; notably the effect of *Age* became more pronounced (see figure 5.17a–b). When all data points were used, a significant correlation (r=0.76, n=19) with *Age* was found in May and (still) no significant correlations were found for the other dates.

Recalling the results shown in table 5.3, in contrast to all other species and dates, the Japanese larch in May shows a strong variation for the stand–averaged γ values (relative to the mean signature). (Some other high values, willow in September and Corsican pine in March, are statistically irrelevant since they are based on a very small number of data points.) This suggests some major cause for variation at that particular moment.

This strong, statistically significant correlation in May with *Age* cannot be explained by any of the other object parameters of table V.3, which quantitatively describe the physical structure. Qualitative observations made on the day of flight, however, suggest the cause. In May the larch was in the stage forming needles. The needles at the time of measurement had a length of roughly 2 cm. The fully grown needle has a length of 3.5 to 4.0 cm. The larch was thus in a (short) transitional phase between the winter stage (bare trees, relatively strong backscatter, as for the March measurement) and the summer stage (completely foliated trees, relatively weak backscatter, as for the June measurement). This point is also illustrated in figure 5.4. The younger trees form their needles a little faster and consequently arrive at the "summer stage" earlier and thus show lower backscatter levels. This mechanism, which applies to a period of a few weeks, thus provides a plausible causal explanation for the backscatter variations.

The results for the August 1984 and July 1985 flights are given in table V.4b. The results apply to the same stands and the same phenologic stage, but the range of grazing angles differs for the two datasets: 10° to 35° for 1984 and 35° to 60° for 1985. The stand–averaged γ values of the 1985 measurement, shown in figure V.8, are clearly confined to a small band. This is in agreement with the results presented here, which show no statistically significant correlations with any of the object parameters for the 1985 measurements. Also the 1984 measurements (at smaller grazing angles) show no statistically significant relationships with the exception of R_{ct} for which, at the 98% confidence level, the null hypothesis is rejected. Also in subsets of the data, this parameter often shows very significant relationships. This parameter describes the ratio between the number of crowns in the upper canopy and the number of trees and is therefore directly related to canopy roughness. A causal relationship with canopy roughness is thus suggested.

Scots pine

The analysis of Scots pine was conducted at two sites. Tables V.5a and V.6a relate to the Kootwijk site, tables V.5b and V.6b relate to the Speulderbos site. The stand–averaged γ values for these two sites are shown in figures V.7–8 and 5.9.

At the Kootwijk site, all Scots pine stands investigated were planted in the period 1929–1933. The main variations in stand and tree parameters (table V.5a) are caused by differences in site factors, environmental conditions and seed origin. (In this period, there was a shortage of seeds from indigenous varieties. Other varieties were imported, which, to some extent, were not resistant to endemic diseases.) Also air pollution had (and still has) an impact on the physiology of the trees at this site. In this analysis, three parameters were included that reflect the main differences in physiological appearance, namely the crown depth (*cd*), the number of years of green needles (*nn*) and the crown cover (*cc*).

Results for three datasets are shown in table V.6a. The data from image Kw1 (1984) cover the range of 17° to 30° grazing angle. The data from images Kw2 and Kw3 (both measured in 1985) cover the range of 40° to 55° grazing angle. The results for the two images recorded in 1985 (same track, same date) are highly inconsistent. The reason is that at this site and on this date, for some unknown reason, prominent "fringes" appeared (amplitude ≈1 dB) in the images. It is not feasible to correct for this phenomenon, so the results for these images should not be taken too seriously and will not be discussed further. For the Kw1 image, three parameters showed statistically significant (the null hypothesis is rejected at the 95% level of confidence) relationships with backscatter, namely N, d_{cr} and *nn*. A causal relationship with *nn* seems plausible. The backscatter level of Scots pine is low in the X–band. The backscatter levels of bare trees, on the contrary, are relatively high. When the tree loses a significant number of needles (as actually occurs in this forest), the physical structure more and more resembles the bare tree structure and may therefore cause a rise in backscatter level. This point is elaborated in section 5.9.4.

Table V.6b shows the results for the Scots pine at the Speulderbos site. In this forest, the growth of Scots pine is normal and the age of the plantations under research varies from 22 to 93 years. The correlation matrix of stand and tree parameters (in table V.5b) shows a high correlation of *Age*, h_{dom} and *dbh*. The radar data were collected in July 1985 and are divided over three datasets covering three angular ranges: measurements at the 25° to 35° range of grazing angles from image Sp18, the 35° to 45° range from image Sp17 and the 45° to 60° range from images Sp16 and Sp18.

Age, h_{dom} and *dbh* show significant correlations with backscatter, and these correlations become stronger for larger grazing angles. The probable physical explanation for these

statistical relationships does not follow from these object parameters and is as follows. The oldest stands have a low percentage of crown closure (40 to 50%) and five of these stands have a heavy understory of oak and show a high backscatter level. Since the backscatter level of oak is significantly higher (figure 5.13) and the radar effectively "sees" a mixture of oak and pine, notably at larger grazing angles, it is hardly surprising that this relationship was found.

Some concluding remarks

The results presented in tables V.2, V.4 and V.6 relate to simple (linear) mathematical relationships. It is well–known that empirically established relationships do not necessarily imply causation. In this investigation, in a few instances, statistically significant relationships were found and plausible causal physical explanations were suggested, but often involving other (qualitative) factors. On the other hand, where no correlations were found it is possible that other (correlated) factors have masked the effect. For forests in general, and for the stands studied, many object parameters are highly correlated (tables V.1, V.3 and V.5). Support from physical models or theories (which are scarcely developed) will eventually be needed to draw firm conclusions. For X–band with HH polarization and for the range of grazing angles studied, however, the fact remains that variation of the stand–averaged γ around a species–dependent signature is small (i.e. stands with a very low degree of crown closure excluded). Any physical relationships between γ and stand and tree parameters (if they are significant) are therefore not expected to have major effects on the backscatter level.

5.4 X–band canopy transmissivity

During the summers of 1984 and 1985, measurements of forest canopy transmissivity were made to obtain data supportive to model development. The corner reflector experiment design and the analysis procedure of the (raw) SLAR data were described in section 3.3. The results are described here in relation to the forest stand architecture and tree characteristics.

The reflectors were placed (at a specific site and date) on the ground surface in two or three forest stands. They were aligned and positioned in such a way that all reflectors could be observed by the sensor within a single track, at a 45° grazing angle and in the direction of the maximum radar cross section of the reflectors. On all occasions, tracks with corner reflectors were flown at least twice. For each run, the actual track and altitude were reconstructed after the flight (on the basis of the radar image and flight data). In this way the actual aspect of the corner reflector related to the sensor and canopy features (gaps, crowns) could be compared with the planned geometry of the experiment. Small deviations (in the order of 1° to 3° in elevation and/or azimuth) could be established and were used to make corrections on the radar cross section of the reflector. (Herewith a new variable, the actual radar cross section σ_c', is introduced.) The corner reflectors were deployed during three X–band SLAR flights. The basic results are contained in tables 5.6, 5.7 and 5.8. In this section, the (two–way) transmissivity τ_e is expressed at the logarithmic dB scale as τ_e [dB] = $-10\log(\tau_e)$ dB.

Table 5.6 gives the results for the first flight (14 August 1984) over the Roggebotzand. The three 45.4 dBm^2 reflectors were placed in a stand of poplar (*Populus* x *euramericana* 'Robusta') and the three 38.0 dBm^2 reflectors were placed in a stand of oak (*Quercus robur*). The track (number 8) was flown twice (yielding images Rbz6 and Rbz17).

The transmissivity could not be estimated in all cases. For example, corner reflectors 1, 5 and 6 did not yield a perceivable signal in the raw data of recording Rbz16. This fact is indicated in the table as n.v. (not visible). Only lower limits could therefore be extracted. On the other hand, the signal from corner reflector 3 in recording Rbz16 probably saturated the radar receiver, since $\sigma_{max} \simeq \bar{\sigma}_{b+ca}$. An upper limit is therefore given.

Table 5.7 shows the results for the second flight (9 July 1985) over the Roggebotzand. The reflectors were placed in stands of Austrian pine (*Pinus nigra* 'nigra') and Corsican pine (*Pinus nigra* 'corsicana'). The track (number 9) was flown five times (yielding images Rbz18 to Rbz22). Actually, only two runs were planned but the first run was aborted too soon (yielding measurements over only four reflectors). After the next two runs, a

Table 5.6. Corner reflector measurements at the Roggebotzand site (14 August 1984; recordings Rbz16 and Rbz17). The species name, corner reflector number, the radar cross section of the background ($\bar{\sigma}_b$), the maximum radar cross section related to the level given by the link budget (σ_{max}), the radar cross section of background plus target ($\bar{\sigma}_{b+ca}$), the actual radar cross section of the corner reflector, i.e. corrected for deviations from the main direction (σ_c') and the estimated (two–way) transmissivity (τ_e) are shown. τ_e is expressed at the logarithmic dB scale as τ_e [dB] = $-10\log(\tau_e)$ dB. Also all σ–values are expressed at the dB–scale.

Rbz16	no.	$\bar{\sigma}_b$	σ_{max}	$\bar{\sigma}_{b+ca}$	σ_c'	τ_e
poplar	1	16.3	38.	n.v.	44.6	> 28
poplar	2	16.3	38.	32.2	44.6	12.5
poplar	3	16.3	38.	37.9	44.6	< 7
oak	4	14.9	38.	18.0	37.3	22.2
oak	5	14.9	38.	n.v.	37.3	> 22
oak	6	14.7	39.	n.v.	36.0	> 21
Rbz17	no.					
poplar	1	16.9	42.	n.v.	45.4	> 28
poplar	2	16.9	42.	24.7	45.4	21.5
poplar	3	16.9	42.	35.5	45.4	10.0
oak	4	16.8	42.	21.8	37.9	17.7
oak	5	16.8	42.	n.v.	37.9	> 21
oak	6	16.3	43.	18.9	38.0	22.6

navigation error was detected (as a consequence the reflectors were viewed at a 33° grazing angle) and it was decided to make two more runs.

Table 5.8 shows the results for the third flight over the Kootwijk site two days later (11 July 1985). The reflectors were placed in stands of Scots pine (*Pinus sylvestris*). The track (number 8) was flown two times (yielding images Kw2 and Kw3).

Interpretation of these results requires a description of the forest stand architecture.

Poplar and oak (table 5.6)

The poplar (clone 'Robusta') plantation was 23 years old at the time of measurement. The trees are planted on 8 m centres in rows 8 m apart. There is thus a pattern of 8 m x 8 m squares. The dominant tree height is approximately 28 m. The canopy is not completely closed; open space between tree crowns ranges from 1 m to 2.5 m. The radar look direction was in row direction at 45° grazing angle.

Corner reflector 1 was placed in a row. As a result, four trees (two crowns and two stems) were between the corner reflector and the sensor. These trees completely blocked any perceivable signal from the reflector. Corner reflector 3 was placed in the middle between two rows, and only a few branches were between sensor and reflector. This resulted in low

attenuation. The transmissivity figure was found to be 10 dB for the second run and even less for the first run (resulting in a strong response that saturated the receiver). Corner reflector 2 was placed between rows, 2 m from one row and 6 m from the other. The outer parts of two crowns were between sensor and reflector. The difference in estimated transmissivity (12.5 dB versus 21.5 dB) could be explained qualitatively by between–run variation of the relative orientation of sensor, crowns and the corner reflector. On the basis of these results, a direct relationship between the transmissivity and the amount of vegetative matter between the reflector and sensor is suggested. The poplar crown could completely block the response of the large corner reflectors.

The oak (*Quercus Robur*) plantation , also 23 years old at the time of measurement, has a high percentage of crown closure; there are small gaps in the canopy (smaller than 1 m^2) but almost no big gaps. The dominant tree height is approximately 10 m; the tree spacing varies in the range of 1 to 2 m.

The three (38 dBm^2) corner reflectors were placed at random. In three of the six tests, no signal was perceived; weak signals were perceived in the other three from which (two–way) transmissivity values of 22.0, 22.6 and 17.7 dB were estimated. These values are high. (20 dB implies that the corner reflector response, if no canopy were present, should be 100 times stronger.)

Austrian and Corsican pine (table 5.7)

The pine (*Pinus nigra*) plantations were 27 years old and have a high degree of crown closure. The stand and tree parameters are given in table V.8 (compartments N85, N87 and N89). The dominant tree height is approximately 13 m, the tree spacing is in the order of 4 m. As discussed in section 5.1, the Corsican pine shows a higher backscatter level which, presumably, is related to the loss of needles (caused by a fungus infection called "Brunchorstia").

The corner reflectors were placed in such a way that direct illumination of the reflector or parts of the reflector through gaps in the canopy was impossible. For the first three recordings, no signal was perceived from reflectors 1, 2, 3 and 4. Reflectors 5 and 6, two of the four corner reflectors placed in Corsican pine stands, yielded a weak and in one instance (recording Rbz19) a clear signal. The transmissivity was estimated at 13.8, 17.3, 17.9 and 18.4 dB. In the last two recordings, reflector 3, also located in the Corsican pine stands, was clearly visible and the two reflectors visible in the first recordings were no longer visible. The transmissivity was estimated at 23.0 and 27.2 dB for the reflector in the last two recordings.

Table 5.7. Corner reflector measurements at the Roggebotzand site (9 July 1985; recordings Rbz18, Rbz19, Rbz20, Rbz21 and Rbz22). The corner reflectors in Rbz19 and Rbz20 were measured at 33° grazing angle.

Rbz18	no.	$\bar{\sigma}_b$	σ_{max}	$\bar{\sigma}_{b+ca}$	σ_c'	τ_e
Austrian pine	1	14.6	31.4	n.v.	44.9	> 30
Austrian pine	2	14.5	31.4	n.v.	37.5	> 23
Corsican pine	3	15.2	31.4	n.v.	44.9	> 29
Corsican pine	4	15.1	31.5	n.v.	44.9	> 29
Rbz19	no.					
Austrian pine	1	13.5	29.3	n.v.	43.3	> 29
Austrian pine	2	13.5	29.4	n.v.	35.8	> 22
Corsican pine	3	15.2	29.4	n.v.	43.1	> 27
Corsican pine	4	15.2	29.4	n.v.	42.8	> 27
Corsican pine	5	15.1	29.5	22.5	35.4	13.8
Corsican pine	6	15.1	29.4	19.8	35.3	17.3
Rbz20	no.					
Austrian pine	1	12.9	29.0	n.v.	42.6	> 29
Austrian pine	2	12.9	28.7	n.v.	35.0	> 22
Corsican pine	3	14.4	28.4	n.v.	42.6	> 28
Corsican pine	4	14.4	28.4	n.v.	42.2	> 27
Corsican pine	5	14.4	28.3	18.8	34.7	17.9
Corsican pine	6	14.4	28.4	18.5	34.8	18.4
Rbz21	no.					
Austrian pine	1	14.8	31.8	n.v.	44.8	> 30
Austrian pine	2	14.8	31.7	n.v.	37.4	> 22
Corsican pine	3	15.8	31.7	22.8	44.8	23.0
Corsican pine	4	15.7	31.5	n.v.	44.9	> 29
Corsican pine	5	15.8	31.7	n.v.	37.4	> 21
Corsican pine	6	15.7	31.5	n.v.	37.5	> 21
Rbz22	no.					
Austrian pine	1	13.7	31.5	n.v.	45.0	> 31
Austrian pine	2	13.7	31.5	n.v.	37.7	> 24
Corsican pine	3	15.9	31.5	20.0	45.1	27.2
Corsican pine	4	15.8	31.5	n.v.	45.0	> 29
Corsican pine	5	15.8	31.5	n.v.	37.7	> 21
Corsican pine	6	15.8	31.5	n.v.	37.6	> 21

The visibility of different reflectors in different runs is explained by the change of aspect. In the first three recordings, the reflectors, erroneously, were viewed at 33° instead of 45° grazing angle.

The results show low transmissivity for the Austrian pine. As far as can be concluded, the τ_e values are larger than 22 and 29 dB for the two reflectors, respectively, and at both viewing angles. Similar values were found for the Corsican pine, but in three cases the reflectors were visible at one of the two viewing angles and in two cases (reflectors 5 and 6) values below 20 dB were found.

Table 5.8. Corner reflector measurements at the Kootwijk site (11 July 1985; recordings Kw2 and Kw3).

Kw2	no.	$\bar{\sigma}_b$	σ_{max}	$\bar{\sigma}_{b+ca}$	σ_c'	τ_e
Scots pine	1	20.5	47.8	26.6	44.9	19.5
Scots pine	2	20.5	47.8	26.8	44.9	19.3
Scots pine	3	20.5	48.	n.v.	44.9	> 24
Scots pine	4	20.5	47.8	n.v.	37.5	> 17
Scots pine	5	20.6	48.	32.6	37.5	5.2
Scots pine	6	20.6	48.	27.5	37.5	11.0
Kw3	no.					
Scots pine	1	20.8	49.	26.4	45.4	20.4
Scots pine	2	20.7	48.7	25.1	45.4	22.2
Scots pine	3	20.7	48.3	n.v.	45.4	> 24
Scots pine	4	20.8	49.	n.v.	38.0	> 17
Scots pine	5	20.9	50.3	32.1	38.0	6.2
Scots pine	6	20.8	49.8	23.4	38.0	18.1

Scots pine (table 5.8)

The pine (*Pinus Sylvestris*) plantation at the Kootwijk site was 55 years old at the time of measurement. The stand and tree parameters are given in table V.5a (compartment 39). The dominant tree height is approximately 11 m, the tree spacing is in the range of 3 m to 4 m, the crown coverage was estimated as 62%.

The site factors do not favour vigourous growth. The degree of crown closure is small and crowns are mostly small and light (see section 5.3). Corner reflectors 1 to 4 and 6 were carefully placed behind groups of crowns, thereby avoiding illumination of the corners through large gaps in the canopy.

Reflector 5 was placed at a large open spot (this was done mainly to get a reference point in the raw data from which the location of the other reflectors could be derived. No salient features that could serve this purpose are present in this area.).
The results show that reflector 5 could be perceived clearly, as expected, as well as three of the other reflectors. As far as can be concluded, only reflector 3 had a transmissivity value definitely higher than 20 dB. Notably reflector 6 had a low value considering the fact that the reflectors were carefully positioned behind the tree crowns and gaps in the canopy were absent in the direct vicinity of the line of sight through the canopy.

A high between–run variation found for reflector 6 and low variations for reflectors 1 and 2 might be explained from measurement geometry (eq. 3.30) and the fact that the size of reflector 6 was smaller.

Concluding remarks

It can be concluded that the attenuation of the forest canopy in general fluctuates strongly and depends on relative orientations of gaps with respect to the sensor. The attenuation of crowns of deciduous trees is high. The attenuation of crowns of coniferous trees may be lower but is still in the order of 20 dB (two–way). For X–band, the contribution of scatterers of the understory and forest floor is therefore determined primarily by canopy architecture (i.e. factors such as crown closure, crown shapes, etc.) and angle of measurement.

5.5 Description of Dutscat dataset

Basic results of the Dutscat C–band and L–band flights made in 1984 and 1985 over the Roggebotzand and Speulderbos sites are contained in tables V.7 and V.8 and figures V.11a–x, V.12a–t and 5.18a–b.

An overview of all radar signatures shown in figures V.11, V.12 and 5.18 is given in table V.7. Figures V.11 (C–band) and V.12 (L–band) show the stand–averaged γ values as a function of mean incidence angle for six wave parameter combinations with the nominal values: 15°, 30°, 45°, 60° and 75° incidence angle with HH polarization and 45° with VV polarization. Figure 5.18 (C–band) shows the stand–averaged γ values as a function of six nominal look directions (see table V.7) and three wave parameter combinations with the nominal values: 30°, 45° and 60° incidence angle with HH polarization. The averaging of γ and the incidence angle was done over all samples within the stand boundaries and over all recordings for the same nominal wave parameter combination. The total number of samples is shown in table V.7 for each wave parameter combination and for each signature presented in these figures.

Table V.8 contains data on stand and tree parameters for all stands in the Roggebotzand measured by Dutscat. Only those data were collected that could be readily extracted from the stand registers. Note that the years of measurement (indicated in the last column) vary, but in no case deviates much from the years of radar measurement.

The C– and L–band systems provided relatively calibrated data. The results from different flights can therefore be compared directly and presented on the logarithmic dB scale. The absolute level of the backscatter is unknown, however.

5.6 Discussion of C–band results

Look direction dependence

In section 5.1, look direction dependence was noted for the X–band SLAR data. Since the wavelength difference between X– and C–bands is not very large (3.2 cm and 5.7 cm, respectively), the same behaviour was anticipated for the C–band. For this reason it was decided to take all measurements of poplar stands from approximately the same direction (225° to 265°) and to carry out a dedicated experiment to study the phenomenon in more detail.

In contrast to the SLAR measurements, scatterometer measurements are more flexible in the sense that many tracks can be flown. The scatterometer is thus the more appropriate instrument to study such phenomena as directional dependence. Many tracks were flown, not only to obtain measurements from many different directions (six in this experiment), but also to repeat these tracks at different incidence angles (this was done on one occasion for three angles). The SLAR measurements, on the contrary, were taken from only two directions (namely 45° and 225°) and were limited to two or four images per flight.

In figures 5.18a and 5.18b, the C–band look direction dependence of a poplar stand with clone 'Robusta' (four signatures) and a beech stand (one signature) are shown. Smooth variations in (stand–averaged) backscatter level as a function of look angle can be noted. The differences between maximum and minimum levels are ≈1.5 to 2 dB (in the same range as X–band data). The measurement on 6 September 1984 was made over both stands at 45° incidence angle. On 28 August 1985, the poplar stand was remeasured but this time at three different incidence angles (see the top three signatures in figure 5.18a). The angular dependence appears to be almost independent of look direction (only the 30° incidence angle, 30° look angle level is relatively a little stronger). The most remarkable result, however, is that the look angle dependence for this poplar stand differed between the two dates of observation (differences between dates of observation were also noticed in the X–band!). This implies that some kind of dynamic process underlies the phenomenon, and that it cannot be explained (solely) by static factors (e.g. tree row direction). The cause for the directional variations of γ is still a matter of speculation. This topic is elaborated in section 5.9.3.

Canopy roughness differences in old beech forest

In the Speulderbos, C–band signatures from four old beech stands were measured (figures V.11u–x). These stands differ significantly in canopy structure. (This point is elaborated in the discussion on image texture in section 6.4.) These differences in structure ranged from a

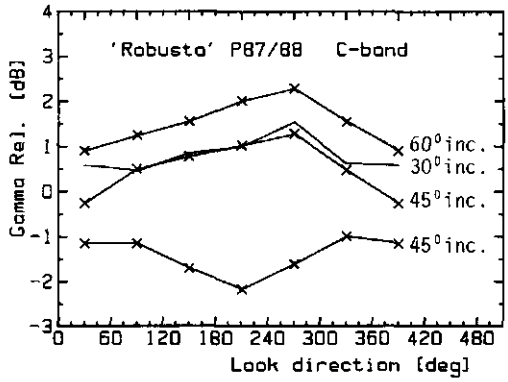

Figure 5.18a. Look direction dependence (C–band, HH pol.) for poplar clone 'Robusta' at the Roggebotzand measured with DUTSCAT at two dates and several incidence angles. Look direction 0° means looking north, 90° means looking east, etc. The lower curve shows the result (at 45° inc.) for 6 September 1984 (local time: 7.30–8.00; wind direction: 30°; wind speed: 8 m/s). The three upper curves show the results (at 30°, 45° and 60° inc.) for 28 August 1985 (local time: 15.30–17.30; wind direction: 230°; wind speed: 4 m/s).

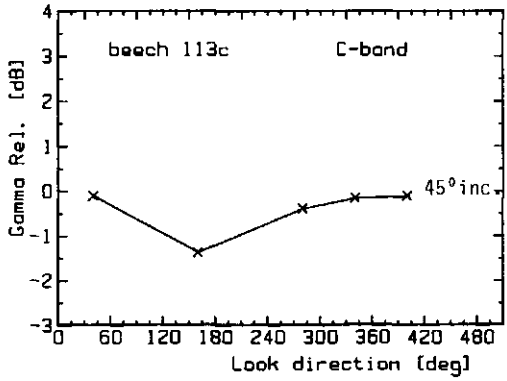

Figure 5.18b. As figure 5.18a for beech at the Speulderbos site (date: 6 September 1984; local time: 10.00–11.00; wind direction: 10°; wind speed: 3.5 m/s).

smooth and closed canopy (compartment 22e), via a rough and 60 to 70 % closed canopy (compartments 22b and 23g) to a smooth canopy with large (≈20 m) gaps and a 60 to 70% closure (compartment 23o). Despite these significant structural differences, the corresponding radar signatures do not show clear differences. (Note that the same was experienced for the X–band!)

Poplar

The total number of stands measured by the scatterometer was not very large. For most species, only one or two stands were measured. For poplar, however, a relatively large number of stands are present in this dataset. It could be concluded that all stands with poplar clones 'Robusta' and 'Heidemij' show approximately the same backscatter properties. All data points are confined to a small ± 0.5 dB band around the (weighted) mean signature (figure 5.19a). The stand and tree parameters for these stands vary over a considerable range, as can be concluded from table V.8. Even the significant structural

difference between stand N71n, a relatively young stand planted in 1968, and the other stands, planted in the period 1958–1962, is not reflected in the backscatter behaviour.

The 'Oxford' stand and the 'Geneva' stand (belonging to another taxonomic group of poplars, table 5.5a) have almost identical signatures. The (weighted) mean signature for these two stands and their individual signatures are shown in figure 5.19b. The mean signature of the 'Geneva'/'Oxford' group, however, is clearly different from the mean signature of the 'Robusta'/'Heidemij' group (table V.9). A similar behaviour was noticed for the X–band (figure 5.8). For the X– as well as the C–band, the poplars of group IV ('Oxford' and 'Geneva') show, with respect to the poplars of group II ('Robusta' and 'Heidemij'), a lower backscatter level for the large incidence angles and a higher level for the small incidence angles. Also the angular dependencies are the same, with 'Oxford' and 'Geneva' showing a relatively steep decrease with incidence angle. Even the cross–over point at $\approx 45^{\circ}$ is at the same angle. (It is noted that the exact angular dependence for the X–band is not known. A small 1 to 2 dB offset as a function of grazing angle might still be present, but this fact does not violate the conclusion of obvious similarities between X– and C–band backscatter for the observed poplar clones.)

Overview of all species

Figure 5.20a gives an overview of the C–band HH polarized data of the Roggebotzand. For most species (spruces, pines and willow), the signatures relate to a single stand. For ash and Scots pine, only one data point was obtained (at the nominal angle of 45°). Beech and oak were found together in a mixed stand. For the two poplar groups, the mean signatures are shown.

Within the group of coniferous species, more or less the same relationships are found as in the X–band (figure 5.13); the spruces show higher levels than the pines and the Corsican pine shows a higher level than Austrian pine. The only exception, possibly (there is only one data point), is the Scots pine, which shows the same level of backscatter as Corsican pine in the X–band (as can be seen in figure V.10) but a clearly higher level in the C–band. Compared with the X–band, the poplars show a relative decrease in backscatter level within the group of deciduous species. Also the group of deciduous species as a whole shows a decrease with respect to the coniferous species and is confined to a strip between the spruces and the Corsican and Austrian pine. (In the X–band, the deciduous species showed the highest backscatter levels with only a small overlap with the coniferous species.)

All species, as far as can be concluded on the basis of this dataset, show a flat angular response. The only exceptions are the poplars from group IV ('Geneva' and 'Oxford') which show a clear decrease as a function of incidence angle (the same was noticed in the

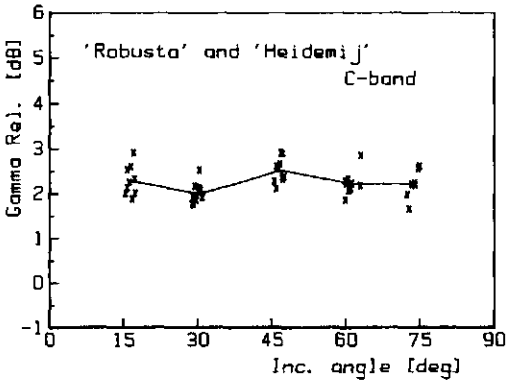

Figure 5.19a. Averaged (weighted mean) signature at C–band (HH pol.) for the poplar clones 'Robusta' and 'Heidemij'. The crosses indicate stand–averaged γ values for the individual stands (the exceptional cases where n —see table V.7— is smaller than 10 are not shown in this figure).

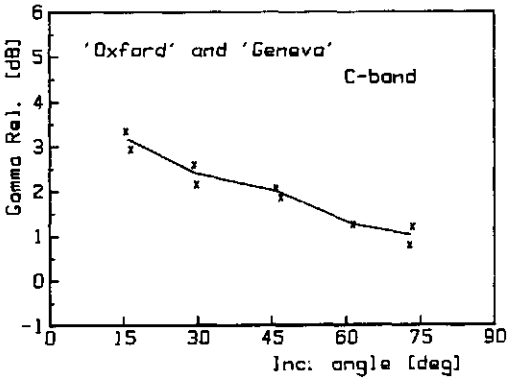

Figure 5.19b. Averaged (weighted mean) signature at C–band (HH pol.) for the poplar clones 'Oxford' and 'Geneva'. The crosses indicate stand–averaged γ values for the individual stands.

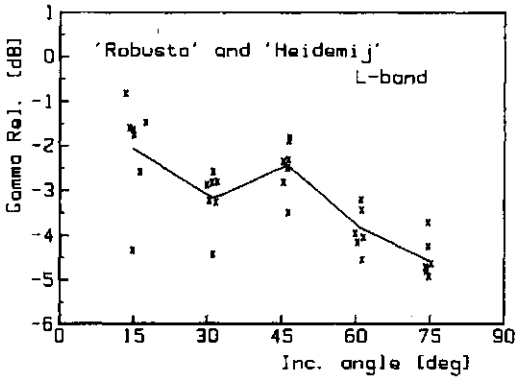

Figure 5.19c. As figure 5.19a for the L–band mean signature.

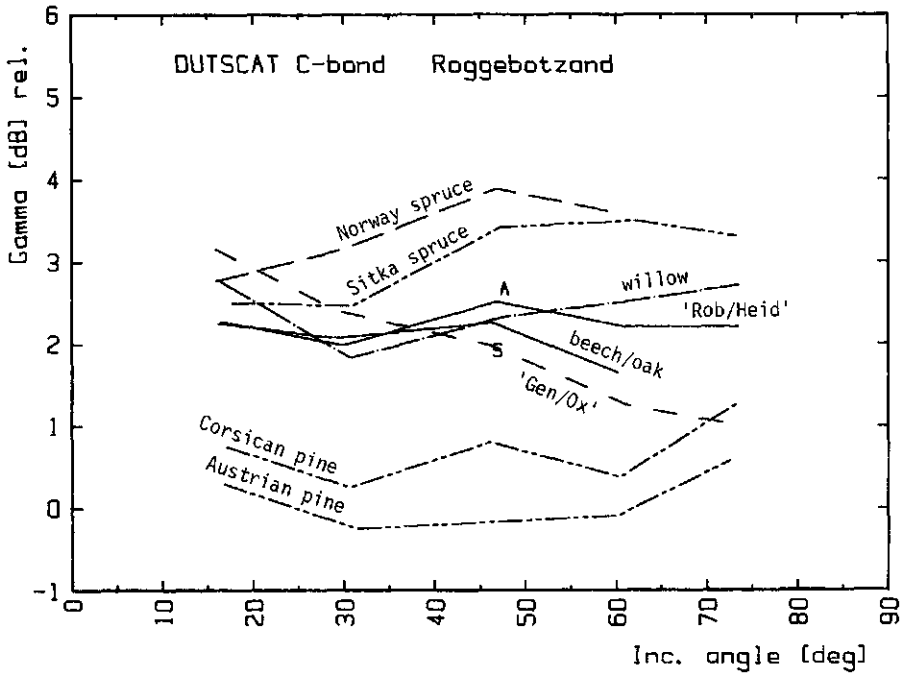

Figure 5.20a. Overview of C–band (HH pol.) signatures. The 'Geneva'/'Oxford' and the 'Robusta'/'Heidemij' signatures are the mean signatures, the others apply to individual stands. For ash (A) and Scots pine (S) only data at a single nominal viewing angle were obtained.

X–band). The VV polarized data (at 45° incidence angle), shown in figures V.11a–x, differ from the HH polarized levels (at 45° inc. angle) only in the sense that the first are a little higher (in the range of 0 to 1 dB). This behaviour does not seem to differ significantly between the species. (It is noted that the system was not absolutely calibrated. An unknown offset between the VV and HH polarized data is therefore still present.)

5.7 Discussion of L–band results

The radar backscatter properties of forests in the L–band were studied on the basis of Dutscat data obtained in flights FL1584 and FL1585 over the Roggebotzand on 18 July 1985. The results are shown in figures V.12a–t and table V.7.

A striking phenomenon in the L–band dataset is the fact that all signatures show a local maximum (deciduous species) or an absolute maximum (conifereous species) at 45°

incidence angle. This may be an artefact, but for two of the three agricultural fields —crop "A" (figure V.12m) and crop "E" (figure V.12o)— no (local) maximum was found. If it is a real phenomenon (meaning it is caused by the object), it might be related somehow to the typical structure of forests or forest components.

In the L–band dataset, as for the C–band, the total number of stands is not very large. Most species are represented by only one stand, but there are a relatively large number of poplar stands. The discussion below will be limited to poplars and a comparison between species.

Poplars

Seven poplar stands with clones 'Robusta' and 'Heidemij' were measured. The (weighted) mean signature and the individual signatures are shown in figure 5.19c. At first glance, there seems to be a lot of variation around the mean signature. When the stand in compartment N47b is excluded, however, the lowest value for each nominal incidence angle can be discarded in this figure and the remaining standard deviation is only ≈0.5 dB (which is the same as found in the C– and X–bands). Even the significant structural difference between stand N71n, a relatively young stand planted in 1968, and the six other stands, is not reflected in the backscatter behaviour (as was noted for the C–band too!).

The stand in compartment N47b, however, does not differ significantly in any tree or stand parameter from the other stands (table V.8). The only difference is that the poplar stand in N47 (and only in the strip the scatterometer was measuring) has an understory of beech planted in 1978, whereas the other stands have a grassy ground surface. The differences in γ with the six other stands is the strongest at low incidence angles (≈2.5 dB) and smoothly vanishes as a function of incidence angle. At 75° the difference almost disappears.

Three other poplar stands were measured: a 'Gelrica' stand, a 'Geneva' stand and a stand with a mixture of clones. The mixed stand and the 'Geneva' stand, though they belong to other taxonomic groups, show no significant deviations from the mean 'Robusta'/'Heidemij' signature. The 'Gelrica' stand, however, which belongs to the same taxonomic group (and same species) as 'Robusta' and 'Heidemij' shows an increased backscatter level (≈1 dB over the whole angular range), as can be seen in figure 5.20b. This may relate to a significant difference in stand parameters. In this stand, every other row of trees had been cut. This was also true of the willow stand, which has comparable values for stand and tree parameters and also shows a high backscatter level compared with this mean signature, but this comparison is less unambiguous since it relates to another species.

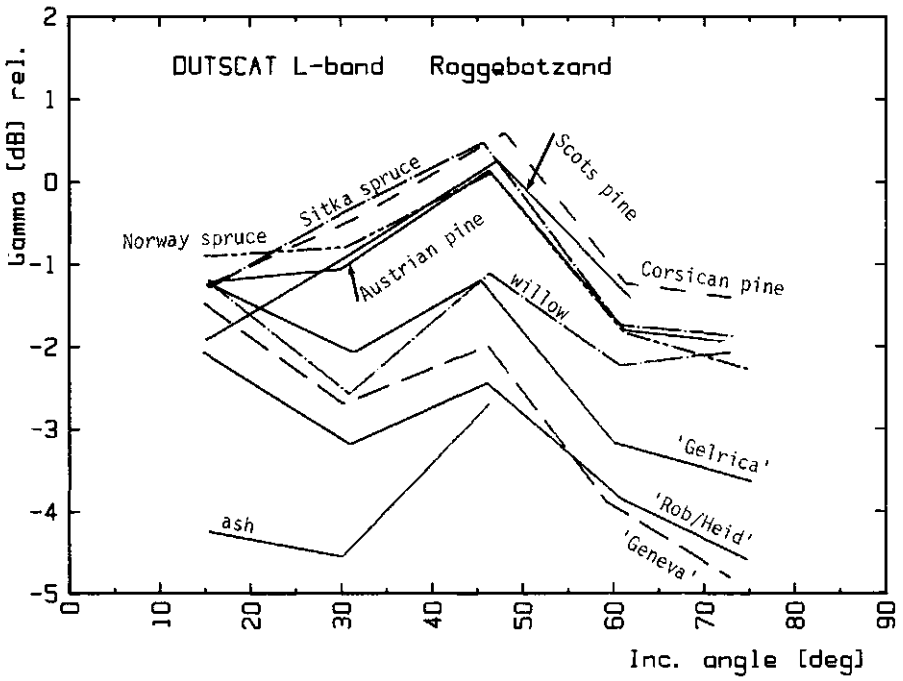

Figure 5.20b. Overview of L–band (HH pol.) signatures. The 'Robusta'/'Heidemij' signature is the mean signature, the others apply to individual stands.

Overview of all species

An overview is given in figure 5.20b of the L–band HH polarized data of the Roggebotzand. For the group of 'Robusta' and 'Heidemij' stands the mean signature is shown; for all other species, the signatures relate to single stands. The differences are small within the group of coniferous species. The group as a whole exhibits the highest levels of backscatter, notably at the medium and large incidence angles. The level of Corsican pine (as with the C–band and X–band) is higher than the level of Austrian pine. The backscatter signatures of the deciduous species are more difficult to describe. The poplar shows a lot of variation, but in contrast to the X– and C–bands, this is not related mainly to (species dependent) morphologic features. The 'Gelrica' stand exhibits a relatively strong backscatter level, which is possibly related to the fact that half of the trees (every other row) have been cut (this difference does not show up in X–band). The poplar stand 'Robusta' in compartment N47b showed an anomalous behaviour which might be related to the understory of beeches. As far as can be concluded from this dataset, its behaviour resembles that of the ash stand which, together with the N47b stand, shows the lowest levels. At 15° incidence angle, these

two stands have the same low relative value (≈ –4 dB) while every other stand has a relative value in the range of –1 to –2 dB. The willow shows a high backscatter level, which at 15° and 75° matches the levels of the coniferous species.

The angular responses differ clearly from the C–band. The coniferous species show a maximum at 45°. The deciduous species, in general, show a local maximum at 45° and an overall decrease with increasing incidence angle. The VV polarized data (at 45° incidence angle), shown in figures V.12a–t, differ from the HH polarized levels (at 45° incidence angle) only in the sense that the first are lower (in the order of 0 to 2 dB). This behaviour does not seem to differ significantly among the different species and stands. The only exception might be (the anomalous) stand N47b. In this case, VV is stronger than HH while for all other poplar stands HH is 1 to 2 dB stronger than VV. (As remarked, the system was not absolutely calibrated. An unknown offset between the VV and HH polarized data is therefore still present.)

5.8 C– and L–band canopy probing data

Results for poplar stands at the Roggebotzand site

When operated at relatively low altitudes, Dutscat can provide information on the vertical distribution of backscattering sources through inversion of the multilevel model introduced in section 3.2. In this section, results are given for several poplar (*Populus spec.*) stands measured in the L– and C–bands and at 60° and 15° angles of incidence and HH polarization. To increase accuracy, the inversion was applied to the averaged return signal from a stand. Since an independent sample of the radar backscatter is obtained every 30 to 35 cm (depending on frequency band) and an individual stand is usually approximately 220 m wide, the influence of speckle in all cases is, even for the smaller stands, very small. All measurements were repeated four times; some were rejected afterwards because of non–negligible aircraft roll (i.e. more than ± 1° from the average value) during the measurement of the selected stand. The L–band measurements were taken on 8 July 1985 and the C–band measurements on 6 July 1984, both at the Roggebotzand site. The poplar stands were fully foliated.

In the C–band and at 16.5° angle of incidence, the four–level 9 m spacing model was applied (figures 5.21a–d). Among others, three stands with the poplar clones 'Robusta', 'Oxford' and 'Geneva', in compartments O57b, O61a and N64f, respectively (see table V.8), were measured. These three stands differ in structure. The 'Robusta' stand has a lower degree of crown closure and the trees are a few meters taller. A significant part of the radar return (≈40%) originates (according to model assumptions) from the ground, the rest

from layers 2 and 3 corresponding to the tree crowns. Layer 1, corresponding to a layer beneath the crowns where only stems are present, does not contribute significantly. It is not apparent from these data whether or not the stems contribute through multiple reflections via the ground. (These contributions have the longest delay time, longer than the returns from the ground, but are assigned to level 0 in this model.) The 'Oxford' and 'Geneva' stands have smaller trees (≈24 m). The model assigns no significant contributions to the 27 m level in these cases. The 'Oxford' stand has a heavy understory of beech (*Fagus sylvatica*) with a height of 6 to 7 m. This explains the relatively strong contribution of layer 1. For comparison, and as a check on the algorithm, the same inversion was applied to a grass field in the same track (figure 5.21d). Within the confidence intervals shown, and as could be expected, all backscatter contributions are assigned to the ground level.

At 60° and for the L–band cases, the returns from individual layers become more difficult to disentangle. A three–level version of the model, with 12.5 m spacing between the levels, was therefore selected as a more appropriate choice. In these cases only a 'Robusta' stand (compartment N47b) was analysed.

According to the model assumptions, in the C–band at 60° most of the returns originate from the crowns; only a small amount (10 to 15%) originates from the ground or from stem–ground interactions (figure 5.21e).

In the L–band at 14.5° incidence angle, ≈75% of the backscatter originates from the ground or stem–ground interactions (figure 5.21f). Since the degree of crown closure is larger than 80%, it is probable that the (fully foliated) crowns are very transparent at this frequency, or, possibly, the forest ground surface (lower parts of trunks included) has a very much higher level of backscattering. The crowns (layers 1 and 2) contribute ≈25% of the backscattered power. For comparison, the same inversion (three–level) was applied to an adjacent grass field (figure 5.21g). Also for this case the model correctly assigned all backscatter contributions to the ground level.

In the L–band at 61.5°, both crowns (layers 1 and 2) and ground contribute (figure 5.21h). Even at this angle, where the path of propagation through the canopy is very long, scatterers near the ground still contribute significantly.

Through mere coincidence, the poplar stand selected for the L–band inversion is the anomalous stand in compartment N47b (see preceding section). This stand does not differ significantly from the other poplar stands in canopy structure or stand and tree parameters, but instead of a grassy ground surface like the other stands, it has an understory of young beech with a height of ≈2 m in a strip coinciding with the Dutscat track. The total backscatter, notably at the small incidence angles, was found to be

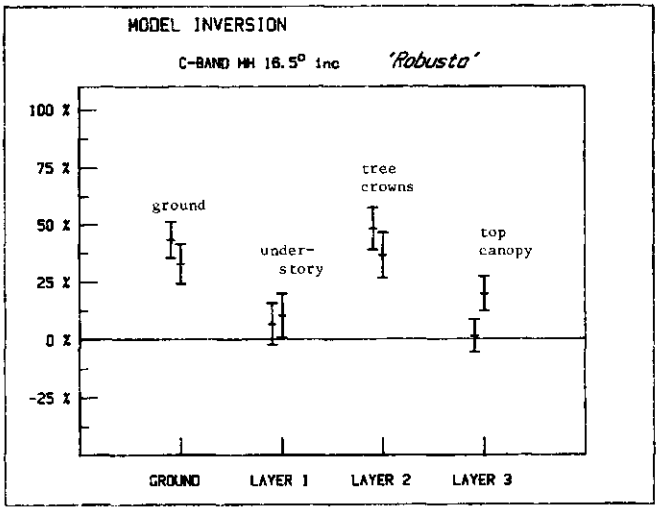
MODEL INVERSION
C-BAND HH 16.5° inc
'Robusto'
100 %
75 %
50 %
25 %
0 %
-25 %
ground
under-
story
tree
crowns
top
canopy
GROUND
LAYER 1
LAYER 2
LAYER 3

(a)

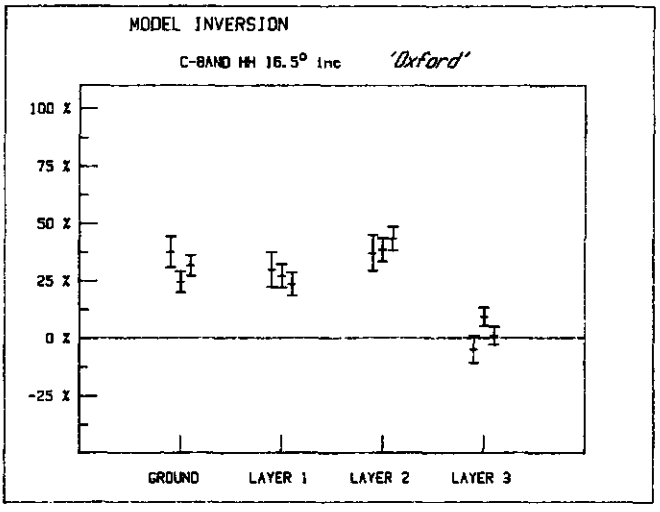
MODEL INVERSION
C-BAND HH 16.5° inc
'Oxford'
100 %
75 %
50 %
25 %
0 %
-25 %
GROUND
LAYER 1
LAYER 2
LAYER 3

(b)

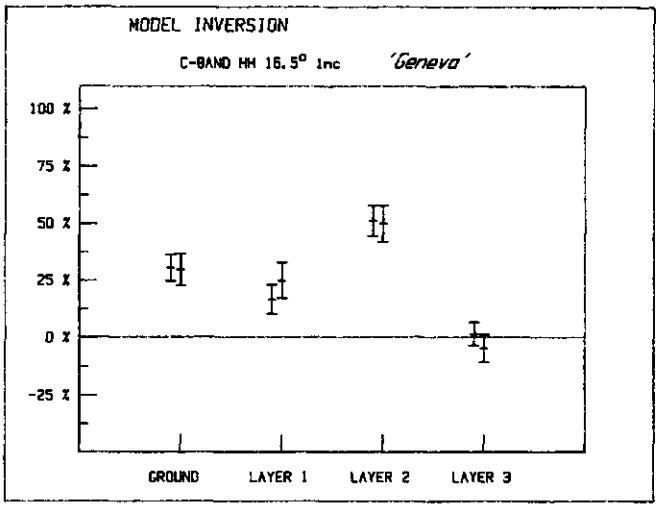
MODEL INVERSION
C-BAND HH 16.5° inc
'Geneva'
100 %
75 %
50 %
25 %
0 %
-25 %
GROUND
LAYER 1
LAYER 2
LAYER 3

(c)

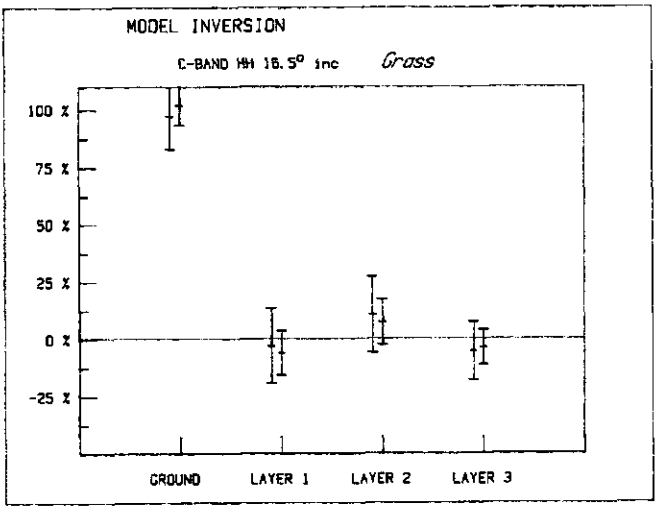
MODEL INVERSION
C-BAND HH 18.5° inc
Grass
100 %
75 %
50 %
25 %
0 %
-25 %
GROUND
LAYER 1
LAYER 2
LAYER 3

(d)

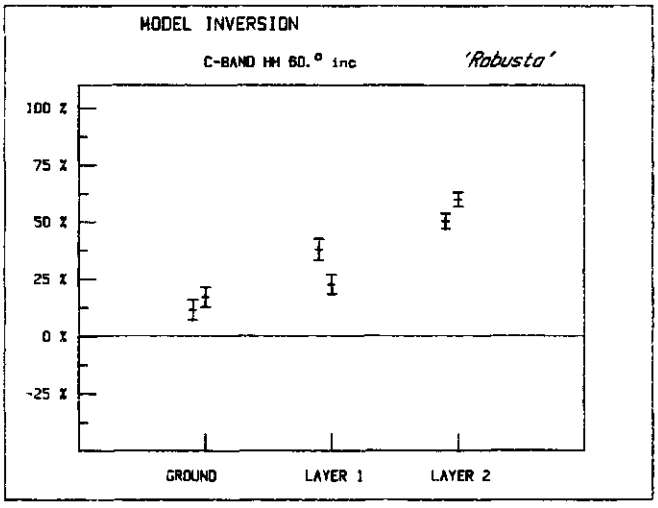
MODEL INVERSION
C-BAND HH 60.° inc
'Robusta'
100 %
75 %
50 %
25 %
0 %
-25 %
GROUND
LAYER 1
LAYER 2

(e)

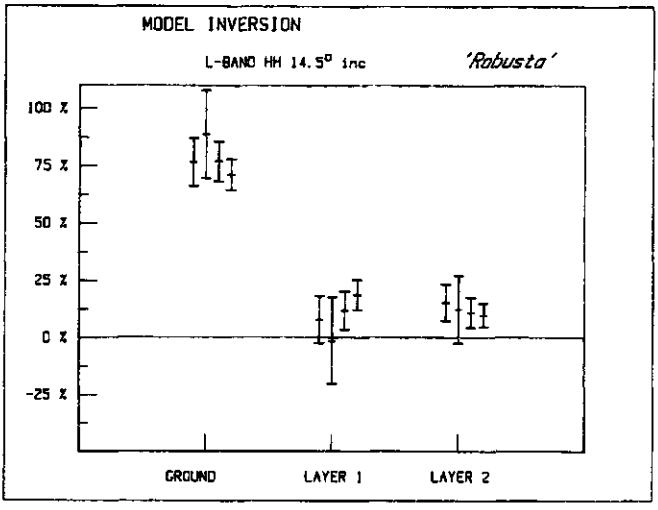
MODEL INVERSION
L-BAND HH 14.5° inc
'Robusta'
100 %
75 %
50 %
25 %
0 %
-25 %
GROUND
LAYER 1
LAYER 2

(f)

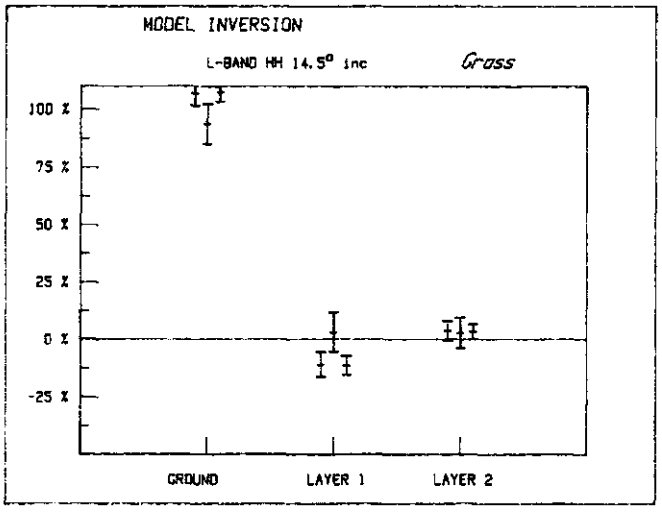

(g)

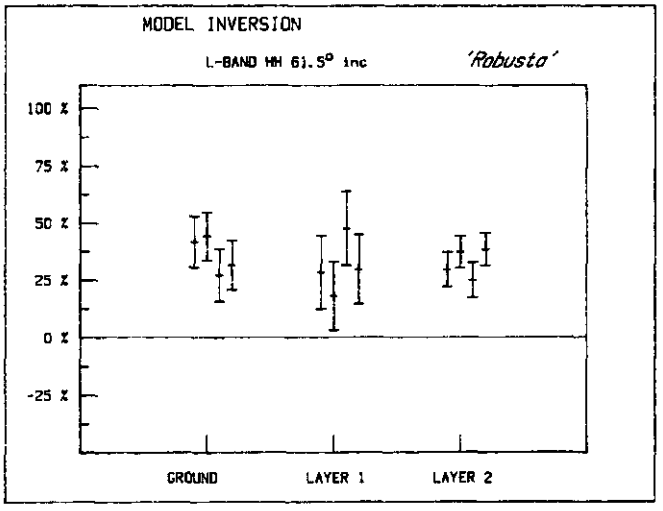

(h)

Figure 5.21 (a–h). The relative contributions A_i / γ (expressed as a percentage), according to the assumptions of the multilevel model, from layers in the forest canopy and the ground. Each bar represents a 50% confidence interval for the corresponding estimates. In each figure two, three or four results are grouped for each layer.

anomalously low. It seems plausible that this is caused, somehow, by the understory. Despite the relatively low backscatter level found at 15^{o} for this stand, the inversion suggests that scatterers near the ground level still dominate the backscatter at 15^{o}.

On the basis of theoretical considerations, it is often suggested (see also discussion in section 5.9) that ground–trunk interactions, the trunk and ground surface acting as a dihedral corner reflector, have a prominent effect and that the strongest contributions can be expected when the ground surface acts as a specular reflector. When the grassy and flat ground surface of the other poplar stands acts as a better (specular) reflector than the beech understory, which is (also on the basis of theoretical considerations) likely for L–band, the difference can be explained qualitatively.

As remarked in section 3.2, there are some limitations inherent in inversion techniques of this type and results should therefore be interpreted with care. The multilevel model is a simple scatter model designed to obtain a more elaborate geometric correction in the radar equation. Inversion of the received signal, without additional data, is mathematically possible. The physical meaning of this inversion, however, is not totally unambiguous. Distinguishing between contributions of multiple scattering and those of single scattering, for example, is hardly possible.

5.9 Synthesis and evaluation of results

5.9.1 Basic empirical results

X–band signatures from a multitude of tree species were obtained with the SLAR (sections 5.1 to 5.3). The first series of measurement flights, carried out throughout the June 1982 – May 1983 period, resulted in the assessment of relative backscatter levels for different phenologic stages. All other measurement flights, with the SLAR and Dutscat, were made in summer. The employment of an array of calibration corner reflectors and the SLAR's internal calibration in 1985 yielded absolute γ data within a few dB. A direct comparison between tree species at all four sites was made on this occasion.

C– and L–band signatures could be assessed with Dutscat (sections 5.5 to 5.7), but these data apply to a considerably smaller number of stands and have internal calibration only.

Overview of X–, C– and L–band basic data

In X–band, the figures found for the standard deviations of γ values (or speckle level) within homogeneous stands, with spatial structural elements smaller than the system's spatial resolution, are in close agreement with the expected minimum on the basis of the theoretical concept of Rayleigh fading (0.80 dB for 30 independent samples). For some homogeneous stands, with relatively large spatial structural elements, significantly higher values, in the order of 1.1 to 1.3 dB, were found. (Similar results were found for C– and L–bands , but these have not been included in this thesis.)

In X–band, the standard deviations of stand–averaged γ values relative to a "class" characteristic mean signature were found to be in the order of 0.5 dB for almost all tree classes, all times of observation and over the whole angular range studied. For the other frequency bands, no firm conclusions could be drawn because of the limited number of stands per tree class. Only for poplars were a reasonable number of stands present. For the C–band, for the 12 'Robusta' and/or 'Heidemij' stands measured, the same figure of 0.5 dB was found. For the L–band, for the seven 'Robusta' and/or 'Heidemij' stands measured, a significant variation of stand–averaged γ values relative to the mean signature was found.

The overall range of stand–averaged γ values, over all species, is not large. For example, for the summer observations of the Roggebotzand and with HH polarization, an approximate range of 9 dB range was found for X–band, 5 dB for C–band and 6 dB for L–band.

It could be concluded that backscatter properties depend on wave parameters, species dependent (presumably morphologic) features and other, not necessarily species dependent, factors such as stand and tree parameters, needle loss or undergrowth. In the X–band and, possibly, the C–band the influence of these other factors was found to be small except for a few specific cases. For the L–band, the interaction mechanism is likely to be more complex. This point is described in the next section.

In X–band differences in backscatter level in general seem to be governed by species (or variety) dependent morphologic features. It could be concluded on the basis of several considerations that this is probably true for C–band too. The main difference found between X– and C–bands is the complete rearrangement of the mutual backscatter level differences of the species. In X–band, deciduous species show the highest backscatter level, followed by the spruces and pines. In C–band, spruces have the highest levels, followed by the deciduous species and pines.

Relationship of morphologic features with X–band backscatter

In X–band, the differentiation in radar backscatter level shows a clear link with the taxonomic differentiation and, probably, with the related characteristic morphologic features. The radar backscatter signatures of the poplar clones of the Horsterwold, for example, could be differentiated according to their taxonomic classification. A possible relationship with leaf tilt angle distribution was suggested.

For Japanese larch, an anomalously high figure was found for the standard deviation of stand–averaged γ values relative to the mean signature in May. This could be related to morphologic variation at the time of observation. (The trees were in a transitional phase between the bare stage and having fully grown needles. The younger trees appeared to have longer needles at that particular time.)

Relationship of biophysical characteristics with X–band backscatter

Through an analysis of empirical relationships, an attempt was made to trace physical relationships with other biophysical characteristics (stand and tree parameters, diagnostics, undergrowth, etc.).

For poplars 'Robusta' and 'Heidemij', a relationship with tree diameter and height was suggested for the March and May observations by statistically significant figures for the correlation coefficient. A plausible physical cause could not be indicated, however.

For Japanese larch, no statistically significant correlations between backscatter level and the biophysical characteristics studied were found except for R_{ct}, which is related to canopy roughness.

For the Scots pines at the Kootwijk site, a relationship between an increased backscatter level and needle loss was suggested. (This point is described in section 5.9.4.)

For the Scots pines in the Speulderbos, a statistically very significant relationship with age was found. A careful analysis of the stand properties suggested clearly the following physical explanation. Most of the old stands have a very low degree of crown closure and a heavy understory of oak, which has a relatively high backscatter level. In these cases, a high stand–averaged mean backscatter level was found. For other old stands, systematic differences with younger stands were not found.

Similar effects were noticed at the Horsterwold site for very young plantations. The canopies are not closed yet and show backscatter signatures that deviate from the backscatter signatures of older stands of the same species with closed canopies. Clearly, a mechanism is suggested for stands with a low degree of crown closure that explains these deviations by mixing with radar backscatter contributions of that part of the ground surface and/or undergrowth which is not covered by a crown canopy.

5.9.2 Notes on transmissivity and probing measurements

Though estimates of transmittance (or extinction coefficients) for agricultural crops, together with comprehensive object descriptions, have been published by several investigators, published data are very scarce for forests. Currie et al. (1975) made measurements in the X– and K–bands (VV and HH polarization) using corner reflectors in an oak and a mixed forest. The X–band results are not inconsistent with the results presented here. A real comparison cannot be made, however, since the published dataset does not include the relevant biophysical data. Churchill and Keech (1985) performed an experiment in Scots pine stands in Thetford forest (U.K.) involving the use of corner reflectors and the X–band with HH polarization. These reflectors had smaller dimensions (65 cm) than the ones used in The Netherlands test sites and were not visible in the radar data. This result is consistent with the data presented in this thesis. It is likely that the relatively small radar cross section (6.2 dB lower than the smallest used in The Netherlands, see also eq. 3.24) in combination with the strong attenuation caused by coniferous tree crowns (in The Netherlands it was found to be in the order of 20 dB) makes the reflectors invisible.

No other estimates of transmittance or transmissivity for forest canopies have been found in literature except for the C–band, in which other techniques, i.e. canopy probing techniques, were utilized. Several other research groups, although taking other approaches than described in this thesis, recently examined the problem of probing thick vegetation canopies to obtain microwave properties beyond backscattering coefficient. Paris (1986a) and Pitts et al. (1985) used a C–band narrow–beam FM–CW scatterometer to measure the backscatter properties as a function of height.

Paris measured backscatter of a peach orchard and developed a differential backscatter coefficient as a function of slant range. He found that this function decays exponentially once the beam is totally immersed in the canopy. By assuming that only single scattering is present and that the canopy is homogeneous, he could estimate the extinction coefficient (for that part of the canopy corresponding to the exponential decaying part of the function).

Pitts measured a high density aspen canopy. Also in this experiment, a specific inversion scheme was adopted to develop a differential backscatter coefficient as a function of slant range and to estimate the extinction coefficient. The values Pitts found agree well with results of transmittance measurements by means of an active radar calibrator placed on the ground. Both Pitts and Paris found, for the C–band, figures for total canopy transmissivity in the range of 5 to 10 dB. This is much lower than the figures given here for X–band and the figures given by other investigators for X– and K–bands. Since these results apply to different stands and a lower frequency, however, an unambiguous comparison is not possible. Pitts obtained his measurements throughout a large part of the growing season. It is interesting to note that he found an empirical relationship between the decrease in the extinction coefficient and the decrease in the water content of the leaves.

Zoughi and his colleagues (1986) used a short–range (4 m) very–fine–resolution (11 cm) narrow beam (16 cm diameter) FM–CW X–band VV polarization scatterometer to measure isolated tree branches. By using several defoliation stages, they were able to identify primary contributors to the backscatter and attenuation. For pines, the needles were found to cause the strongest backscatter as well as the strongest attenuation. For the deciduous species investigated, the leaves caused the strongest backscatter and attenuation, but in the absence of leaves the twigs and branches gave relatively strong backscatter. It was found that when the water content of the leaves decreases, both attenuation and backscatter of the leaves decreases.

Laboratory measurements of very small trees with very–fine–resolution FM–CW scatterometer systems were made by Mougin et al. (1987) and Hirosawa et al. (1986). Mougin obtained his measurements in an anechoic chamber with X–band and VV and HH

polarization. Very detailed radar cross section profiles of trees (pines and spruces) were obtained. The penetration depth was shown to be dependent on both polarization and moisture content.

It can be concluded that many research groups, independent of each other, have recently developed techniques to measure microwave properties beyond the backscattering coefficient of forests or forest components. The (spatially very detailed) X–band measurements made under laboratory conditions by Zoughi and Mougin may yield data of major importance in modelling studies, but it is not yet clear how these results can be extrapolated to real forests. The Dutscat results and the results presented by the groups of Pitts and Paris relate to forests under normal conditions, but the inversion schemes developed have inherent limitations. Strictly speaking, they can be applied only under the assumptions of a layered forest structure and single scattering.

5.9.3 Effect of leaf orientation

On the basis of theoretical considerations, Eom and Fung (1984) predicted a dependence of γ on leaf orientation distribution. One of the phenomena predicted by their model, for example, is that the shape of the backscatter level signature as a function of observation direction (in elevation and azimuth) resembles, more or less, the shape of the probability density function of the direction of normal vectors on the (deciduous) leaves. Significant effects are anticipated especially at the higher frequencies. Though it is difficult to validate this theoretical model (measurements of leaf orientation distribution of trees are very complex and tedious), the results presented in the preceding sections are not inconsistent with this theory and, in some cases, clearly support the theory in a qualitative sense.

Incidence angle dependence

The pronounced difference in angular dependence between the poplars of group II (erectophile distribution) and group IV (planophile distribution), in X–band as well as C–band, can be related to the typical leaf tilt angle distributions. Also the observations that most species show a more or less flat angular response for γ and that the poplars of group IV and the maple (both have a planophile distribution) show a steep decrease of γ with incidence angle are predicted qualitatively.

Look direction dependence

In addition to an angular dependence, a directional dependence related to non–uniform azimuthal distribution of leaf orientation is predicted theoretically. The directional

dependence observed for some poplar clones ('Robusta' and 'Heidemij') and beech in X– and/or C–band might be explained qualitatively from this model. This view is strongly supported by the observation (for poplars) that directional dependence can differ between times of observation. Hence static factors, such as tree row direction, can be ruled out as single causal factors. The significance of a dynamic structural change, however, such as a change in (azimuthal) distribution of leaf orientation, is very plausible. These changes may be caused by wind (the leaves of these poplars are easily moved by wind) or by heliotropic behaviour (they are known to exhibit such behaviour). The latter means that leaf orientation, to some extent, is a response to the Sun's position and level of irradiance.

Synthesis of empirical results for 'Robusta'

An overview of the potential factors of relevance is given in table 5.9 for the C–band as well as the X–band measurements of poplar 'Robusta'. The March measurement is not included in this table. At that time, poplars were not foliated and no look direction dependence was detected. The last column indicates the radar look direction for which the maximum levels were found. Note that the X–band measurements were made in only two (opposite) directions.

The empirical results do not yield decisive answers. On the one hand, the wind directions seem to match the radar look directions at which the maximum levels were measured (meaning the backscatter is strongest when measured towards the wind). On the other hand, a wind speed of 4 m/s or less is barely sufficient to cause any relevant changes in the leaf angle orientation distribution. The only effect noticed at these low wind strengths was a small vibration (around the rest position) of the leaves and the smaller twigs. Only on 6 September 1984 (8 m/s) might a relevant change in leaf angle orientation have occurred because of wind. For this date, both the beech stand (figure 5.18b) and the poplar stand 'Robusta' (figure 5.18a, bottom curve) show a minimum level for observations in the southern directions. When this date is excluded, since wind may be only one causal factor, the remaining cases show a maximum backscatter for observations in the approximately south–west directions with the (possible) exception of June, when no clear difference was observed. The June measurement was the only measurement made in the evening. Therefore neither the effects of wind nor heliotropic effects can be ruled out. Finally, it should be noted that the strength of the look direction dependence as observed in X–band differs significantly between the 'Heidemij' and 'Robusta' clones (figure 5.3). Since this difference can be related, theoretically, to a difference in (the dynamics of) leaf orientation distribution, radar may be regarded as a potentially useful instrument in the study of physiologic differences between poplar clones.

Table 5.9. Overview of local time, wind direction, wind speed and the radar look angle at which the maximum backscatter was observed for poplar 'Robusta' for all X–band (SLAR) and C–band (Dutscat) flights of interest.

date	local time	wind direction	wind speed	direction(s) of maximum backscatter
X–band:				
15 June 1982	19.00	020°	1.5 m/s	none
9 September 1982	9.00	180°	3 m/s	225°
17 May 1983	10.30	220°	3 m/s	225°
C–band:				
6 September 1984	7.30–8.00	030°	8 m/s	–30°/30°/90°
28 August 1985	15.30–17.30	230°	4 m/s	210°/270°

5.9.4 Effect of needle loss

Pinus nigra

The lowest level of backscatter at the Roggebotzand site in the X–band was found for the *Pinus nigra* variety 'nigra' (or Austrian pine). For the variety 'corsicana' (Corsican pine), with almost identical morphologic and biophysical properties, a 1 to 2 dB higher level of backscatter was found, however. Further, for all SLAR measurements, the backscatter of the Corsican pine was found to be very similar in strength to that of the Scots pine. This contrasts with the results reported by Churchill and Keech (1985) for the Thetford forest (U.K.). In this forest, where both Scots and Corsican pine occur and no excessive needle loss was found, the backscatter level of Corsican pine is 1 to 2 dB less than for Scots pine in the X–band. This result suggests that the backscatter level of Corsican pine in the Roggebotzand forest is the anomalous one. Also in the C–band, the backscatter level of Corsican pine is significantly higher than the level of Austrian pine.

At the Roggebotzand, some morphologic features of the Austrian, Corsician and Scots pines were measured and qualitative observations were made. Also some stand and tree parameters could be obtained from the stand register. The same was done for Scots pine. Table 5.10 gives an overview of the results. The differences in stand and tree parameters are not very large. The dimensions of the needle cross section and the number of needles in a new shoot are almost equal. Differences in the morphologic appearance emanate mainly from the needle length and the number of years of needles. (Shoots lose their needles after several years.) For the last parameter, normal figures were found for the Austrian and Scots pine. The Corsican pine showed an excessive loss of needles, however, which was caused by the disease "Brunchorstia" (a fungus infection). Also the density of needles in the crowns, which seemed to form fewer shoots, was clearly less for the Corsican pine.

Table 5.10. Some morphologic features, stand and tree parameters of Austrian pine, Corsican pine and Scots pine at the Roggebotzand site. The stand and tree parameter values date from 1982; the observations of morphologic features date from 1985.

parameter/ feature	Austrian pine	Corsican pine	Scots pine
compartment	N85	N88	N89
needle length	9–11 cm	13.5–16 cm	6–7 cm
needle diameter	0.8x1.4 mm	0.8x1.4 mm	0.8x1.6 mm
needle years	4 year	3 year	2.5 year
needle pairs per shoot	120–125	120–125	120–125
volume (V)	153	176	133
number of trees (N)	1240	1478	1167
trunk diameter (dbh)	15.1	14.3	14.2
tree height (h_{dom})	12.75	14.00	13.75

Pinus sylvestris

The measurement results suggest a relevant effect of needle loss for Scots pine as well. When the data of the Roggebotzand are compared with the data of the Kootwijk site (figure 5.9), it becomes clear that the backscatter level of the Scots pine at the Roggebotzand site, which has 2.5 years of needles, is significantly less then the backscatter level of Scots pine at the Kootwijk site, where the years of needles ranges from 1.1 to 1.6. Even within the Kootwijk site, such a relationship appeared to be statistically significant (section 5.4).

For three different cases, namely *Pinus nigra* at the Roggebotzand, Scots pine at the Kootwijk site and the comparison of Scots pine at different sites, a causal relationship is therefore suggested between the loss of needles and the increase of the backscatter level. In the next section, the nature of the microwave interaction mechanism for pines and the impact of needle loss on backscatter level is described on the basis of theoretical considerations (cloud model) and transmissivity data (sections 5.4 and 5.9.2).

5.9.5 Comparison of X–, C– and L–band results

The backscatter properties of forests in X– and C–bands show many similarities. In both cases, variations in stand and tree parameters or undergrowth have negligible effects. Differences in backscatter levels seem to be governed by species (or variety) dependent morphologic features. For example, the differentiation between Austrian pine and Corsican pine or the differentiation between the taxonomic groups of poplar clones found in the X–band are also found in the C–band. For the tree classes measured in the X–band, as

well as the poplar group 'Heidemij'/'Robusta' in the C–band (the only tree class represented by a large number of stands), the variation of stand–averaged γ values is limited to a small band ($\approx$0.5 dB standard deviation) around the mean signature. In the C–band, γ shows a flat angular response except for the poplars of group IV, which show a relatively steep decrease with increasing incidence angle. The same might be true for X–band. (The SLAR measurements have an unknown angular dependent offset. This offset may be limited to a few dB. In fact, a small overall angular modulation was noticed in figure 5.13.) The look direction dependence of poplar clone 'Robusta' in the C–band also seems to show similarities with the X–band cases. The main difference between X– and C–band is the rearrangement of the mutual backscatter level differences among the tree classes. Notably the poplars show a significant relative decrease and the spruces a significant relative increase in C–band.

The properties of forest L–band backscatter, however, clearly differ. The angular dependence of γ shows a maximum at 45° for coniferous species and a local maximum at 45° for deciduous species. Furthermore, in general, the deciduous trees show an overall decrease of γ with increasing incidence angle. The variation in stand and tree parameters or undergrowth seems to have a more pronounced effect, while variation caused by morphologic features seems to be less important. All coniferous species, in contrast to the other bands, show very similar signatures. And, as can be seen in table V.8, the differences in stand and tree parameters are not very large either. Considerable variation is present within the group of poplar clones, which seems to be primarily related to differences in stand and tree parameters or undergrowth, while the differentiation between different taxonomic groups is not evident from these data. For example, poplar clone 'Geneva' belongs to another taxonomic group than the poplar clones 'Robusta', 'Heidemij' and 'Gelrica' (all clones of the species *Populus* x *euramericana*). 'Geneva' and all stands of *Pop.* x *euramericana* species with comparable values for stand and tree parameters have more or less the same signature. The exceptional cases all belong to *Pop.* x *euramericana* stands and, as discussed above, this is likely to be related to the understory (stand N47b) or stand and tree parameters ('Gelrica').

In considering the nature of the backscatter mechanism at the different wavelengths, it is interesting to show how the results presented here compare with results obtained by other investigators during the last few years.

Bernard et al. (1987) reported results from a C–band scatterometer campaign over the French Guyana rainforest. In such forests, hundreds of species can be found (sometimes within a hectare) and none of them is dominant. The tracks were flown over large parts covering a variety of forest types (therefore a certain variation in biophysical parameters and species composition can be presumed). Measurements were obtained in the 15° to 55°

range of incidence angles. In this range, a flat angular response for γ was found with an absolute level of –8.35 dB ± 0.3 dB. Not only the spatial variation was small; also the variations caused by rainfall, diurnal effects and look direction were all found to be within ± 0.5 dB. The flat angular response and the presumably low sensitivity for variations in biophysical characteristics are in agreement with the C–band results presented here.

Sieber (1985) compared X– and L–band data for coniferous and deciduous species in forests near Freiburg. No further differentiation for the species or values for stand and tree parameters were supplied, and the radar data were presented as uncalibrated density classes. As far as can be concluded, however, the results are in complete agreement with the results presented here. In the L–band, the coniferous species show higher backscatter levels than the deciduous species. In the X–band, the relationship is reversed and there is a small overlap.

Wu (1987a) published results of L–band, multipolarization SAR measurements in the angular range of 30^0 to 40^0 incidence angle for several forest classes. Arranged in the order of increasing backscatter level, the results for HH polarization are (the radar backscatter levels indicated as uncalibrated density classes): clearcut (76.4), young pine (92.4), natural pine (107), hardwood (178), swamp forest (190), wet clearcut (203) and flooded swamp forest (223). Here the reverse is true: deciduous species show higher backscatter levels than coniferous species. The young pine plantations are three years old and 2 m high and show the lowest backscatter levels. For the natural pine stands, for which the figures given for stand and tree parameters are in the same range as the pines in the Roggebotzand, the backscatter level is a little higher. The deciduous species show, in contrast to the Roggebotzand, higher values than the pines, but the physical structure also differs significantly. For the hardwood areas (maple and oak), the values given for biomass are extremely low compared with the Roggebotzand. The other areas with deciduous trees have standing water or a very wet ground surface (swamp forest), or are flooded (flooded swamp forest).

Imhoff et al. (1986) reported results from SIR–B (L–band) measurements over mangrove forests in southern Bangladesh. This analysis revealed a high degree of transparency for the mangrove forest canopy in L–band over the whole angular range studied (26^0 to 58^0 incidence). Standing water could be identified as a function of tidal inundation. Clear relationships with vegetation structure and density, if any, could not be established. The presence of standing water (even beneath a complete forest cover) was identified as the dominating factor.

Similar results were reported by Skidmore et al. (1986) for the Riverina forests in south–east Australia. On SIR–B images, the flooded forest areas could be clearly

delineated on the basis of bright returns. There are some indications that within these flooded areas the backscatter level relates to forest density.

Wu (1987a) studied the relationships between height, basal area and total tree biomass of pine stands and L–band backscatter level. Results were given for three polarizations (HH, VV and HV) based on 13 test plots. The HV polarization yielded the highest correlations, with r–values of 0.50, 0.82 and 0.77, respectively. Based on 21 test plots in another study area, Wu (1987b) reported the following results for pines. For age and biomass, and for all three polarizations, r–values were found in the range of 0.74 to 0.89. The results for height were less significant. Le Toan and Riom (1981) reported very significant correlations between the backscatter level in L–band (at both polarizations measured, HH and HV) and height and age for pine plantations in southern France.

Also in this study (section 5.3), a significant correlation (for Scots pine) was found between backscatter level (in X–band) and age, height and trunk diameter, but the (empirical) relationships could be explained by the presence of an oak understory in some old stands with a low degree of crown closure. Though statistically significant correlations were found in this case, there is no direct causal link with the object parameters. In fact, no causal relationships with age or stand and tree parameters were found at all for any of the tree classes studied in the X–band.

The L–band Dutscat data and the results given by other investigators suggest such relationships exist in the L–band. Moreover, in the L–band, the canopy seems to be transparent to a certain degree. The beech undergrowth in stand N47b under a fully closed poplar canopy is "visible", and other authors report standing water under a closed canopy to have a dramatic effect.

The relationship between backscatter level and the taxonomic classification found in X–band is not clear for the L–band. This seems logical if the canopy layer, which contains the leaves and needles, is highly transparent. For L–band at the Roggebotzand site, and also at the Freiburg site, the coniferous species show the highest backscatter level. Wu reported the reverse. Stand and tree parameter dependent variation seems to be relevant for L–band, as was suggested by the poplar data of the Roggebotzand and the pine data analyzed by Wu and Le Toan.

5.10 The interaction mechanism

X– and C–bands

It was concluded from the corner reflector experiment that the X–band attenuation of crowns of deciduous trees is very high and that the attenuation of crowns of coniferous trees may be lower but still is in the order of 20 dB (two–way) or more (section 5.4). It was also concluded that if scatterers near the ground surface are in direct line of sight of the sensor (through large gaps in the canopy), they may contribute significantly.

From the Dutscat multilevel model inversion, it was concluded that in C–band and at 60° incidence angle, most of the backscatter originates from the top layers, i.e. the tree crowns. At 15° incidence angle, scatterers near the ground surface and of the understory were shown to yield major contributions (section 5.8). At this steep angle, however, a significant part of the scatterers of the lower layers might have been in direct line of sight. (The crown cover was more than 80% in these cases. This means that in nadir direction this fraction of the lower layers is covered by tree crowns. At larger angles from nadir, however, depending on crown architecture and angle of view, the effective crown cover is much higher or may even be complete.)

If the range of very steep angles is excluded and the degree of crown cover is substantial, it may be hypothesized, on the basis of these findings, that the forest canopy acts as an opaque volume for the X– as well as the C–band. It will be shown that this view is consistent with other findings.

The theoretical concept of the cloud model, introduced in section 3.1, might clarify some of the possible implications. For an opaque and homogeneous volume, only scatterers in the upper layers are not attenuated significantly and may therefore contribute significantly. Theoretically, the height of this upper layer depends on the incidence angle and the degree of opaqueness. The degree of opaqueness, in turn, depends on many factors (properties of individual scatterers, density of scatterers and wave parameters). If the cloud model is assumed to be applicable (meaning it is allowed to ignore multiple scattering and electro–magnetic coupling) and an opaque volume is assumed, the backscatter level does not depend on the depth of the relevant layer but only on the properties of individual scatterers found in this layer.

For the conditions given, it might be assumed that the relevant scatterers are in the upper layers (the upper or outside parts of the crown volume) which contain leaves or needles and twigs. It then follows that this layer determines the actual backscatter signature. And if the cloud model is assumed to be applicable, it follows that the actual backscatter

signature is determined by the electro–magnetic properties and orientation of the individual components (such as leaves, needles, twigs). The latter implication is consistent with the result that (1) a clear link between radar backscatter level and the taxonomic differentiation was found and (2) a probable relationship with leaf orientation (tilt angle and azimuthal distribution) was found.

Also the angular responses found do not contradict the assumption of an opaque volume scatterer. An opaque medium with isotropic volume scattering will theoretically yield a flat angular response for γ. In C–band, and probably X–band, this behaviour was actually found for most species. The only exceptions are deciduous species with a planophile leaf orientation distribution (some poplar clones, maple) which show a significant decrease in backscatter level with incidence angle. This behaviour can be explained by theoretical (non–isotropic) volume scatter models (Eom and Fung, 1984). (This particular model of Eom and Fung applies to a layer of discs and was developed to model agricultural crops. Under the circumstances assumed here, however, such a model may also be applicable to trees.)

Laboratory measurements made at X–band frequencies (Zoughi et al., 1986 and Mougin et al., 1987, see also section 5.9.2) have indicated that for pines the needles cause the strongest backscatter as well as the strongest attenuation, and that for deciduous species the same applies for leaves. In the absence of leaves, however, the twigs and branches give a relatively strong backscatter. These results are consistent with the inference made above that the backscatter level is probably strongly related to (species) characteristic morphologic features. Leaves and needles have dimensions, shapes and orientations that are to a large extent species dependent.

The relationship between needle loss and backscatter level increase might be explained theoretically on the basis of a multiconstituent version of the cloud model. If pine trees are modelled as an opaque and homogeneous layer with only one type of scatterer (representing the needle), needle loss does not have any effect as long as this layer does not become transparent. A plausible explanation can follow when this (opaque) layer is assumed to have two types of scatterers, representing needles and twigs (or branches). When the number of needles decreases, the ratio between the numbers of these two types of scatterers changes and thus the backscatter level can change.

A similar explanation might be inferred also from the experimental results. From the laboratory experiments mentioned above, it was concluded that needles are the primary contributors to backscatter and are the strongest cause for attenuation. The needles in normal situations might therefore determine the actual backscatter level. When the number of needles decreases, (1) the backscatter from the needles decreases (theoretically

this is the case for a single–constituent transparent layer but also for a multiconstituent layer) and (2) the backscatter contributions from the twigs or branches is attenuated less. Since twigs and branches give a relatively strong backscatter, the net result of needle loss is a backscatter increase. The other result of needle loss, the decrease of attenuation, can also in principle be measured. Though the transmissivity measurements did not yield decisive answers in this respect, the results were not inconsistent. In a few cases, relatively low figures were estimated for canopy transmissivity of Corsican pine but never for Austrian pine. For Scots pine at the Kootwijk site, which had a high degree of needle loss, the transmissivities were found to be among the smallest. In no case, however, was transmissivity found to be so small that the proposed concept of an opaque volume scatterer has to be rejected.

L–band

The backscatter properties of forests in L–band are very likely to be completely different. The results of this research and published results elsewhere indicate that deciduous canopies are transparent to a high degree and that trunks, the ground surface and undergrowth have major effects.

L–band radar signatures appear not to be related to species dependent features to the same extent found for the X– and C–bands. Moreover, much stand and tree parameter dependent variation seems to be present in L–band, as was suggested by the poplar data of the Roggebotzand and the pine data analysed by Wu and Le Toan (section 5.9.5).

The results from the multilevel model inversion of L–band Dutscat data clearly indicated the high degree of crown canopy transparency for poplars (section 5.8). At an angle of 15^{o} incidence, ≈75% of the backscatter was found to originate from the ground surface or, possibly, stem–ground interactions. Even at an angle of 60^{o}, where the path of propagation through the canopy is very long, scatterers near the ground surface were still found to contribute significantly.

The anomalously low level of backscatter found for a poplar stand with a beech undergrowth was explained as another indication of the high degree of canopy transparency (section 5.8). This low level was believed to be caused by relatively low contributions of the beech understory (compared with the grassy underfloor found for the other stands) either from direct scattering or, as was suggested, from a reduced stem–ground interaction contribution.

The angular responses in L–band differ clearly from the other bands. The coniferous species showed a maximum at 45^{o}. The deciduous species, in general, showed a local maximum at

45° and an overall decrease with increasing incidence angle. The local or absolute maximum at 45° might be related to the trunk–ground interactions. Theoretically, if the trunk and ground surface act as a dihedral corner reflector, a maximum can be expected at 45°. The overall decrease of backscatter with increasing incidence angle found for deciduous trees does not suggest that a relatively simple mechanism, such as a pure volume scatterer, is likely.

These results imply a potentially complicated interaction mechanism for the L–band. Theoretically, the backscatter might be modelled by three basic components.

(1) A volume scatter component representing the canopy. In contrast to X– and C–bands, the volume is transparent and, as a consequence, the effects of trunks and the large branches cannot be ignored anymore.

(2) A surface scatter component representing the soil surface (including undergrowth). The backscatter from this surface is attenuated by the volume.

(3) A component describing the interaction between volume and surface. Notably the interaction between trunks and the surface (which could be seen as a dihedral corner reflector mechanism) may be an important effect.

Because of these complications, realistic forest backscatter models have not been developed yet. Richards et al. (1987) developed a theoretical L–band forest model incorporating these terms. The excessive number of object parameters in this model, however, might prevent any practical use (see also chapter 7). For X– and C–bands, the situation is simpler. If scattering can be assumed to originate from the upper parts of the canopy or the outside parts of tree crowns, relatively simple volume scatter models, such as those developed for agricultural crops, may be applicable.

6. POTENTIAL APPLICATIONS: CLASSIFICATION AND SPATIAL ANALYSIS

Emphasis has been given to the relationship between object parameters and backscatter levels. Imaging radar data, however, also inherently comprise the spatial relationships between these backscatter levels. These spatial relationships may be associated with object dependent spatial (structural) characteristics. Spatial relationships can be used to delineate or identify (classify) objects in an image. Moreover, through appropriate spatial analysis techniques, parameters describing the spatial structure of an object may be estimated. Three different techniques are described below: (1) the analysis of speckle, (2) the analysis of image texture and (3) the analysis of large deterministic spatial structures. All three methods can be used to extract structural information from predefined areas within homogeneous stands or natural forest areas, or to delineate and/or classify objects.

6.1 Classification potential of radar

6.1.1 General considerations

On the basis of the results discussed in the preceding sections, some important conclusions can be drawn regarding the classification potential of radar.

Classification of trees is in principle possible when different tree classes exhibit distinct backscatter behaviour. In the preceding sections, it could be concluded that backscatter properties depend not only on species dependent (presumably morphologic) features but also on other, not necessarily species dependent factors such as stand and tree parameters, needle loss or undergrowth. In the X–band, and possibly the C–band, the influence of these other factors was found to be small except for a few specific cases (chapter 5). For most tree classes and most dates of flight, the stand–averaged γ values were found to be confined to a narrow band around a mean signature. The standard deviation of the stand–averaged γ values relative to the mean signature was found to be in the order of 0.5 dB, regardless of incidence angle, time of flight or tree class. The mean signatures differ considerably among the different tree classes. The remaining and as yet largely unexplained variation within tree classes (at a specific date) is relatively small and might be caused by differences in stand and tree parameters, ecologic factors, environmental conditions or may even be attributed to the sensor. Only in a few cases were clues found for the probable cause of the variation. The impact on classification for some of these cases is illustrated below.

(1a) Much variation was found in the Japanese larch in the May 1982 measurement: The standard deviation of stand–averaged γ values relative to the mean signature is 1.26 dB.

This large value could be related to the fact that in this period the Japanese larch is in a transitional phase between the bare tree stage and the fully foliated stage, and different stages of development (related to tree age) were found at the time of measurement (section 5.3).

(1b) In the May measurement of oak, significant deviations in the backscatter level showed up for a few stands. This did not occur in the March measurement, however. At both times, the oak trees were bare. The anomalous stands were found to contain deciduous undergrowth, which was already largely foliated in May.

These two examples illustrate the point that was considered in section 4.2. Periods of principal interest for classification are those in which the vegetation structure of the tree species involved is relatively stable. In The Netherlands, the periods most suitable for classification purposes therefore seem to be winter (i.e. roughly December – March) when deciduous trees and the needle–shedding larch are bare and summer (i.e. roughly June – August) when deciduous trees and the larch have a complete coverage of green leaves and needles.

(2a) For Scots pine, a significant variation between sites, notably between the Roggebotzand and Kootwijk sites, was found which might be related to needle loss (section 5.9.4).

(2b) Also the difference between Austrian and Corsican pine at the Roggebotzand site might be related to needle loss of the Corsican pine (section 5.9.4).

These examples illustrate the possible impact of diseases or stress situations on classification. In these cases, tree stands in a particular area or of a particular variety showed significant deviations in backscatter behaviour.

(3) For some poplar clones under certain circumstances, strong directional variations in radar backscatter level were found to occur in the X–band as well as the C–band (section 5.9.3). When the physical mechanism behind this phenomenon is more clearly understood, it can be used and might add to the accuracy of classification or determination of biophysical properties of the forest. On the other hand, if the phenomenon of directional variation is not accounted for at all then the reverse may be true.

The backscatter properties in L–band were not found to be related to species dependent features to the same extent as found for the X– and C–bands. The results of this research and other published results (section 5.9) indicate that deciduous canopies in L–band are transparent to a high degree and that trunks, the ground surface and undergrowth have

major effects. For pine stands, significant relationships between backscatter level and stand and tree parameters were reported in literature. The L–band may thus be a less appropriate choice for species classification. It may be useful, however, for discrimination of broad classes such as coniferous and deciduous species, clearcut areas and flooded forest areas. The latter class may even be properly classified by L–band radar only.

For the moment, the classification potential of radar might be summarized as follows. X–band frequencies, and probably higher frequencies (e.g. Ku–band), and possibly C–band frequencies, can in principle be utilized successfully for tree species classification in the periods with relatively stable vegetation structure (i.e. summer and winter). Look direction effects and effects of diseases should be accounted for, whenever feasible. Very young or very old plantations (with a low degree of canopy closure) might yield anomalous backscatter levels (sections 5.2 and 5.3). The use of L–band seems restricted to the delineation of broad forest classes, but may offer some unique capabilities.

6.1.2 Classification simulation on the basis of experimentally obtained X–band radar signatures

Though a necessary condition for successful classification, i.e. the existence of class characteristic signatures, is likely to be fullfilled at the shorter wavelengths, the ultimate success of classification will depend strongly on many other factors as well. Relevant factors, for example, are the wave parameter choice, the time(s) of observation and the relative occurrence of tree classes in a specific area, together with the separability of the main classes.

To elucidate some of the relevant factors, the separability of tree classes occurring in the Roggebotzand and Speulderbos sites on the basis of the empirically established multitemporal X–band backscatter characteristics (the 1982–1983 data) are discussed below. The results of this case study were published earlier (Hoekman, 1985a).

To analyse class separability, a simple empirical backscatter model for the stand–averaged value of γ will be used. On the basis of the experimental data obtained for the X–band, it seems realistic to assign to each class a deterministic angular and time–dependent radar signature and to add a stochastic component with a Gaussian distribution and a standard deviation of 0.6 dB (this value is a little higher than the mean values shown in table 5.3). Using this empirical model, results can be simulated for forest areas having a certain number of the tree classes. For the moment, the effect of speckle will be omitted. This is a realistic assumption if stand borders are known a priori and the stands are of reasonable size. Thus forest data can be synthesized for all possible combinations of grazing angles and

dates of flight. This can be done for both "one–dimensional" and "multidimensional" cases (each dimension containing the values of γ for a specific wave parameter combination and a specific time of measurement).

Suppose that the deterministic part is denoted by $\gamma_d(\theta_i,t_j,\omega_n)$ with θ_i denoting (a discrete) grazing angle, t_j denoting the date of flight and ω_n denoting the class and that the stochastic part (normally distributed with zero mean and standard deviation σ) is denoted by $\epsilon = N(0,\sigma)$. Then the synthesized γ is

$$\gamma_s(\theta_i,t_j,\omega_n) = \gamma_d(\theta_i,t_j,\omega_n) + \epsilon \tag{6.1}$$

which is the sum of the deterministic and stochastic parts.

A field with a synthesized value is recognized as belonging to the class ω_n for which $P(\omega_n|\gamma_s)$ is maximal. It can be proved that the Bayes decision rule for minimum error yields the minimum number of erroneous classifications, i.e.

$$P(\omega_n|\gamma_s) = \frac{P(\gamma_s|\omega_n)\cdot P(\omega_n)}{P(\gamma_s)} \tag{6.2}$$

is maximal.

Since at this moment it is not the actual probability but the maximum probability (maximum likelihood) that is of interest, $P(\gamma_s)$, which is independent of ω_n, need not be known. Two classifiers are suggested:

(1) A "Bayesian classifier", which assigns a stand to the class for which the expression $P(\gamma_s|\omega_n)\cdot P(\omega_n)$ is maximal.

(2) A so–called "Euclidian classifier" when the a priori probabilities of class occurrence frequencies $P(\omega_n)$ are not known (and are supposed to be equal), which assigns a stand to the class for which the expression $P(\gamma_s|\omega_n)$ is maximal. (Because in this case, using the analogue procedure for more–dimensional classifications, the method degenerates to using the Euclidian distance to the distribution centre in feature space as a classifier.)

Simulations were made for both the Roggebotzand and Speulderbos sites for all possible combinations of the grazing angles (θ_1=15°, θ_2=25° and θ_3=35°) and dates of flight (t_1=June '82, t_2=September '82, t_3=March '83, t_4=May '83). The corresponding radar data are shown in table 5.4. The selected classes and their relative occurrences are shown in table 6.1.

Table 6.1. Relative occurrence frequency of tree classes under research (expressed as a percentage of the studied areas).

Roggebotzand site:		Veluwe site:	
poplar 'Robusta'	30 %	old beech forest	58 %
poplar 'Heidemij'	12 %	Scots pine	12 %
willow	2 %	Japanese larch	6 %
ash	4 %	oak	18 %
oak	5 %	Douglas fir	6 %
beech	2 %		
Norway spruce	22 %		
Sitka spruce	7 %		
Corsican pine	3 %		
Scots pine	2 %		
Austrian pine	11 %		

Table 6.2a. Simulated classification result.

Scatter diagram for the synthesized Roggebotzand site;
classifier type : Bayesian
s.d. stochastic part : 0.60 dB
number of dimensions : 2; (θ_1,t_2) and (θ_1,t_3)

Class (9 sets)	No	1	2	3	4	5	6	7	8	9	Synthesized fields
set poplar	1	419	1	0	0	0	0	0	0	0	420
willow	2	1	6	10	1	2	0	0	0	0	20
ash	3	0	3	36	1	0	0	0	0	0	40
oak	4	0	0	3	44	2	1	0	0	0	50
beech	5	0	1	0	14	4	1	0	0	0	20
set spruce	6	0	0	0	0	0	284	3	3	0	290
Corsican pine	7	0	0	0	0	0	17	7	2	4	30
Scotch pine	8	0	0	0	0	0	15	1	3	1	20
Austrian pine	9	0	0	0	0	0	0	8	0	102	110

Correctly classified fields from 1000: 905

Table 6.2b. Simulated classification result.

Scatter diagram for the synthesized Veluwe site;
classifier type : Bayesian
s.d. stochastic part : 0.60 dB
number of dimensions : 2; (θ_1,t_2) and (θ_1,t_3)

Class (5 sets)	No	1	2	3	4	5	Synthesized fields
beech forest	1	559	11	3	7	0	580
oak	2	10	104	6	0	0	120
Jap. larch	3	15	32	13	0	0	60
Scots pine	4	16	0	0	153	11	180
Douglas fir	5	0	0	0	24	36	60

Correctly classified from 1000: 865

Table 6.2a shows a classification result for synthesized Roggebotzand data with the Bayesian classifier type, two dimensions (March and September at 15° grazing angle) and with 0.6 dB standard deviation of the stochastic part. A thousand (stand averaged γ) values were generated for an occurrence of classes proportional to the actual relative occurrence frequency. Further, a "set" definition was introduced for the poplars and spruces. For the poplars, this means that if the probability of a stand belonging to either poplar 'Heidemij' or poplar 'Robusta' is higher than the probability of belonging to another class or set of classes, it is classified as belonging to the set of poplars. A set can contain one or more classes. The results in table 6.2a therefore apply to nine sets. Of course, the results are strongly dependent on the set definition preferred.

The results of this classification are that almost 100% of the poplars are correctly identified (419 stands of the 420 stands synthesized). Of the 20 stands with willow, only 6 are correctly classified, 10 willows are misinterpreted as ash, 1 as poplar, 1 as oak and 2 as beech. Ash and oak are classified very well. Beech is mostly falsely classified as oak. Spruce is classified very well (284 of 290). The same applies to Austrian pine, but most of the other pines are misinterpreted as spruce. The overall result is that 905 stands of the 1000 stands synthesized (90.5%) are correctly classified.

An overview of classification simulations started from several assumptions is presented in table 6.3. The two–dimensional case for a Bayesian classifier and a standard deviation of 0.6 dB of the stochastic part has been discussed. The availability of sufficient a priori knowledge on deterministic radar signatures and class occurrence frequencies was assumed. When a priori knowledge of occurrence frequencies is absent and the deterministic radar signatures are not known within limits of, for example ± 0.5 dB (because of such factors as climatic or environmental conditions, which may be seen as an independent source of stochastic variation), however, it is realistic to use the Euclidian classifier with a standard deviation of 0.8 dB of the stochastic part. Thus the accuracy for the Roggebotzand forest decreases to ≈84% (table 6.3a). When only the discrimination between decidious and coniferous trees is important (i.e. there are only two "sets" of tree types), more than 99% seems achievable (table 6.3b). Table 6.2b and tables 6.3c–d show the results for the Speulderbos site.

The assumption of statistical independence between the stochastic parts of the synthesized γ values is essential when using this model to simulate classification results in the multidimensional case. Although in practice this is true for sensors, it is not necessarily true for the objects. For example, some observed stands of the poplar clone 'Heidemij' yielding relatively high radar backscatter levels in the May flight, yielded relatively high levels again in the June and September flights. Whatever the reason for these small but consistent differences, the class of the clone 'Heidemij' acts for a long period as a set of

Table 6.3. Number of correctly classified stands from 1000 synthesized stands for several classifier types and standard deviations of the stochastic part. In the case "occ. 1/11" for the synthesized Roggebotzand site and the case "occ. 1/5" for the synthesized Veluwe site, the relative occurrence frequencies for the tree classes under research are chosen equal. (In this case the Bayesian and Euclidian classifiers yield the same results.) Two one–dimensional, two two–dimensional and two three–dimensional combinations are presented. The meaning of the parameter values (θ_1,t_1)...etc. is given in section 6.1.2. The two scatter diagrams of table 6.2 elaborate one case for the Roggebotzand site and one case for the Veluwe site.

(a) Roggebotzand, 9 sets (see table 6.2a)

classifier type	s.d.	θ_2,t_2	θ_1,t_2	θ_1,t_3 θ_1,t_2	θ_2,t_3 θ_2,t_2	θ_2,t_1 θ_2,t_2 θ_2,t_3	θ_1,t_4 θ_1,t_2 θ_2,t_1
Bayesian	0.6 dB	850	841	905	881	905	924
Euclidian	0.6 dB	807	806	871	836	875	873
Bayesian	0.8 dB	813	805	867	837	887	874
Euclidian	0.8 dB	772	765	837	821	820	822
occ. 1/11	0.8 dB	520	524	639	609	670	669

(b) Roggebotzand, 2 sets: decidious/coniferous

classifier type	s.d.	θ_1,t_3	θ_2,t_3	θ_1,t_3 θ_1,t_2	θ_2,t_3 θ_2,t_2	θ_2,t_1 θ_2,t_2 θ_2,t_3	θ_1,t_4 θ_1,t_2 θ_2,t_1
Bayesian	0.8 dB	984	985	994	945	993	971
Euclidian	0.8 dB	984	982	991	932	998	952

(c) Veluwe, 5 sets (see table 6.2b)

classifier type	s.d.	θ_1,t_3	θ_2,t_3	θ_1,t_2 θ_1,t_3	θ_1,t_1 θ_1,t_3	θ_1,t_1 θ_1,t_2 θ_1,t_3	θ_1,t_3 θ_2,t_3 θ_2,t_1
Bayesian	0.6 dB	780	783	865	866	889	871
Euclidian	0.6 dB	583	566	830	801	867	781
Bayesian	0.8 dB	714	741	798	798	831	815
Euclidian	0.8 dB	520	478	719	706	766	670
occ. 1/5	0.8 dB	530	550	658	645	686	687

(d) Veluwe, 3 sets: decidious/larch/coniferous

classifier type	s.d.	θ_1,t_3	θ_2,t_3	θ_1,t_2 θ_1,t_3	θ_1,t_1 θ_1,t_3	θ_1,t_1 θ_1,t_2 θ_1,t_3	θ_2,t_1 θ_2,t_3 θ_1,t_3
Bayesian	0.8 dB	903	901	896	902	904	937
Euclidian	0.8 dB	876	791	870	858	869	869

subclasses. This problem might be avoided when using different radar wave parameters. Statistical independence may, on the other hand, be achieved by a drastic change in the physical structure of the objects (e.g. trees with leaves versus bare trees). Without more elaborate insight into the physics of the interaction mechanism, we should be careful when interpretating results of models like the one formulated here. Classification improvements when using more than one dimension might be less than suggested by this model. In this case, when using only X–band radar, only HH polarization and only a limited range of grazing angles, we can use no more than two dimensions, namely one image taken in winter and one image taken in summer, to be reasonably sure the stochastic parts (for deciduous trees) will be independent. Better physical insight may suggest more elaborate classification models.

Some preliminary conclusions

The results presented above illustrate how classification potentials are affected by the choice for a specific combination of incidence angle(s) and time(s) of flight and by other aspects, such as the relative occurrence of classes or a priori knowledge of this relative occurrence. Also the degree of differentiation needed (e.g. between poplar clones, between all species or between the coniferous and deciduous species only) has an impact on the feasibility of classification.

We may conclude that a "dual–temporal" approach is likely to give accurate results. The combination of one summer and one winter (X–band) observation yields overall error fractions ranging from 10% to 16% at the Roggebotzand site (for nine "sets") and 14% to 28% at the Veluwe site (for five classes). When the differentiation between deciduous and coniferous species is pursued, error fractions drop to less than 1% for the Roggebotzand site. For the Speulderbos, the latter differentation is less accurate because of the presence of the needle–shedding larch.

6.2 Classification and delineation

6.2.1 Application of processing tools

To support the automated analysis of radar images, image processing tools have to be utilized, among other things, (1) to properly handle the speckle (an inherent feature of radar data), (2) to recognize coherent image segments, which are more or less homogeneous in a certain property, or (3) to recognize other image components (such as edges).

Many potentially useful image processing techniques have been developed during the last

decades. For a detailed discussion on this topic, the reader is referred to the handbooks of Castleman (1979) or Rosenfeld and Kak (1982). Some of the techniques used here are described below.

Statistical properties of image data

The use of these techniques for radar image analysis can be elucidated on the basis of models describing the statistical properties of radar data (including speckle). As has been discussed above (section 2.1 and Appendix I), most distributed targets can be described adequately on the basis of the Rayleigh fading concept. For the (logarithmically–scaled) processed SLAR data used in this research, the following statistical properties may be assumed. The grey level of each pixel represents an (unbiased) estimation of γ and the underlying distribution is normal with a known standard deviation of 0.8 dB (30 independent samples). Moreover, when an extended target (corresponding to many pixels), such as a forest stand or forest area, is homogeneous at the scale of the resolution cell (i.e. structural elements are smaller than the resolution), the mean grey level of that extended target is a very accurate and almost unbiased (–0.07 dB; Appendix I) estimate of γ and the standard deviation of the grey levels is 0.8 dB. The bias, a consequence of averaging logarithmically–scaled data, is very small and may be neglected.

For many practical purposes, a radar image, or relevant parts of it, may be imagined as a collection of such homogeneous segments. On the basis of the assumed statistical properties (of the logarithmically–scaled SLAR data) and the spatial relationships, the effect of image processing techniques can be indicated.

Filters

A large group of operators on image data is based on the concept of "filters". The mathematical operation, inspired by analogue signal processing procedures, is performed on the pixels contained in a spatial window of certain shape, size and orientation. The result is assigned to a new pixel, in general corresponding to the position of the window's centre pixel. The operation can be applied to every possible spatial position of the window in the "original image" and, consequently, a new image, the "tranformed image", results.

Filters, among other things, are applied to reduce the effect of speckle, i.e. to improve the estimation of γ. Possible operators are (1) the determination of the mean value or (2) the median value. Both operators yield an unbiased estimation of γ. If the window contains fractions of two adjacent segments, the "mean–value filter" yields (an unbiased estimation of) the weighted mean. The result for the "median filter", however, is expected to be closer to the mean value of the largest fraction. Since the central pixel in most cases (e.g. near

straight edges) is located in the largest fraction, this yields a better result in the latter case. For very small segments, for line features (a special type of segment) and near sharp corners the reverse is true, however.

Some of the difficulties encountered in the application of image processing techniques are illustrated here. The mean filter improves radiometric accuracy, but this improvement is traded against loss in spatial detail. The median filter has the advantage that edges are better preserved, but it introduces geometric deformations (loss of small or thin segments and sharp curves in edges). Another advantage of the median filter is that the estimation is more robust in the sense that the effect of outliers is less. (These can be caused by system artefacts or the presence of man–made objects such as buildings or cars in extended homogeneous targets.)

Image segmentation

Filter operators are so–called "local operators", meaning that the properties assigned to pixels (in the transformed image) are based completely on the grey levels of pixels in a small local region (in the original image). Moreover, a decision at a certain point is not influenced by decisions at other points. Other types of techniques may be more appropriate since certain features (such as edges, lines or segments) have a spatial extent often considerably exceeding this local region.

A very useful concept in the processing of (log–scaled) radar images is "split–and–merge" segmentation, a sequential region–growing technique. This approach to segmentation as developed by Horowitz and Pavlidis (1976) was elaborated for (Dutch X–band) SLAR images by Gerbrands and Backer (1983). It was found to be superior to techniques based on edge detection (because of the speckle, edges are relatively difficult to detect in the Dutch X–band SLAR images). The algorithm developed by Gerbrands and Backer is based on the assumption that the scene comprises homogeneous areas. Pixel values in each area are assumed to be normally distributed with a fixed variance (e.g. 1.0 dB). The algorithm starts with a tentative partitioning of the image into squares of size $2^n \times 2^n$. Decision criteria based on statistical tests for the variance are used to decide whether four adjacent squares can be "merged" to a single square of size $2^{n+1} \times 2^{n+1}$ or, if negative, some of these squares need to be "split" into four squares of size $2^{n-1} \times 2^{n-1}$. Following this procedure over all possible levels, the image is partitioned into squares of different sizes, each square assumed to be contained within a homogeneous area. Subsequent statistical tests are used to decide whether adjacent squares (of any size) can be "grouped" into larger segments. When the grouping is completed, the computed segments approximate the homogeneous areas (figure 6.1).

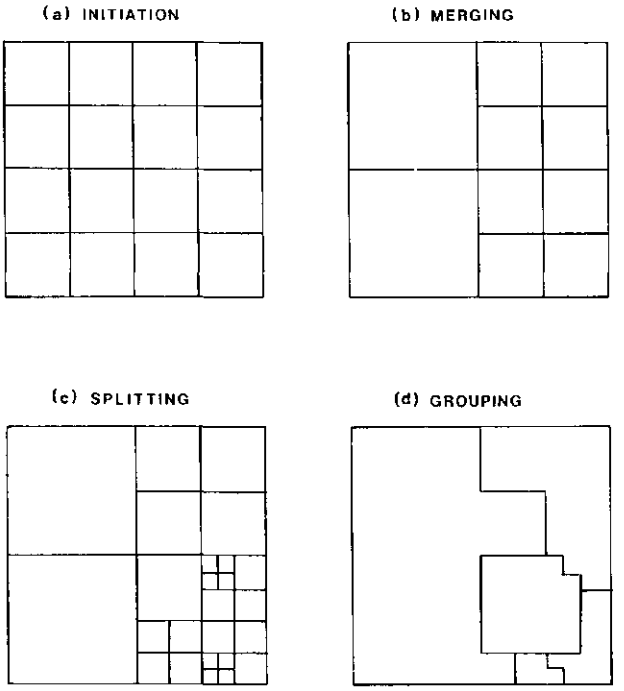

Figure 6.1. Image segmentation using the split–and–merge algorithm: (a) initial partitioning of image, (b) result of merging, (c) result of splitting, and (d) result of grouping segments.

Topographic data

The mathematical operations performed by filter–type processing techniques are applied locally (within a spatial window) but can be applied in another way as well. If the locations of coherent image regions are known a priori, as may be a result of the application of a segmentation algorithm or the integration of the image with topographic data, these operations can be applied to the integral region. Several advantages are evident. Operations on pixels belonging to different regions are recognized and can be avoided. The accuracy of the estimation of certain image features (such as the mean, texture measures or speckle spectra) can be increased since the operation can be applied directly to the largest possible group of pixels.

Straightforward strategies in image processing are difficult to indicate. For example, a segmentation procedure may fail if based on pixel values, but may be successful if based on image texture. The effectiveness of processing strategies may eventually depend on many factors such as the type of images, the availabilty of a priori knowledge (topographic data, physical models, etc.) and the application.

6.2.2 Classification and delineation of forest stands

Compared with "pixel–based" classification (i.e. spatial relations are not used), classification accuracy based on remotely sensed radar data can be improved in a number of fundamentally different ways. The image data can be linked with a topographic database containing stand borders. In this case, classification can be based on stand–averaged γ values, and the speckle problem and the problem of "mixed" pixels (corresponding to resolution cells crossing borders) are largely avoided. In addition to the use of a priori knowledge on the location of coherent units, three other ways, potentially of equal importance, can be indicated to improve results. These are;

(1) the reduction of the effect of speckle by utilization of image processing techniques,

(2) technical modifications of the radar system to achieve a better speckle reduction per unit area (such as a larger bandwidth and a smaller pulse length) and

(3) an appropriate choice of wave parameters (frequency, but also incidence angle and polarization) and time(s) of observation.

All three approaches are relevant, especially if stand borders are unknown. The latter approach is always relevant, i.e. for both pixel–based and unit–based classifications. It is assumed that the spatial resolution of the system is appropriate for the chosen application. If stand areas are small and comprise a very small number of independent samples, the second approach is very relevant even if stand borders are known a priori. Only the impact of the three approaches mentioned above will be described here.

Case study of Roggebotzand radar data

To investigate the utility of image processing techniques for classification improvement, a case study was conducted with the NLR's image processing system RESEDA (Nooren and Hoekman, 1987). Three X–band SLAR images and one L–band Seasat image of the Roggebotzand site were selected. The SLAR images were recorded on 9 September 1982 (image Rbz5), 3 March 1983 (Rbz9) and 17 May 1983 (Rbz11). The Seasat image was recorded at 28 August 1978. The images were brought into geometrical registration. The speckle level, i.e. the standard deviation, in the (resampled) images was found to be $\approx$0.9 dB for the SLAR and $\approx$4.8 dB for Seasat. The angle of incidence is 20° for the Seasat image and is in the range of 62° to 74° for the SLAR images. These images were subsequently processed by application of a median filter and the split–and–merge segmentation algorithm.

Some large and homogeneous training areas were selected to extract signatures for a number of classes (mean, standard deviation and covariance were calculated and a

Gaussian distribution was assumed; this was done for the processed as well as the unprocessed images). For most classes, signatures were based on one training area, for others on a few. In the latter case, the differences in stand–averaged mean were found to be negligibly small (< 0.1 dB). On the basis of these signatures, pixel–based classifications were performed for the pixels contained in the training areas. This was done before as well as after the application of image processing techniques.

It was pursued to investigate the impact of image processing techniques and to compare and evaluate the impact of the three different approaches mentioned above. Since assessment of absolute classification result was not pursued for this particular case study, the choice of the observation dates and frequency bands is not very relevant. Though the L–band in general and the X–band observation in May may in practice appear to be less appropriate for species classification (as was concluded in section 6.1.1), the dataset obtained might be considered representative for a multitemporal and dual–frequency forest dataset.

Classification potential simulation

To evaluate the results of the actual classifications, the classification potential for a number of image combinations and speckle levels was studied first using the simple simulation model introduced in section 6.1. This time, however, simulations were performed for individual pixels and not for stands. Speckle could therefore not be omitted and was modelled as an independent stochastic term (with normal distribution). On the other hand, this dataset was prepared in such a way that the influence of the variation of stand–averaged mean within classes could be omitted. Hence the simulation model was the same but the stochastic part had another physical meaning.

Table 6.4. Overview of simulated classification results for different image combinations and different values for the s.d. of the stochastic part.

Combination		s.d.	pixels correctly classified
1)	X–band: September, March, May	1.6 dB	54.7%
2)	X–band: September, March, May	0.9 dB	72.0%
3)	X–band: September, March, May	0.6 dB	78.5%
4)	L–band: August; X–band: September, March	1.6 dB	68.7%
5)	L–band: August; X–band: September, March	0.9 dB	87.1%
6)	L–band: August; X–band: September, March	0.6 dB	95.3%
7)	L–band: August; X–band: September	0.9 dB	81.5%
8)	L–band: August; X–band: September	0.6 dB	92.5%

Table 6.4 shows simulated results for several combinations of frequency bands and dates of observation and for standard deviations of the stochastic part of 1.6 dB, 0.9 dB and 0.6 dB (i.e. the speckle level). As could be anticipated, the results for a certain combination improve with decreasing speckle level. The positive effect of combining L– and X–band data is large. The latter point may be explained as follows. In the preceding section, it was shown that for X–band data a multitemporal approach is likely to yield good results. An X–band summer image is usefull to discriminate deciduous species, an X–band winter image is useful to distinguish deciduous from coniferous species. As concluded in section 5.9.1, the deciduous species, the pine species and the spruce species show distinct backscatter behaviour as a function of frequency. The relative backscatter levels for these three groups show completely different arrangements for the X– and C– bands, as well as the L–band. A multifrequency approach, in general, is thus likely to yield further improvements. This is illustrated in table 6.4 by the comparison of the results of combination 2 or 3 (presumed to be representative for X–band multitemporal observation) and combination 7 or 8 (presumed to be representative for a single dual–frequency observation in summer). With the first approach, a good deciduous/coniferous discrimination is achieved because of the winter observation. With the second approach, a good deciduous/pine/spruce discrimination is achieved because of the distinct backscatter behaviour as a function of frequency.

The results in table 6.4 illustrate the importance of two of the three approaches. An appropriate choice of wave parameters and times of observation may yield significant improvement of classification results (approach 3). Decreasing the standard deviation of the stochastic part simulates the anticipated effects of speckle reduction through radar system modifications and therefore also approach number 2 is likely to improve classification results significantly. Moreover, these two approaches are independent and may be combined. In addition to speckle reduction through the system (approach 2), the effect of speckle can be reduced by application of image processing techniques (approach 1). This type of "speckle reduction" is fundamentally different, however, and improvements on the basis of theoretical considerations are more difficult to predict.

Utility of image processing tools

For the three SLAR images, the effect of speckle was reduced by utilizing two different techniques (see section 6.2.1), namely "median filtering" with a 5 x 5 pixel window size and a three–dimensional split–and–merge segmentation algorithm. The latter method used different sets of decision criteria for the split, merge and grouping operations. The Seasat image was processed separately. Table 6.5 shows the overall classification results. After processing, the standard deviation within stands was reduced from ≈0.9 dB to ≈0.6 dB for the SLAR images and from ≈4.8 dB to ≈2.0 dB for the Seasat image. The overall result for

the unprocessed SLAR image set was compared with the simulated result (with 0.9 dB standard deviation). The overall improvements after application of processing techniques are of the same order as the simulated results, but a more detailed analysis, i.e. comparison of numerical results for individual classes and inspection of stand delineation in the classified images, showed some major differences.

In general, speckle reduction by means of image processing is attained by mathematical operations involving the neighbourhood of pixels. Consequently, γ values of pixels within a particular stand are influenced by the γ values of pixels in the neighbourhood of this stand. Unpredictable effects may result, depending on the type of mathematical operation and the backscatter properties of neighbouring units. In general, geometric and radiometric deformations occur in the image. As a result of the median filter, thin lines, stand corners and small units disappeared and the stand–averaged γ values changed (up to 0.2 dB for the SLAR and up to 0.5 dB for Seasat). The geometric deformations introduced by segmentation depend strongly on the decision criteria applied in the split–and–merge algorithm. The segment borders do not follow the stand borders accurately and the block structure obtained after the split phase stays locally visible. As a result of the segmentation procedure, the stand–averaged γ values changed (also in this case up to 0.2 dB for the SLAR and up to 0.5 dB for Seasat). Since segmentation itself was not the objective in this experiment, but merely a tool to increase classification accuracy, the best result was obtained for a set of decision criteria yielding a "fragmented" result, i.e. stands after processing usually comprised a number of segments.

The advantage of increased speckle reduction (in the context of image processing, it might be better to speak of local variance reduction) at a certain point does not counter–balance the disadvantages introduced by these deformations. Classification results will no longer improve and will even detoriate. Two major effects were noticed.

(1) The first effect, as was noted for both the median filter and segmentation, is the change of stand–averaged γ values. The differences between neighbouring stands, on average, have a tendency to decrease and the decrease is larger as the neighbourhood involved in the mathematical operations gets larger (and the standard deviation within stands smaller).

(2) The second effect was noticed for segmentation only. Adjacent segments that are close in feature space can, depending on the decision criteria applied, be grouped into larger segments or a single segment. A strong grouping is advantageous for those classes that are isolated in feature space (however, these classes are easy to classify anyway). A strong grouping is disadvantageous for discrimination between classes that are close in feature space.

Table 6.5. Overview of classification results utilizing different processing techniques for the (three–dimensional) SLAR dataset (images Rbz5, Rbz9 and Rbz11) and for the (one–dimensional) Seasat dataset.

Technique	s.d.	pixels correctly classified
SLAR data set:		
No image processing	≈0.9 dB	70.6%
Median filter, 5x5 window	≈0.6 dB	85.2%
Split & Merge segmentation (3–D)	≈0.6 dB	85.8%
SEASAT data set:		
No image processing	≈4.8 dB	24.0%
Median filter, 5x5 window	≈2.0 dB	45.8%
Split & Merge segmentation (1–D)	≈2.0 dB	42.3%

Overall classification results for the Seasat images are less than for the SLAR data. This is not surprising considering the fact that only one observation was used and the speckle level is very high. In figure 6.2, the unprocessed Seasat image is shown together with the results after application of the median filter and the segmentation.

Figure 6.2 (a–c). Seasat image of the Roggebotzand recorded on 28 August 1978: (a) unprocessed image, (b) result of median filter with 5 x 5 pixel window, (c) result of split–and–merge segmentation.

Some preliminary conclusions

From the results presented here, it can be concluded that the classification accuracy can be improved in three different ways, which are potentially of equal importance. These are (1) an appropriate choice of wave parameters (frequency, but also incidence angle and polarization) and time(s) of observation, (2) speckle reduction (by the system) and (3) the reduction of the effect of speckle by using image processing techniques. The last approach should be handled with care. If non–linear techniques (such as the median filter or split–and–merge) are used, geometric and radiometric deformations are introduced. When pushed too far, for example as a result of a larger window size for the median filter or a less fragmented result for the segmentation, the advantages do not balance the negative effects introduced. In this experiment, for example, it was noticed that shifts in the stand–averaged means result or that segments belonging to different species are grouped. These effects, however, are to a large extent unpredictable since they depend on neighbouring stands or units and not on the stands in question. Speckle reduction, or reducing the effect of speckle, becomes at a certain point less meaningful since also other (non–species dependent) object parameters affect the backscatter level. For the X–band, and possibly the C–band, standard deviations of $\approx$0.5 dB in stand–averaged γ values within a single class were found empirically. This figure may determine the actual limits of classification accuracy.

Finally, it is noted that the application of a priori knowledge provides an alternative way to handle the speckle problem. For example, from topographic databases and digital thematic maps, "hard" boundaries such as forest stand borders, roads and canals can be extracted. Segmentation procedures can thus be directed to detect the remaining ("soft" or more dynamic) boundaries and/or to detect changes in the "hard" boundaries. This approach is advantageous in the sense that the computational effort can be considerably reduced and the accuracy of segmentation can be significantly improved. For the moment, this remark will suffice. The use of added data and knowledge will be elaborated in the next chapter.

6.3 The effect of canopy surface geometry

Imaging with SLR is based on the principle of projection of range differences between the objects and sensor for a certain scanline. This is unlike optical systems in which imaging is based on projection of angular differences. As a result of the specific parallax introduced by radar systems, small relief differences can be perceived well, notably at small grazing angles. Moreover, since radar is an active system, spatial structures can be accentuated by the effects of radar shadow in a geometrically well–defined way (if the effects of diffraction

can be ignored).

Theory

The actual effects of relief on the radar backscatter level can be predicted on the basis of physical models. The conjecture to model a forest stand as an opaque object featuring isotropic volume scattering seems appropriate for X– and C–bands, for most forest species and forest types (section 5.10). This theoretical model predicts flat angular responses for γ. Of course, the effect can be calculated for other physical models as well.

For an opaque isotropic volume scatterer, γ does not depend on grazing angle, but will depend on the slope of the canopy surface (see figure 6.3). Always, and therefore also for the three cases shown in this figure, the ratio between intercepted power and the re–radiated power is the same for every resolution cell. Processing algorithms (which are based on the geometric optics approximation) to compute γ, however, start from the assumption that the terrain is flat, and hence assume the intercepted power is proportional to $\frac{1}{2}c\tau\cdot\tan(\theta)$ (see figure 6.4). In fact, it is proportional to $\frac{1}{2}c\tau\cdot\tan(\theta+a)$, where a is the angle of slope in range direction. The value of γ in the processed image is therefore related to the value γ_f, for an identical object with the upper surface oriented parallel to the horizontal plane, as

$$\gamma = \gamma_f \cdot \frac{\tan(\theta+a)}{\tan(\theta)} \tag{6.3}$$

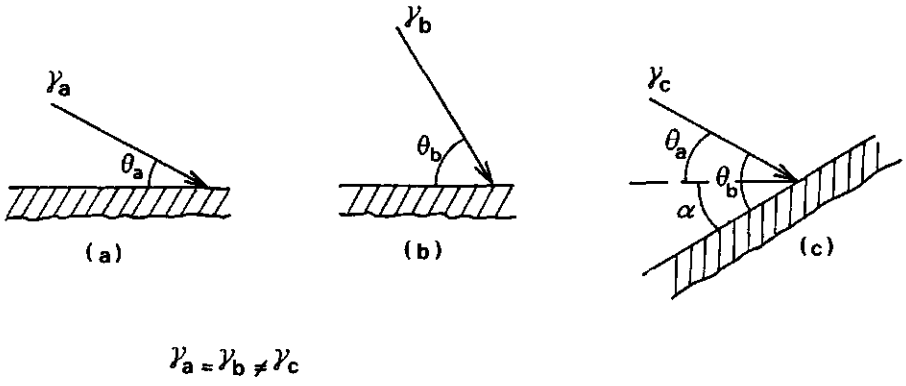

Figure 6.3. For an opaque isotropic volume scatterer, γ is independent of grazing angle θ (cases a and b) and dependent on slope a (case c). Both grazing angle and slope are defined as the angle with the horizontal plane in the direction of the sensor.

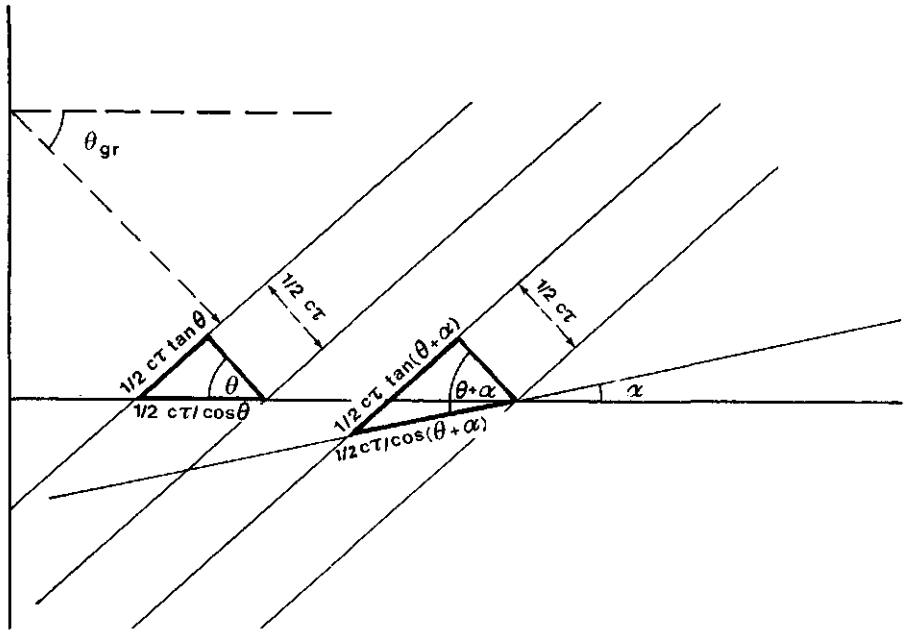

Figure 6.4. Measurement geometry for a flat surface (of the canopy) and a tilted surface.

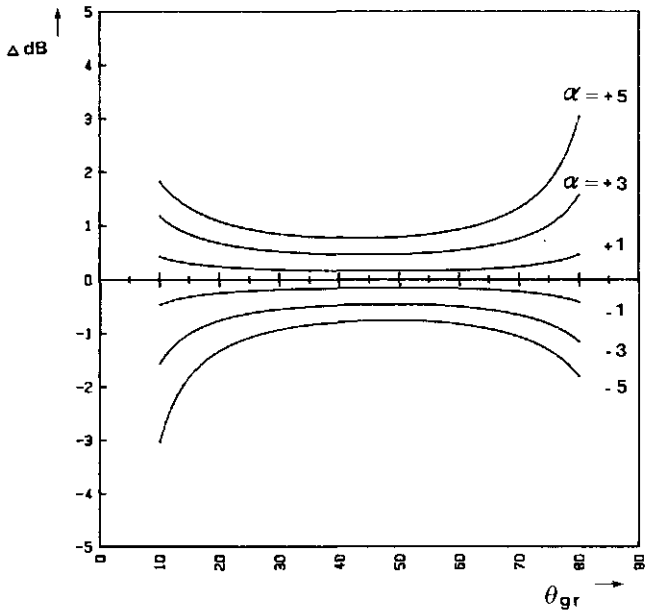

Figure 6.5. Effect of canopy undulations if an opaque isotropic volume scatter mechanism applies. Changes in γ level as a function of grazing angle θ and angle of slope α are shown.

Figure 6.5 shows this relationship in graphical form. The ratio γ/γ_f is shown at the dB scale as a function of grazing angle and for several slope angles. It can be concluded that, if this mechanism applies, small slopes observed at very small or very large grazing angles have strong effects on the backscatter level. Furthermore, it can be shown that the effects of canopy surface undulations average out for this model in the sense that the (linear) average of γ, for any area within a perimeter located at a horizontal plane and not showing radar shadow, is independent of the degree and location of slopes.

Observations at the Horsterwold site

On the basis of model assumptions, the relatively large spatial patterns (often found in radar images within presumed homogeneous areas) can be related quantitatively to the three–dimensional physical structure of the upper canopy surface. In the context of this research programme, an actual experiment for quantitative validation of the proposed model was not carried out since it would require many (tedious) measurements. Qualitative observations were made, however, and some results for the Horsterwold are described.

The Horsterwold forest in southern Flevoland (a polder area) is on very flat terrain. Height differences in the upper canopy surface reflect differences in tree height only. The effect of terrain relief can be neglected. In the radar images, the regular pattern of the rectangular forest stands appeared to be disturbed at some places by small faint circular patterns, sometimes crossing stand borders. Local field inspection proved that the (poplar) trees at these spots showed subtle growth differences with respect to other trees. These trees were a little smaller, the trunk diameter was a little less, branches and twigs were a little shorter and the node distance was a little shorter. The small growth deficiency found is probably caused by local soil conditions. In the past, at the time of the construction of the polder, sand from small canals was deposited at these spots. Also along a larger canal, somewhere in the middle of the forest, sand was deposited on a strip now occupied by the edge of a row of forest stands. The radar image clearly shows this strip, but not in all stands. It was found that not all species (in the different stands) respond in the same way. Some show increased growth, some decreased growth and some show equal growth in this strip. These different conditions could be linked, qualitively, with the patterns found in the images.

6.4 Spatial structure assessment through an analysis of texture

Image texture may be seen as a spatial pattern arising from a deterministic or random repetition of local subpatterns or primitives (i.e. pixels), with or without a preferred direction. It can be utilized to discriminate regions of interest or to delineate objects in an image. In radar images, (natural) forest types can be differentiated if sizes of resolution

cells are comparable or smaller than the sizes of major structural (or architectural) canopy components. The relevance of texture as a discriminating tool in forest type classification is emphasized by the fact that differences and temporal dynamics in (mean) radar backscatter level in some forests, especially natural forests, seem relatively small (hence discrimination based on mean γ levels is difficult). Since textural phenomena can be linked to spatial properties, quantification of texture may be a useful tool in the characterization of forest architecture (Oldeman, 1983 and 1985).

A multitude of approaches and models to compute texture measures from digital images has been investigated (Haralick et al., 1973; Galloway, 1975; Haralick, 1979; Conners et al., 1980; Blom et al.,1982). In this study, textural phenomena are described with statistical texture measures computed from the elements of the grey level co–occurrence (GLCO) matrix and grey level difference (GLD) vector. These approaches have been found among the most useful (Weszka et al., 1976; Shanmugan et al., 1973 and 1981).

The elements of the GLCO matrix and GLD vector represent grey level second–order statistics of the pixel pairs contained in a certain image segment or spatial window. The i,j–th entry in the GLCO matrix $p(i,j)$ is defined as the relative frequency of pixel pairs, for each possible pixel pair realization in the area of interest, for which the "source" pixel with grey level i is at position (x,y) and the "target" pixel with grey level j is at position $(x,y)+\vec{d}$, where $\vec{d}$ is the so–called "displacement vector". The i–th entry in the GLD vector $v(i)$ is defined as the relative frequency of pixel pairs, for each possible pixel pair realization, for which the source pixel with grey level k is at position (x,y) and the target pixel with grey level $k+(i-1)$ or $k-(i-1)$ is at position $(x,y)+\vec{d}$. Thus for the GLCO approach as well as the GLD approach, the results depend on $\vec{d}$, i.e. depend on a displacement length $|\vec{d}|$ and a displacement direction ϕ.

Mathematical operations on the elements of the GLCO matrix or GLD vector define a number of textural features. Six textural features based on the GLCO matrix and three based on the GLD vector were used (table 6.6). These nine features were calculated for a number of displacement vectors. Since directional differences were not considered of interest, all values corresponding to a certain displacement length were averaged. Displacement lengths of 1, 2, 3, and 4 pixels were choosen. Thus the total number of features investigated was 36 (4 x 9). A detailed description of the measures and procedures adopted in this research is given in a paper of Hoekman (1985b). A brief experiment description and an overview of the main experimental results are given below.

Table 6.6. Some commonly used textural features extracted from the GLCO matrix (1–6) and the GLD vector (7–9). N_g stands for the number of grey levels in the digitized image and m_x, m_y, s_x and s_y stand for, respectively, the mean values and standard deviations of the row and column positions of the counts in the GLCO matrix.

(1)	Angular Second Moment :	$\sum_{i=1}^{N_g}\sum_{j=1}^{N_g} p^2(i,j)$
	(GLCO–ASM)	
(2)	Contrast :	$\sum_{i=1}^{N_g}\sum_{j=1}^{N_g} p(i,j)\cdot(i-j)^2$
	(GLCO–CONT)	
(3)	Correlation :	$\sum_{i=1}^{N_g}\sum_{j=1}^{N_g} p(i,j)\cdot\frac{(i-m_x)(j-m_y)}{s_x\cdot s_y}$
	(GLCO–COR)	
(4)	Entropy :	$-\sum_{i=1}^{N_g}\sum_{j=1}^{N_g} p(i,j)\cdot\log(p(i,j))$
	(GLCO–ENT)	
(5)	Inverse Difference Moment :	$\sum_{\substack{i=1\\ i\neq j}}^{N_g}\sum_{j=1}^{N_g} p(i,j)\cdot\frac{1}{1+(i-j)^2}$
	(GLCO–IDM)	
(6)	Maximum Probability :	$\max_{i,j} p(i,j)$
	(GLCO–MAX PROB)	
(7)	Angular Second Moment :	$\sum_{i=1}^{N_g} v^2(i)$
	(GLD–ASM)	
(8)	Entropy :	$-\sum_{i=1}^{N_g} v(i)\cdot\log(v(i))$
	(GLD–ENT)	
(9)	Mean :	$\sum_{i=1}^{N_g} (i-1)\cdot v(i)$
	(GLD–MEAN)	

The "Drieersingels" beech forest test area.

Experiments were performed to elucidate the usefulness and behaviour of these statistical texture measures (for a more detailed description see also Hoekman 1985b). As a case study, a part of a SLAR image of the Speulderbos with high spatial resolution (showing the "Drieersingels" beech forest complex and its surroundings) was selected (figure 6.7a). This subscene features several large stands of mature beech forest and one large stand of oak forest. Further, it comprises small stands of Douglas fir, Scots pine, young beech, larch, agricultural sites and stands with strip cutting and clear–cut areas. The mature beech forests could be differentiated, for the purpose of this analysis, into three major classes according to tree crown canopy structure. Structure differences emanate mainly from forest management. The first structure (referred to as type 1) is characterized by a smooth upper canopy. The second structure (type 2) is characterized by a rough upper canopy. The crown cover is in the order of 60 to 70% whereas type 1 has a crown cover of almost a 100%. The third structure (type 3) has a smooth canopy like type 1, a crown cover of 60 to 70% like type 2, but has large (30 m x 30 m) gaps in the canopy. These gaps are small clear–cut areas created for forest regeneration experiments.

The 36 texture measures were calculated for all image segments (integrally) representing relatively large forest regions with homogeneous structures. A tentative analysis revealed that the test area comprised six major texture classes. These represent the following canopy structures:

(1) type 1 beech forest,
(2) type 2 beech forest,
(3) type 3 beech forest,
(P) young forest in the so–called "pole phase", but also mature beech stands with a very smooth and closed canopy,
(M) mixed areas, e.g. beech forest with small stands of pine or Douglas fir or mixtures of very small stands in the pole phase (with different radar backscatter levels),
(E) (edges) strips of increased radar backscatter (caused by layover) and strips of radar shadow resulting from boundaries between stands with relevant height differences.

The last class is not actually a real texture, since there is no repetition of subpatterns. Strip cutting sometimes falls into this class and sometimes in class 'M', depending on the geometry of the strips and the geometry of radar imaging.

The optimization of feature choice and window size.

The analysis was continued with six large training areas, each representing one of the major texture classes found. For these areas, the texture measures were calculated within a small (square) spatial window. This was done for all spatial realisations of this window within the training area and for window sizes of 5, 7, 9, 11, 13 and 15 pixels. Subsequently, a mean and a standard deviation were calculated for all measures and for all window sizes and texture classes presumed. Figures 6.6a and 6.6b show some results. Window sizes 5 and 7 were found to yield inferior results. Standard deviations increased with decreasing window sizes and at the same time differences between (the mean values of) texture measures decreased (in some cases drastically). Hence discrimination of texture classes detoriates strongly with decreasing window size. On the other hand, window sizes of 15 (or more) pixels were found to be too large in the sense that the number of realisations of spatial windows completely contained within (the presumed) homogeneous areas is small. Hence a filter type way of processing may be impractical. For the images studied, a window size of ± 11 pixels was considered as a good compromise. The features yielding the best discrimination for window sizes 9, 11 and 13 were found to be GLCO "correlation" at displacement length 1 (GLCO–COR[1]) and GLD "entropy" at displacement length 4 (GLD– ENT[4]). The search was continued to find a second–best feature in combination with the first one. It yielded four combinations, namely:

	GLCO–COR[1]	with GLCO–CONT[3],
	GLCO–COR[1]	with GLCO–COR[4],
	GLD–ENT[4]	with GLCO–COR[1],
and	GLD–ENT[4]	with GLCO–COR[4],

(where CONT stands for contrast). Most measures are strongly correlated and, as a result, combinations with third–best features did not improve the discrimination significantly. A mathematical elaboration of this phenomenon is given by the theory of generalized texture measures (van der Lubbe, 1983).

GLCO–COR[1] was found to be related (in this case study) to an image property often referred to as "coarseness". The measure is sensitive to the size of clusters of more or less the same grey level and the contrast between these clusters (image cluster sizes correspond to sizes of structural elements of the forest canopy such as crowns, groups of crowns or gaps). GLCO–COR[4] was found to act as the inverse of GLCO–COR[1]. This could be explained by the ratio of spatial dimensions of these clusters and the pixel size. When the coarseness is very high, however, for example at edges, COR[4] acts like COR[1] and as a result the combination of COR[1] and COR[4] is useful in discriminating the edges (see figure 6.6b). GLD–ENT[4] as well as GLCO–CONT[3] were found to be related to the

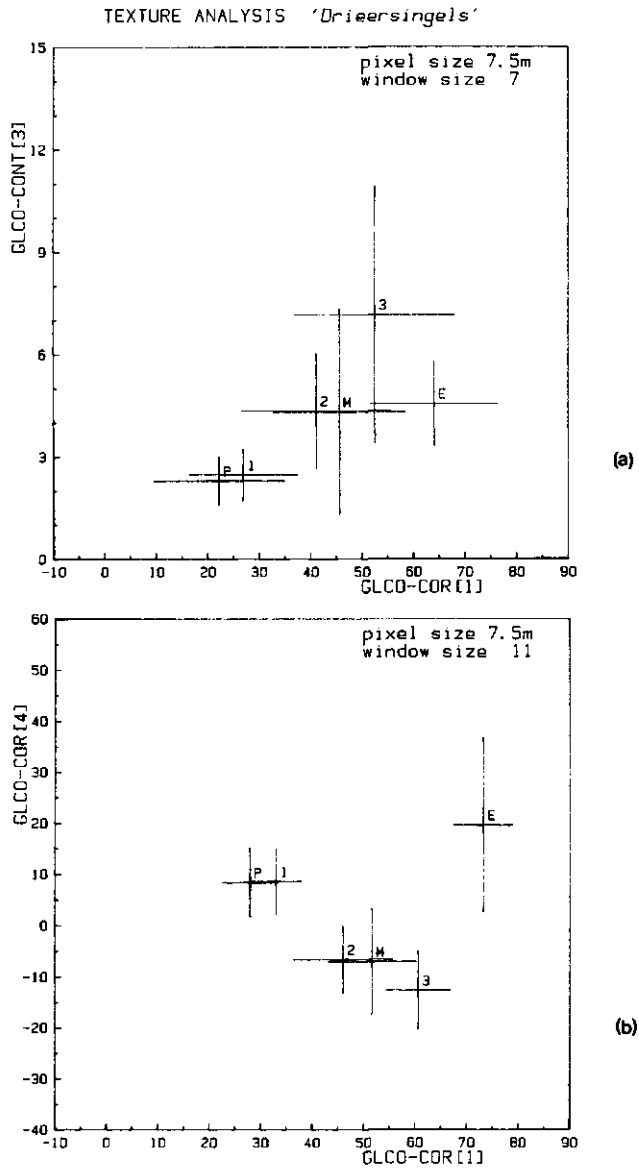

Figure 6.6. **(a)** Results for texture measures GLCO–COR[1] and GLCO–CONT[3] for the six major texture classes are shown in a two–dimensional texture feature space. The bars indicate the +/− 1 standard deviation intervals and the window size applied is 11x11 pixels. **(b)** Idem for texture measures GLCO–COR[1] and GLCO–COR[4].

variance of the grey level distribution (see also table 6.7 and figure 6.6a).

The results suggest that other approaches, for example a combination of an edge detector, a variance filter and GLCO–COR, might provide good alternatives. It was experimentally found that GLCO–COR combined with a variance filter has a slightly better performance than an approach based on GLCO–COR combined with GLCO–CONT[3] or GLD–ENT[4]. The first–order statistics presented in table 6.7 alone do not suffice to differentiate these six classes properly.

Table 6.7. First–order statistics of the six training areas.

texture class	mean γ (dB rel.)	s.d. of γ (dB)
(P)	0.00	1.00
(1)	–0.66	1.04
(2)	–0.18	1.42
(M)	–0.88	1.62
(3)	–1.04	1.96
(E)	–0.90	1.66

Classification results

Having established effective measures to differentiate the major texture classes, a filter type processing can be utilized to classify (the pixels of) the scene. This was done in two steps. So–called "texture transformed" images, resulting from application of an 11x11 "texture" filter, were made first. Results for GLCO–COR[1] and GLCO–COR[4] are shown in figures 6.7b and 6.7c. A two–dimensional classification of the scene, based on these two texture measures and using the empirical results from the training areas, was performed next. Results of this classification in general were found to be in good agreement with ground truth. Some interesting phenomena were noticed:

(1) A large area within an extended oak forest in the pole phase, class 'P', appeared in the classification as class 'M'. The correctness of this unexpected result could be established after re–examining this oak forest by stereoscopic viewing of low–altitude aerial photographs. The part of the area classified as class 'M' appeared to contain clusters of emerging birches!

(2) Sometimes small areas in beech 'type 3' forest showed up as beech 'type 1' forest. This could be explained by the local absence of the large gaps in the smooth upper canopy and the spatial dimensions of the window applied.

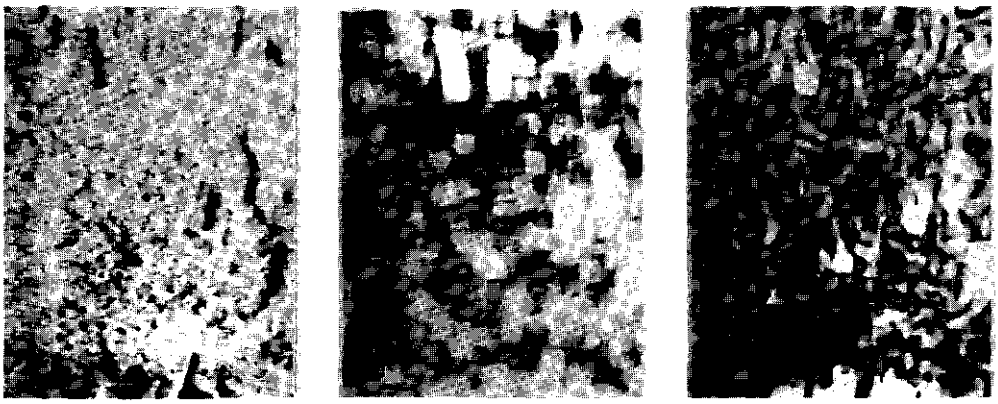

Figure 6.7. **(a)**. X–band SLAR image of the test area (recorded on 14 August 1984; pixels corresponding to 7.5 m square scene elements; ground range resolution ≈9 m; azimuthal resolution ≈10 m; angular range of 22° (right) to 32° (left) grazing angle). The size of the area shown is approximately 1600 m x 1250 m. **(b)** Texture transform made with GLCO–COR[1] and window size 11. **(c)** Idem for GLCO–COR[4].

(3) If a pixel was assigned the label 'pole', the whole local region contained in the corresponding spatial window was likely to be forest in the pole phase (with homogeneous backscattering properties). The same property could be noticed for the pixels labeled with the texture class 'type 1'. It can be explained from the fact that these texture classes are among the smoothest, and mixing with other texture classes always results in "rougher" textures. This property of texture transformations can be taken advantage of in a more elaborate classification approach (see below).

(4) As a consequence of the spatial resolution of the SLAR (which is in the order of 10 m x 10 m), the texture class 'pole' comprises several forest structures. Differentation between stands in the pole phase, seedlings, saplings and even mature stands with a very smooth canopy could not be made through an analysis of texture. The analysis of speckle might be an appropriate technique in this case.

(5) In general, the other texture classes ('type 2', 'type 3', 'mixed' and 'edges') were also classified well. But, as could be expected, in small textural regions and at boundaries of textural regions, the results were disturbed. This is a consequence of the low spatial resolution inherent to texture transforms.

Some considerations on classification approaches

The insights obtained into classification potentials (i.e. on the basis of textural features and/or mean backscatter level) suggest that an integrated approach, combining several image processing techniques and physical models, is recommendable. In the Roggebotzand test area, the classification procedure was simple and straightforward. When a priori knowledge of boundaries is not available, automated segmentation procedures (such as split–and–merge) are applicable. Since all stands of the Roggebotzand forest are in the pole phase (and spatial structural elements greater than or equal to the pixel size are absent), texture analysis will not yield additional information. Classification has to be based on (stand–averaged) γ values and, possibly, on speckle spectra.

In the Veluwe test area, the matter is more complex. Since this area comprises stands in the pole phase as well as mature beech forests which give rise to "rough" textures (and high within–stand variation of γ), automated segmentation procedures not incorporating texture will largely fail. When suitable texture transforms are used, however, a more sophisticated approach can be followed. It was found that if pixels are labeled as 'pole' or 'type 1', the whole region covered by the corresponding spatial window is likely to be of the same structure. Then the centre pixel (or even the integral window) may be classified on the basis of models using texture and mean backscatter level and the speckle problem is largely avoided through (weighted) averaging over that local region. In a way, the window can be considered to cover a coherent image unit or segment. This is not necessarily true of pixels assigned to other ("rougher") texture classes. Moreover, an accurate estimation of γ for areas with a "rough" texture can be obtained only through averaging over a relatively large local region. Since values of texture measures are always based on a relatively large local region (in this case 11 x 11 pixels correspond to an 82.5 x 82.5 m^2 area), it implies that parts of the scene with a rough texture are always (inherent to its nature) classified with low spatial resolution (i.e. if a priori knowledge on boundaries of coherent units is not available).

Preliminary conclusions

The results presented here show that the technique of classification using image texture is feasible if sizes of structural elements of the forest canopy (i.e. crowns, gaps, etc.) are larger than or comparable to the size of the resolution cell. To obtain good discrimination between the forest structure types present, the computation of texture measures has to be based on a certain minimum area. For the Speulderbos study, a window size with minimal dimensions of 11 x 11 pixels was found necessary empirically. Since this size is large compared with the related spatial extent of the forest stands, a priori knowledge on stand boundaries is required to obtain good results. In general, the actual choice of texture

measures and texture analysis procedures will depend on the forest types of interest and sensor characteristics (notably spatial resolution).

6.5 Spatial structure assessment through an analysis of speckle

Under certain conditions, speckle, an inherent feature of radar data, may contain information on the geometric arrangement of scatterers at the subresolution cell level (section 3.1 and Appendix II). It was shown, on the basis of theoretical considerations, that the autocorrelation function of the spatial backscatter signature in azimuth can be retrieved from power density spectra (of azimuth time signals) in a straightforward way (eqs. II.12b, II.27a and II.28). Moreover, the stochastic behaviour of the amplitude of the (discrete) components in the power density spectrum could be described in a statistical sense (eq. II.34).

To assess the feasibility of this technique, an experiment with the X–band SLAR was conducted at the Horsterwold site. The radar was flown perpendicular to the tree row direction. In this way, the spatial backscatter signature in azimuth direction is linked to the periodic tree row structure and may also be assumed to be periodic. Since the autocorrelation of a periodic function is also periodic, a power density spectrum with periodic features is anticipated, according to theory.

Within a forest stand, different realisations of the azimuth (time) signal could be obtained from adjacent strips parallel to the line of flight. The corresponding total areas typically correspond to ≈0.5 hectare. Using the digital Fourier transform, a series of discrete frequency components (of the power density spectrum) could be calculated for each realization and these frequency components were averaged afterwards to obtain an averaged power density spectrum.

Two typical results are shown in figures 6.8 and 6.9. The first result (figure 6.8) shows a typical speckle spectrum of a forest stand with a closed and flat upper canopy surface. The spectrum is a more or less smoothly decaying function of frequency. Such a shape was also found for sites with agricultural crops. The second result (figure 6.9) clearly shows a spectrum with a periodicity. This was found to be typical for forest stands which do not have a flat upper canopy surface and have regular tree row spacing. In this example, the row spacing is 6.2 m and the relative maxima in the power spectrum are located at multiples of 14 Hz.

The expectation of the power density spectrum of a forest stand can be simulated on the basis of an appropriate model for the radar cross section function in azimuth (or x)

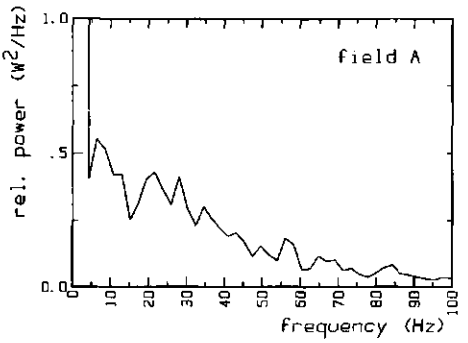

Figure 6.8. The averaged power density spectrum of a (50 m x 150 m) homogeneous sample area with oak (field A). The oak stand has a closed and smooth canopy.

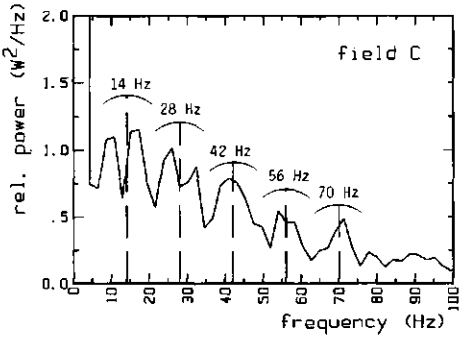

Figure 6.9. The averaged power spectrum of a (50 m x 150 m) homogeneous sample area with poplar (field C). The poplar stand has a regular tree row spacing of 6.2 m and does not have a smooth canopy. In the spectrum a periodicity, relative maxima at multiples of 14 Hz, is clearly perceivable.

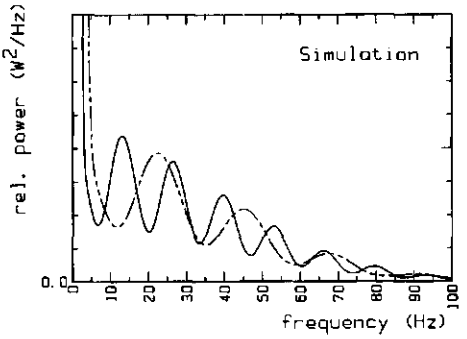

Figure 6.10. Two simulations of SLAR speckle power density spectra. In both cases, the model parameters have the same values (a=1, b=1 and the row spacing x_s=6). The distance r_0 was varied from 2600 m (solid curve) to 1400 m (broken curve).

direction. In a forest stand with a periodic row structure, a periodic function for the radar cross section (with a period length corresponding to the row spacing) can be anticipated. The exact shape of such a function, however, is not known and should be modeled. This can be done by assuming a large number of discrete scatterers to be located at random positions with a strength depending on the x–coordinate as

$$\sigma_i(x_i) = a + b \cdot \cos(2\pi \frac{x_i}{x_s}), \tag{6.4}$$

with a, b = constants ($a > b$),

x_s = row spacing in meters

and x_i = x–coordinate of scatterers.

The expectation of the autocorrelation function $\phi_{11}(x)$ of $\sigma(x)$ then follows as

$$E(\phi_{11}(x)) = a + \tfrac{1}{2}b^2 \cdot \cos(2\pi\frac{x}{x_s}). \tag{6.5}$$

Two simulations were made using this model (figure 6.10). The model parameters a, b and x_s have the same values (a=1, b=1 and x_s=6) for both cases. The distance sensor – sample area r_0 was changed from 2600 m (solid curve) to 1400 m (broken curve). All other parameter values correspond to the SLAR specifications given in table 2.2. The speed of flight v_0 is 180 knots (or 92.6 m/s).

Experimental results

Using this theoretical model as a reference, some experimental results of speckle power density spectra determination are described below. An overview is given in table 6.8. Data and results of four stands are presented. A is an oak stand (*Quercus robur*) with a closed and smooth canopy, planted in 1974. B is a beech stand (*Fagus sylvatica*) planted in 1974, also with a closed and smooth canopy, planted in rows 1.5 m apart, but recently every 6th row was cut and removed. Consequently, strips of trees occur at 9 m intervals. C is a poplar stand (*Populus* x *euramericana* 'Agathe F.') planted in 1975. Stand H is a poplar stand (*Populus* x *euramericana* 'Dorschkamp') mixed with ash (*Fraxinus excelsior*) planted in 1984 in a somewhat irregular pattern.

Table 6.8 gives data on field code (on forest map), the species name and year of planting, the distance sensor – sample area, the angle of incidence, the number of lines in azimuth, the number of samples per line, the frequency uncertainty $\Delta f_{min} = B$ (eq. II.30), the row spacing measured in the field and the (fitted) row spacing estimated from the speckle power density spectra.

Table 6.8. Overview of some experimental results from the Horsterwold site.

label	A	L	C	H
field code	Pz29 j3	Pz29 m1	Pz41 a1	Pz40 d1,d3
species	oak'74	beech'74	poplar'75	poplar'84
r_0 [m]	2590	2218	2590	2292
inc. angle [deg]	57.0	50.5	57.0	50.0
number of lines	50	30	50	40
number of samples/line	100	150	100	150
Δf_{min} [Hz]	2.2	2.6	2.2	2.5
row spacing [m]	1.5	9.0	6.2	4.15
fitted row spacing [m]	(closed)	8.55	6.15	4.10

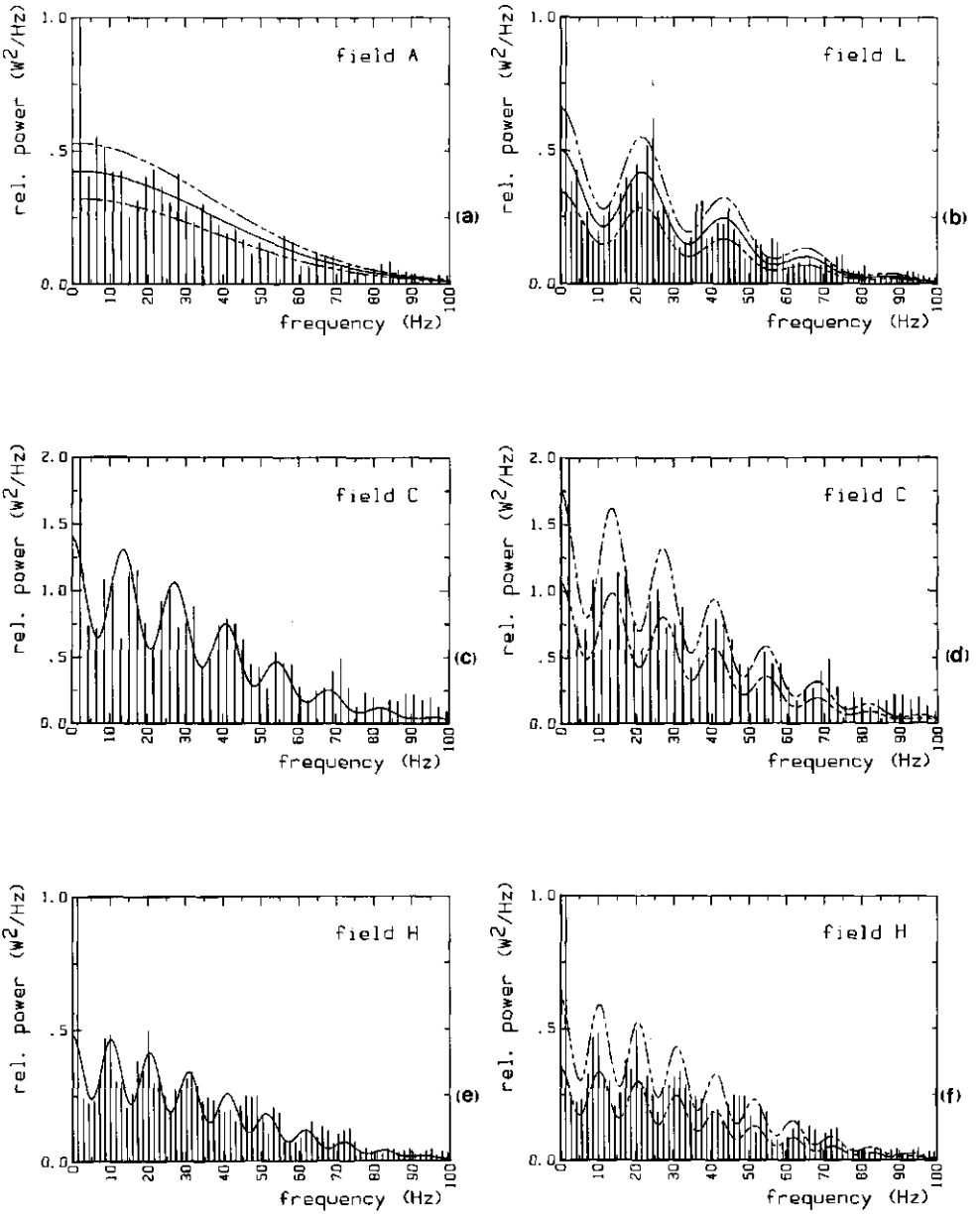

Figure 6.11. **(a)** Averaged components of the speckle power density spectrum for field A (vertical lines). The solid curve is a fit (fluctuating part only), using the model introduced. The broken curves represent a +/− 1 standard deviation interval for the fitted curve.

(b) Idem for field L.

(c) Results for field C with fitted curve.

(d) Field C with the +/− 1 standard deviation interval drawn separately.

(e) Results for field H with fitted curve.

(f) Field H with the +/− 1 standard deviation interval drawn separately.

Figures 6.11a–f show the averaged power density spectra components as vertical lines. The first component, at frequency zero, is very large, approximately as large as the sum of all other components together, and consequently is off–scale. The second component is also too large to be shown. A fit of the expectation of the power density spectrum (the fluctuating part only, i.e. $S_{<\text{speckle}>}(f)$, eq. II.27a), using the model introduced above, is shown as the solid curve. Optimal values for the model parameters a, b and x_s were determined by means of an iterative fitting procedure. The broken curves show the +/– 1 standard deviation intervals for the fitted data (eq. II.34c).

The fitted values for row spacing were found to be in good agreement with the values measured in the field (table 6.8). When a number of periods of the autocorrelation function are clearly visible in the power spectrum, the accuracy of the row fitting procedure can be quantified as follows. The width of the power spectrum is 52 Hz (eq. II.29). The frequency uncertainty B is in the order of 2 Hz. A theoretical accuracy of $\approx$ 2 Hz/ 52 Hz = 4% thus follows. Or, equivalently, the frequency uncertainty B corresponds to an uncertainty in the differential distance in x–direction of a half–antenna length (eq. II.31). The resolution cell size in x–direction is in the order of 25 m. Again a theoretical accuracy of $\approx$ 1 m/ 25 m = 4% follows. This figure agrees well with the actual results. The accuracy increases linearly with the distance r_0 (or, equivalently, with the observation time for each scatterer pair). In practical situations, however, the distance r_0 is limited by the forest stand size and the requirement that the illuminated spots, corresponding to (a certain minimum of) succesive samples in azimuth, must fall well within the stand borders.

When averaging is done over a much larger area, and consequently the confidence intervals of the components in the power spectrum are much smaller, accurate information on the radar cross section function can be obtained in principle. When the frequency uncertainty B is kept low, a fairly good approximation of the autocorrelation function can in principle be retained. The autocorrelation function, in turn, can tell much about the shape of the radar cross section funtion in x–direction. This can be done with fine spatial detail (the resolution is theoretically a half–antenna length).

Potential applications

The application of the speckle analysis technique may be two–fold. It can be used to support the study of the microwave interaction mechanism of forests (backscatter modelling), and it can be used in the application of remote sensing (forest structure determination).

For modelling, it is of interest to retain very accurate autocorrelation functions of small–scale spatial backscatter signatures. The relative contributions to σ^0 of various structural elements may thus be indicated. High accuracy could be achieved by averaging spectra obtained from very large forest stands with a homogeneous structure. It is obvious that forest plantations are more suitable in this type of study since their spatial structures are less complicated and ground truth is easier to assess than for natural forests.

In remote sensing, this technique could be applied to extract information on small–scale spatial features of the forest structure (e.g. mean crown size or mean tree spacing), and could be useful in forest type classification. Or the technique might be used to monitor forest development (e.g. the development from an open structure to a closed and smooth upper canopy).

6.6 Synthesis of potential applications

6.6.1 Spatial information extraction

The three approaches discussed in sections 6.3–6.5 are different in the sense that they are based on totally different concepts, apply to different scales and relate to different (physical) characteristics of the spatial structure of the objects.

Through the analysis of speckle (section 6.5), the smallest spatial details can be revealed, smaller than the size of the resolution cell, but not smaller than the half–antenna length, which is a fundamental limit. The system design and the design of flight geometry should be carefully adapted to the (type of) application. Spatial information can be extracted for one direction only (the azimuth or flight direction) and all spatial details in azimuth at different ranges within the range resolution are averaged. (The range resolution must therefore be small enough in relation to the application.) The statistics of small spatial details, such as tree spacing (in forest stands with regular tree row spacing), can be estimated accurately. Very smooth and closed canopies can probably be recognized as such. In principle, this technique, when applied in natural forests, can reveal characteristics such as mean crown size and mean tree spacing.

The analysis of image texture (section 6.4) applies to details larger than the size of the resolution cell, and therefore might be considered complementary to speckle analysis. Differences in the statistics of spatial (image) details can be quantified. The physical meaning of this quantification is complex and depends on many factors (such as wave parameters, spatial resolution, texture measures and analysis procedures). The technique can be utilized to classify forest types and the stages of forest development.

Through an analysis based on appropriate interaction models, large deterministic spatial patterns (in homogeneous areas) can be analyzed quantitatively and geometric properties, such as the slope of the upper canopy surface, can be estimated (section 6.3). Indirectly, this analysis can yield important information on local differences in forest growth or terrain topography. Also, the effects of radar shadow and foreshortening at (stand or forest) boundaries might be used to estimate properties such as (relative) tree height or to detect clearcut areas.

The spatial relationships in a radar dataset are important potential sources of information. This point is emphasized by the fact that the total range of (mean) radar backscatter levels within forested areas is not large (section 5.9.1). Especially for natural forests, which usually have mixed species compositions and therefore an even more limited dynamic range of radar backscatter can be expected, the spatial relationships in the radar data might be the most important source of information.

The techniques and results of spatial information extraction presented here relate to the X–band (SLAR) images studied. At relatively long wavelengths (e.g. L–band), because of the high degree of canopy transparancy, different (types of) results can be expected theoretically. This aspect could not be studied in the framework of this research.

6.6.2 Potential information content of forest radar data

To be able to indicate potential applications in forestry, it is important to assess the type and nature of relevant information that can be extracted from radar data, to asess the accuracy of parameter estimation and to establish how this depends on wave parameters and data acquisition and data processing methods. To date, it is not feasible to give an exhaustive overview of the potential information content and related accuracies. Especially for the lower frequency range, much research needs to be done.

Based on results obtained in this research (chapters 5 and 6), a tentative, and likely far from complete, summary of the potential information content and application of radar data is given below. Because of the limited insight gained so far and the presumed totally different behaviour for the longer wavelengths, these will be treated separately.

"Small" wavelengths

In X–band, and probably C–band, morphologic features were found to be the main determining factors of (mean) radar backscatter level (chapter 5). As a consequence, the range of higher frequencies (X–band and, probably, the C– and Ku–bands) are expected to

be useful for species classification and monitoring of several types of dynamic processes. A number of potential areas of application can be distinguished.

(1) *Forest inventory, i.e. delineation of stands, acreage determination and forest species/type classification.* The actual accuracy will depend on many factors. A multifrequency or multitemporal approach is likely to yield good results for species discrimination (sections 6.2 and 6.3). In addition to the (locally averaged) backscatter values, the thematic differentiation can be based on the spatial parameters assessed through an analysis of image texture or speckle (sections 6.5 and 6.6) or any combination of these (types of) parameters.

(2) *Monitoring of phenologic development and physiologic processes.* Leaf formation and loss can be detected (section 5.1) and, as laboratory measurements by other investigators suggest (see section 5.9), leaf and needle moisture content changes can be detected in principle. From the results obtained in this research, it could be inferred that certain plant physiologic processes can be studied with radar. For example, the needle formation of Japanese larch was found to be age dependent. The presumed heliotropic behaviour of some poplars was found to differ between the clones 'Robusta' and 'Heidemij' (chapter 5).

(3) *Detection of disease or stress conditions.* It was concluded that needle loss can be detected (section 5.9.4) and, on the basis of theoretical considerations, that leaf angle changes (leaf wilting) can be detected in principle (section 5.9.3).

(4) *Monitoring of forest development.* It was found that, in principle, four stages in forest stand development can be recognized on the basis of stand–averaged backscatter levels, namely (1) very young plantations, (2) the stage with a high degree of crown coverage, (3) the old or senescent stage and (4) clear–cut (chapter 5). Also the (spatial) parameters that can be assessed through analysis of texture or speckle are relevant in the description of forest development (sections 6.4 and 6.5).

"Large" wavelengths

For L–band, the main determining factors of (mean) radar backscatter level could not be assessed clearly. The presumably high degree of canopy transparency, however, offers some unique potential applications.

(1) In *forest inventories*, L–band might be unfit to contribute significantly to species classification, but might be utilized to differentiate between broad classes or broad forest types. For example, L–band radar was found to be useful to delineate flooded areas under a complete crown cover (Imhoff et al., 1986), which is not possible at short wavelenths.

Moreover, L–band is useful to distinguish forested areas from other types of land cover and to discrimate between deciduous and coniferous species (chapter 5).

(2) Information can be obtained from the *undergrowth*. For example, the results of this study suggest the possibility of mapping beech undergrowth under a complete poplar crown cover (chapter 5).

(3) L–band offers *unique potential* for biophysical parameter estimation. Some authors (section 5.9.5) report statistically very significant relationships between the backscatter level of pine plantations and some stand and tree parameters (biomass, basal area, height) and age. Since the underlying mechanisms are not well established and are potentially complex, however, it is as yet unclear how the latter results should be extrapolated to forests in general.

7. APPLICATIONS AND PROCESSING STRATEGY

7.1 Implementation of radar remote sensing in forestry

7.1.1 General areas of application

Any assessment of the areas of application of radar in remote sensing is necessarily a preliminary one. Radar's potential in remote sensing still has to be established in its full extent, especially in the lower frequency range (P–, L–, and S–bands). The same is true for the use of the full polarization/phase information of waves as measured with polarimetric radar, an emerging technique in (civil) remote sensing.

Some advantages of the use of radar in remote sensing are obvious, however. Radar can be deployed day and night and in atmospheric conditions that are adverse for optical systems (cloud cover, rain, fog, atmospheric dust, etc.). Moreover, since radar systems in principle can be calibrated well, information collected at different areas and at different times can be compared directly. The unique possibility of gathering data in a synoptical and repeatable way at desired times makes radar an ideal instrument for monitoring in every possible time scale.

To assess the ultimate impact of radar remote sensing in forestry, several points have to be considered, namely:

(1) What are the potential applications?

(2) What is the rationale for introducing a new technique, i.e. can radar substitute for or complement existing techniques at competitive costs or can radar introduce new techniques cost–effectively?

(3) What basic research and technical developments are still needed?

The introduction of radar remote sensing can be seen as a technology push, confronting potential users with an innovative tool. The process of defining applications for these new tools is an iterative one. Areas of application need to be recognized, tools need to be adapted to specific user requirements and, subsequently, on the basis of newly gained insights, areas of application may be redefined. Considering the needs and interests expressed by potential users, the possibilities suggested by basic research (section 6.6) and the technical solutions offered to date or foreseen for the near future, a tentative assessment of the areas of application of radar remote sensing in forestry may be made (table 7.1).

It is useful to distinguish between cultivated and natural forests and between the temperate

and tropical zones, because of the different conditions and types of problems encountered. In the extensive and poorly accessible tropical rainforest environments, where other remote sensing techniques fail because of an almost permanent cloud cover, a major role for radar can be anticipated. This is especially true for monitoring. Any monitoring system under these conditions necessarily has to be based on sensors with an "all–weather capability". Thus radar, notably spaceborne radar, can be expected to become a major tool in surveillance and management of tropical rainforests. In view of the developments in radar technology, airborne systems may continue to play an important role in survey (chapter 1).

Table 7.1. A tentative list of potential applications of radar remote sensing in forestry.

(a) Forest plantations in temperate zones	
Forest surveillance	– control of reforestation obligations – control of concessions for timber extraction – detection of illegal cutting
Forest management	– monitoring forest development, forest regeneration, new plantations – detection (early warning) of disease or stress conditions – damage assessment (insects, disease, air pollution) – survey after natural disasters (effects of storms or fire)
(b) Natural forests in humid tropics	
Forest survey	– inventory of forest types and acreages, – thematic mapping (of biophysical, edaphic and hydrologic parameters) – topographic mapping (forest types, drainage patterns, geomorphic features)
Forest management and surveillance	– monitoring: timber exploitation, deforestation, reforestation, shifting cultivation, forest burning, colonization settlements, land use change (agriculture, cattle ranges), agro–forestry, forest plantations, erosion, secundary forest growth – control of reforestation obligations – detection of diseases and stress, monitoring spread of diseases – rapid survey of the effects of natural disasters (fire, flooding, drought) or hydroelectric power plants
Forest science	– study of eco–unit development and dynamic processes in general (seasonal changes) – assessment of forest architecture

For the temperate zones, radar can be anticipated to be utilized in forest surveillance and, notably, forest management.

The objectives of this research have been limited to an assessment of potential applications. Assessment of the full rationale for applying radar data in forestry is beyond the scope of this study. Two example are given, however, to illustrate types of considerations foresters are likely to encounter.

(1) In Flevoland, ash–dieback and watermark disease in willow appear. The total amount of timber has a large financial value (these species cover 950 ha). Experience indicates that the frequent cloud coverage in The Netherlands severely hinders operational use of aerial photography for forest disease detection (van der Pas, 1988). If these diseases can be detected by radar (preliminary results show certain prospects), a comparison has to be made with the existing techniques. Radar is likely to detect the disease at a later stage but, on the other hand, can be used frequently. Premature felling is imperative for two reasons, namely to save marketable timber and to stop the spread of the disease. The first requires timely information and the second requires information as soon as possible within financial constraints. Clearly a choice has to be made by the forest manager between alternative stategies on the basis of a cost–benefit analysis.

(2) Another example is found in the extensive Canadian forests (Kirby, 1987). Every year, on average, 2 million ha are burnt. Not all timber is destroyed in a forest fire. Trees may be damaged beyond recovery, but the core wood may still be of marketable quality. Salvage operations must start as soon as possible to minimize degradation through drying, splitting, insect attack and fungal attack. Because of the economic importance and the lack of realistic alternative ways to make timely damage assessments over these vast regions, the usefulness of radar for fire damage assessment is being studied in Canada. When radar's potential uses for this type of application are understood better, radar's cost–effectiveness may be demonstrated.

In general, potential users of radar remote sensing data will have to decide, weighing alternative strategies and based on the importance ascribed to economic or environmental factors, whether radar remote sensing is an attractive option or not. Having briefly addressed radar's potential and the rationale for its application, a tentative assessment of necessary and/or potential useful future developments is presented below.

7.1.2 Implementation of strategies

To benefit from the opportunities radar offers, the appropriate "strategies" should be implemented at a number of (conceptual) levels. These strategies should be directed towards a certain application or package of applications. To elucidate this, a generalized scheme is introduced (figure 7.1). The concept of "potential data" is defined here as the most complete dataset that can be acquired within physical limits (i.e. with sensors covering the full range of remote sensing observables at all possible sampling times, scales, etc). Many technical factors limit acquisition of this potential dataset.

(Level 1) At level 1 in this scheme, the potential data flow is limited by system and sensor design. For a spaceborne system, for example, depending on mission objectives, technical feasibility and costs, a certain payload, sensor performance and orbit must be selected.

(Level 2) After a certain technical solution is selected (usually a compromise to meet a number of mission objectives), data acquisition strategies must be defined for specific applications. Unfortunately, not all sensors can be utilized simultaneously and data handling facilities have a limited capacity. A compromise between swath widths (the width of the strip observed), resolutions, number of remote sensing observables and frequency of observation is therefore imperative.

(Level 3) The processing of the backscatter signal may involve the use of flight (or orbit) data and topographic data (ground control points, digital terrain model). There may thus be several options for radar data delivery to users, e.g. as raw data (including flight data), geometrically and/or radiometrically corrected data or as "geocoded" data. Because of this so–called "preprocessing", potential remote sensing data are lost to some extent, but, since context is added (i.e. stated more precisely), interpretation of the remaining dataset is improved. The loss of potentially relevant data is illustrated well by the technique of speckle analysis (section 3.1). Spatial information at the subresolution cell level can be obtained correctly only from the (SLAR's) raw data, and not from geometrically corrected data! In general, the user of radar remote sensing data should take care that relevant data for the intended application are not lost during the preprocessing phase.

(Level 4) Data analysis for forestry applications starts with the data resulting from signal preprocessing (usually images) and (other) added information. Image processing techniques (such as texture transforms or segmentation algorithms) and interpretation models can be utilized (such as classification models or biophysical parameter estimation algorithms). Depending on the application, any combination of these tools can be used, with or without additional knowledge (such as topographic, meteorologic or biophysical data). During the process of analysis, more context is added, the potential data flow is limited further and specific information is extracted.

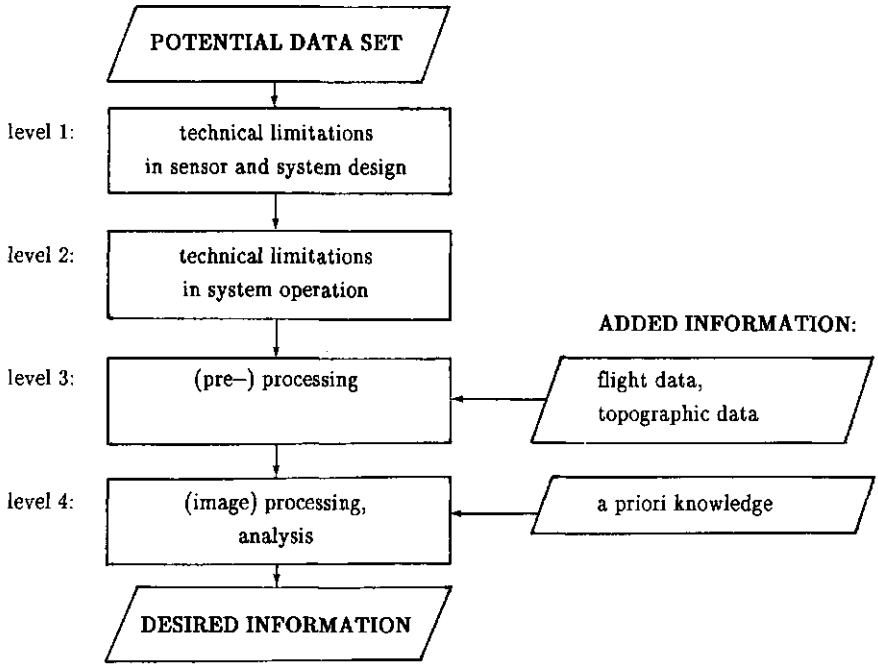

Figure 7.1. Impact of strategies on potential data flow.

Throughout the total process (i.e. levels 1 to 4), because of several types of limitations (of the system, survey strategy, processing, etc.), potential remote sensing data are lost but other types of data can be added intentionally. The enhanced context of the remaining data will facilitate interpretation for the intended applications. The user of remote sensing data should therefore understand what can be measured within physical limits (the potential dataset), define what information is desired and define appropriate strategies to be implemented at the conceptual levels introduced. Loss of relevant potential data should be avoided as much as feasible at each level. The presented scheme suggests a hierarchy for the implementation of strategies. This may be a top–down approach (following the data flow) or, more likely from the user's point of view, a bottom–up approach (starting from the desired output). Care should be taken, however, since certain strategies may have an impact at several levels simultaneously, or different strategies at different levels may be used for the same purpose. The latter point is illustrated, for example, by classification (section 6.2). To improve results, image processing techniques can be used (level 4), an appropriate choice of wave parameter combinations and observation times can be selected (level 2), the bandwith of the radar system can be increased to reduce speckle (level 1) or, of course, any appropriate combination can be made using these three strategies.

7.2 Towards an integrated analysis approach

7.2.1 The types of application

Radar is expected to be used in forestry for a large range of applications (see table 7.1). To facilitate discussion of analysis techniques, these applications may be structured according to "type". Type in this context relates not only to application but, as will be shown, also to the physical description involved. A basic hierarchy is suggested in figure 7.2. The scheme shows that remotely sensed data are used to

(1) classify (and delineate) objects,

(2) estimate (bio)physical parameters and

(3) monitor temporal changes (in classes, their spatial extent, in physical parameters or, simply, in the backscatter parameter γ).

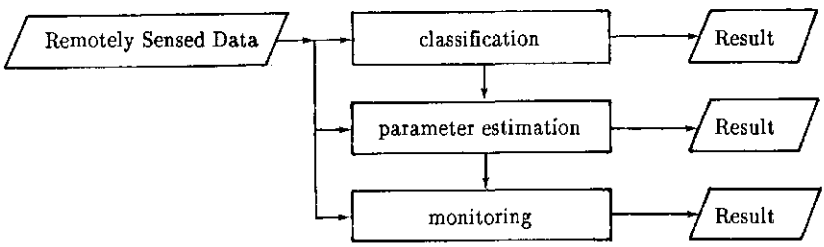

Figure 7.2. Generalized structure of analysis techniques.

For classification, it suffices to describe the object by means of empirically established radar signatures and textures. If these characteristics are sufficiently class–specific, classification techniques can be applied succesfully (e.g. as was found for the X– and C–bands, see chapter 5).

For parameter estimation, objects need to be described by electromagnetic wave interaction models on a statistical basis. Since these models are usually valid for a single class or a specific type of classes (see also section 7.2), these classes need to be known beforehand. This knowledge by itself, however, may be a product of remote sensing classification techniques (type 1).

For monitoring applications, the objects need to be described as a state in a dynamic process. This can be done by a crop growth model, a forest development model, a

hydrologic model, a water/nutrients/energy budget model, etc. These models do not describe the object's interaction with radar waves but with the (natural) environment. It is essential, however, that some of the (process) parameters in these models are parameters (or classes) that can be assessed with remote sensing techniques, i.e. classification (type 1) and/or parameter estimation (type 2).

For many applications, relatively simple empirical models to analyse radar data may suffice. It may be postulated, however, that this analysis can benefit significantly from accurate physical electromagnetic wave interaction (or backscatter) models. These backscatter models can be utilized to

- indicate under which conditions (e.g. certain frequency bands or phenologic stages) classification models can be applied accurately (type 1),
- develop parameter estimation techniques and/or to indicate the conditions for their validity (type 2),
- directly relate backscatter level changes to object parameter value changes and to indicate the sensitivity and accuracy of this relationship under different conditions (type 3).

7.2.2 Vegetation backscatter modelling approaches

The physical properties affecting radar backscatter level can be divided in two groups: the wave parameters and the object parameters. Because of the complex geometry of vegetation canopies, the description of the interaction mechanism is a tedious task. A multitude of modelling approaches has been employed, but, as yet, no clear consensus has been reached. For agricultural crops, substantial progress was made during the last decades, but the few explicit forest backscatter models are not well or fully developed.

Proposed backscatter models can be grouped into three broad classes:

(1) the models with a strong physical basis,
(2) the semi–empirical models, which in fact have a physical basis but contain some empirical (object related) parameters, and
(3) the empirical models, which have no physical basis.

To support backscatter model development, other approaches, such as modelling transmission properties or permittivity, are of interest. The types of approach, their mutual relationships and their significance are discussed below.

(1) Physical model type

The physical modelling of backscatter from vegetation canopies requires an appropriate

combination of surface–scattering (for the ground surface) and volume–scattering (for the vegetation volume) models. The interaction mechanism can be described in mathematically manageable equations only for a very simplified physical representation (i.e. of the statistical description and the geometric properties of the object's components as well as the microwave interaction with the object's components).

Of special interest are models based on the radiative transfer approach, since these can account for strong dielectric fluctuations (as commonly encountered in vegetation layers), multiple scattering (i.e. to a certain extent) and can include surface–volume interaction contributions (Tsang, Kubacsi and Kong, 1981; Fung and Chen, 1981; Karam and Fung, 1983). The resulting algorithms are computationally complex. Promising results have been obtained recently for non–layered media with a high degree of opaqueness utilizing the (mathematical) matrix–doubling method for the actual computation of radiative transfer (Twomey et al., 1966; Eom and Fung, 1984; Fung, 1987).

Validation of the physical models is difficult, since not only backscatter measurements have to be obtained but also many and sometimes complex measurements of the plant's structural and material properties. None of these models can be regarded as adequately validated against extensive datasets. This is especially true for forest vegetations (Fung and Chen, 1986).

(2) Semi–empirical model type

A completely different and more pragmatic approach is implied in the semi–empirical model type. From an applications point of view, it is seldom necessary to actually know the effect of all factors involved. The value of some variables (especially structure related ones such as leaf distributions and dimensions) usually varies little within a single species and phenologic stage and the effect of these small variations on gamma can be neglected, while other variable values vary significantly within the group of objects belonging to a single species (e.g. of biomass, timber volume, soil moisture content). Often only the latter are of interest in remote sensing. The approach then followed is that species–characteristic values of physical variables are assumed to be represented adequately by empirical parameters (species–dependent constants). As a result, the generality of the physical model type (valid in principle for many plant species and wave parameters) is lost and exchanged for a considerable simplification of the model. The values of empirical parameters have to be determined experimentally for each species, phenologic stage and wave parameter combination of interest. Model validation is easier, since fewer physical object parameters are involved, but validation is still required for many cases.

In a number of instances, good results have been obtained with models based on

mathematical simplifications of the radiative transfer approach. Eom and Fung (1984) showed that when the radiative transfer approach is applied to a medium having no definable upper boundary, as occurs with vegetation, the formulation simplifies to a summation of three terms representing:

(1) a diffuse scattering contribution from the vegetation volume,

(2) a direct surface backscattering contribution from the soil surface, including two–way attenuation and

(3) a diffuse surface–volume interaction contribution.

Allen et al. (1984) generated approximate expressions for the three individual terms. A still stronger simplification is obtained by limiting the solution of the radiative transfer equations to single scattering (the first–order solution). Then only two, very simplified, terms are left:

(1) a direct backscattering contribution from the vegetation and

(2) a direct backscattering contribution from the soil, including two–way attenuation.

The basic concept of the cloud model as formulated by Attema and Ulaby (1978) is based on this first–order solution and assumes scatterering from a homogeneous layer of identical discrete scatterers. The effective backscatter and attenuation cross section of the scatterers have to be determined empirically, and the number of scatterers is taken to be proportional to the plant moisture content per unit area (see also section 3.1). This concept proved to be successful in many cases. Many modifications have been suggested to account for more complex canopies and to improve accuracy, however. To account for different types of scatterers, Hoekman et al. (1982) introduced a multilayer concept (e.g. wheat heads in upper layer, wheat leaves and stalks in lower layer), and Ulaby, Allen and Eger (1984) introduced the very similar multiconstituent concept (e.g. corn leaves, stalks and fruits mixed in a single layer). Other succesful modifications followed (Le Toan, Lopes and Huet, 1984; Paris, 1986b).

(3) Empirical model type

The simplest approach is the (purely) empirical model. It is merely a set of empirically established relationships or look–up tables. This approach is of practical use when one (dominating) parameter is involved. This model type is unlikely to be of much general use for vegetation studies and, consequently, application will be restricted to specific cases. Though this model type may be inadequate for parameter estimation in general, it may be well suitable for other purposes, such as classification (section 6.1).

Forest backscatter models

The models mentioned above have been shown to be applicable for agricultural crops. Because of the greater geometric complexity of trees and forest canopies, however, it is unlikely that they will be directly applicable for forest vegetation in general. This is especially true at the larger wavelengths. The scattering and absorption properties of trunks and branches differ significantly from the properties of the smaller constituents, such as leaves or needles and twigs. To account for the diversity of component types, it is likely that the multilayer and multiconstituent concept should be adopted for forests too. The role of the tree trunk, because of its large size and structure, may be very important, especially for the lower frequency range where the canopy transmittance is large. As has been suggested by several authors, the trunk, via a trunk–ground interaction mechanism, may contribute significantly.

Richards et al. (1987) recently developed a theoretical L–band forest model incorporating terms describing

(1) the foliage volume scattering,
(2) surface scattering from the ground,
(3) canopy–to–ground forward scattering and
(4) trunk–ground interaction.

In the last term, the trunk–ground interaction is modelled as specular reflection by a dihedral corner reflector. The resulting expression, however, contains many components which require validation themselves. The excessive number of potentially important parameters in this model might prevent any practical use. To date, research has focused on an expansion of previously developed models based on the radiative transfer approach (Fung, 1987). In these models, leaves are modelled as dielectric discs and needles as small dielectric cylinders. To account for the typical forest structure (i.e. trunks and branches), large dielectric cylinders will be added.

Comparison of model types

The empirical model type has obvious and severe limitations, but the other two model types discussed here also have limitations. The physical models provide some theoretical insight into the relationships among backscatter level, wave parameters and the parameters of very simple well–defined structures. For the time being, this model type should thus be seen mainly as being supportive to other model types.

Semi–empirical models, notably those based on the first–order solution of radiative transfer, seem to be the most promising for practical use (and are sometimes referred to as "user models"). The use of empirical parameters, however, implies a limited range of

applicability. A set of empirical values is usually valid for a single frequency band and polarization and a limited range of morphologic and geometric variations (which does not necessarily have to coincide with the botanical range of a species). The latter restriction is difficult to interpret without a deeper physical understanding of the backscatter mechanism. Unfortunately, experimental validation is a tedious task, since many object and wave parameters as well as classes of vegetation are of interest.

Supporting approaches in model development

To facilitate model development, dedicated approaches can be utilized. Physical models, including simplified solutions of radiative transfer, as well as semi–empirical models usually break–down into several model components. Instead of validating (complete) backscatter models, these model components can be validated separately. To this aim, dedicated measurements made under laboratory conditions and/or with special microwave equipment are made in addition to straightforward backscatter measurements.

In this study, canopy transmissivity (section 5.4) and backscatter properties of subcanopy elements, i.e. forest canopy layers and ground layer (section 5.8), were determined. To describe the relationship between the return signal and these physical canopy properties, the cloud model was used (section 3.4). Hence, these measurements support the cloud model development directly. Of course other, more elaborate, models may be used to describe this return signal.

Waveguide transmission and waveguide resonance systems have been employed to measure and support modelling of the dielectric properties of vegetation material as a function of moisture content and frequency (Carlson, 1967; de Loor, 1968; Tan, 1981; Ulaby and Jedlicka, 1984).

Other approaches have been utilized lately to support model development. For example, simulation studies have been carried out by Blanchard and Fung (1986). They established backscatter signatures from artificial structures (simulating crops and trees) experimentally to study the effect of small structure changes under highly controlled conditions.

These indirect approaches are of major significance for model development and model validation. This may be especially true for forest vegetation because of its complex geometry.

7.2.3 The inversion problem

Most model research in radar remote sensing has focused on an accurate prediction of γ as a function of object and wave parameters. For applications, however, the "inverse problem", namely the accurate estimation of object parameters based on radar observations, employing a number of appropriate wave parameter combinations, is of interest. Once the direct problem has been solved within acceptable statistical limits, the inverse problem can be analysed for specific cases. It may be clear from the discussion of modelling above that much research is still needed, especially for forest vegetations. In this stage of research, however, some relevant implications of this so–called "inverse problem" can already be considered.

Strictly speaking, the inverse problem, i.e. the estimation of object parameters, cannot be solved when the number of unknown (object) parameters in the model(s) exceeds the number of remotely sensed observables. In the other case, depending on the occurrence of singularities and boundary conditions, a solution may be possible.

Despite the general tendency of limiting the number of object parameters in (semi–empirical) models as much as possible for this reason, without compromising too much with respect to accuracy (e.g. by omitting some parameters of minor importance or substituting strongly correlated object parameters for a single parameter), backscatter models may still contain (too) many independent object parameters. Again, this may be especially true for forest vegetation.

Two fundamentally different approaches can be indicated to handle this problem. The first approach is to extend remote sensing data collection beyond the microwave backscatter observables, for example observables obtained in the optical region. Although this may add "physically independent" observables of the object, it also may increase the number of object parameters in the (extended) set of model equations. This aspect is not studied very well, so the impact of the synergism is not yet clear.

The second approach is to include a priori knowledge. This is done to reduce the number of unknown object parameters. The latter approach is more straightforward. For a certain application, specific a priori knowledge may be available and, consequently, a limited set of specific observables is required. These follow directly from the appropriate models. The problem is most simply dealt with in the semi–empirical model type. When the class (species) is known, a lot of a priori information (characteristic features of the species) is implicitly contained in empirically established parameter values.

7.2.4 Supporting data

The analysis of a (multiparameter) radar image or a particular sequence of radar images (e.g. a time sampling sequence in a growing season) is strongly supported by auxiliary data. This can be a priori knowledge (including process knowledge) or other types of additional data, such as meteorologic data, data from in situ measurements and additional remote sensing data (e.g. from optical systems or microwave radiometers).

For many applications, the use of a priori knowledge and additional data is beneficial. For example, ambiguity problems arising from the use of backscatter models may be solved and spatial analyses may be supported significantly. Notably databases in which empirically established physical properties can be accumulated and topographic databases are expected to play a major role. The geographic reference can provide a means to integrate data of different types and formats and can provide a link with geographic information systems. The latter systems can facilitate data analysis and can also use and archive these results for subsequent analysis steps.

Several types of a priori knowledge can be recognized, including geographic data such as digital terrain models, (digital) topographic maps, forest maps or other thematic maps. These data enable the interpreter to link spatial features in the image with some ("hard") boundaries and broad thematic units. Furthermore, they can place the image data, after geometric transformation and resampling, in a geocoded reference system or, the other way around, can place the map topology into the image. The ability to compute terrain slope and link it to image elements is essential for the analysis of images from accidented terrain. Second, previously collected (and archived) remote sensing data and derived data products can play an important role, especially for monitoring applications. In this way, changes (e.g. in the backscatter parameter γ), can be detected and subjected to analysis. Third, a priori knowledge of object characteristics is of relevance. These characteristics are expressed in radar signatures, backscatter models and models of the interaction between the object and its physical environment (including contextual relationships).

In addition to a priori knowledge, other types of supporting data can be utilized. These data types, i.e. meteorologic, in situ and additional remote sensing data, are not collected well in advance but shortly before, during or shortly after the radar data measurements and hence may be called "data of current interest". Agricultural crop data must be collected in the same growing season and the same growing season is preferred for forests. These data are usually collected with a particular application in mind and are therefore directed to that application, or are needed afterwards as a result of (unanticipated) interpretation problems. These types of data have in common that they add independently to the description of the nature and condition of objects in the scene. They may thus add

to the solution of ambiguity problems or can be used to increase the accuracy of parameter estimation, or may add to understanding newly discovered phenomena (such as the emergence of a previously unobserved type of plant damage or stress).

In the general discussion of radar image analysis procedures, it is relevant to make a second type of division between the data types involved, in which the radar data and their supporting data are divided into two groups. The first group contains all data with a clear geographic component and of compatible scales (the radar images, other remote sensing images and maps). The second group contains all other relevant data including data with a geographic component but not spatially compatible. This can be in situ sampled data of selected areas (or sampling points), data at very large scales (e.g. aerial photographs) or background knowledge on the object's physical or other properties (such as contextual relationships). To facilitate analysis procedures (at digital image analysis facilities), the data of the first group should be brought into spatial registration, preferably in a (geocoded) spatial reference system. The data of the second group, then, could be regarded as parameters (or data from which parameters can be extracted) in spatial analysis procedures using data of the first group.

7.2.5 Data integration level

In general, analysis tools can be more effectively utilized when the degree of "data integration" or "coherence" is greater. Three aspects can be distinguished: (1) spatial cohesion, (2) semantic cohesion and (3) temporal cohesion. (Semantic cohesion refers to the functional relationships of thematic features and remote sensing observables within models or processes.) These aspects are described below.

The degree of spatial cohesion increases from the level of the basic picture element (pixel), through basic coherent units (segments, edges, linear features, etc) to the level at which contextual relationships between coherent units are present. Furthermore, spatial cohesion can be enlarged by incorporating image texture (description of spatial cohesion is an intrinsic property of textural features). It might not always be possible to indicate (or define) the exact spatial extent of objects. In these cases, spatial cohesion may be expressed in the form of grey level gradients or gradients in texture (e.g. in transition zones between forest types).

The potential possibilities of data extraction and interpretability increase with the level of spatial cohesion. A clear illustration can be found in classification techniques (section 6.2). A classification technique is more successful if it is based on averaged radar backscatter values of larger segments than on single pixel values, because of small–scale

inhomogeneities and the speckle problem. The incorporation of image texture may add independent features and thus further potential discrimination. A classification technique would be still more successful, however, if also contextual (spatial) relationships were incorporated.

The second aspect of data integration level is related to the semantic cohesion. The semantic (or physical) features of an object can be thought of as a collection of remote sensing observables and additional (thematic) data. In principle, potential information extraction increases with the number of semantic features. This is a well–known effect in applying (the conventional) classification techniques. Adding features (i.e. dimensions) may yield a better clustering of objects in feature space. It should be emphasized, however, that not only an increased number of semantic features but also an understanding of its cohesion is of relevance. This was brought out above in the discussion on parameter estimation in section 7.2.3. The cohesion of the semantic features is implicitly expressed in the electromagnetic interaction models. Ambiguity problems can be solved only when different remote sensing observables and additional data types have a meaning within a single model or within a set of connected models. Through the functional relationships described in these models, a synergistic effect can be obtained.

The third aspect of data integration level is related to temporal cohesion. Additional observations in time may also increase the potential information extraction. The periods of observation and time intervals, however, should be chosen carefully. They should be adapted to the time scales at which processes of interest take place. In vegetation studies, the dynamic behaviour of vegetation is of interest. Plant growth is not random but controlled by genetic properties and influenced by ecologic relationships and abiotic (weather, climate, soil) factors. Analysis of observations taken at appropriate times might yield information describing these dynamic processes (plant growth, forest development). On the other hand, knowledge of predictable processes, e.g. the succession of phenologic stages, can be utilized for other purposes. It was shown in section 6.1 that classification success can be increased significantly if an observation in winter (bare deciduous trees and larch) is combined with an observation in summer (with all trees fully foliated).

It is obvious that potential information extraction from radar images increases with the level of data integration or cohesion, which has spatial, semantic and temporal aspects. As an important implication, it follows that the utilization of remote sensing techniques requires not only appropriate data analysis procedures (with their spatial, semantic and temporal aspects) but also appropriate data acquisition (system resolutions, wave parameter choice and time(s) of observation). The latter point was already made in another context (section 7.1.2).

8. SUMMARY AND CONCLUSIONS

The capabilities of airborne imaging radar and its utilization for surveying vast areas of forested terrain were widely recognized during the late 1960s and early 1970s. Within a decade after the introduction of this novel technique (in 1965), millions of km^2 of previously unmapped woodland, mostly tropical rainforest, had been mapped successfully. Since then, as a result of several technologic developments, the capabilities of airborne radar systems have been firmly upgraded and, consequently, the potential applications —already considered impressive from an early stage— have increased to a significantly higher level.

Though radar's full potential for vegetation studies still has to be determined, it is clear that radar will continue to play a major role alongside the established surveying techniques for two reasons: (1) the unique property of microwave remote sensing systems to function almost unimpeded by adverse atmospheric conditions (which prevent the use of optical systems) and (2) the property of (coherent) microwaves to enable measurement of certain object parameters which cannot be assessed through other remote sensing systems, and thus can be considered complementary.

It is technically feasible to deploy radar from orbiting platforms. Though little experience has been gained to date, it can be envisaged that future spaceborne radar systems will offer enormous potentials. It is evident that logistics problems related to the execution of airborne surveys can then be avoided. The major application of spaceborne radar, however, is likely to be of another type. Because of radar's unique "all–weather" capability, Earth observing satellites equipped with radar will become reliable monitoring instruments. Radar may thus be particularly useful for monitoring applications. It is likely that for some applications in forestry, and vegetation studies in general, as well as for the global environmental research programmes, such monitoring systems will be of decisive importance.

The interpretation of forest radar data has not been and —though considerable progress has been made— still is not without difficulties. There are several reasons, including (1) the fact that, compared with optical systems, totally different physical and geometric principles underlie radar imaging, (2) the lack of sufficient (systematic and consistent) empirical knowledge and (3) the general lack of understanding of microwave interaction with vegetated terrain.

Through this study, a substantial increase of empirical knowledge was obtained systematically and, moreover, these empirical findings could be generalized on the basis of

basic physical descriptions of the radar return signal. At the same time, through these descriptions, specific measurement capabilities (for forests) of the research instruments Dutscat and the X–band SLAR could be recognized and fully utilized, and proper data extraction algorithms could be developed.

A thorough description of speckle, an inherent feature of radar data, was given. Probability density functions for the (averaged) signal strength of so–called "Rayleigh fading" targets were recalled. It was shown that speckle statistics of logarithmically scaled data (the usual form of presentation for radar data) can be described by simple analytic expressions using Riemann's zeta function and Euler's psi function (App.I).

On the basis of theoretical considerations, it was shown that the power density spectrum of the backscatter signal (i.e. of the speckle), as measured by a moving sensor observing a homogeneous "frozen" distributed target, contains spatial information in a statistical sense. If an antenna with a Gaussian–shaped azimuthal directivity function is used, the autocorrelation function of the azimuthal components of spatial features can be assessed in a relatively simple and straightforward way. Moreover, the statistical properties of such power spectra have been described. It turns out that the minimum size of spatial detail that can be resolved from the power spectrum is fundamentally limited to the half–antenna length and that the accuracy of estimation of this autocorrelation function is directly related to the spatial dimensions of the sample area, as well as to sensor characteristics (App.II).

To describe the backscatter mechanism, the "cloud model" was used. This model is based on a first–order solution of the radiative transfer equations and describes a forest as a number of horizontally oriented non–interacting canopy layers on top of a soil layer, each layer having distinct attenuation and backscatter properties.

The use of Dutscat for forest measurements was investigated. By modelling the forest as a collection of horizontal layers —the "multilevel model"— the scatter properties of the forest radar return signal could be analyzed. It appeared that, because of the relatively large height of forest canopies and the small beam widths of the scatterometer, a more general form of the radar equation (based on backscattered energy instead of power) is imperative to avoid gross errors in the computation of the backscatter parameter γ. The same multilevel model allowed the development of an inversion algorithm for an unambiguous determination of the relative contributions of these scatter planes to γ. On the basis of theoretical considerations and experimental data, it was shown that, if the canopy height is on the order of, for example, 25 m, it is well feasible to divide γ into contributions of three or four arbitrarily chosen layers (i.e. canopy layers plus a forest floor layer), depending somewhat on the wave parameters selected.

An experiment with corner reflectors placed on the forest floor allowed study of the microwave (X–band) forest canopy transmissivity. On the basis of several theoretical considerations (which could be supported by empirical findings), a description of the attenuated corner reflector return signal was given. Using this description for all reflector occurrences, a value for the transmissivity could be estimated, or upper or lower boundaries for this value could be indicated. The consistency of the theoretical bases of the cloud model and the data extraction techniques for canopy probing and canopy transmission measurements was elucidated. It was shown that the multilevel model is fully compatible with a multilayer cloud model and that the parameter for (two–way) canopy transmissivity is identical to the parameter for total canopy attenuation in the cloud model. Hence, these experimental techniques are of direct relevance for the theoretical elaboration and validation of the cloud model.

Experiments were conducted at four test sites in the Netherlands: the Roggebotzand and Horsterwold sites in Flevoland and the Speulderbos and Kootwijk sites in the Veluwe. Together, these test sites comprise a fair range of species, age classes, soil types and other environmental conditions. Within certain technical and logistic constraints, and capitalizing on the specific measurement capabilities the research instruments appeared to offer (for forest measurements), a systematic research programme was carried out. Altogether, nine Dutscat flights (on five dates) and seven SLAR flights were executed in the years 1982 through 1985.

A substantial amount of experimental data could be collected. A summary of the basic empirical findings as well as an evaluation and synthesis of the results were given in sections 5.9 and 5.10 of this thesis. This can be summarized very briefly as follows. The backscatter properties of trees were found to depend on (1) wave parameters, (2) species dependent (presumably morphologic) features and (3) other, not necessarily species dependent, factors such as stand and tree parameters, needle loss or undergrowth. In the X–band and, possibly, the C–band, the influence of these last factors was found to be small, except for some specific cases. For L–band, these last factors seem to be more important while, on the contrary, the species dependent features seem to be less important.

On the basis of the theoretical concept of the cloud model, the results of backscatter signature measurements and the probing and transmissivity measurements were evaluated. The consistency of the empirical findings was shown, indicating that for X– and C–bands the forest canopy acts as an opaque volume scatterer and for L–band as a transparent volume scatterer. In the last case, the contribution of the backscatter term related to the ground layer cannot be ignored. Moreover, it seems appropriate to modify the cloud model by adding explicitly a trunk–ground interaction term.

In X–band for stands with a (sufficiently) closed canopy, a clear link was found between the differentiation in radar backscatter level and the taxonomic differentiation. Anomalous backscatter behaviour could be linked to stands with a very open canopy structure, such as very young plantations (one or two years old) or some of the older stands. For these cases, it is likely this behaviour is caused by a major contribution of the soil and/or undergrowth. Other findings also clearly illustrate the effects of structure and morphology related characteristics. The substantial variation in radar backscatter level found for the Japanese larch in May could be linked to the different stages of needle development. For some poplar clones, directional dependencies of the backscatter level were found to occur (for X– as well as C–band) which may be related to heliotropic behaviour. For X–band, obvious relationships between backscatter level and biophysical properties were not found, except for the effect of needle loss. A synthesis of the results for pines clearly showed an increase of backscatter level, which can be as much as 2–3 dB, related to a decrease of the number of years green needles are retained.

For the L–band, some basically different results were found. A clear example is the empirical result that the presence of a 2 m tall beech understory under a 25 m tall fully closed and fully foliated poplar canopy yielded a significant decrease (as much as 2.5 dB, depending on θ_i) in backscatter level!

To investigate which type(s) of information can be acquired through the practical use of radar images, several promising information extraction techniques were evaluated.

Radar's potential use in classifying objects was studied on the basis of the empirical data and theoretical considerations. It was concluded that the shorter wavelengths (i.e. C–band and higher–frequency bands), because of the presumably strong relationship between backscatter level and morphologic (species dependent) properties, are the most appropriate for species classification. L–band, itself or in addition to the other bands, appears to be useful for the differentiation of some broad vegetation classes, such as the coniferous/deciduous, forest/non–forest and flooded/non–flooded forest class discrimination. Dual–temporal, i.e. summer (fully foliated trees) combined with winter (defoliated deciduous trees), or multifrequency approaches, are likely to give good classification results in general.

Furthermore, the utility of image processing tools was studied. These appear to be useful for handling the "speckle problem", but, especially when a substantial reduction of the effect of speckle is pursued, significant geometric and radiometric deformations of the data are introduced. There are alternative strategies to improve classifications results, not having these problems: (1) an upgrading of the radar system to get more independent samples per unit area and (2) an appropriate choice of wave parameters and time(s) of

observation. Of course, any combination of these techniques can be utilized and we may capitalize on the use of a priori knowledge. The actual limits of classification accuracy, however, may be determined by the empirically established value for the standard deviation of stand–averaged gamma values. This figure was found to be approximately 0.5 dB for almost all classes and wave parameters (i.e. for X– and C–bands) and may be related to ecologic and environmental variation.

The spatial relationships contained in imaging radar data are important potential sources of information. This may be particularly true for natural forests, which usually have mixed species compositions and, consequently, may show a very limited dynamic range of radar backscatter level.

Three approaches to extract spatial information have been evaluated: (1) the analysis of speckle, (2) the analysis of texture and (3) the analysis of (large) canopy patterns on the basis of appropriate interaction models. These approaches differ in the sense that they are based on fundamentally different concepts, apply to different scales and relate to different (physical) parameters of the forest canopy's spatial structure. These approaches can therefore be considered as highly complementary. A summary of the properties and potentials of these techniques was given in section 6.6.1.

The technique of texture analysis appears to be useful for forest structure discrimination (related to type and/or development stage).

On the basis of simple geometric considerations and the assumption that the canopy acts as an opaque isotropic volume scatterer (e.g. for X–band), large deterministic patterns within presumably homogeneous areas can be analyzed. The slopes of the canopy surface can be estimated accurately and, indirectly, may be related to other forest properties, such as local differences in forest growth, etc.

The feasibility of the technique to assess spatial information in a statistical sense through an analysis of speckle, using the raw SLAR data, was shown. Using a simple geometric backscatter model for the canopy surface, tree row spacing could be estimated with an accuracy of a few decimeters! In general, the application of the latter technique may be two–fold, namely: (1) to support the study of the microwave interaction mechanism of forests in a fundamentally new way and (2) as an approach in remote sensing to determine forest structure in a quantitative and physically well–defined way (i.e. through the autocorrelation function).

A tentative summary of potential areas of application was given in section 6.6.2. The "small" wavelengths (C– and X–bands) are expected to be useful for the following types of

application:

(1) forest inventory, i.e. delineation of stands, acreage determination and forest species/type classification,
(2) monitoring of phenologic development and physiologic processes,
(3) detection of disease or stress conditions and
(4) monitoring of forest development.

Because of the limited insights gained to date, it is much more difficult to indicate the application potential for L–band. In relation to the apparent high degree of canopy transparancy, however, "large" wavelengths are likely to offer some unique possibilities for forest inventory and forest monitoring.

For exploitation of radar's full potential, more basic research is needed. Notably the qualities of the lower–frequency bands (P–, L– and S–bands) and the potential of polarimetric radar are still largely unknown. Since these are likely to offer some new potential applications, especially for forestry, major (and systematic) research efforts are recommended. A start has already been made. Research will be carried out in The Netherlands using data collected in August 1989 over the Horsterwold and Speulderbos sites with a polarimetric P–, L– and C–band SAR (developed and built by the Jet Propulsion Laboratory, Pasadena). Furthermore, the present development of a polarimetric C–band SAR, called PHARUS, and the anticipated upgrading of the SLAR to a polarimetric X–band SLAR (by FEL–TNO) are expected to result in new research capabilities within a few years. Of course, the multiband DUTSCAT system, which is likely to provide accurately calibrated data, is also expected to play a major role in future research. Dedicated data acquisition campaigns may be necessary to develop certain applications. These are envisaged, for example, in areas with other environmental conditions, such as the tropical rainforest biome, or in areas with forests under stress conditions.

In addition to the need to increase empirical knowledge, it is important to elaborate on forest backscatter modelling. Several approaches were indicated. Such modelling efforts are expected to support the development of techniques for the estimation of (bio–)physical object parameters and, indirectly, the development of classification and monitoring techniques. Ambiquity problems may arise, however, especially when the number of unknown object parameters in such models exceeds the number of (independent) radar data parameters that can be acquired. An obvious solution is the exploitation of available (a priori) knowledge and the utilization of archived remote sensing products and additional data (from other types of sensors). To analyze radar data more efficiently, to handle the so–called "inversion problem", to improve the accuracy and, in general, to increase the potential applications, the development of an "integral" analysis approach seems to be very

advantageous. Several relevant aspects of such an approach have been discussed in the epilogue of this thesis.

Though more basic research as well as a substantial conceptual development of (an integral) data acquisition/analysis strategy remains to be done, radar promises to become one of the key sensors in future remote sensing systems. Independent of the Sun's illumination and largely unimpeded by atmospheric conditions, radar seems to be the only reliable solution for small–scale surveys in cloudy regions, as well as the only reliable solution for global (spaceborne) monitoring systems. Hence, because of these general properties and because of the specific potential applications discussed here, it is likely that radar remote sensing will have a large impact in future forestry practice.

REFERENCES

Abramowitz, M. and I.A. Stegun, 1965, Handbook of Mathematical Functions, Dover Publ., New York.

Allen, C.T., B. Brisco and F.T. Ulaby, 1984, Modeling the temporal behaviour of the microwave backscattering coefficient of agricultural crops, RSL Tech. Rep.360–21, Univ. of Kansas, Lawrence.

Allen, C.T. and F.T. Ulaby, 1984, Modelling the polarization dependence of the attenuation in vegetation canopies, Proc. IGARSS'84 Symp., Strasbourg 27–30 Aug. 1984, Vol.1, pp.119–124.

Attema, E.P.W. and F.T. Ulaby, 1978, Vegetation modelled as a water cloud, Radio Science, Vol.13, pp.357–364.

Attema, E.P.W. and P. Snoeij, 1985, DUTSCAT, a 6–frequency airborne scatterometer, Proc. EARSeL Workshop 'Microwave Remote Sensing Applied to Vegetation', Amsterdam, 10–12 Dec. 1984, ESA SP–227, Jan. 1985, pp.127–129.

Azevedo, L.H.A. de., 1971, Radar in the Amazon, Proc. 7th Int. Symp. on Remote Sensing of Environment, 17–21 May 1971, Ann Arbor, Michigan.

Barnes, M.B., 1981, SAR 580 point targets for registration of images (X and C), Space Department, R.A.E. Farnborough, 26 Feb., Rep. No. MOD(PE).

Bernard, R., P. Lancelin and G. Laurent, 1987, Radar observation of the Guyana rain forest, Note Technique CRPE/156, CRPE, Paris.

Blanchard, A.J. and A.K. Fung, 1986, Backscatter measurements from simulated vegetation structures, Proc. 3rd Int. Coll. on Spectral Signatures of Objects in Remote Sensing, Les Arcs, France, 16–20 Dec. 1985, ESA SP–247, pp.93–98.

Blom, R.G. and M. Daily, 1982, Radar image processing for rock–type discrimination, IEEE Transactions on Geoscience and Remote Sensing, Vol.GE–20, pp.343–351.

Brigham, E.O., 1974, The Fast Fourier Transform, Prentice–Hall, Englewood Cliffs, New Jersey.

Brownlee, K.A., 1965, Statistical Theory and Methodology in Science and Engineering (Chapter 17), 2nd ed., John Wiley and Sons, New York.

Carlson, N.L., 1967, Dielectric constant of vegetation at 8.5 GHz, Tech. Report 1903–5, ElectroScience Laboratory, Ohio State Univ., Columbus, Ohio.

Castleman, K.R., 1979, Digital Image Processing, Prentice–Hall, Englewood Cliffs, New Jersey.

Churchill, P.N. and M. Keech, 1985, Multifrequency analysis of SAR–580 imagery for woodland determinations in Thetford forest, England, European SAR–580 Campaign Investigators' Final Report, pp.533–550, JRC.

Churchill, P.N., A.I.D. Horne and R. Kessler, 1985, A review of radar analyses of woodland, Proc. EARSeL Workshop 'Microwave Remote Sensing Applied to Vegetation', Amsterdam, 10–12 Dec. 1984, ESA SP–227, pp.25–32.

Cihlar, J., M.C. Dobson, T. Schmugge, P. Hoogeboom, A.R.P. Janse, F. Baret, G. Guyot, T. Le Toan and P. Pampaloni, 1987, Procedures for the description of agricultural crops and soils in optical and microwave remote sensing studies, Int. J. Remote Sensing, Vol.8, pp.427–439.

Cimino, J.B., B. Holt and A.H. Richardson, 1988, The Shuttle Imaging Radar B (SIR–B) experiment report, JPL publ. 88–2, Pasadena.

Colwell, R.N., (editor), 1983, Manual of Remote Sensing, American Society of Photogrammetry, 2nd ed., Falls Church, Virginia.

Conners, R.W., and C.A. Harlow, 1980, A theoretical comparison of texture algorithms, IEEE Transactions on Pattern Analysis and Machine Intelligence, Vol.PAMI–2, pp.204–222.

Correa, A.C., 1980, Geological mapping in the Amazon jungle – a challenge to side–looking radar, in: Radar Geology: An Assessment, JPL publ. 80–61, Pasadena, pp.351–364.

Crandell, C.J., 1969, Radar Mapping in Panama, Photogram. Eng., Vol.35, pp.641–647.

Currie, N.C., E.E. Martin and F.B. Dyer, 1975, Radar foliage penetration measurements at millimeter wavelengths, Georgia Institute of Technology, Rep No. EES/GIT–A–1485–TR–4, AD–A023838, N77–10427.

Cutrona, L.J., W.E. Vivian, E.N. Leith and G.O. Hall, 1961, A high resolution radar combat surveillance system, IRE Trans., MIL–5, pp.127–131.

Cutrona, L.J. and G.O. Hall, 1962, A comparison of techniques for achieving fine azimuth resolution, IRE Trans., MIL–6, pp.119–133.

Daus, S.J., and D.T. Lauer, 1971, Testing the usefulness of side looking airborne radar imagery for evaluating forest vegetation resources, Report of research cont. CRINC 1775–9 for Center for Research, Inc., Univ. of Kansas, Forestry Remote Sensing Lab., Univ. of California, Berkeley, California.

Dellwig, L.F., 1980, A new look at Togo through the eyes of SLAR, in: Radar Geology: An Assessment, JPL publ. 80–61, Pasadena,
pp.351–364.

Elachi, C., 1986, Earth surface sensing in the '90s, Proc. ISPRS Symp. Progress in Imaging Sensors, 1–5 Sept. 1986, Stuttgart, ESA SP–252, pp.1–11.

Engheta, N. and C. Elachi, 1982, Radar scattering from a diffuse vegetation layer over a smooth surface, IEEE Transactions on Geoscience and Remote Sensing, Vol.GE–20, pp.212–216.

Eom, H.J. and A.K. Fung, 1984, A scatter model for vegetation up to Ku–band, Remote Sensing of Environment, Vol.15, pp.185–200.

ESA, 1987, Remote sensing for advanced land applications, Land Applications Working Group, ESA SP–1075, ESTEC, Noordwijk.

Ford, J.P., R.G. Bloom, M.L. Bryan, M.I. Daily, T.H. Dixon, C. Elachi and E.C. Xenos, 1980, Seasat views North America, the Caribbean, and Western Europe with Imaging Radar, JPL publ. 80–67, Pasadena.

Ford, J.P., J.B. Cimino and C. Elachi, 1983, Space Shuttle Columbia Views the World with Imaging Radar: the SIR–A Experiment, JPL publ. 82–95, Pasadena.

Francis, D.A., 1976, Possibilities and problems of radar–image interpretation for vegetation and forest types with particular reference to the humid tropic, Proc. IUFRO Cong., Remote Sensing in Forestry, Oslo, Norway, pp.79–86.

Froidevaux, C.M., 1980, Radar, an optimum remote sensing tool for detailed plate tectonic analysis and its application to hydrocarbon exploration (An example in Irian Jaya, Indonesia), in: Radar Geology: An Assessment, JPL publ. 80–61, Pasadena, pp.451–501.

Fung, A.K. and M.F. Chen, 1981, Scattering from a Rayleigh layer with an irregular interface, Radio Science, Vol.16, pp.1337–1347.

Fung, A.K. and M.F. Chen, 1986, Scattering models for coniferous and deciduous vegetation, Proc. 3rd Int. Coll. on Spectral Signatures of Objects in Remote Sensing, Les Arcs, France, 16–20 Dec. 1985, ESA SP–247, pp.151–156.

Fung, A.K., 1987 (personal communication).

Galloway, M.M., 1975, Texture analysis using gray level run lengths, Computer Graphics and Image Processing, Vol.4, pp.172–179.

Gerbrands, J.J. and E. Backer, 1983, Segmentation of multitemporal side–looking airborne radar (SLAR) images, Proc. SPIE, 19–22 Apr. 1983, Geneva, Vol.397, pp.173–179.

Gerbrands, J.J., 1985, Multiple–input segmentation algorithm for SLAR–imagery, Proc. EARSeL Workshop Microwave Remote Sensing Applied to Vegetation, Amsterdam, 10–12 Dec. 1984, ESA SP–277, pp.35–39.

Gradshteyn, I.S. and I.M. Ryzhik, 1980, Table of Integrals, Series and Products, Academic Press, New York.

Graham, L.C., 1974, Synthetic interferometer radar for topographic mapping, Proc. IEEE, Vol.62, pp.763–768.

Haralick, R.M., 1979, Statistical and structural approaches to texture, Proc. IEEE, Vol.67, pp.786–804.

Haralick, R.M., K. Shanmugan and I. Dinstein, 1973, Textural features for image classification, IEEE Transactions on Systems, Man and Cybernetics, Vol.SMC–3, pp.610–621.

Hardy, N.E., J.C. Coiner and W.E. Lockman, 1971, Vegetation mapping with SLAR: Yellowstone National Park, Conf. on Propagation Limitations in Remote Sensing, Advisory Group for Aerospace Research and Development, NATO, Neuilly–Sur–Seine, France. Pre–print No.90, pp.11–1 to 11–19.

Hardy, N.E., 1981, A photo interpretation approach to forest regrowth monitoring using SLAR – Grant County, Oregon, Int. J. Remote Sensing, Vol.2, pp.135–144.

Helfferich, O.W., 1987, (in Dutch) De radarverstrooiingscoefficient als functie van (bos)opstandsparameters, Report 1988–1, Vakgroep Landmeetkunde, Wageningen Agricultural University.

Hirosawa H, H. Ishida, T. Ochi and Y. Matsuzaka, 1986, Measurements of microwave backscatter from trees, Proc. 3rd Int. Coll. on Spectral Signatures of Objects in Remote Sensing, Les Arcs, 16–20 Dec. 1985, pp.451–454.

Hockeborn, H.A., 1971, Extraction of positional information from side–looking radar, Bildmessung und Luftbildwesen, Vol.39, pp.55–58.

Hoekman, D.H., L. Krul and E.P.W. Attema, 1982, A multilayer model for radar backscattering from vegetation canopies, Proc. Int. Geoscience and Remote Sensing Symp., Munich, 1–4 June 1982, Vol.2, TA–1, pp.4.1–4.7.

Hoekman, D.H., 1983, (in Dutch) Basisrapportage SLAR 1982/1983 bossen, Report Vakgroep Landmeetkunde en Boshuishoudkunde, Dec. 1983, Wageningen Agricultural University.

Hoekman, D.H., 1984, (in Dutch) Technische rapportage SLAR 1982/1983 bossen, Report Vakgroep Landmeetkunde, March 1984, Wageningen Agricultural University.

Hoekman, D.H., 1985a, Radar backscattering of forest stands, Int. J. Remote Sensing, Vol.6, pp.325–343.

Hoekman, D.H., 1985b, Texture analysis of SLAR images as an aid in automized classification of forested areas, Proc. EARSeL Workshop 'Microwave Remote Sensing Applied to Vegetation', Amsterdam 10–12 Dec. 1984, ESA SP–227, Jan. 1985, pp.99–109.

Hoekman, D.H., 1986a, Experiments on modelling radar backscatter of forest stands and research on classification, Proc. 3rd Int. Coll. on Spectral Signatures of Objects in Remote Sensing, Les Arcs, 16–20 Dec. 1985, ESA SP–247, pp.127–132.

Hoekman, D.H., 1986b, (in Dutch) Radaronderzoek aan bosbestanden, Fotonica, Vol.12, No.4, pp.38–54.

Hoekman, D.H., 1987a, Measurements of the backscatter and attenuation properties of forest stands at X–, C– and L–band, Remote Sensing of Environment, Vol.23, pp.397–416.

Hoekman, D.H., 1987b, Multiband scatterometer data analysis of forests, Int. J. Remote Sensing, Vol.8, pp.1695–1707.

Hoekman, D.H., 1988a, Extraction of small–scale spatial information from SLAR raw data of forests through an analysis of speckle, Proc. IGARSS'88, 13–16 Sept. 1988, Edinburgh, pp.1257–1261..

Hoekman, D.H., 1988b, A colour composite of different date images for tree species discrimination, in: M.G. Wooding (ed.), Imaging Radar Applications in Europe, ESA TM–01.

Hoekman, D.H., 1989, An analysis of speckle from forest stands with periodic structures, IEEE Transactions on Geoscience and Remote Sensing, Vol.27, pp.316–325.

Hoekman, D.H., 1990a, (in Dutch) Radarsignatuur en bosvegetatie (Ch.11), Inzet van digitale radargegevens op Nederlandse en tropische bossen (Ch.27), in: Remote Sensing, theorie en toepassingen van landobservatie, H.J. Buiten and J.P.G.W. Clevers (eds.), Pudoc Wageningen.

Hoekman, D.H., 1990b, A brief review of microwave forest signature measurements in The Netherlands and the perspective for a European research programme, Int. J. Remote Sensing (scheduled).

Hoekman, D.H., 1990c, Speckle ensemble statistics of logarithmically scaled data, IEEE Transactions on Geoscience and Remote Sensing (scheduled).

Hoel, P.G., 1962, Introduction to Mathematical Statistics, pp.166–168, John Wiley and Sons, New York.

Hoogeboom, P., 1982, On the design and operation of a SLAR system with digital recording, Proc. Int. Geoscience and Remote Sensing Symp., Munich, 1–4 June 1982, Vol.1, WP–9, pp.4.1–4.5.

Hoogeboom, P., P. Binnenkade and T.Veugen, 1984, An algorithm for radiometric and geometric correction of digital SLAR data, IEEE Transactions on Geoscience and Remote Sensing, Vol.GE–22, pp.570–576.

Hoogeboom, P., 1986, (in Dutch) De verwerking van het interne calibratiesignaal van de Nederlandse digitale SLAR, BCRS Report 86–01.

Hooijmans, P.W., 1984, Part I (in Dutch): Calibratie van een Sideways Looking Airborne Radar, Part II (in English): Scatterometer calibration measurements, Report 05–1–533–A109–84, Delft University of Technology.

Horowitz, S.L. and T. Pavlidis, 1976, Picture segmentation by a direct split–and–merge procedure, J. of the ACM, Vol.17, pp.368–388.

Huynen, J.R., 1970, Phenomenological Theory of Radar Targets, Ph.D. thesis, Tech. Univ., Delft, Drukkerij Bronder–Offset, Rotterdam.

Imhoff, M. et al., 1986, Forest canopy characterization and vegetation penetration assessment with space–borne radar, IEEE Transactions on Geoscience and Remote Sensing, Vol. GE–24, pp.535–542.

Karam, M.A. and A.K. Fung, 1983, Scattering from randomly oriented circular discs with application to vegetation, Radio Science, Vol.18, pp.557–567.

Keen, K.M., 1983, New technique for the evaluation of the scattering cross–sections of radar corner reflectors, Proc. IEE, Vol.130, Pt.H, No.5, August, pp.322–326.

Kessler, R., 1986, Radarbildinterpretation für forstliche Anwendung und Landnutzungsinventur, Entwicklungsstand und Entwicklungschancen, Ph.D. Thesis, Albert–Ludwigs–Universität, Freiburg.

Kirby, M.E., 1987, pers. comm.

Koopmans, B.N., 1974, Should stereo SLAR imagery be preferred to single strip imagery for thematic mapping?, ITC Journ. 1974–3, pp.424–444.

Krul, L., 1983, Principles of radar measurement, Proc. EARSeL Workshop 'Radar Calibration', Alpbach, 6–10 Dec. 1982, ESA SP–193, Feb. 1983, pp.11–20.

Krul, L., 1987, The microwave remote sensing program for agriculture and forestry in the Netherlands, Proc. ISPRS Comm. VII Symp. on Remote Sensing for Resources Development and Enviromental Management, Enschede, The Netherlands, 25–29 Aug. 1986, pp.1033–1040.

Leberl, F., 1974, Evaluation of SLAR image quality and geometry in PRORADAM, ITC Journ. 1974–4, pp.518–546.

Loor, G.P. de, 1968, Dielectric properties of heterogeneous mixtures containing water, J. Microwave Power, Vol.3. pp.67–73.

Loor, G.P. de, 1969, Possibilities and uses of radar and thermal infrared systems, Photogrammetria, Vol.24, pp.43–58.

Loor, G.P. de, P. Hoogeboom and E.P.W. Attema, 1982, The Dutch ROVE program, IEEE Transactions on Geoscience and Remote Sensing, Vol.GE–20, pp.3–7.

Lubbe, J.C.A. van der, 1983, Generalized texture measures for classification and image quality assesment of remote sensing images, Proc. 9th Int. Symp. on Machine Processing of Remotely Sensed Data, 21–23 June 1983, Purdue Univ., Lafayette.

MacDonald, H.C. and W.P. Waite, 1971, Soil moisture detection with imaging radars, Water Resources Research, Vol.7, pp.100–110.

Marshall, J.S. and W. Hitschfeld, 1953, Interpretation of the fluctuating echo from randomly distributed scatterers. Part I, Canadian Journal of Physics, Vol.31, pp.962–994.

Meyer, D.P. and H.A. Mayer, 1973, Radar Target Detection, Academic Press, New York.

Morain, S.A. and D.S. Simonett, 1966, Vegetation analysis with radar imagery, Proc. 4th ERIM Symp. on Remote Sensing of Environment, Univ. of Michigan, pp.605–622.

Morain, S.A. and D.S. Simonett, 1967, K–band radar in vegetation mapping, Photogram. Eng., Vol.33, pp.730–740.

Mougin, E., et al., 1987, Backscattering measurements at X–band on young coniferous trees, Proc. IGARSS'87, Ann Arbor, 18–21 May 1987, pp.287–292.

NASA, 1986, Earth observing system (Eos Volume I), Science and Mission Requirements Working Group Report, NASA Goddard Space Flight Center, Greenbelt.

NASA, 1987, From pattern to process: the strategy of the Earth observing system (Eos Volume II), Eos Science Steering Committee Report, NASA Goddard Space Flight Center, Greenbelt.

Nooren, G.J.L. and D.H. Hoekman, 1987, (in Dutch) Resultaten van de beproeving van het segmentatieprogramma op RESEDA, BCRS Report 87–01.

Norton, K.A., L.E. Vogler, W.V. Mansfield and P.J. Short, 1955, The probability distribution of the amplitude of a constant vector plus a Rayleigh distributed vector, Proc. IRE, Vol.43, pp.1354–1361.

Oldeman, R.A.A., 1983, Tropical rain forest, architecture, silvigenesis and diversity, Tropical Rain Forest: Ecology and Management, pp.139–150, Blackwell Scientific Publ., Oxford.

Oldeman, R.A.A., 1985, Forest architecture research for conservation decisions, IUCN Bulletin.

Paris, J.F., 1986a, Probing thick vegetation canopies with a field microwave scatterometer, IEEE Transactions on Geoscience and Remote Sensing, Vol. GE–24, pp.886–893.

Paris, J.F., 1986b, The effect of leaf size on the microwave backscattering by corn, Remote Sensing of Environment, Vol.19, pp.81–95.

Parry, D.E. and J.W. Trevett, 1979, Mapping Nigeria's vegetation from radar, The Geographical J., Vol.145, pp.265–281.

Pas, J.B. van der, 1988, pers. comm.

Pavlidis, T., 1977, Structural Pattern Recognition, Springer Verlag, Berlin.

Pellemans, A.H.J.M., 1986, (in Dutch) Onderzoek naar de bruikbaarheid van 'speckle–analysis' in beeldvormende radarsystemen, BCRS Report 86–05, Delft Univ. of Technology.

Peters, H.C., 1985, (in Dutch) Een analysemethode van speckle in beeldvormende radarsystemen, BCRS Report 85–01, Delft Univ. of Technology.

Pitts, D.E., G.D. Badhwar and E. Reyna, 1985, Estimation of biophysical properties of forest canopies through inversion of microwave scatterometer data, Digest 1985 Int. Geoscience and Remote Sensing Symp., Univ. Mass., Amherst, Vol.1, pp.313–320.

Pouwels, H., 1986, (in Dutch) De radiometrische bewerkingen op SLAR meetwaarden door het PARES programma, BCRS Report 86–04.

Pratt, W.K., 1978, Digital Image Processing, John Wiley and Sons, New York.

RADAM–reports, 1973–1978, Ministério das Minas e Energia Departamento Nacional da Produçao Mineral, Projeto Radambrasil – Programa de Integraçao Nacional, Rio de Janeiro.

Rice, S.O., 1945, Mathematical analysis of random noise, Bell System Tech. J., Vol.24, pp.46–156.

Richards J,A., G. Sun, and D.S. Simonett, 1987, L–band radar backscatter modeling of forest stands, IEEE Transactions on Geoscience and Remote Sensing, Vol. GE–25, pp.487–498.

Riom, J. and T. le Toan, 1980, Étude préliminaire d'images radar en bande L de fôrets de pins maritimes dans le sud–ouest de la France, Soc. Française de Photogrammétrie et de Télédétection, No.79–80, pp.21–29.

Roessel, J.W. van, and R.C. de Godoy, 1974, SLAR mosaics for Project RADAM, Photogram. Eng., Vol.40, pp.583–595.

Rosenfeld, A. and A.C. Kak, 1982, Digital Picture Processing, Academic Press, New York.

Sanden, J.J. van der, 1985, (in Dutch) Radarbackscatter als functie van struktuurparameters voor populier en japanse larix, Report 1985–1, Vakgroep Landmeetkunde, Wageningen Agricultural University.

Shahin, M.S., 1980, Traitement d'images radar en vue de l'étude de surfaces agricoles et forestières par télédétection, Ph.D. thesis, L'Université Paul Sabatier de Toulouse, France.

Shanmugan K.S., and R.M. Haralick, 1973, Computor classification of reservoir sandstones, IEEE Transactions on Geoscience and Electronics, Vol.GE–11, pp.171–177.

Shanmugan, K.S. et al., 1981, Textural features for radar image analysis, IEEE Transactions on Geoscience and Remote Sensing, Vol.GE–19, pp.153–156.

Sherwin, C.W., J.P. Ruina and R.D. Rawcliffe, 1962, Some early developments in synthetic aperture radar systems, IRE Trans., MIL–6, pp.111–116.

Shuchman, R.A., R.F. Rawson and B. Drake, 1975, A dual frequency and dual polarisation synthetic aperture radar system and experiments agriculture assessment, Proc. Nat. Aerospace and Electronics Conference, 10–12 June 1975, Dayton, Ohio, pp.133–140.

Shuchman, R.A., R. Inkster, R.T. Lowry and M. Wride, 1978, Multi–channel synthetic aperture radar sensing of forest tree species, Proc. 5th Canadian Symp. on Remote Sensing, Aug. 1978, Victoria B.C., pp.373–381.

Sicco Smit, G., 1974, Practical applications of radar images to tropical rain forest mapping in Columbia, Mitteilungen der Bundesforschungsanstalt für Forst– und Holzwirtschaft, Nr.99, pp.51–64.

Sicco Smit, G., 1975, Will the road to the green hell be paved with SLAR?, ITC Journ. 1975–2, pp.245–266.

Sicco Smit, G., 1976, Experiences with the use of SLAR in forest and land–use classification in the tropics, UN/FAO Training Sem. on Remote Sensing, Aug. 1976, Munich, pp.149–155.

Sicco Smit, G., 1978, SLAR for forest type–classification in a semi–decidious tropical region, ITC Journ. 1978–3, pp.385–401.

Sieber, A.J., 1985, Forest signatures in imaging and non–imaging microwave scatterometer data, ESA Journ., Vol.9, pp.431–448.

Silver, S. (ed.), 1949, Microwave Antenna Theory and Design, MIT Radiation Laboratory Series, Vol.12, McGraw–Hill, New York.

Skidmore, A.K., P.W. Woodgate and J.A. Richards, 1986, Classification of the Riverina forests of south–east Australia using co–registered Landsat MSS and SIR–B radar data, ISPRS Comm. VII Symp. on Remote Sensing for Resources Development and Environmental Management, 25–29 Aug. 1986, Enschede, pp.517–520.

Skolnik, M.I., 1980, Introduction to Radar Systems, 2nd ed., McGraw–Hill, New York.

Snoeij, P. and P.J.F. Swart, 1987, The DUT airborne scatterometer, Int. J. of Remote Sensing, Vol.8, pp.1709–1716.

Snoeij, P., 1985, (in Dutch) Interne SLAR calibratie, BCRS Report 85–03.

Tan, H.S., 1981, Microwave measurements and modelling of the permittivity of tropical vegetation samples, Applied Physics, Vol.25, pp.351–355.

Toan, T. le, and J. Riom, 1981, Relations entre des types de forêts de pins maritimes et la rétrodiffusion radar en bande L, Proc. ISP Int. Coll. on Spectral Signatures of objects in Remote Sensing, 8–11 Sept. 1981, Avignon, France, pp.455–467.

Toan, T. le, A. Lopes and M. Huet, 1984, On the relationships between radar backscattering coefficient and vegetation canopy characteristics, Proc. IGARSS'84, Strasbourg 27–30 Aug. 1984, Vol.1, pp.155–160.

Toan, T. le, A. Lopes and A. Malavaud, 1984, Relations entre le rétrodiffusion radar et les paramètres d'un couvert végétal, 2nd Int. Coll. on Spectral Signatures of Objects in Remote Sensing, Bordeaux, 12–16 Sept. 1983, Edited INRA Publ. 1984 (Les Colloques de l'INRA, No.23), pp.601–615.

Tsang L., M. Kubacsi and J. Kong, 1981, Radiative transfer theory for active remote sensing of a layer of small ellipsoidal scatterers, Radio Science, Vol.16, pp.321–329.

Twomey, S., H. Jacobowitz and H.B. Howell, 1966, Matrix method for multiple scattering problems, J. Atmos. Science, Vol.23, pp.289–296.

Ulaby, F.T., 1982, Review of approaches to the investigation of the scattering properties of material media, Proc. Int. Geoscience and Remote Sensing Symp., Munich 1–4 June 1982, Vol.2, TA–1, pp.1.1–1.5.

Ulaby, F.T., R.K. Moore and A.K. Fung, 1981 Microwave Remote Sensing, Vol.I, Addison–Wesley, Reading, Mass.

Ulaby, F.T., R.K. Moore and A.K. Fung, 1982, Microwave Remote Sensing, Vol.II, Addison–Wesley, Reading, Mass.

Ulaby, F.T., C.T. Allen and G. Eger III, 1984, Relating the microwave backscattering coefficient to leaf area index, Remote Sensing of Environment, Vol.14, pp.113–133.

Ulaby, F.T. and R.P. Jedlicka, 1984, Microwave dielectric properties of plant materials, IEEE Transactions on Geoscience and Remote Sensing, Vol.GE–22, pp.406–415.

Ulaby, F.T., R.K. Moore, A.K. Fung, 1986, Microwave Remote Sensing, Vol.III, Artech House, Washington.

Viksne, A., T.C. Liston and C.D. Sapp, 1970, SLR reconnaissance of Panama, Photogram. Eng., Vol.36, pp.253–259.

Visser, A.H., 1986, (in Dutch) De radarverstrooiingscoefficient als functie van opstandsparameters en de inkijkhoek, Report 1986–7, Vakgroep Landmeetkunde, Wageningen Agricultural University.

Wedler, E., S. Pala and A. Jano, 1980, SAR image response over a conifer regeneration site, Proc. 6th Canadian Symp. on Remote Sensing, 21–23 May 1980, Halifax, Nova Scotia, pp.179–186.

Weissman, D.E. and J.W. Johnson, 1979, Rough surface wavelength measurement through self mixing of Doppler microwave backscatter, IEEE Transactions on Antennas and propagation, Vol.AP–27, pp.730–737.

Weszka, J.S., C.R. Dyer and A. Rosenfeld, 1976, A comparitive study of texture measures for terrain classification, IEEE Transactions on Systems, Man and Cybernetics, Vol.SMC–6, pp.269–285.

(World Soil Map), FAO–Unesco, 1974, Soil Map of the World (1:5,000,000), Vol.I, Legend, Unesco, Paris.

Wu, S.T., 1987a, Multipolarization SAR data for surface feature delineation and forest vegetation characterization, IEEE Transactions on Geoscience and Remote Sensing, Vol. GE–25, pp.67–76.

Wu, S.T., 1987b, Potential application of multipolarization SAR for the pine–plantation biomass estimation,IEEE Transactions on Geoscience and Remote Sensing, Vol. GE–25, pp.403–409.

Zijl, J.J. van, H.A. Zebker and C. Elachi, 1987, Imaging radar polarization signatures: Theory and observation, Radio Science, Vol.22, pp.529–543.

Zoughi, R., L.K. Wu and R.K. Moore, 1986, Identification of major backscattering sources in trees and shrubs at 10 GHz, Remote Sensing of Environment, Vol.19, pp.269–290.

APPENDIX I

I. Speckle ensemble statistics of logarithmically scaled data

I.1 Introduction

If the "Rayleigh fading" concept applies to an electro–magnetic wave – target interaction, the amplitude (U) of the electric field, as detected for example by radar, is known to have a *Rayleigh* distribution.

$$p(U) = U/\sigma^2 \cdot \exp(-U^2/2\sigma^2), \tag{I.1}$$

σ^2 is the variance and $\bar{U}=\sigma\sqrt{\pi/2}$ is the mean.

Often the power instead of the field strength of the scattered signal is detected (as, for example, with the Dutch X–band SLAR). The distribution of the amplitude (I) of the power signal follows from the Rayleigh distribution and is known to have an *exponential* distribution.

$$p(I) = 1/\bar{I} \cdot \exp(-I/\bar{I}), \tag{I.2}$$

with $\bar{I}$ is the mean *and* the variance.

Both the Rayleigh and exponential distributions are single parameter distributions. If an object is known to behave as a "Rayleigh fading target", all information is contained in the mean value of this distribution. (Under certain circumstances, another type of information can also be extracted; see section 3.1.) To reduce the effects of the large stochastic fluctations of the received signal (called speckle), averaging is usually applied. The distribution of the averaged signal follows from the distribution of the "raw" signal. Averaging over k independent power samples is known to result in the *gamma* distribution for the amplitude of the averaged power I_k (Marshall and Hitschfeld, 1953, or Krul, 1983);

$$p(I_k) = \frac{k^k \cdot I_k^{k-1} \cdot \exp(-kI_k/\bar{I})}{(k-1)! \cdot \bar{I}^k}, \tag{I.3}$$

with $\bar{I}$ is the mean of the non–averaged or "raw" signal (eq. I.2).

From the distribution of the averaged (power) signal, a standard deviation and a mean can be calculated. The standard deviation can be considered as a simple measure for the speckle level and, for a pure Rayleigh fading mechanism, is directly related to k. From equation I.3 it follows simply (as will be shown hereafter) that the expectation of the mean of the averaged power signal is equal to the mean of the "raw" power signal and that the

expectation of the standard deviation of the averaged power signal is $\sqrt{k}$ times smaller than the standard deviation of the "raw" power signal.

In remote sensing, the radar data are expressed as γ or σ^0 values. The parameters γ and σ^0 are linearly related to the (averaged) power signal and therefore the same distributions apply. These parameters, however, are usually presented at the logarithmic dB scale (as is the case, for example, for Dutch X–band SLAR imagery). When the Rayleigh fading mechanism applies, the impact of this non–linear transformation of the data on the estimation of mean and standard deviation can be derived mathematically.

I.2 The linear scale

For comparison, the linear mean $\bar{I}_k$ of the linearly averaged power samples and the variance κ_k^2 at a linear scale of the linearly averaged power samples are derived first. The linear mean $\bar{I}_k$ follows from the expression;

$$\bar{I}_k = \int_0^\infty I_k \cdot p(I_k)\, dI_k. \tag{I.4}$$

Using the substitution $x=I_k/\bar{I}$ it follows;

$$\bar{I}_k = \frac{k^k}{(k-1)!} \cdot \bar{I} \int_0^\infty x^k \cdot e^{-kx}\, dx. \tag{I.5}$$

And using the standard integral

$$\int_0^\infty c^{k+1} \cdot x^k \cdot e^{-cx}\, dx = \Gamma(k+1) = k! \tag{I.6}$$

it follows;

$$\bar{I}_k = \bar{I}. \tag{I.7}$$

The variance κ_k^2 at a linear scale follows from the expression;

$$\kappa_k^2 = \int_0^\infty (I_k - \bar{I}_k)^2 \cdot p(I_k)\, dI_k. \tag{I.8}$$

Using the result $\bar{I}_k=\bar{I}$ (eq. I.7) and the substitution $x=I_k/\bar{I}$ it follows;

$$\kappa_k^2 = -2\bar{I}^2 + \frac{k^k}{(k-1)!} \cdot \bar{I}^2 \cdot \left[\int_0^\infty x^{k-1} \cdot e^{-kx}\, dx + \int_0^\infty x^{k+1} \cdot e^{-kx}\, dx \right]. \tag{I.9}$$

Using the standard integrals

$$\int_0^\infty c^k \cdot x^{k-1} \cdot e^{-cx}\, dx = \Gamma(k) \text{ and} \tag{I.10}$$

$$\int_0^\infty c^{k+2} \cdot x^{k+1} \cdot e^{-cx}\, dx = \Gamma(k+2) \text{ it follows;} \tag{I.11}$$

$$\kappa_k^2 = \bar{I}^2/k. \tag{I.12}$$

These simple results (eqs. I.7 and I.12) are well–known. Matters get more complicated when data are presented at the logarithmic dB scale. The corresponding (analytic) expressions cannot be found in literature and are derived hereafter.

I.3 The logarithmic scale

The mean at the logarithmic scale of the linearly averaged power samples will be denoted as $\bar{J}_k$. The variance at the logarithmic scale of the linearly averaged power samples will be denoted as λ_k^2. Since, per definition,

$$J_k = 10^{10}\log(I_k) \quad [\text{dB}], \tag{I.13}$$

J_k can be written as

$$J_k = A \ln(I_k), \text{ with } A = 10/\ln(10). \tag{I.14}$$

Thus

$$I_k = e^{J_k/A} \tag{I.15}$$

and

$$dJ_k = A \frac{dI_k}{I_k}. \tag{I.16}$$

The probability density function $p(J_k)$ follows from $p(I_k)$ as

$$p(J_k) = p(I_k) \frac{dI_k}{dJ_k}, \text{ therefore} \tag{I.17}$$

$$p(J_k) = \frac{1}{A}\frac{k^k}{(k-1)!}\frac{I_k^k}{\bar{I}^k}\cdot e^{-kI_k/\bar{I}}. \tag{I.18}$$

The logarithmic mean $\bar{J}_k$ follows from the expression:

$$\bar{J}_k = \int_{-\infty}^{\infty} J_k \cdot p(J_k)\, dJ_k. \tag{I.19}$$

After a straightforward development and using the substitution $x=I_k/\bar{I}$, and thus $\ln(I_k) = \ln(x) + \ln(\bar{I})$, it follows;

$$\bar{J}_k = 10^{10}\log(\bar{I}) + A\frac{k^k}{(k-1)!}\cdot\int_0^{\infty} x^{k-1}\cdot e^{-kx}\cdot\ln(x)\, dx \tag{I.20}$$

This result will be elaborated later. The variance λ_k^2 at the logarithmic scale follows from the expression;

$$\lambda_k^2 = \int_{-\infty}^{\infty} (J_k-\bar{J}_k)^2\cdot p(J_k)\, dJ_k \tag{I.21}$$

and can be developed into the expression;

$$\lambda_k^2 = A^2\cdot\frac{k^k}{(k-1)!}\cdot\int_0^{\infty} x^{k-1}\cdot e^{-kx}\cdot(\ln(x))^2\, dx - A^2\cdot\left[\frac{k^k}{(k-1)!}\cdot\int_0^{\infty} x^{k-1}\cdot e^{-kx}\cdot\ln(x)\, dx\right]^2. \tag{I.22}$$

Using the following results from Gradsteyn and Ryzhik (equations 4.352 and 4.358, respectively);

$$\int_0^{\infty} x^{\nu-1}\cdot e^{-\mu x}\cdot\ln(x)\, dx = \frac{\Gamma(\nu)}{\mu^{\nu}}\cdot[\Psi(\nu)-\ln(\mu)] \tag{I.23}$$

and

$$\int_0^{\infty} x^{\nu-1}\cdot e^{-\mu x}\cdot(\ln(x))^2\, dx = \frac{\Gamma(\nu)}{\mu^{\nu}}\cdot\left\{[\Psi(\nu)-\ln(\mu)]^2 + \zeta(2,\nu)\right\} \tag{I.24}$$

and by substituting $\mu=\nu=k$, the results for $\bar{J}_k$ and λ_k^2 follow as;

$$\bar{J}_k = 10^{10}\log(\bar{I}) + A\cdot[\Psi(k)-\ln(k)] \tag{I.25}$$

and

$$\lambda_k^2 = A^2 \cdot \zeta(2,k) \tag{I.26}$$

$\Psi(\nu)$ is known as the psi function of Euler. A table of the psi function for integer values can be found in the handbook of Abramowitz (table 6.3).

$\zeta(z,\nu)$ is known as the Riemann zeta function. Tables for $\zeta(2,\nu)$ are not included in the handbook of Abramowitz nor in the handbook of Gradsteyn, but the factor $\zeta(2,k)$, with k as an integer value, can be computed simply according to the following rule:

$$\zeta(2,1) = \pi^2/6 \text{ and } \zeta(2,k) = \pi^2/6 - \sum_{n=1}^{k-1} \frac{1}{n^2} \tag{I.27}$$

Before contemplating the meaning of these results, a table with some numeric examples for mean ($\bar{I}_k$ and $\bar{J}_k$) and standard deviation (κ_k and λ_k) are given (table I.1).

Table I.1. Some numerical examples for mean values ($\bar{I}_k$ and $\bar{J}_k$) and standard deviations (κ_k and λ_k) of Rayleigh fading objects.

k	$\bar{I}_k$	κ_k	$\bar{J}_k$ [dB]	λ_k [dB]
1	$\bar{I}$	$\bar{I}$	$10^{10}\log\bar{I} - 2.507$	5.570
2	$\bar{I}$	$\bar{I}/\sqrt{2}$	$10^{10}\log\bar{I} - 1.174$	3.488
4	$\bar{I}$	$\bar{I}/\sqrt{4}$	$10^{10}\log\bar{I} - 0.565$	2.314
10	$\bar{I}$	$\bar{I}/\sqrt{10}$	$10^{10}\log\bar{I} - 0.221$	1.408
20	$\bar{I}$	$\bar{I}/\sqrt{20}$	$10^{10}\log\bar{I} - 0.109$	0.983
30	$\bar{I}$	$\bar{I}/\sqrt{30}$	$10^{10}\log\bar{I} - 0.073$	0.800
60	$\bar{I}$	$\bar{I}/\sqrt{60}$	$10^{10}\log\bar{I} - 0.036$	0.563
100	$\bar{I}$	$\bar{I}/\sqrt{100}$	$10^{10}\log\bar{I} - 0.022$	0.435

I.4 Conclusions

The following conclusions can be drawn.

Averaging at a logarithmic scale of radar data, which themselves result from the linear averaging over k independent samples or "looks", introduces an offset dependent on the number k only.

The offset does not depend on the mean level of the signal and therefore is the same for all Rayleigh fading objects.

This result does not apply to other types of objects. For example, a corner reflector or a Luneberger lens returns signals with a constant amplitude and averaging at a logarithmic scale introduces no offset.

Care should be taken with data presentation at a logarithmic scale. For example, when 16 independent samples or looks are presented by four pixels of four looks instead of one pixel of 16 looks, a different offset will be introduced if data (pixel values) are averaged (like calculation of a field–averaged mean) at the logarithmic scale.

If the number k is not small (as occurs for the Dutch X–band SLAR with k=30 and Dutscat with k=±25), the offset is small (in the order of 0.1 dB) and may be neglected.

The standard deviation (or speckle level) for Rayleigh fading objects is a constant at a logarithmic scale and depends on the number k only.

APPENDIX II

II. Theoretical description of compound target fading

II.1 The summation of Doppler shifted components

Suppose the sensor is in uniform motion at a velocity v_0 along the s–axis (figure II.1). Two point scatterers, denoted k and l, are located at positions (x_k, y_k, z_k) and (x_l, y_l, z_l), respectively. Their mutual spacing in x–direction is denoted as $\Delta x = x_l - x_k$ and in y– and z–directions as $\Delta y = y_l - y_k$ and $\Delta z = z_l - z_k$, respectively. Then the phase difference of the two backscattered signals is a function of time, dependent on the difference in path lengths as a function of time, and can be written as

$$\phi(t) = 2k \cdot (r_k(t) - r_l(t)) + \phi_1, \qquad \text{(II.1)}$$

with ϕ_1 a constant

and $k = 2\pi/\lambda$, the wave number.

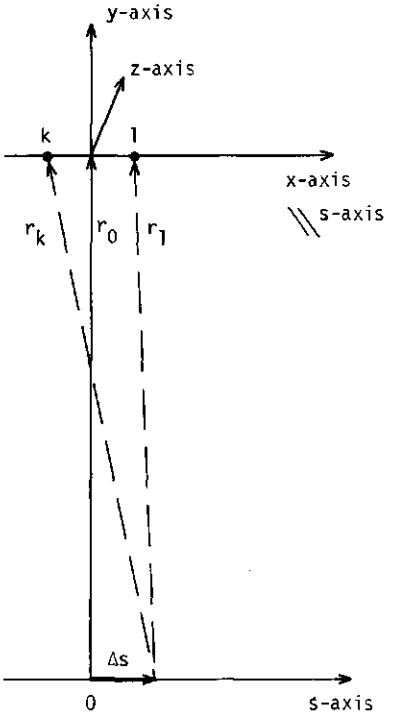

Figure II.1. Measurement geometry. The sensor moves along the s–axis and observes scatterers (l and k) in the x,y,z coordinate system.

When, for the moment, Δy and Δz are assumed to be zero and Δs is time dependent because of the sensor's motion, then

$$r_1^2(t) = r_0^2 + (\Delta s - x_1)^2 \tag{II.2}$$

and, when $\Delta s - x_k$ and $\Delta s - x_1$ are small (necessarily Δx is small too), the path length difference can be approximated by

$$r_k(t) - r_1(t) \simeq \frac{\Delta x \cdot \Delta s}{r_0} + \frac{\frac{1}{2}(x_k^2 - x_1^2)}{r_0}. \tag{II.3}$$

It can be shown that this approximation is very accurate for any pair of scatterers within the beam width of the SLAR antenna. Then

$$\phi(t) \simeq \frac{4\pi}{\lambda} \cdot \frac{\Delta x \cdot \Delta s}{r_0} + \phi_1 + \phi_2 \tag{II.4}$$

with ϕ_2 a constant. The frequency of the fading follows as

$$f = \frac{1}{2\pi} \cdot \frac{d}{dt}(\phi(t)) = \frac{2 \cdot \Delta x \cdot v_0}{\lambda \cdot r_0}. \tag{I.5}$$

It can be shown that in the case of Δy and Δz not being zero, but very small, however, equations II.4 and II.5 still hold. In practice this is the case for any pair of scatterers within the same resolution cell of this radar system; the approximation is valid within a few per thousand. Further, it is assumed that the spacing between any pair of scatterers is large enough to avoid mutual coupling. It can be demonstrated that the frequency of the fading f equals the difference in Doppler shifts for the two scatterers. The Doppler shift for scatterer l can be written as

$$f_{D_1}(t) = 2/\lambda \cdot \frac{d}{dt}(r_1(t)) \tag{II.6a}$$

and the Doppler shift for scatterer k can be written as

$$f_{D_k}(t) = 2/\lambda \cdot \frac{d}{dt}(r_k(t)). \tag{II.6b}$$

The differential Doppler shift thus follows as

$$f_{D_1}(t) - f_{D_k}(t) = 2/\lambda \cdot \frac{d}{dt}(r_k(t) - r_1(t)) = \frac{2}{\lambda} \cdot \frac{\Delta x \cdot v_0}{r_0} \tag{II.7}$$

which is the same frequency as given by equation II.5. Thus it follows that, though the

Doppler shifts vary with time, the differential Doppler shift, which is equivalent to the frequency introduced in equation II.5, remains approximately constant for the time the pair of scatterers can be observed by the radar and is proportional to Δx.

Suppose one single scatterer k, having a radar cross section σ_k, is present. The reflected complex electric field strength detected by the receiver is denoted as

$$E = E_k \cdot \exp(j2kr_k(t) + j\phi_k) \tag{II.8}$$

and the received power of this isolated scatterer is denoted as

$$p_k = \eta_0^{-1} \cdot E_k \cdot E_k^* = c \cdot \sigma_k \tag{II.9}$$

with η_0 as the impedance of free space and with c a constant following from the radar equation. Now suppose a second scatterer, scatterer l, with a radar cross section σ_l, is added. The combined complex electric field strength is written as

$$E_t = E_k \cdot \exp(j2kr_k(t) + j\phi_k) + E_l \cdot \exp(j2kr_l(t) + j\phi_l) \tag{II.10}$$

and thus the received power

$$\begin{aligned} P(t) &= \eta_0^{-1} \cdot E_t \cdot E_t^* \\ &= \eta_0^{-1}\Big[|E_k|^2 + |E_l|^2 + 2|E_k| \cdot |E_l| \cdot \cos(2\pi f_{kl} \cdot t + \phi_{kl})\Big] \end{aligned} \tag{II.11}$$

$$\text{with } f_{kl} = f_{D_l}(t) - f_{D_k}(t) = \frac{2v_0 \cdot \Delta x}{\lambda r_0},$$

$$\Delta x = |x_k - x_l|$$

$$\text{and } \phi_{kl} = \phi_k - \phi_l,$$

becomes a constant plus a term fluctuating with the frequency f_{kl} corresponding to the differential distance Δx in flight direction according to equation II.5. In general, for a collection of n scatterers, the expression for the total received power follows as

$$P_T(t) = \eta_0^{-1} \sum_{i=1}^{n} |E_i|^2 + \eta_0^{-1} \sum_{\substack{i=1 \\ i \neq j}}^{n} \sum_{j=1}^{n} |E_i| |E_j| \cdot \cos(2\pi f_{ij} t + \phi_{ij}) \tag{II.12a}$$

which again is a constant plus a fluctuating term, but now the fluctuating term contains contributions from every possible pair of scatterers at their corresponding fading frequencies f_{ij}. The constant simply represents the mean of the detected power and will be denoted as $P_{<p>}(t)$. The fluctuating term will be denoted as $P_{\text{speckle}}(t)$. Thus, in a concise

notation, equation II.12a can be written as

$$P_T(t) = P_{<p>}(t) + P_{\text{speckle}}(t). \tag{II.12b}$$

All scatterer pairs (i,j) with the same differential distance $\Delta x_a = |x_i - x_j|$ contribute to the fluctuating part of the compound fading signal with a signal at the same frequency $f_a = \Delta x_a \cdot 2v_0/\lambda r_0$ (eq. II.5) but with a different phase $\phi_{ij} = \phi_i - \phi_j$. Since the range of distances between scatterers is several orders of magnitude larger than the wavelength λ, it can be assumed that, in case of scatterers in a vegetation canopy, the phase differences ϕ_{ij} are uniformly distributed at the interval $[0,2\pi]$. The various contributions at the same fading frequency can therefore be assumed to add incoherently. Thus the detected time signal at a particular frequency f_a can be written as

$$P_{\text{speckle},f_a}(t) = \eta_0^{-1} \sum_{\substack{i=1 \\ |x_i - x_j| = \Delta x_a}}^{n} \sum_{j=1}^{n} |E_i| \cdot |E_j| \cdot \cos(2\pi f_a t + \phi_{ij}), \tag{II.13a}$$

with the summation condition meaning (incoherent) summation over all scatterer pairs (i,j) for which the condition $|x_i - x_j| = \Delta x_a$, corresponding to the frequency f_a, applies. Because of the assumed incoherency, the expectation of this time signal component can be written as

$$\left\langle P_{\text{speckle},f_a}(t) \right\rangle = \eta_0^{-1} \left[\sum_{\substack{i=1 \\ |x_i - x_j| = \Delta x_a}}^{n} \sum_{j=1}^{n} |E_i|^2 \cdot |E_j|^2 \right]^{\frac{1}{2}} \cdot \cos(2\pi f_a t + \phi_a). \tag{II.13b}$$

The power density spectrum of the expectation of $P_{\text{speckle}}(t)$, denoted $S_{<\text{speckle}>}(f)$, is taken proportional to the square of the modulus of the Fourier transform of $\langle P_{\text{speckle}}(t) \rangle$. Therefore the component at frequency f_a (eq. II.13b) follows as

$$S_{<\text{speckle}>}(f_a) = \delta(f - f_a) \cdot \eta_0^{-2} \sum_{\substack{i=1 \\ |x_i - x_j| = \Delta x_a}}^{n} \sum_{j=1}^{n} |E_i|^2 \cdot |E_j|^2. \tag{I.14a}$$

Through equation II.9, detected electric field strength, detected power and radar cross section are related. If the various scatterers i with radar cross sections σ_i are represented as a discrete function of their position on the x–axis, i.e. $\sigma_i(x) = \sigma_i \cdot \delta(x - x_i)$, then equation II.14a can be written as

$$S_{<\text{speckle}>}(f_a) = \sum_{\substack{i=1 \\ |x_i - x_j| = \Delta x_a}}^{n} \sum_{j=1}^{n} P_i \cdot P_j = c^2 \cdot \sum_{\substack{i=1 \\ |x_i - x_j| = \Delta x_a}}^{n} \sum_{j=1}^{n} \sigma_i(x_i) \cdot \sigma_j(x_j). \tag{II.14b}$$

The power density spectrum for the (total) fluctuating term of the compound fading signal follows as

$$S_{<\text{speckle}>}(f) = \sum_{\substack{i=1 \\ i \neq j}}^{n} \sum_{j=1}^{n} P_i \cdot P_j = c^2 \sum_{\substack{i=1 \\ i \neq j}}^{n} \sum_{j=1}^{n} \sigma_i(x_i) \cdot \sigma_j(x_j) \tag{I.14c}$$

$$\text{with } f = |x_i - x_j| \cdot 2v_0/\lambda r_0.$$

Equation II.14c can be recognized as the autocorrelation function of $\sigma_i(x)$.

The power density spectrum of the constant term of the compound fading signal follows as

$$S_{<p>}(f) = \delta(f) \cdot \left[\sum_{i=1}^{n} |E_i|^2 \right]^2 = \delta(f) \cdot c^2 \left[\sum_{i=1}^{n} \sigma_i \right]^2 \tag{II.15}$$

and, since both parts are independent, the total power density spectrum follows as

$$S_T(f) = S_{<p>}(f) + S_{<\text{speckle}>}(f) \quad [\text{W}^2/\text{Hz}]. \tag{II.16}$$

Further, it should be recognized that the square of the mean of the fading signal is given by equation II.15 and the variance of the fading signal follows from equation II.14c as the sum of all components of $S_{\text{speckle}}(f)$:

$$c^2 \cdot \sum_{\substack{i=1 \\ i \neq j}}^{n} \sum_{j=1}^{n} \sigma_i \sigma_j. \tag{II.17}$$

The ratio R of standard deviation and mean of the compound fading signal thus can be formulated as

$$R = \frac{\left[\sum_{\substack{i=1 \\ i \neq j}}^{n} \sum_{j=1}^{n} \sigma_i \sigma_j \right]^{\frac{1}{2}}}{\sum_{i=1}^{n} \sigma_i}. \tag{II.18}$$

The ratio R approaches unity when the number of (independent) scatterers n is large and

the averaging of samples is performed over a sufficient time period. This result is in agreement with the statistics of a Rayleigh fading signal: the standard deviation of the received power is equal to the mean of the received power (Ulaby et al., 1982).

II.2 The influence of the antenna on the measurement

The compound fading signal is influenced by the radiation pattern of the antenna and the limited time of observation of individual scatterers. These effects have an impact on the description of the fading signal as derived in the previous subsection and will be discussed next in a heuristic way. It was experimentally established (Hooijmans, 1984) that the Gaussian shape is a very good approximation for the radiation pattern in azimuth direction and that the (two–way) beam width $\varphi_B = 0.66\lambda/L_x$ (in radians). A normalized (two–way) antenna pattern in azimuth (or x–) direction is introduced now and denoted as

$$g(x) = \exp(-bx^2),$$
$$\text{with } b = \frac{2\ln 2}{0.66^2}\cdot\frac{{L_x}^2}{\lambda^2 {r_0}^2} \simeq \pi\cdot\frac{{L_x}^2}{\lambda^2 {r_0}^2}. \tag{II.19}$$

Equation II.12a shows that the compound signal is written as the sum of products of the received electrical field strengths from scatterer pairs $|E_i|\cdot|E_j|$. These products, in the description of an actual measurement, have to be multiplied by the values of the normalized antenna pattern at their corresponding positions x_i and x_j, which is a factor $F = g(x_i)\cdot g(x_j)$. It should be remarked that similar factors exist for the y– and z–directions. These factors are omitted here, however, since they are not relevant for this analysis, as can be shown, and disappear in the final equations (eqs. II.27 and II.28).
Suppose one pair of scatterers is present at the same position x in x–direction, but with different positions in y– and z–directions (figure II.2) and a second pair of scatterers, with a differential distance $\Delta x = a$ in x–direction, is present at positions $x+\frac{1}{2}a$ and $x-\frac{1}{2}a$. Then the factor F can be written as a function of Δx and x as $F(\Delta x,x)$. For the first pair as

$$F(\Delta x,x) = F(0,x) = g(x)\cdot g(x) = \exp(-2bx^2) \tag{II.20}$$

and for the second pair as

$$\begin{aligned} F(\Delta x,x) = F(a,x) \quad &= g(x+\tfrac{1}{2}a)\cdot g(x-\tfrac{1}{2}a) \\ &= \exp(-\tfrac{1}{2}ba^2)\cdot\exp(-2bx^2) \\ &= F_a\cdot F_t. \end{aligned} \tag{II.21}$$

It thus becomes clear that, for a Gaussian–shaped radiation pattern, the factor $F(\Delta x,x)$ can

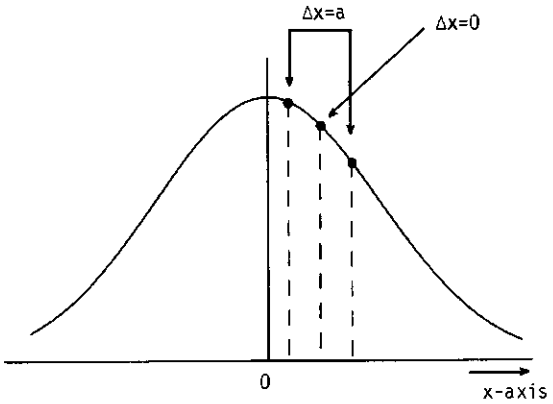

Figure II.2. The influence of the antenna pattern on the fading component of two scatterers at a mutual distance $\Delta x=a$ in x–direction (eq. II.21) and on two scatterers at a the same position in x–direction (eq. II.20).

be written as the product of a factor F_a related to the differential distance Δx and a factor F_t related to the center position x. The product $F_a.F_t$ physically represents the product of a (Gaussian) spectral weighting function and a (Gaussian) time window. Since Δx is related to the fading frequency f(eq. II.5) as $\Delta x = f\cdot\lambda r_0/2v_0$ the factor F_a, using equation II.19, can be written as

$$F_a(f) = \exp(-\tfrac{1}{4}b\cdot\Delta x^2) = \exp\left[\frac{-\pi}{8}\frac{L_x^2}{v_0^2}f^2\right]. \tag{II.22}$$

And since x is related to the velocity v_0 of the sensor as $x = v_0.t$, the factor F_t, again using equation II.19, can be written as

$$F_t(t) = \exp(-2bv_0^2t^2). \tag{II.23}$$

Thus it follows that in the time domain each component $|E_i|\cdot|E_j|$ has to be multiplied by a factor $F(\Delta x,x)$, which, in this case (Gaussian pattern), can be written as the product $F_a(f).F_t(t)$. In the frequency domain, this factor follows as the convolution of $F_a(f)$ and the Fourier transform of $F_t(t)$. The Fourier transform

$$F_t(t) = \exp(-2bv_0^2t^2) \;\Leftrightarrow\; H(f) = c_2\cdot\exp\left[\frac{-\pi^2f^2}{2bv_0^2}\right], \tag{II.24}$$

$$\text{with } c_2 = (\pi/2bv_0^2)^{\frac{1}{2}}.$$

In the power spectrum each component $|E_i|^2 \cdot |E_j|^2$ or $\sigma_i \cdot \sigma_j$ is multiplied by a factor

$$F_a^2(f) = \exp\left[\frac{-\pi}{4}\frac{L_x^2}{v_0^2} f^2\right] \tag{II.25}$$

and convolved with the square of the Fourier transform of $F_t(t)$, namely a factor

$$H^2(f) = c_2^2 \cdot \exp\left[\frac{-\pi^2 f^2}{b v_0^2}\right] = c_2^2 \cdot \exp\left[-\pi \frac{\lambda^2 r_0^2}{v_0^2 L_x^2} f^2\right]. \tag{II.26}$$

Introducing $\tau_A = \frac{1}{2} L_x / v_0$ and $\tau_B = \lambda r_0/(v_0 L_x)$, and thus $c_2^2 = \frac{1}{2}\tau_B^2$, and using the symbol "*" to denote the operation of convolution, equations II.14c and II.15 can be rewritten for the actual measurement as

$$S_{<\text{speckle}>}(f) = \tfrac{1}{2} c^2 \cdot \tau_B^2 \exp(-\pi \tau_B^2 \cdot f^2) * \left\{ \sum_{\substack{i=1 \\ i \neq j}}^{n} \sum_{j=1}^{n} \exp(-\pi \tau_A^2 \cdot f^2) \cdot \sigma_i(x_i) \cdot \sigma_j(x_j) \right\},$$
$$\text{with } |x_i - x_j| = \frac{\lambda r_0}{2 v_0} \cdot f \tag{II.27a}$$

and

$$S_{<p>}(f) = \tfrac{1}{2} c^2 \cdot \tau_B^2 \exp(-\pi \tau_B^2 \cdot f^2) * \delta(f) \cdot \left\{ \sum_{i=1}^{n} \sigma_i \right\}^2 \tag{II.28}$$

Performing a term–by–term convolution, equation II.27a can be written as

$$S_{<\text{speckle}>}(f) = \tfrac{1}{2} c^2 \cdot \tau_B \cdot \sum_{\substack{i=1 \\ i \neq j}}^{n} \sum_{j=1}^{n} \frac{\exp(-\pi \tau_A^2 \cdot f^2/(1+a^2))}{(1+a^2)^{\frac{1}{2}}} \cdot \sigma_i(x_i) \cdot \sigma_j(x_j),$$
$$\text{where } a = \tau_A/\tau_B = L_x^2/2\lambda r_0. \tag{II.27b}$$

For far field measurements $a \simeq 0$ and the expression may be simplified to obtain

$$S_{<\text{speckle}>}(f) = \tfrac{1}{2} c^2 \cdot \tau_B \cdot \sum_{\substack{i=1 \\ i \neq j}}^{n} \sum_{j=1}^{n} \exp(-\pi \tau_A^2 \cdot f^2) \cdot \sigma_i(x_i) \cdot \sigma_j(x_j). \tag{II.27c}$$

The spectral weight factor F_a acts like a low–pass filter. It follows from equation II.25 that components in the power spectrum are attenuated to a factor $1/e$ at the frequency

$$f_c = \frac{2v_0}{L_x\sqrt{\pi}} = \frac{1}{\tau_A\sqrt{\pi}} \quad [\text{Hz}] \tag{II.29}$$

which is 52 Hz for the system used at a v_0 of 180 kts.

The limited observation time results in an uncertainty in the determination of the fading frequency. The spectral width B of this uncertainty follows from equation II.26 as

$$B = \frac{v_0 L_x}{\lambda r_0} = \frac{1}{\tau_B} \quad [\text{Hz}]. \tag{II.30}$$

The minimum frequency differences Δf_{min} that can be detected are equal to B. Using equation II.5, an uncertainty Δx_{min} in the differential distance in x–direction follows as

$$\Delta x_{min} = \frac{\Delta f_{min} \cdot \lambda \cdot r_0}{2v_0} = \frac{L_x}{2} \quad [\text{m}] \tag{II.31}$$

which is the half–antenna length.

III.3 Fading statistics

The value of each frequency component in the power spectrum (eq.II.14) is written as the sum $\Sigma\Sigma P_i \cdot P_j$ for all scatterer combinations i,j yielding a differential distance $\Delta x_a = |x_i - x_j|$ corresponding to that frequency. Note that $\Sigma\Sigma P_i \cdot P_j$ can be written as $\Sigma P_i \cdot \Sigma P_j$. It should be recognized that equation II.14 describes the expectation of the spectrum. In deriving equation II.14a from equation II.13, it was assumed that, because of the incoherency, the expectation of $|\Sigma\Sigma E_i E_j|^2$ equals $\Sigma\Sigma P_i \cdot P_j$. This factor can be written as $|\Sigma E_i|^2 \cdot |\Sigma E_j|^2$; therefore ΣP_i equals $E(|\Sigma E_i|^2)$. The modulus of the sum of the electric field strengths $|\Sigma E_i|$ is known to be Rayleigh distributed and the square of the modulus (the power) $|\Sigma E_i|^2$ is known to have the negative exponential distribution (Marshall and Hitschfeld, 1953). Hence the underlying distribution of the factor ΣP_i is the negative exponential distribution. To describe statistics of the fading properly, the factors $\Sigma\Sigma P_i \cdot P_j$ $(=\Sigma P_i \cdot \Sigma P_j)$ will be written as the product of two independent stochastic variables $\underline{P}_\alpha$ and $\underline{P}_\beta$, both having a negative exponential distribution;

$$p(\underline{P}_\alpha) = \frac{1}{\bar{P}_\alpha} \exp(-\underline{P}_\alpha / \bar{P}_\alpha), \tag{II.32a}$$

$$p(\underline{P}_\beta) = \frac{1}{\bar{P}_\beta} \exp(-\underline{P}_\beta / \bar{P}_\beta) \tag{II.32b}$$

and with an expectation

$$E(\underline{P}_\alpha) = \bar{P}_\alpha = \Sigma P_i, \tag{II.33a}$$

$$E(\underline{P}_\beta) = \bar{P}_\beta = \Sigma P_j. \tag{II.33b}$$

In order to arrive at a good estimation of this product, averaging over many independent samples of the product $\underline{P}_\alpha \cdot \underline{P}_\beta$ is necessary. This was done experimentally (section 6.5) by averaging spectra from a large number (30 to 50) of azimuthal lines. The probability density function of the mean of products $\underline{P}_\alpha \cdot \underline{P}_\beta$ can in principle be determined, but this is a tedious task. In this case, however, the variance of the product can be calculated easily and, since the central limit theorem is applicable, the variance of the mean of n samples ($n > 10$) can be determined accurately (and the probability density function of the mean may be assumed normal). The expectation

$$E(\Sigma\Sigma P_i \cdot P_j) = E(\underline{P}_\alpha) \cdot E(\underline{P}_\beta) = \bar{P}_\alpha \cdot \bar{P}_\beta \tag{II.34a}$$

and the variance

$$\begin{aligned} var(\Sigma\Sigma P_i \cdot P_j) &= var(\underline{P}_\alpha \cdot \underline{P}_\beta) \\ &= E((\underline{P}_\alpha \cdot \underline{P}_\beta)^2) - (E(\underline{P}_\alpha \cdot \underline{P}_\beta))^2 \\ &= E(\underline{P}_\alpha^2) \cdot E(\underline{P}_\beta^2) - (E(\underline{P}_\alpha \cdot \underline{P}_\beta))^2 \\ &= 2\bar{P}_\alpha^2 \cdot 2\bar{P}_\beta^2 - \bar{P}_\alpha^2 \cdot \bar{P}_\beta^2 = 3 \cdot \bar{P}_\alpha^2 \cdot \bar{P}_\beta^2. \end{aligned} \tag{II.34b}$$

In case of n independent samples, the variance of the mean follows as $(3/n) \cdot \bar{P}_\alpha^2 \cdot \bar{P}_\beta^2$ and the standard deviation as

$$s.d. = (3/n)^{\frac{1}{2}} \cdot \bar{P}_\alpha \cdot \bar{P}_\beta \tag{II.34c}$$

(or $(3/n)^{\frac{1}{2}}$ times the mean).

APPENDIX III

III. Intercalibration and radar signature determination

III.1 Mathematical definition

To indicate the procedures adopted for intercalibration and radar signature determination, a mathematical definition of the problem, contained in the following seven points, needs to be given first.

(1) Each object is a homogeneous forest area amply within stand borders and each object is assigned a unique number n with n ranging from 1 to $n_{\max}$.

B is the set of all objects within a particular forest area.

(2) A_i is the set of all objects belonging to tree class i with i ranging from 1 to $i_{\max}$ and $B = A_1 \cup A_2 \cup \cdots \cup A_{i\max}$.

(3) C is the set of (four) images from a particular forest area and particular date. Each image is assigned a unique symbol denoted by the variable u or v with $u, v \in C$ and $C = \{a,b,c,d\}$.

$\mathcal{D}$ is the set of all possible image pairs. Each pair is assigned a unique symbol pair denoted by the variable pair uv with $uv \in \mathcal{D}$ and $\mathcal{D} = \{ab,ac,ad,bc,bd,cd\}$.

(4) For each object n in image u, the observed stand–averaged mean is denoted by the stochastic variable $\bar{g}_{n,u}$, the observed standard deviation (s.d.) is denoted by the stochastic variable $s_{n,u}$, the mean grazing (or incidence) angle is denoted as $\theta_{n,u}$ and the number of pixels is denoted as $N_{n,u}$.

> Remark: Because of the stand dimension in range direction, the viewing angle ranges over a small interval, typically 1–2 degrees wide. In the actual analysis $\theta_{n,u}$ simply is taken as the middle of this interval.

Each object n has a deterministic signature $\bar{\gamma}_n(\theta)$. The signature is defined as the expectation of the mean, as a function of θ, of the (absolute) radar backscatter level of object n. The levels are assumed to follow a normal distribution;

$$p(\gamma_n(\theta)) = N(\bar{\gamma}_n(\theta),\sigma_n). \tag{III.1}$$

$s_{n,u}$ is an unbiased estimation of σ_n and $\bar{g}_{n,u}$ is an estimation of $\bar{\gamma}_n$, biased with the image

offset δ_u (see point 7).

It is noted that the s.d. σ_n is assumed to be angular independent. Further, since Rayleigh fading is assumed, the s.d. may range from the theoretical minimum (0.8 dB for 30 independent power samples) to higher values, depending on the size of structural elements as compared with the system's spatial resolution. Experimentally established estimates of σ_n, averaged for tree classes and dates, are listed in table 5.2.

(5) Each class i has a deterministic mean signature $\bar{\gamma}_i(\theta)$. The signature is defined as the expectation of the mean, as a function of θ, of the (absolute) radar backscatter level of pixels belonging to class i. The levels are assumed to follow a normal distribution;

$$p(\gamma_i(\theta)) = N(\bar{\gamma}_i(\theta),\sigma_i). \tag{III.2}$$

It is noted that $\sigma_i > E(\sigma_n)$ (with $n \in A_i$). σ_i results from variation (variance = σ_n^2) within stands (caused by speckle and spatial structure) and from variation (variance = σ_m^2) of stand–averaged means (e.g. caused by differences in ecological factors, biophysical parameters, etc.). These sources of variation are independent, therefore, $\sigma_i^2 = \sigma_m^2 + E(\sigma_n^2)$.

Estimations for $\bar{\gamma}_i(\theta)$ and σ_i follow from regression analysis (section III.2) on the basis of observations of $\bar{y}_{n,u}$ and $s_{n,u}$ and on the basis of $\theta_{n,u}$ and $N_{n,u}$ for all $n \in A_i$ and $u \in C$.

It is noted that, because of present lack of physical knowledge of radar scattering of forests, polynomials, rather than physical models are used, to fit the data.

$\bar{\gamma}_i(\theta)$ will be modelled as a j–th degree polynomial $\bar{\gamma}_{ij}(\theta)$. Thus,

$$\gamma_{i1}(\theta) = a_{i1} + b_{i1}\theta, \tag{III.3a}$$
$$\gamma_{i2}(\theta) = a_{i2} + b_{i2}\theta + c_{i2}\theta^2, \tag{III.3b}$$
$$\gamma_{i3}(\theta) = a_{i3} + b_{i3}\theta + c_{i3}\theta^2 + d_{i3}\theta^3, \text{ etc.} \tag{III.3c}$$

Experimentally established estimates of σ_m, the standard deviation of the stand–averaged means relative to the class characteristic mean signature, for all tree classes and dates, are listed in table 5.3. As stated above, σ_m may depend on factors such as ecologic differences, variation in biophysical properties, etc. The estimation of σ_m, however, may also depend on the adopted model. Overestimation may result if the model is inappropriate (i.e. not appropriate to fit the angular dependency properly). From the experimental results no indications were obtained that this is the case, however.

(6) Each image u has an absolute (and unknown) offset δ_u (with $\delta_u \in \{\delta_a, \delta_b, \delta_c, \delta_d\}$. Under the condition $\theta_{n,u} = \theta_{n,v}$ the following expression holds

$$E(\bar{g}_{n,u}(\theta_{n,u})) - \delta_u = E(\bar{g}_{n,v}(\theta_{n,v})) - \delta_v. \tag{III.4}$$

(7) A new stochastic variable $q_{n,uv}$ will be introduced and defined as

$$q_{n,uv} = \bar{g}_{n,u}(\theta_{n,u}) = \bar{g}_{n,v}(\theta_{n,v}) \tag{III.5}$$

and the condition $\theta_{n,u} = \theta_{n,v}$ in the following, will be assumed to be implied for this variable. Thus

$$E(q_{n,uv}) = \delta_v - \delta_u. \tag{III.6}$$

It is noted that this condition has not been interpreted very strictly in the actual analysis. To compromise between the obscuring effects of angular dependency and the number of combinations (for statistical reasons a sufficiently large number is needed), any combination under the condition $\theta_{n,u} - \theta_{n,v} \leq 5^o$ was considered as a valid observation of the parameter $q_{n,uv}$.

With these seven points, the problem is defined mathematically. Next some of the major steps and considerations towards the solution of the problem will be indicated. First the estimation of the factors δ_u which is the so–called intercalibration, will be discussed. Second, the estimation of the radar signatures $\gamma_i(\theta)$ and the parameters σ_n and σ_i (and thus σ_m) will be discussed.

III.2 Estimation of intercalibration factors and signatures

Since γ_n was assumed to be normally distributed, the stochastic variables $\bar{g}_{n,u}$ and, thus, $q_{n,uv}$ are normally distributed too. Following the least squares criterion, estimations for δ_u follow from minimalization of the cost function

$$Q = \sum_{uv} \sum_{n} (q_{n,uv} - (\delta_u - \delta_v))^2,$$

$$\text{for } uv \in \mathcal{V} \text{ and } n \in \mathcal{B}. \tag{III.7}$$

This problem cannot be solved, as could be anticipated, unless one of the four offsets is known or is assumed to be known. In the latter case, the solution yields relative intercalibration factors. Since no absolute data were obtained, the offset of run a (image a)

was taken as zero and thus intercalibration is done relatively to run a. Relative calibration factors are thus defined as

$$\delta_a' = \delta_a - \delta_a = 0, \tag{III.8a}$$
$$\delta_b' = \delta_b - \delta_a, \tag{III.8b}$$
$$\delta_c' = \delta_c - \delta_a, \tag{III.8c}$$
$$\delta_d' = \delta_d - \delta_a. \tag{III.8d}$$

The factors δ_b', δ_c' and δ_d' can be estimated now.

It seems realistic to assume the method may be improved when the size of the stands is taken into account. If weight factors are chosen proportional to the size of the area (or the number of pixels), it can be shown that the following (weighted) cost function Q_W results

$$Q_W = \sum_{uv} \sum_{n} \left[\frac{N_{n,u} \cdot N_{n,v}}{N_{n,u}+N_{n,v}}\right] \cdot (q_{n,uv} - (\delta_u'-\delta_v'))^2, \quad \text{for } uv \in \mathcal{D} \text{ and } n \in \mathcal{B}. \tag{III.9}$$

It also seems realistic to incorporate the factor $s_{n,u}$ in the estimation of intercalibration factors. The smaller the variance σ_n^2 the smaller the variance of $\bar{g}_{n,u}$ and the better the estimation of $\bar{\gamma}_n$. Objects with a small value of $s_{n,u}$ should therefore have more weight. This view is implied im the maximum likelihood criterion. Estimates of δ_u follow from maximization of a likelihood function ℓ. For this problem it can be shown that this function follows as

$$\ell = \prod_{uv} \prod_{n} \exp\left[-\left[\frac{N_{n,u}}{2\,s_{n,v}^2} + \frac{N_{n,v}}{2\,s_{n,u}^2}\right] \cdot \left[\frac{N_{n,u} \cdot N_{n,v}}{(N_{n,u}+N_{n,v})^2}\right] \cdot (q_{n,uv} - (\delta_u'-\delta_v'))^2\right], \quad \text{for } uv \in \mathcal{D} \text{ and } n \in \mathcal{B}. \tag{III.10}$$

It is remarked that $\ln(\ell)$ is maximal when ℓ is maximal and thus the regression equations for the three relative intercalibration factors simply follow from the equations

$$\frac{\partial \ln(\ell)}{\partial \delta_b'} = 0, \quad \frac{\partial \ln(\ell)}{\partial \delta_c'} = 0 \quad \text{and} \quad \frac{\partial \ln(\ell)}{\partial \delta_d'} = 0. \tag{III.11}$$

Having established the relative intercalibration factors, the observed stand–averaged backscatter levels $\bar{g}_{n,u}$ are corrected as

$$\bar{g}_{n,u}' = \bar{g}_{n,u} - \delta_u'. \tag{III.12}$$

As a consequence of the (unknown) offset δ_a still being present (and common to all data of a particular forest area and date), the backscatter signature model $\gamma_{ij}(\theta)$ (meaning the signature of tree class i modelled as a j–th degree polynomial) will be denoted as $\gamma'_{ij}(\theta)$. Estimation of the polynomials' coefficients a'_{ij}, b_{ij}, c_{ij} and d_{ij} follows from the regression equations which result from minimization of a cost function. Following analogous lines of reasoning, the following cost functions have been established.

$$Q = \sum_u \sum_n \left[\gamma'_{ij}(\theta_{n,u}) - \bar{g}'_{n,u}(\theta_{n,u})\right]^2, \quad \text{for } u \in C \text{ and } n \in A_i, \tag{III.13}$$

$$Q_W = \sum_u \sum_n N_{n,u} \cdot \left[\gamma'_{ij}(\theta_{n,u}) - \bar{g}'_{n,u}(\theta_{n,u})\right]^2, \quad \text{for } u \in C \text{ and } n \in A_i \tag{III.14}$$

and

$$-\ln(\ell) = \sum_u \sum_n \frac{N_{n,u}}{s^2_{n,u}} \cdot \left[\gamma'_{ij}(\theta_{n,u}) - \bar{g}'_{n,u}(\theta_{n,u})\right]^2, \quad \text{for } u \in C \text{ and } n \in A_i. \tag{III.15}$$

From an analysis of variance, confidence intervals for the estimated coefficients as well as for the estimated signature can be calculated. This technique is described well by Brownlee (1965) and will not be discussed here.

APPENDIX IV Maps of test sites.

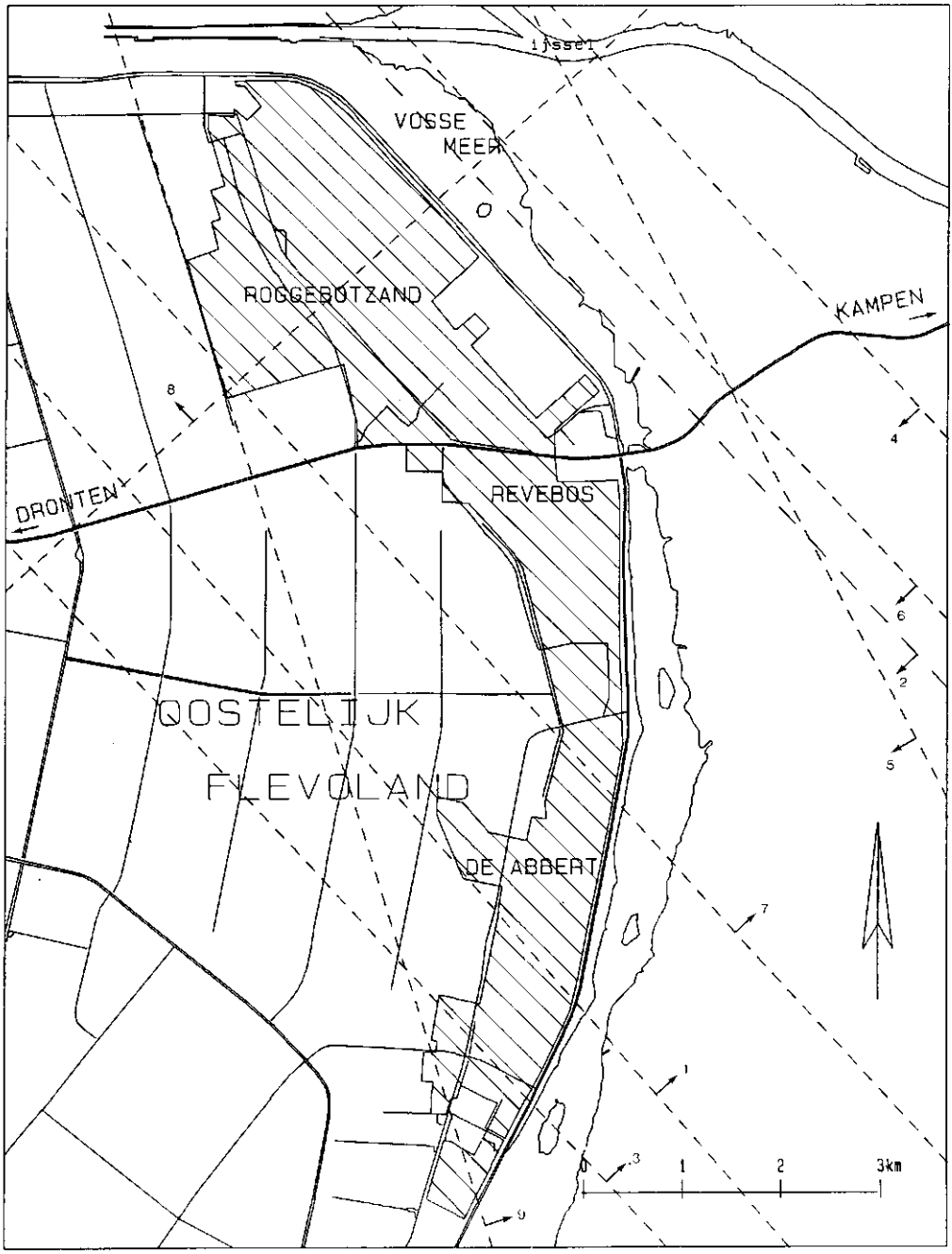

Figure IV.1. The Roggebotzand site and location of SLAR tracks.

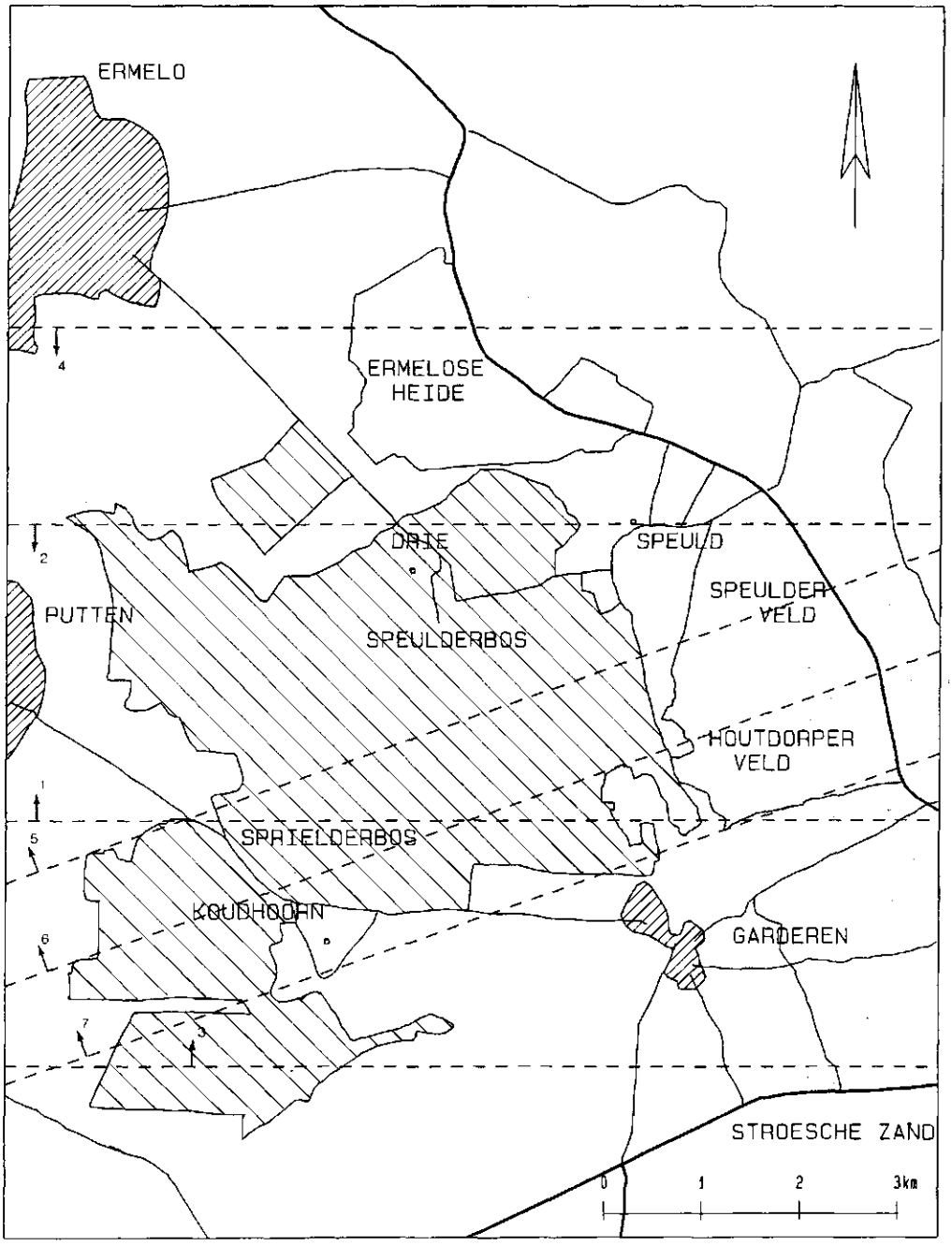

Figure IV.2. The Speulderbos site and location of SLAR tracks.

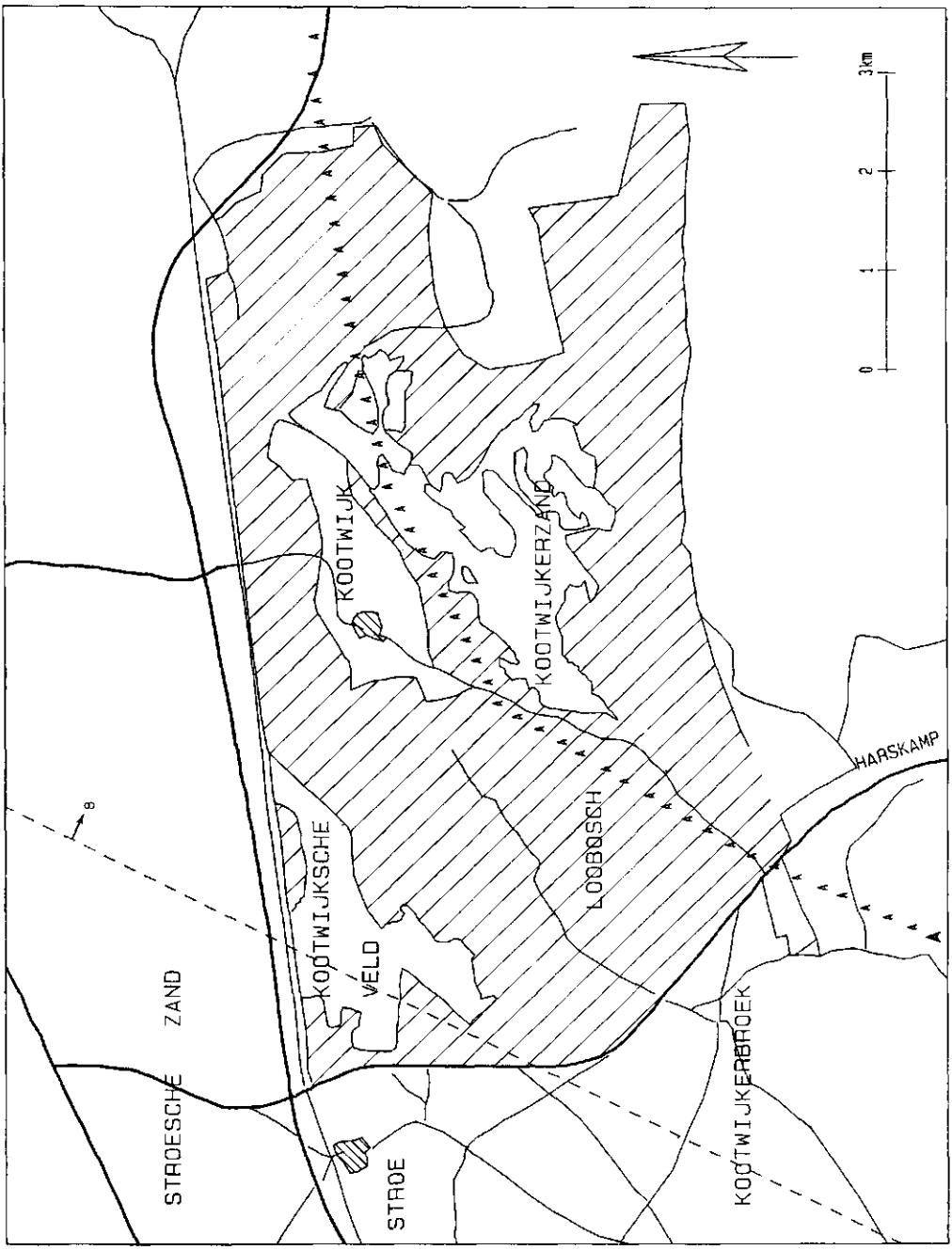

Figure IV.3. The Kootwijk site and location of SLAR track.

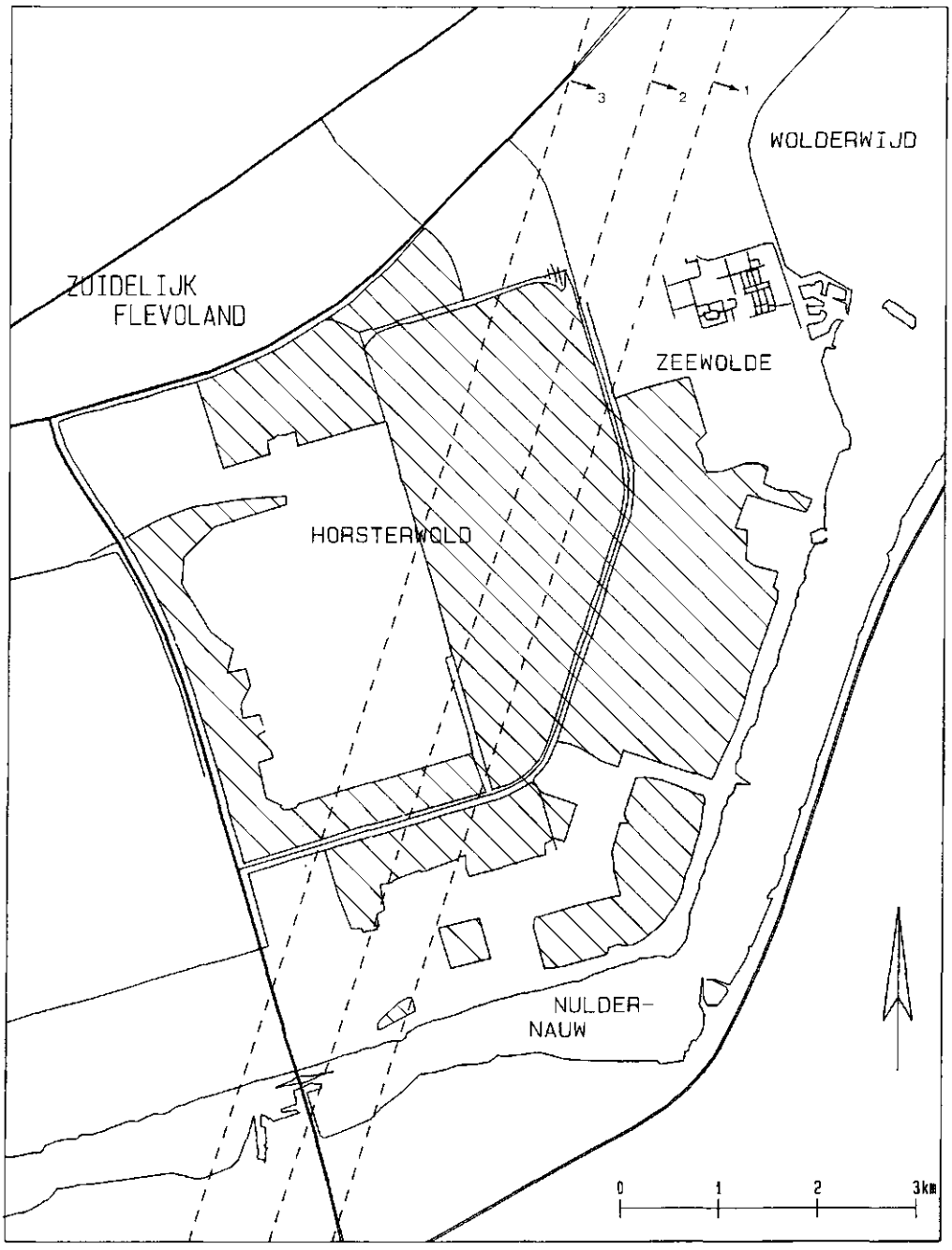

Figure IV.4. The Horsterwold site and location of SLAR tracks.

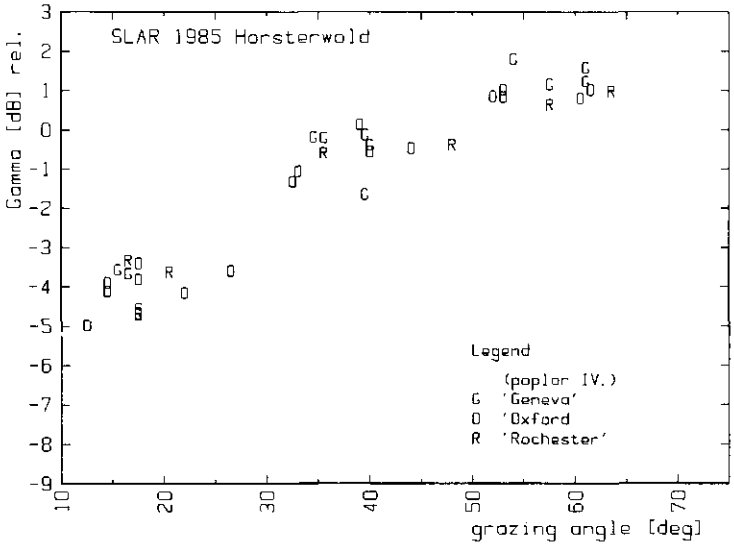

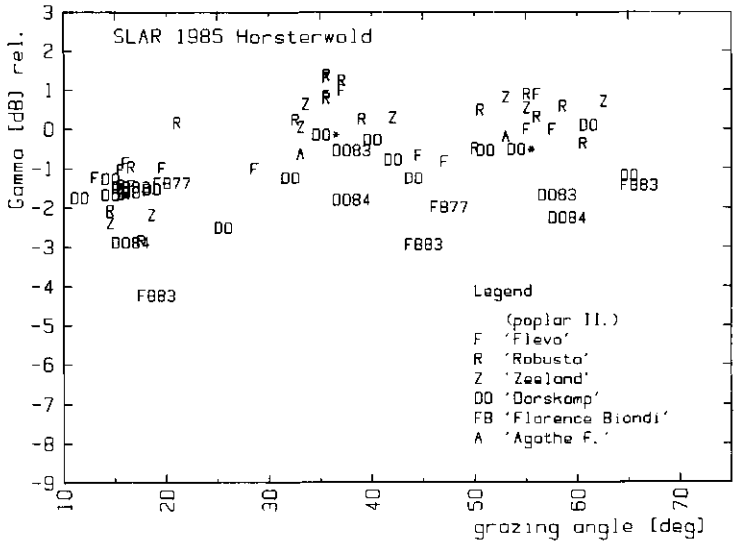

Figure V.1. Mean γ values of selected stands at the Horsterwold site as a function of grazing angle (X–band SLAR; 11 July 1985; images: Hw1–3). The γ values are relative, however, because of the internal calibration, the same for all images recorded in 1985. The data in the figures V.1–10 are therefore fully comparable. In this figure, the poplar clones from group IV of table 5.5a (Section Aigeiros x Tacamahaca) are shown.

Figure V.2. Mean γ values of selected stands at the Horsterwold site as a function of grazing angle (X–band SLAR; 11 July 1985; images: Hw1–3). The poplar clones from group II (*Pop.* x *euramericana*) of table 5.5a are shown. Note that two 'Florence Biondi' stands (FB'77 and FB'83) and two 'Dorskamp' stands (DO'83 and DO'84) were not planted in the 1973–1976 period.

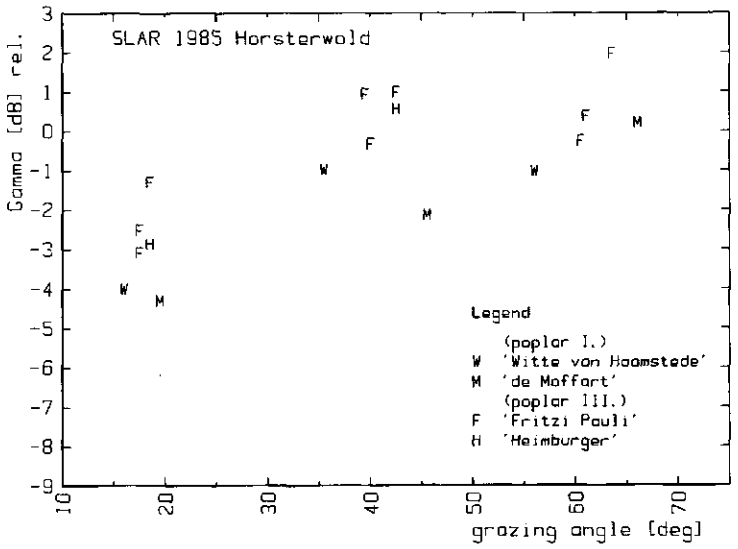

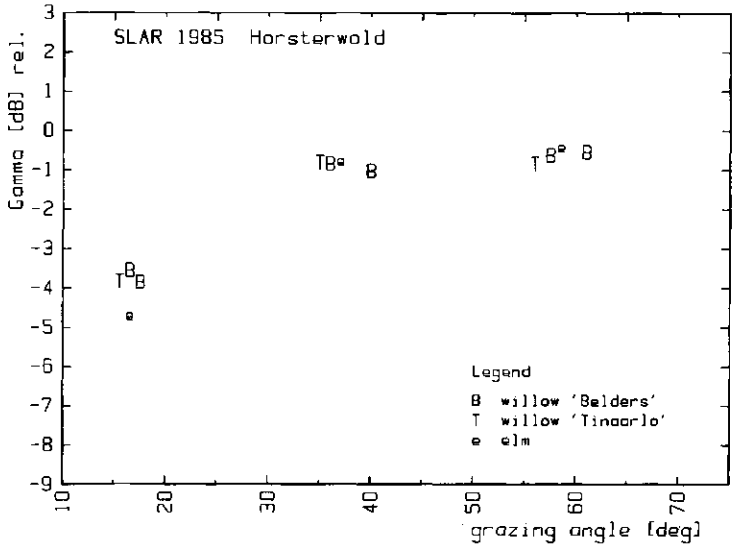

Figure V.3. Mean γ values of selected stands at the Horsterwold site as a function of grazing angle (X–band SLAR; 11 July 1985; images: Hw1–3). The poplar clones from group I (*Pop.* x *canescens*) and group III (*Pop. trichocarpa*) of table 5.5a are shown.

Figure V.4. Mean γ values of selected stands at the Horsterwold site as a function of grazing angle (X–band SLAR; 11 July 1985; images: Hw1–3). Willow and elm are shown.

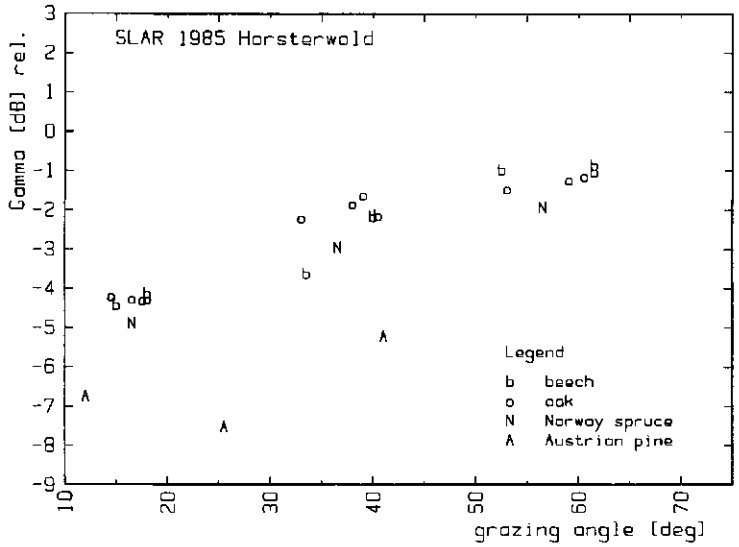

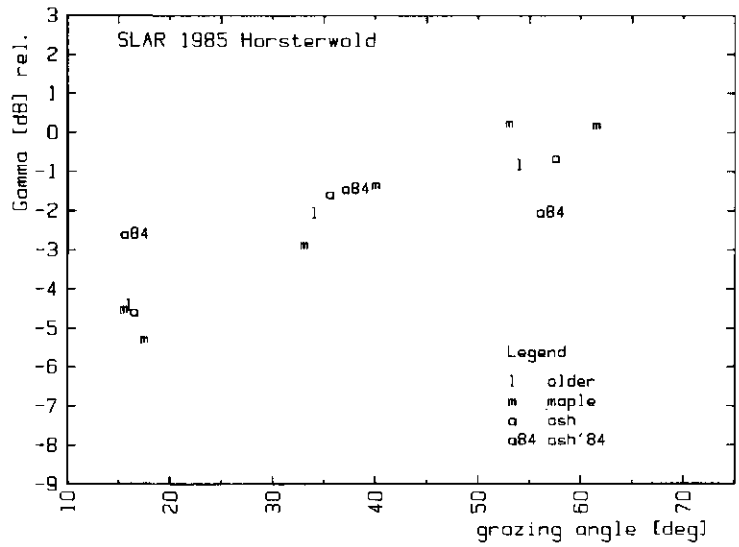

Figure V.5. Mean γ values of selected stands at the Horsterwold site as a function of grazing angle (X–band SLAR; 11 July 1985; images: Hw1–3). Beech, oak, Norway spruce and Austrian pine are shown.

Figure V.6. Mean γ values of selected stands at the Horsterwold site as a function of grazing angle (X–band SLAR; 11 July 1985; images: Hw1–3). Alder, maple and ash stands and an ash stand planted in 1984 are shown.

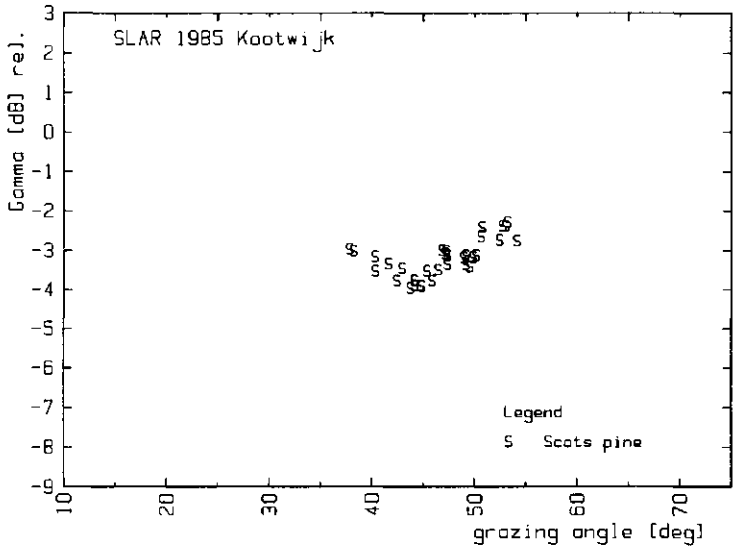

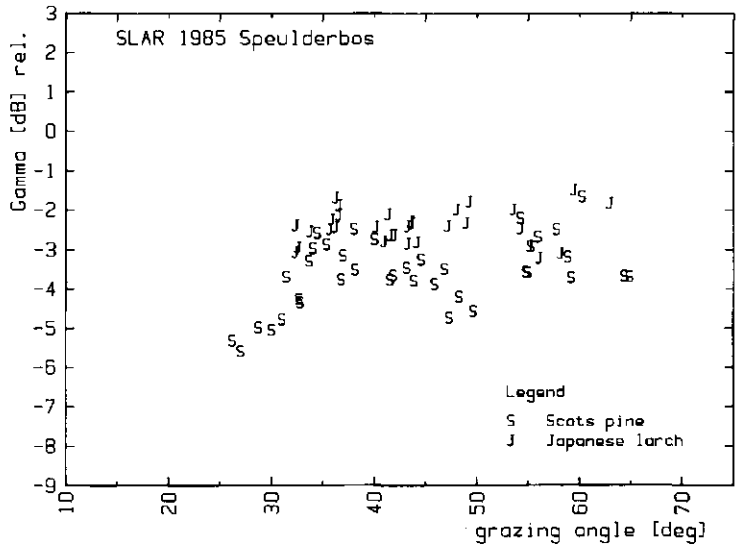

Figure V.7. Mean γ values of selected stands at the Kootwijk site as a function of grazing angle (X–band SLAR; 11 July 1985; images: Kw2–3). Only Scots pine stands were selected.

Figure V.8. Mean γ values of selected stands at the Speulderbos site as a function of grazing angle (X–band SLAR; 11 July 1985; images: Sp16–18). Scots pine and Japanese larch stands are shown.

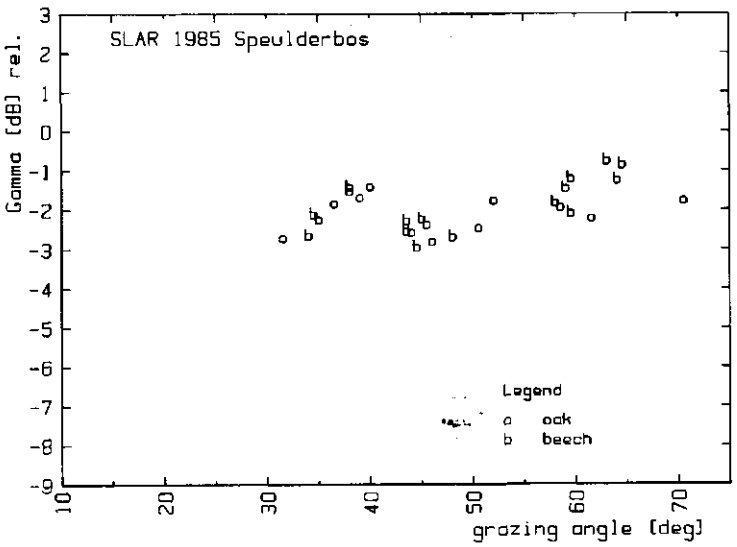

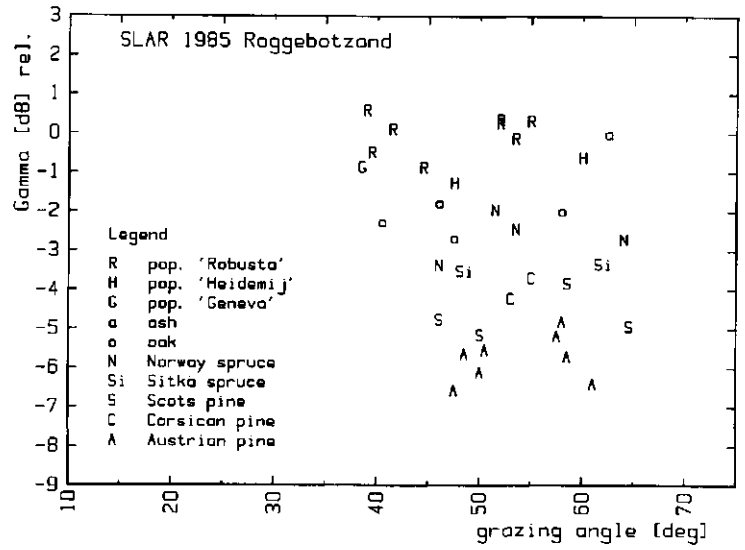

Figure V.9. Mean γ values of selected stands at the Speulderbos site as a function of grazing angle (X–band SLAR; 11 July 1985; images: Sp16–18). Oak and beech stands are shown.

Figure V.10. Mean γ values of selected stands at the Roggebotzand site as a function of grazing angle (X–band SLAR; 11 July 1985; images: Rbz23–24). Stands of poplar 'Robusta' and 'Heidemij' (group II) and poplar 'Geneva' (group IV) are shown together with ash, oak, spruces and pines.

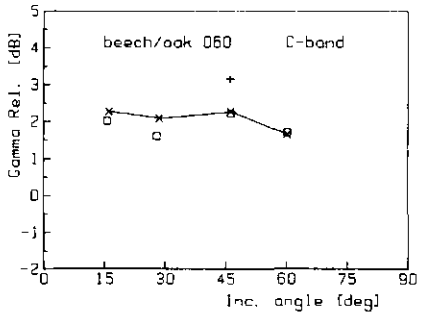
beech/oak 060 C-band
Gamma Rel. [dB]
Inc. angle [deg]

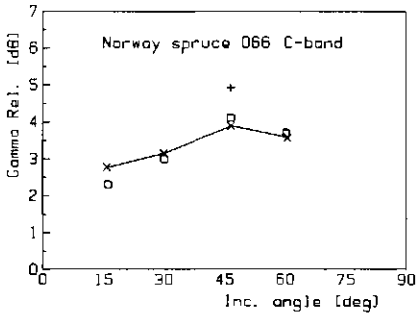
Norway spruce 066 C-band
Gamma Rel. [dB]
Inc. angle [deg]

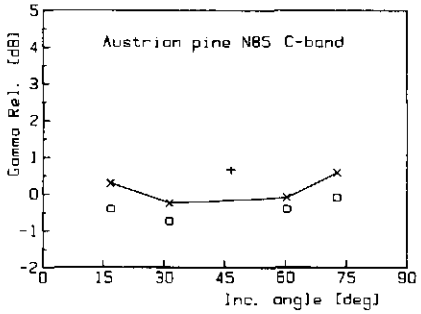
Austrian pine N85 C-band
Gamma Rel. [dB]
Inc. angle [deg]

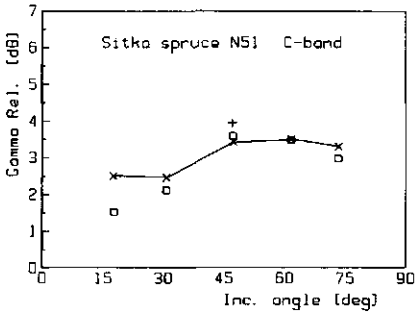
Sitka spruce N51 C-band
Gamma Rel. [dB]
Inc. angle [deg]

V.11a-d

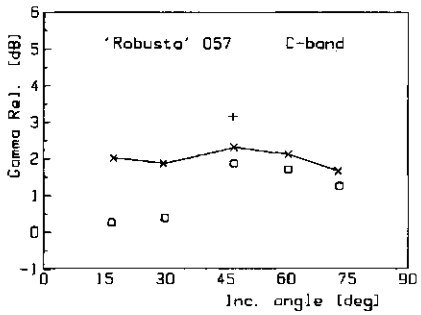
'Robusta' 057 C-band
Gamma Rel. [dB]
Inc. angle [deg]

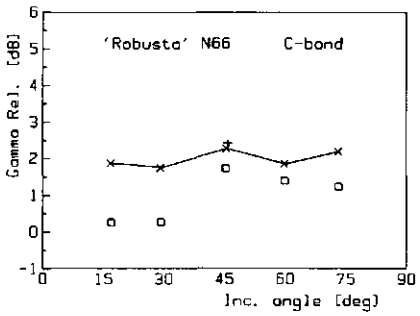
'Robusta' N66 C-band
Gamma Rel. [dB]
Inc. angle [deg]

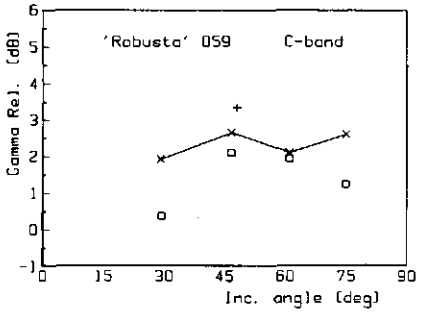
'Robusta' 059 C-band
Gamma Rel. [dB]
Inc. angle [deg]

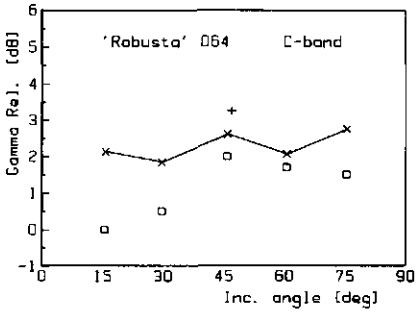
'Robusta' 064 C-band
Gamma Rel. [dB]
Inc. angle [deg]

V.11e-h

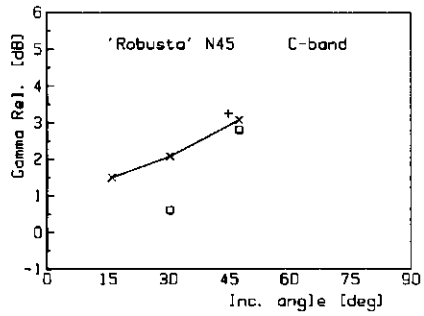
'Robusta' N45 C-band
Gamma Rel. [dB]
Inc. angle [deg]

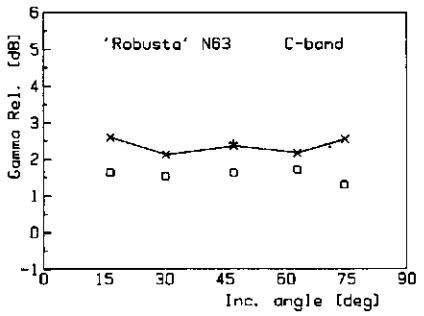
'Robusta' N63 C-band
Gamma Rel. [dB]
Inc. angle [deg]

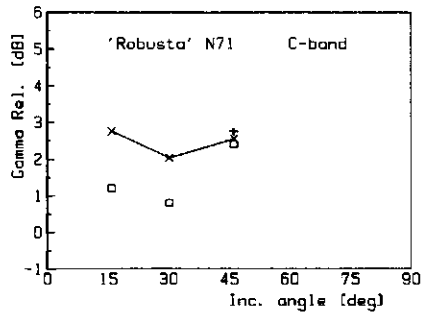
'Robusta' N71 C-band
Gamma Rel. [dB]
Inc. angle [deg]

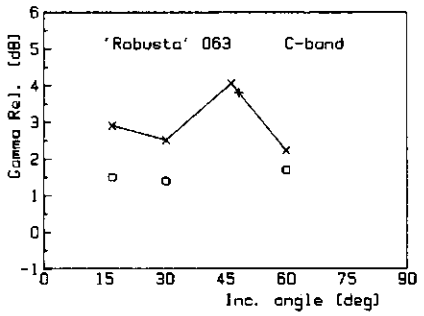
'Robusta' 063 C-band
Gamma Rel. [dB]
Inc. angle [deg]

i-l

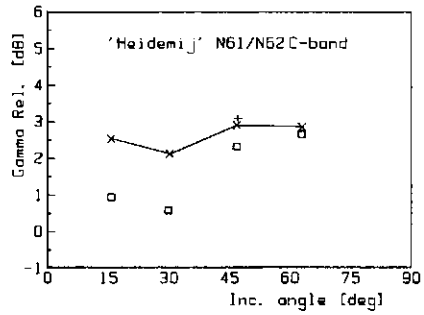
'Heidemij' N61/N62 C-band
Gamma Rel. [dB]
Inc. angle [deg]

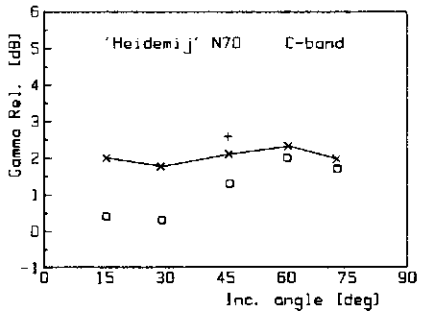
'Heidemij' N70 C-band
Gamma Rel. [dB]
Inc. angle [deg]

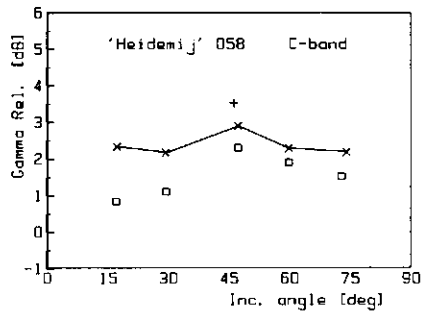
'Heidemij' 058 C-band
Gamma Rel. [dB]
Inc. angle [deg]

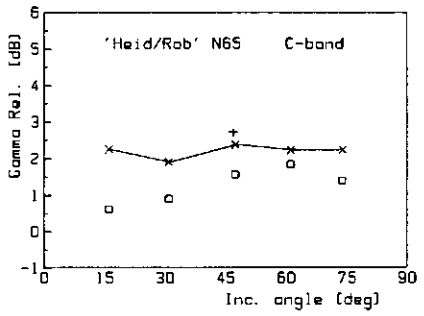
'Heid/Rob' N65 C-band
Gamma Rel. [dB]
Inc. angle [deg]

V.11m-p

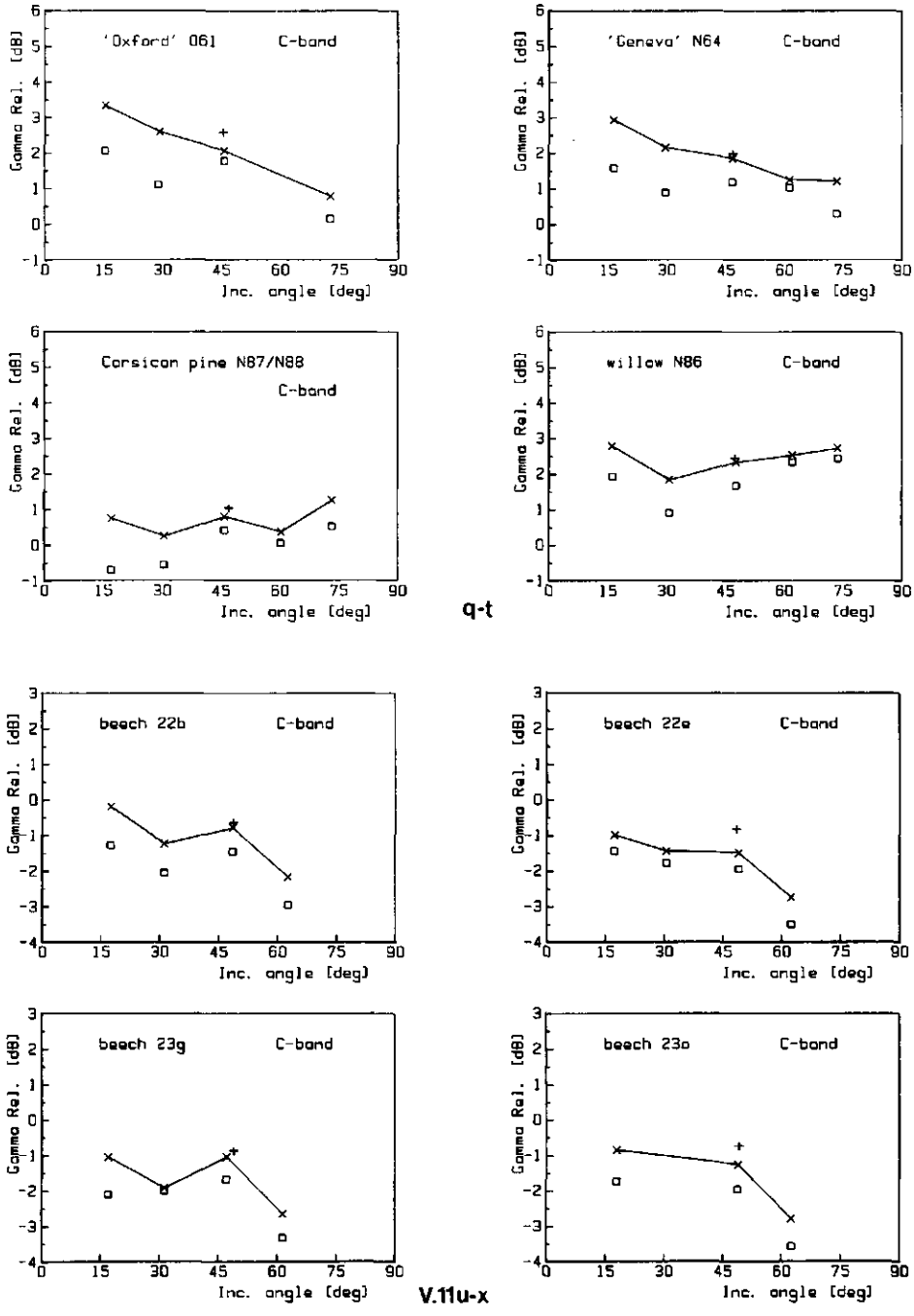

Figures V.11 (a–x). (24 fig.) Radar signatures obtained from DUTSCAT C–band scatterometer flights; x, γ values for HH polarization; +, γ values for VV polarization (45° only). □, for comparison, indicates γ values computed for HH polarization when the 'standard' type of processing is applied (which is less accurate for forests, see section 3.3). Table V.7 gives an overview of the figures and provides additional data.

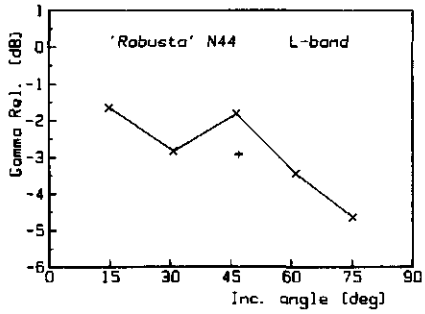
'Robusta' N44 L-band
Gamma Rel. [dB]
Inc. angle [deg]

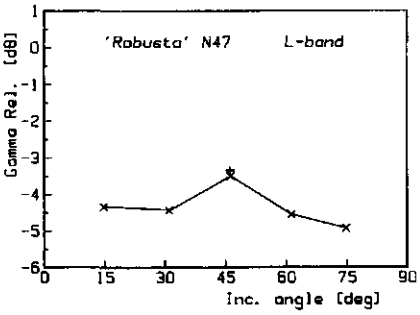
'Robusta' N47 L-band
Gamma Rel. [dB]
Inc. angle [deg]

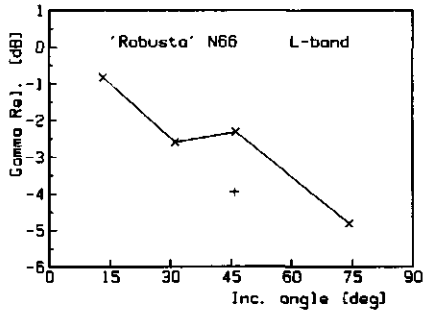
'Robusta' N66 L-band
Gamma Rel. [dB]
Inc. angle [deg]

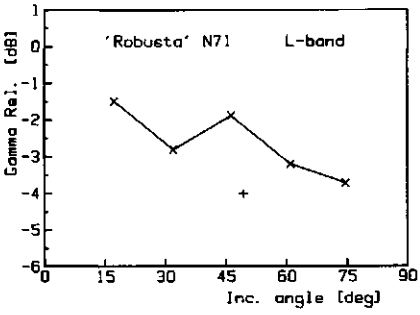
'Robusta' N71 L-band
Gamma Rel. [dB]
Inc. angle [deg]

V.12a-d

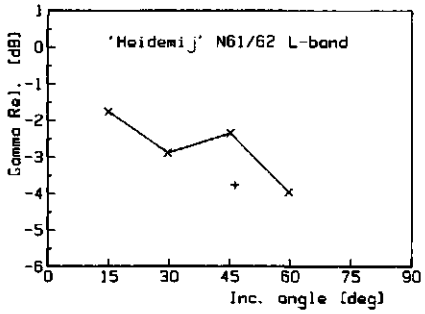
'Heidemij' N61/62 L-band
Gamma Rel. [dB]
Inc. angle [deg]

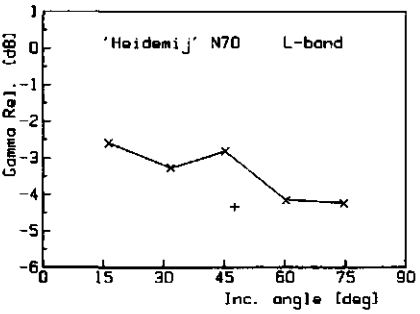
'Heidemij' N70 L-band
Gamma Rel. [dB]
Inc. angle [deg]

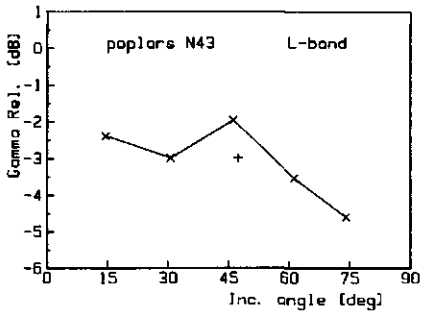
poplars N43 L-band
Gamma Rel. [dB]
Inc. angle [deg]

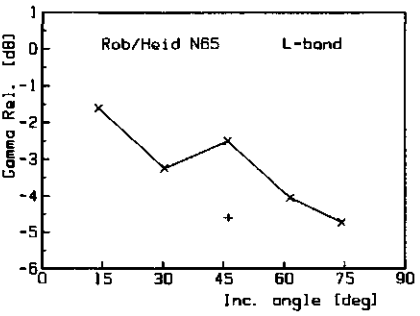
Rob/Heid N65 L-band
Gamma Rel. [dB]
Inc. angle [deg]

V.12e-h

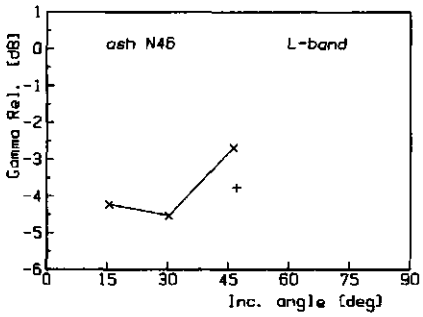
ash N46 L-band
Gamma Rel. [dB]
Inc. angle [deg]

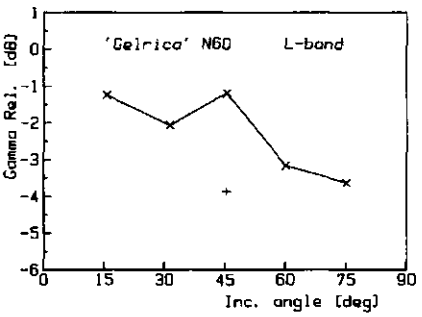
'Gelrica' N60 L-band
Gamma Rel. [dB]
Inc. angle [deg]

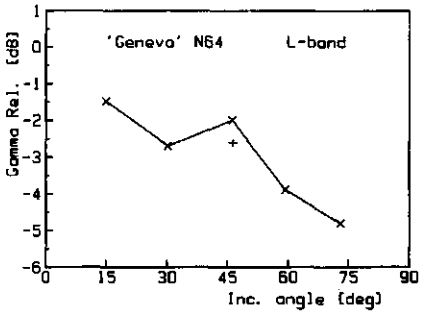
'Geneva' N64 L-band
Gamma Rel. [dB]
Inc. angle [deg]

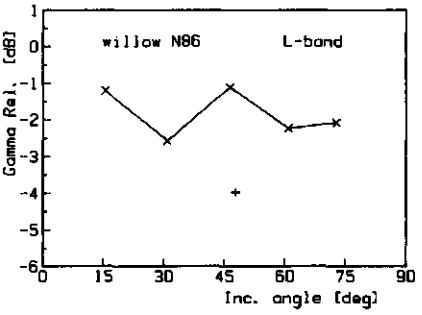
willow N86 L-band
Gamma Rel. [dB]
Inc. angle [deg]

i-l

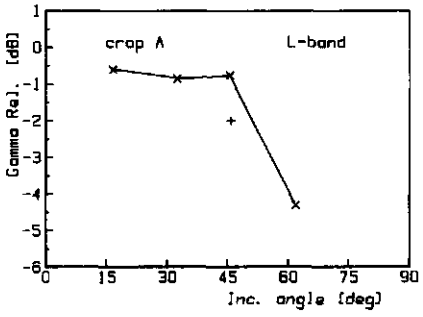
crop A L-band
Gamma Rel. [dB]
Inc. angle [deg]

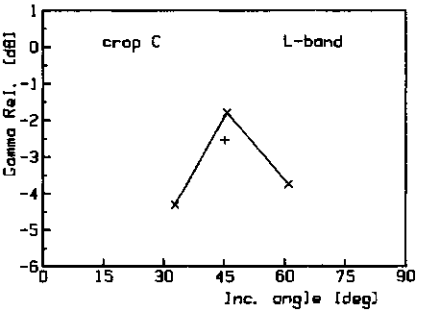
crop C L-band
Gamma Rel. [dB]
Inc. angle [deg]

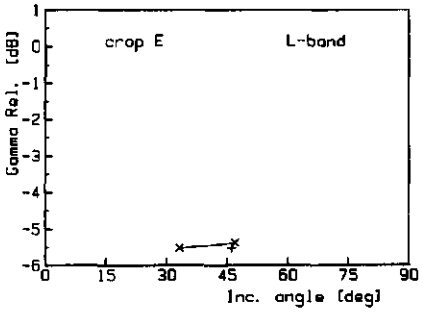
crop E L-band
Gamma Rel. [dB]
Inc. angle [deg]

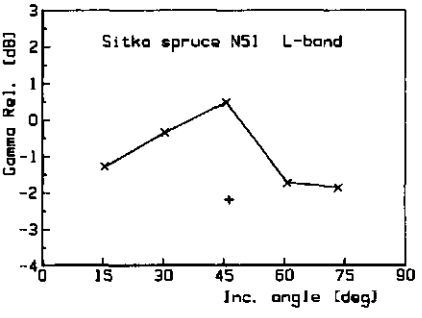
Sitka spruce N51 L-band
Gamma Rel. [dB]
Inc. angle [deg]

V.12m-p

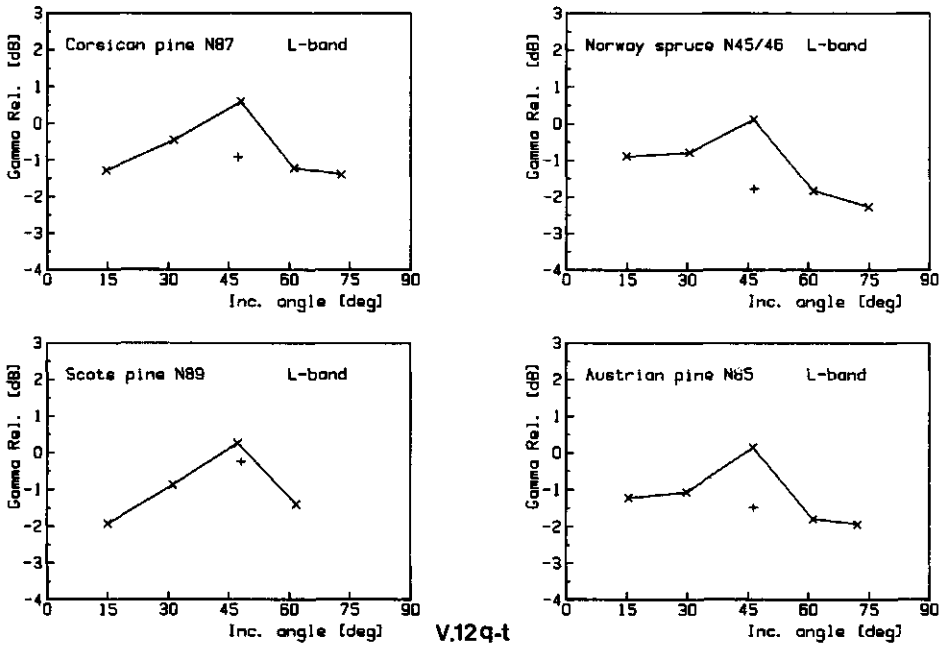

Figure V.12 (a–t). (20 fig.) Radar signatures obtained from DUTSCAT L–band scatterometer flights; x, γ values for HH polarization; +, γ values for VV polarization (45° only). Table V.7 gives an overview of the figures and provides additional data.

Table V.1. Stand and tree parameters and area (in ha) of selected poplar stands at the Roggebotzand site.

No.	clone	compartment	I_m	V	N	dbh	h_{dom}	area
1	Heid '59	N61h/N62h	9.4	134.2	152.0	35.26	23.5	6.35
2	Heid '61	N64e	8.1	97.3	174.8	28.10	22.8	2.94
3	Heid '62	N70e t/m l	9.0	118.9	175.6	30.65	23.4	10.57
4	Heid '62	N70c	9.5	111.8	178.9	29.12	23.9	6.01
5	Heid '59	N81c	8.8	114.8	129.0	34.90	23.5	4.00
6	Heid '58	O56a	10.0	144.2	149.1	35.42	25.0	3.28
7	Heid '59	O58j	7.4	95.6	118.5	34.43	22.5	4.11
8	Heid '61	O58l	6.9	86.3	106.7	33.68	22.5	3.42
9	Heid '59	O60c	9.4	141.8	113.7	41.70	24.7	2.63
10	Heid '59	O64Ab	9.1	130.2	152.3	34.32	23.5	3.77
11	Heid '60	O75b	8.1	107.0	107.3	38.00	23.2	7.13
12	Heid '60	O73c	10.1	139.4	170.7	34.18	23.8	7.67
13	Rob '60	N47b	8.0	144.8	155.7	35.08	24.6	13.22
14	Rob '61	N44b	8.4	101.0	155.0	29.71	23.4	9.02
15	Rob '59	N63d	9.6	143.1	162.1	34.21	24.6	6.10
16	Rob '61	N66h	9.4	107.5	154.9	31.05	23.6	3.88
17	Rob '62	N66e/N67h	9.7	114.5	173.4	30.61	23.3	9.27
18	Rob '59	N69b	11.5	192.9	191.1	36.99	25.6	4.93
19	Rob '59	N76c/N77c	10.6	158.6	183.0	35.12	24.4	4.54
20	Rob '60	O27a	9.0	127.3	95.8	40.87	26.8	7.62
21	Rob '59	O57b	9.9	141.8	109.2	40.25	26.6	5.53
22	Rob '61	O57l	8.5	112.1	124.2	35.34	24.0	3.31
23	Rob '61	O57n	7.1	94.8	110.6	34.69	24.0	6.74
24	Rob '59	O58b	8.4	128.2	108.0	38.97	26.0	4.64
25	Rob '59	O59c	10.1	149.7	114.8	40.63	26.2	2.90
26	Rob '61	O59k	9.4	118.0	157.5	31.36	24.0	9.58
27	Rob '61	O63h	7.4	87.5	102.5	36.30	24.0	5.61
28	Rob '59	O64Ac	9.9	167.1	189.3	34.30	25.0	4.47
29	Rob '60	O68b/O69a	9.1	118.0	161.9	31.40	23.5	13.49
30	Rob '60	O74b/O74b	8.8	125.4	129.7	36.76	24.4	8.79
31	Rob '60	O72c/O73d	9.7	136.9	173.3	33.03	23.9	18.71
32	Rob '60	P95k	9.0	127.8	157.5	33.28	24.0	8.19
33	Rob '61	P87a/P88a	8.7	93.9	147.6	29.12	23.4	27.69

correlation matrix of stand and tree parameters;

	I_m	V	N	dbh
V	0.82			
N	0.57	0.41		
dbh	0.13	0.43	–0.63	
h_{dom}	0.47	0.63	–0.22	0.70

Table V.2a. Correlations (r–values) between object parameters and γ for stands of poplar clones 'Robusta' and 'Heidemij' at the Roggebotzand site. The first column shows the image from which the γ values are obtained and the second column the number of selected stands (n). The grazing angle varies in the range of 10° to 35°.

image	n	I_m	V	N	dbh	h_{dom}
Rbz1	22	–0.03	0.05	–0.09	0.19	0.00
Rbz2	24	–0.29	–0.21	–0.42	0.22	0.22
Rbz3	20	0.43	0.48	0.13	0.39	0.59
Rbz4	12	0.02	0.15	–0.46	0.49	0.31
Rbz5	23	–0.32	–0.22	–0.38	0.16	–0.12
Rbz6	24	0.13	0.35	–0.19	0.56	0.47
Rbz7	21	–0.12	–0.06	0.03	0.00	–0.14
Rbz8	23	0.03	0.04	0.30	–0.27	–0.14
Rbz9	26	0.24	0.21	–0.25	0.49	0.41
Rbz10	31	0.25	0.33	–0.25	0.52	0.50
Rbz11	26	0.25	0.18	–0.33	0.49	0.47
Rbz12	29	0.13	0.40	–0.22	0.62	0.54 *) fig.5.16

Table V.2b. As table V.2a, but only for stands of poplar clone 'Robusta' (and only for the March '83 and May '83 measurements).

image	n	I_m	V	N	dbh	h_{dom}
Rbz9	17	0.29	0.19	–0.27	0.53	0.43
Rbz10	20	0.10	0.14	–0.21	0.34	0.34
Rbz11	16	0.18	0.09	–0.42	0.57	0.54
Rbz12	18	0.13	0.41	–0.13	0.63	0.62

Table V.2c. As table V.2a, but only for stands of poplar clone 'Heidemij'.

image	n	I_m	V	N	dbh	h_{dom}
Rbz9	9	–0.13	0.05	–0.10	0.14	0.02
Rbz10	11	0.39	0.58	–0.41	0.81	0.56
Rbz11	10	0.43	0.47	–0.13	0.42	0.66
Rbz12	11	0.03	0.32	–0.48	0.66	0.30

Table V.2d. As table V.2a, but only for the stands in the 10°–20° range of grazing angles.

image	n	I_m	V	N	dbh	h_{dom}
Rbz9	21	0.21	0.37	–0.19	0.53	0.50
Rbz10	18	–0.03	–0.07	–0.39	0.32	0.23
Rbz11	21	0.26	0.37	–0.20	0.52	0.54
Rbz12	15	–0.12	0.19	–0.34	0.49	0.46

Table V.2e. As table V.2a, but only for the stands in the 20°–30° range of grazing angles.

image	n	I_m	V	N	dbh	h_{dom}
Rbz9	10	0.31	–0.02	–0.59	0.66	0.52
Rbz10	11	0.62	0.72	0.41	0.45	0.70
Rbz11	11	0.19	–0.24	–0.73	0.56	0.40
Rbz12	13	0.18	0.35	–0.26	0.74	0.49

Table V.3. Stand and tree parameters of selected stands of Japanese larch at the Speulderbos site.

No.	comp.	dbh	h_{dom}	G	N	N_{cr}	d_{cr}	R_{ct}	Age
1	45d	23.9	20.4	22.5	575	375	5.2	0.65	42
2	13c	20.8	19.1	21.0	625	375	5.2	0.60	33
3	20l	18.0	16.2	25.5	975	458	4.7	0.47	22
4	110g	25.6	22.9	19.5	350	333	5.5	0.95	48
5	110pq	32.3	24.1	19.5	250	208	6.9	0.83	55
6	115j	20.2	19.1	13.5	475	250	6.3	0.53	35
7	123m	17.0	16.0	21.8	900	417	4.9	0.46	42
8	124g	14.4	14.2	21.8	1175	417	4.9	0.35	42
9	119b	16.5	16.2	15.8	825	373	5.2	0.45	27
10	117d	27.8	22.4	17.3	400	250	6.3	0.63	51
11	122n	26.9	20.8	16.5	400	209	6.9	0.52	52
12	40l	17.6	18.7	21.8	850	607	4.1	0.71	39
13	40m	22.1	21.3	20.3	525	321	5.6	0.61	50
14	41p	18.8	18.7	20.3	700	437	4.8	0.62	42
15	116a	27.3	21.9	19.5	300	274	6.0	0.91	52
16	10b	21.4	18.5	15.8	575	417	4.9	0.73	29
17	2k	21.5	20.2	16.9	700	389	5.1	0.56	27
18	227s	17.4	17.8	18.9	1165	619	4.0	0.53	37
19	107n	24.3	21.5	21.0	450	365	5.2	0.81	50
20	15p	21.3	18.4	18.9	500	278	6.0	0.56	26
21	10f	22.4	23.7	22.5	450	274	6.0	0.61	38

correlation matrix of stand and tree parameters;

	dbh	h_{dom}	G	N	N_{cr}	d_{cr}	R_{ct}
h_{dom}	0.88						
G	–0.18	–0.10					
N	–0.88	–0.86	0.30				
N_{cr}	–0.70	–0.57	0.34	0.80			
d_{cr}	0.76	0.61	–0.38	–0.80	–0.97		
R_{ct}	0.69	0.74	0.00	–0.69	–0.21	0.22	
Age	0.64	0.59	0.03	–0.49	–0.39	0.45	0.50

Table V.4a. Correlations (r–values) between object parameters and γ for stands of Japanese larch at the Speulderbos site. The first column shows the images from which the γ values are obtained (1982–1983 measurements). The second column shows the number of selected stands (n_1,n_2): n_1 is the number of stands with data on the object parameters; Age, h_{dom}, N_{cr} and d_{cr} and n_2 is the number of stands with data on the parameters G, dbh and N. The grazing angle varies in the range of 10° to 35° for the June and September measurements and in the range of 10° to 20° for the March and May measurements.

image	n_1,n_2	Age	G	dbh	h_{dom}	N	N_{cr}	d_{cr}
Sp1–4 June	(13,11)	0.42	0.14	–0.01	–0.16	–0.36	–0.35	0.31
Sp5–8 September	(13,10)	0.41	–0.32	–0.11	0.35	–0.88	–0.40	0.34
Sp9–10 March	(12,12)	0.33	–0.32	–0.52	–0.41	–0.26	–0.02	–0.01
Sp11–12 May	(10,8)	0.56	–0.06	0.14	0.25	–0.29	–0.50	0.51

Table V.4b. Idem for Japanese larch stands measured in August 1984 (images Sp13–15; 10°–35° range of grazing angles) and measured in July 1985 (images Sp16–18; 35°–60° range of grazing angles).

image	n	*Age*	G	*dbh*	h_{dom}	N	N_{cr}	d_{cr}	R_{ct}
Sp13–15	40	0.25	0.10	0.15	0.24	–0.21	0.07	–0.06	0.37
Sp16–18	31	–0.09	0.00	–0.21	–0.18	0.16	0.20	–0.17	–0.13

Table V.5a. Stand and tree parameters of selected stands of Scots pine at the Kootwijk site.

No.	comp.	G	h_{dom}	*dbh*	N	*cd*	*nn*	*cc*
1	22a	21.47	10.2	16.53	1000	3.1	1.4	60
2	43c	21.86	11.0	17.55	904	3.2	1.3	62
3	23a	21.37	10.3	16.91	951	3.9	1.3	66
4	42d	23.28	9.8	17.12	1011	3.6	1.2	63
5	39	21.06	11.1	17.53	873	4.0	1.2	63
6	39	23.64	10.6	18.93	840	3.5	1.4	62
7	40a	23.63	11.9	18.74	857	3.1	1.3	58
8	40a	23.09	11.4	18.03	904	2.4	1.6	58
9	49b	20.68	10.9	17.74	837	4.1	1.3	60
10	50	22.85	11.2	16.45	1075	4.1	1.4	65
11	50	26.38	10.8	17.10	1148	4.3	1.4	64
12	53	23.10	12.5	19.71	757	3.9	1.2	61
13	18c	20.17	10.6	17.58	831	3.4	1.5	60
14	18c	18.47	11.0	18.68	674	3.1	1.3	62
15	24	21.51	11.1	17.33	912	3.9	1.2	64
16	37	19.59	12.8	21.82	524	4.4	1.1	56
17	51	24.44	13.3	20.70	726	4.1	1.2	65

correlation matrix of stand and tree parameters;

	G	h_{dom}	*dbh*	N	*cd*	*nn*
h_{dom}	0.10					
dbh	–0.08	0.83				
N	0.55	–0.64	–0.86			
cd	0.10	0.27	0.21	–0.05		
nn	0.18	–0.40	–0.47	0.45	–0.60	
cc	0.30	–0.25	–0.43	0.49	0.37	–0.11

Table V.5b. Stand and tree parameters of selected stands of Scots pine at the Speulderbos site.

No.	comp.	G	h_{dom}	dbh	Age
1	30f	24.0	11.8	15.0	24.0
2	31d	24.0	12.2	13.0	23.0
3	48h	21.0	10.2	12.0	23.0
4	45b	20.0	17.0	20.0	39.0
5	52h	20.0	21.0	18.0	47.0
6	25a	24.0	12.0	16.0	23.0
7	123j+p	22.4	15.0	13.5	27.5
8	123n	21.0	13.5	13.0	25.0
9	123e	19.0	19.0	24.0	65.0
10	120g	24.0	12.5	15.0	26.0
11	124d	19.0	10.0	13.0	27.0
12	112j	16.0	12.0	11.0	22.0
13	112e	20.0	13.5	13.0	24.0
14	111q+f	18.5	16.2	16.0	33.0
15	12x	24.0	24.5	36.0	93.0
16	11d	17.0	23.5	27.0	63.0

correlation matrix of stand and tree parameters;

	G	h_{dom}	dbh
h_{dom}	–0.18		
dbh	0.04	0.88	
Age	–0.07	0.91	0.97

Table V.6a. Correlations (r–values) between object parameters and γ for stands of Scots pine at the Kootwijk site. Data are shown for image Kw1 (August 1984) and images Kw2 and Kw3 (July 1985). The range of grazing angles for the selected stands is shown in the second column. The number of selected stands (n) is shown in the third column.

image	θ_i	n	G	h_{dom}	dbh	N	cd	nn	cc
Kw1	17°–30°	17	–0.17	0.31	0.43	–0.46	0.48	–0.45	0.06
Kw2	40°–50°	17	–0.11	–0.21	–0.28	0.18	0.00	0.41	–0.07
Kw3	45°–55°	17	0.59	0.50	0.36	0.00	0.14	0.05	–0.04

Table V.6b. Correlations (r–values) between object parameters and γ for stands of Scots pine at the Speulderbos site. Data are shown for images Sp16–18 (July 1985). The range of grazing angles for the selected stands is shown in the second column. The number of selected stands (n) is shown in the third column.

image	θ_i	n	G	h_{dom}	dbh	Age
Sp16/18	45°–60°	16	–0.25	0.77	0.67	0.68
Sp17	35°–45°	11	–0.42	0.60	0.43	0.47
Sp18	25°–35°	11	–0.38	0.22	0.26	0.33

Table V.7. Overview of C– and L–band radar signatures. The data in the first column refer to the numbering of the corresponding figures. The columns at the right show the number of samples (A–scans) for each sensor parameter combination. Figures V.11a–t show C–band signatures (from flights FL1508/FL1509; 6 July 1984; Roggebotzand). Figures V.11u–x show C–band signatures (flight 1522; 6 September 1984; Speulderbos). Figure V.12 shows L–band signatures (flights FL1584/FL1585; 18 July 1985; Roggebotzand). Figure 5.18 shows C–band look direction dependence (flights FL1522 and FL1596).

figure	species	compartment	n:	15°	30°	45°	60°	75°	45°–VV
11a	beech/oak	O60		29	75	72	58	–	50
11b	Norway spruce	O66		44	76	61	11	–	30
11c	Austrian pine	N85		142	128	–	9	16	66
11d	Sitka spruce	N51		80	89	18	6	10	35
11e	pop. 'Robusta'	O57		54	71	67	60	27	62
11f	pop. 'Robusta'	N66		40	60	56	12	13	50
11g	pop. 'Robusta'	O59		–	79	57	76	12	41
11h	pop. 'Robusta'	O64		37	39	35	22	6	32
11i	pop. 'Robusta'	N45		9	21	10	–	–	6
11j	pop. 'Robusta'	N63		39	56	53	34	26	53
11k	pop. 'Robusta'	N71		7	36	46	–	–	39
11l	pop. 'Robusta'	O63		22	24	5	31	–	10
11m	pop. 'Heidemij'	N61/62		51	83	54	27	–	78
11n	pop. 'Heidemij'	N70		41	56	40	12	21	45
11o	pop. 'Heidemij'	O58		26	39	25	22	16	34
11p	pop. 'Heid/Rob'	N65		41	57	54	31	32	51
11q	pop. 'Oxford'	O61		50	73	69	–	33	58
11r	pop. 'Geneva'	N64		40	58	55	28	37	54
11s	Corsican pine	N87/88		60	128	89	12	42	143
11t	willow	N86		41	44	8	7	14	30
11u	beech	22b		38	14	44	60	–	53
11v	beech	22e		30	53	51	46	–	52
11w	beech	23g		34	10	43	49	–	52
11x	beech	23o		27	–	43	35	–	40

(table V.7 continued)

figure	species	compartment	n:	15°	30°	45°	60°	75°	45°–VV
12a	pop. 'Robusta'	N44		95	72	102	102	94	103
12b	pop. 'Robusta'	N47		80	61	91	81	86	89
12c	pop. 'Robusta'	N66		53	40	50	–	12	51
12d	pop.'Robusta'	N71		20	28	38	40	45	45
12e	pop. 'Heidemij'	N61/62		22	40	50	38	–	51
12f	pop. 'Heidemij'	N70		50	36	46	13	12	49
12g	poplars (mixed)	N43		45	50	88	75	22	61
12h	pop. 'Rob/Heid'	N65		54	39	51	47	39	52
12i	ash	N46		65	32	74	–	–	49
12j	pop. 'Gelrica'	N60		9	6	10	15	17	4
12k	pop.'Geneva'	N64		52	41	50	26	9	53
12l	willow	N86		32	38	47	25	11	52
12m	agric. crop 'A'			54	29	31	8	–	61
12n	agric. crop 'C'			–	8	49	60	–	14
12o	agric. crop 'E'			–	20	22	–	–	15
12p	Sitka spruce	N51		51	67	76	78	11	73
12q	Corsican pine	N87		146	188	194	179	37	191
12r	Norway spruce	N45/46		152	103	144	126	58	152
12s	Scots pine	N89		14	22	31	19	–	31
12t	Austrian pine	N85		99	132	128	68	6	126

5.18a	pop. 'Robusta'	P87/88	(azimuth angle)					
	Flight/ θ_i	n:	30°	90°	150°	210°	270°	330°
	FL1522/ 45		71	83	82	65	83	97
	FL1596/ 30		57	95	94	68	86	72
	FL1596/ 45		61	88	99	65	71	79
	FL1596/ 60		59	38	64	66	26	55

5.18b	beech	113c	(azimuth angle)					
	Flight/ θ_i	n:	40°	100°	160°	220°	280°	340°
	FL1522/ 45		70	–	79	–	77	114

Table V.8. Stand and tree parameters of stands selected at the Roggebotzand site for C– and L–band measurements. The last figure refers to the year of registration.

species	compartment	/year	V	N	dbh	h_{dom}	
Austrian pine	N85	'58	153	1240	15.1	12.8	(1982)
Corsican pine	N87	'58	190	1500	14.8	13.5	(1982)
Corsican pine	N88	'58	176	1478	14.3	14.0	(1982)
Scots pine	N89	'58	133	1167	14.2	13.8	(1982)
Sitka spruce	N51g	'58	126	1503	13.5	10.4	(1986)
Norway spruce	N45c	'60	144	1673	13.5	10.8	(1986)
Norway spruce	N46b	'60	190	2026	14.2	10.8	(1986)
Norway spruce	O66h	'59	356	2021	15.8	16.2	(1987)
ash	N46h	'72	88	1179	11.9	12.5	(1986)
beech/oak (35%/65%)	O60j	'74		1050/ 1950	10.2/ 7.5	8.0/ 6.0	(1987)
pop. mixed	N43b					(not available)	
pop. 'Gelrica'	N60h	'59	122	57	51.0	26.3	(1983)
pop. 'Geneva'	N64f	'61	195	206	35.8	23.5	(1983)
willow	N86a	'59	140	260	29.0	20.5	(1983)
pop. 'Oxford'	O61h	'61	130	170	39.0	24.5	(1987)
pop. 'Rob/And'	O64g					(not available)	
pop. 'Robusta'	N44b	'61	101	155	29.7	23.4	(1983)
pop. 'Heidemij'	N44d	'58	139	157	33.9	25.1	(1983)
pop. 'Robusta'	N45l	'58	174	170	36.1	26.3	(1983)
pop. 'Robusta'	N47b	'60	145	156	35.1	24.6	(1983)
pop. 'Heidemij'	N61h/62h	'59	134	152	35.3	23.5	(1983)
pop. 'Robusta'	N63d	'59	143	162	34.2	24.6	(1983)
pop. 'Heid/Rob'	N65c	'61	79	159	27.5	22.3	(1983)
pop. 'Robusta'	N66h	'61	108	155	31.1	23.6	(1983)
pop. 'Heidemij'	N70e–l	'62	119	176	30.7	23.4	(1983)
pop. 'Robusta'	N71n	'68	110	298	23.9	21.5	(1983)
pop. 'Robusta'	O57b	'59	142	109	40.3	26.6	(1983)
pop. 'Heidemij'	O58l	'61	86	107	33.7	22.5	(1983)
pop. 'Robusta'	O59k	'61	118	158	31.4	24.0	(1983)
pop. 'Robusta'	O63h	'61	88	103	36.3	24.0	(1983)
pop. 'Robusta'	O64Ac	'59	167	189	34.3	25.0	(1983)

Table V.9. Averaged signatures for two groups of poplars in C– and L–bands. For each sensor parameter combination, the averaged γ, averaged incidence angle and the total number of samples (A–scans) are shown. These results are used in figures 5.19 and 5.20.

	15–HH	30–HH	45–HH	60–HH	75–HH
poplars 'Robusta' and 'Heidemij' C–band					
γ	2.3	2.0	2.5	2.2	2.2
θ_i	16.4	29.8	46.6	61.0	73.7
n	(358)	(621)	(502)	(327)	(153)
poplars 'Geneva' and 'Oxford' C–band					
γ	3.2	2.4	2.0	1.2	1.0
θ_i	15.8	29.4	46.2	61.3	73.1
n	(90)	(131)	(124)	(28)	(70)
poplars 'Robusta' and 'Heidemij' L–band					
γ	–2.1	–3.2	–2.4	–3.9	–4.6
θ_i	14.8	30.9	46.0	60.9	74.7
n	(374)	(316)	(428)	(321)	(288)

Samenvatting

Toepassing van radar remote sensing data in de bosbouw

Gedurende het eind van de zestiger jaren en het begin van de zeventiger jaren groeide, met name voor toepassingen in tropisch regenbos, de belangstelling voor beeldvormende vliegtuigradarsystemen sterk. Binnen een decennium na de introductie van deze remote sensing techniek (in 1965) werden miljoenen km^2 tropisch regenbos in een tot voorheen ongekend detail gekarteerd. Nieuwe technologische ontwikkelingen hebben sindsdien de opnamemogelijkheden van remote sensing radar sterk doen toenemen, als gevolg waarvan het potentiële toepassingsgebied sterk is uitgebreid.

Ondanks het feit dat het overzicht van de (potentiële) mogelijkheden van remote sensing radar voor vegetatie–studies nog verre van compleet is, is het duidelijk dat radar naast de optische technieken een belangrijke rol zal blijven spelen. De twee belangrijkste redenen zijn: (1) de unieke eigenschap van microgolf remote sensing systemen om dag en nacht en vrijwel onafhankelijk van atmosferische omstandigheden (die het gebruik van optische systemen kunnen verhinderen) te functioneren en (2) de eigenschap van (coherente) microgolven om bepaalde objectparameters te meten die niet met andere remote sensing systemen te bepalen zijn, en het aldus mogelijk maken complementaire informatie te verzamelen.

Tegenwoordig kunnen ook radarbeelden vanuit satellieten worden opgenomen. Alhoewel hiermee tot nu toe weinig ervaring is opgedaan zijn belangrijke nieuwe toepassingsmogelijkheden goed te voorzien. Het is duidelijk dat de logistieke problemen gerelateerd aan het uitvoeren van meetcampagnes met vliegtuigen vermeden kunnen worden. Het is echter zeer waarschijnlijk dat de belangrijkste toepassing van satellietradar van een ander type zal zijn. Immers, aardobservatie–satellieten uitgerust met radar worden vanwege de unieke "all–weather" eigenschappen betrouwbare monitorings–instrumenten. Dientengevolge zijn deze systemen in staat essentiële informatie te leveren, zowel voor sommige toepassingen in de bosbouw, en voor vegetatie–studies in het algemeen, als voor de mondiale onderzoeksprogramma's voor milieu, klimaat en biosfeer.

De interpretatie van radardata van bossen is, ondanks het feit dat belangrijke vorderingen zijn gemaakt, nooit probleemloos geweest. De belangrijkste oorzaken hiervan zijn (1) het feit dat, in vergelijking met optische systemen, fundamenteel verschillende fysische en geometrische principes ter grondslag liggen aan de totstandkoming van een radarbeeld, (2) het gebrek aan voldoende (systematische en consistente) empirische kennis en (3) het beperkte begrip van de interactie van microgolven met begroeid terrein.

Dankzij deze studie is de empirische kennis systematisch en in belangrijke mate vergroot. Het bleek bovendien mogelijk de empirische resultaten te generaliseren op basis van fysische beschrijvingen van het radar–ontvangstsignaal. Met deze signaalbeschrijvingen werden tegelijkertijd de specifieke meetmogelijkheden van de onderzoeksinstrumenten Dutscat en X–band SLAR onderkend en, dankzij de ontwikkeling van geschikte dataextractie–algorithmen, volledig benut.

Er werd een diepgaande beschrijving gegeven van speckle, een eigenschap die inherent is aan het radarsignaal. Waarschijnlijkheidsverdelingen voor de (gemiddelde) signaalsterkte van objecten die de zogenaamde "Rayleigh–fading" vertonen werden gerecapituleerd. Er werd aangetoond dat de speckle–statistieken van logarithmisch geschaalde data (de gebruikelijk presentatievorm voor radardata) kunnen worden beschreven door simpele analytische uitdrukkingen met behulp van Riemann's zeta–functie en Euler's psi–functie (Appendix I).

Op basis van theoretische overwegingen werd aangetoond dat het vermogensdichtheidsspectrum van het backscattersignaal (de speckle), zoals die wordt gemeten door een bewegende sensor die een homogeen "bevroren" gedistribueerd doel observeert, ruimtelijke informatie bevat in statistische zin. Indien een antenne met een in azimutale richting geïdealiseerd stralingsdiagram volgens een Gausse functie wordt gebruikt kan de autocorrelatie–functie van de azimutale componenten van ruimtelijke structuren verkregen worden op een relatief eenvoudige wijze. Bovendien werden de statistische eigenschappen van dergelijke vermogensdichtheidsspectra beschreven. Het bleek dat de minimale grootte van ruimtelijke details die uit het vermogensdichtheidsspectrum af te leiden zijn fundamenteel beperkt wordt tot de halve antennelengte en dat de nauwkeurigheid van de schatting van de autocorrelatie–functie direct gerelateerd is aan de ruimtelijke afmetingen van het bemonsteringsgebied en sensorkarakteristieken (Appendix II).

Het "cloud model" werd gebruikt om het backscattermechanisme te beschrijven. Dit model is gebaseerd op een eerste–orde oplossing van de radiative transfer vergelijkingen en beschrijft een bos als een aantal horizontale lagen bovenop een bodemlaag. Deze lagen vertonen geen onderlinge wisselwerking en hebben specifieke dempings– en backscattereigenschappen.

Het gebruik van Dutscat voor bosmetingen werd onderzocht. Door het bos als een verzameling horizontale lagen te modelleren —het "multilevel model"— konden de scattereigenschappen van het radar–ontvangstsignaal van bossen worden geanalyseerd. Vanwege de relatief grote hoogte van bossen en de kleine bundelbreedtes van de scatterometer bleek het noodzakelijk te zijn een meer algemene vorm van de

radarvergelijking (gebaseerd op energie in plaats van vermogen) te gebruiken om grote fouten in de berekening van de parameter γ te voorkomen. Tevens kon, uitgaande van het multilevel model, een inversie–algoritme worden ontwikkeld voor een eenduidige bepaling van de relatieve bijdragen van deze lagen aan γ. Deze techniek werd "canopy probing" genoemd. Op basis van theoretische overwegingen en experimentele data kon worden aangetoond dat, indien de boshoogte in de orde van bijvoorbeeld 25 m is, het goed mogelijk is γ te beschrijven als de som van bijdragen van drie of vier naar believen gekozen lagen (boslagen en bodemlaag).

Om de (X–band) microgolf–transmissiviteit van het kronendak te bestuderen werd een experiment uitgevoerd waarbij hoekreflectoren op de bosbodem werden geplaatst. Op basis van verscheidene theoretische overwegingen (welke ondersteund bleken te worden door de experimentele resultaten) kon een beschrijving van het, door het kronendak verzwakte, gereflecteerde hoekreflectorsignaal worden gegeven. Met behulp van deze beschrijving kon voor elke geplaatste hoekreflector een waarde voor de transmissiviteit worden geschat, of konden in elk geval onder– of bovengrenzen voor deze waarde worden aangegeven. De theoretische basis van het cloud model bleek consistent te zijn met die van de ontwikkelde data–extractie technieken voor kronendak probing en transmissiviteit–metingen. Er kon worden aangetoond dat het multilevel model volledig verenigbaar is met een "meerlagen cloud model" en dat de parameter voor (twee–wegs) transmissiviteit identiek is aan de parameter voor de totale demping (van de bodembijdrage) in het cloud model. Om deze redenen zijn bovengenoemde experimentele technieken van direct belang voor de verdere theoretische ontwikkeling en experimentele toetsing van het cloud model.

De experimenten werden uitgevoerd op vier proefgebieden in Nederland: het Roggebotzand en het Horsterwold in Flevoland en het Speulderbos en de boswachterij Kootwijk op de Veluwe. Tezamen bevatten deze proefgebieden een redelijk grote hoeveelheid soorten, leeftijdsklassen, bodemtypes en andere omgevingscondities. Binnen de technische en logistieke mogelijkheden werd een systematisch opgezet onderzoeksprogramma uitgevoerd waarbij de specifieke meetmogelijkheden die de radarsystemen voor bossen bleken te hebben volledig werden benut. In de periode 1982–1985 werden in totaal negen Dutscat vluchten en zeven SLAR vluchten uitgevoerd.

Er werd een aanzienlijke hoeveelheid experimentele data verzameld. Een overzicht van zowel de fundamentele empirische resultaten als een evaluatie en synthese van de resultaten is te vinden in de paragrafen 5.9 en 5.10 van dit proefschrift. Deze resultaten kunnen als volgt beknopt worden weergegeven. De backscattereigenschappen van bomen bleken afhankelijk te zijn van (1) golfparameters, (2) soortafhankelijke (hoogstwaarschijnlijk morfologische) eigenschappen en (3) andere, niet noodzakelijkerwijs soortafhankelijke, factoren zoals opstands– en boomparameters, naaldverlies en ondergroei.

Voor de X–band en, mogelijk ook, de C–band was de invloed van de laatste groep factoren klein, op een aantal specifieke gevallen na. Voor de L–band bleken deze laatste factoren een stuk belangrijker te zijn terwijl, aan de andere kant, de soortafhankelijke factoren van minder belang bleken te zijn.

Op basis van het theoretische concept van het cloud model werden de resultaten van backscatter signatuurmetingen en de probing en transmissiviteit–metingen geëvalueerd. De consistentie van de empirische resultaten kon worden aangetoond waarbij bleek dat bossen zich voor X– en C–band golven gedragen als een ondoorzichtige volume–scatterer en voor de L–band als een transparante volume–scatterer. In het laatste geval kan de bijdrage van de bodem niet meer worden verwaarloosd. Een modificatie van het cloud model, door middel van het toevoegen van een bodem–stam interactieterm, lijkt voor de L–band noodzakelijk te zijn.

Voor opstanden met een (voldoend) gesloten kronendak werd in de X–band een duidelijk verband tussen de backscatterwaarden en de taxonomische indeling gevonden. Uitzonderingen hierop waren opstanden met een zeer open kronendakstructuur zoals jonge aanplant (een of twee jaar oud) of sommige oude opstanden. Het is zeer waarschijnlijk dat voor deze gevallen het afwijkend gedrag veroorzaakt wordt door een substantiële bijdrage van de bodem en/of de ondergroei. Ook andere resultaten illustreren duidelijk het effect van aan structuur en morfologie gerelateerde karakteristieken. De aanzienlijke variatie van het backscatter–niveau die werd gevonden voor de japanse larix in mei, kon in verband worden gebracht met de verschillende stadia van naaldontwikkeling. Voor sommige populiereklonen werden richtingsafhankelijke backscatterniveaus gevonden die mogelijk gerelateerd zijn aan heliotroop gedrag. Duidelijke relaties tussen het backscatterniveau en biofysische eigenschappen, het effect van naaldverlies uitgezonderd, werden voor de X–band niet geconstateerd. Een synthese van de resultaten voor dennen toonde aan dat er een duidelijk verband bestaat tussen een stijging van het backscatterniveau, oplopend tot 2 á 3 dB, en de afname van het aantal jaargangen naalden.

Voor de L–band werden een aantal fundamenteel verschillende resultaten gevonden. De waarneming dat de aanwezigheid van een 2 m hoge ondergroei van beuk, onder een 25 m hoge populierenopstand met volledige sluiting en bladontwikkeling, een aanzienlijke daling van het backscatterniveau veroorzaakt (tot 2.5 dB, afhankelijk van θ_i) is hiervan een duidelijk voorbeeld.

Om te onderzoeken welke typen informatie middels het gebruik van radarbeelden in de praktijk kunnen worden verkregen werden enkele veelbelovende informatie–extractie technieken geëvalueerd.

De potentiële mogelijkheden van radar voor de klassificatie van objecten werd bestudeerd op basis van de empirische resultaten en theoretische overwegingen. Er kon worden geconcludeerd dat de kortere golflengten (C–band en hogere frequentiebanden), vanwege het veronderstelde sterke verband tussen het backscatterniveau en de morfologische (soortafhankelijke) eigenschappen, het meest geëigend zijn voor de klassificatie van soorten. De L–band, alleen of in combinatie met andere banden, bleek geschikt te zijn voor het onderscheid van enkele brede vegetatieklassen zoals naaldhout/loofhout, bos/niet–bos en overstroomd/niet–overstroomd bos. Een observatiemethode waarbij gebruik wordt gemaakt van twee tijdstippen, namelijk zomer (volledige bladontwikkeling) en winter (kaal loofhout), of een multi–frequentie benadering, lijken in het algemeen goede resultaten op te leveren.

Tevens werd het gebruik van beeldbewerkingstechnieken bestudeerd. Deze blijken nut te hebben bij de aanpak van het "speckle probleem". Deze technieken kunnen echter, met name wanneer een forse onderdrukking van het effect van de speckle wordt nagestreefd, leiden tot aanzienlijke radiometrische en geometrische deformaties van de radardata. Alternatieve strategieën om klassificatieresultaten te verbeteren, die deze problemen niet hebben, zijn: (1) een modificatie van het radarsysteem die gericht is op het verkrijgen van meer onafhankelijke bemonsteringen per oppervlakte–eenheid en (2) een verstandige keuze van golfparameters en observatietijdstippen. Natuurlijk kan ook elke combinatie van bovengenoemde technieken worden gebruikt en zou men het resultaat nog verder kunnen verbeteren door het gebruik van voorkennis. De empirisch bepaalde waarde voor de standaard–deviatie van de over de opstand gemiddelde γ waarden zal in de praktijk echter de echte grenzen van de klassificatienauwkeurigheid bepalen. Voor dit getal werd een waarde gevonden van ongeveer 0.5 dB, voor alle klassen en golfparameters (voor de X– en C–band). Deze variatie in gemiddeld backscatterniveau kan veroorzaakt worden door variaties in ecologische en omgevingsfactoren.

De in de beeldvormende radardata vervatte ruimtelijke relaties zijn belangrijke potentiële bronnen van informatie. Dit is met name voor natuurlijke bossen van groot belang aangezien deze meestal een gemengde soortensamenstelling hebben en aldus een gering dynamisch bereik van backscatterwaarden kunnen vertonen.

Er werden drie methoden voor het extraheren van ruimtelijke informatie bestudeerd: (1) de analyse van speckle, (2) de analyse van textuur en (3) de analyse van (grote) kronendakpatronen op basis van geschikte interactiemodellen. Deze benaderingswijzen verschillen in het opzicht dat ze gebaseerd zijn op fundamenteel verschillende concepten, van toepassing zijn op verschillende schalen en gerelateerd zijn aan verschillende (fysische) parameters voor de beschrijving van de kronendakarchitectuur. Deze benaderingswijzen kunnen daarom in sterke mate als complementair worden beschouwd. Een overzicht van de

eigenschappen en mogelijkheden van deze technieken werd gegeven in paragraaf 6.6.1.

De textuuranalyse techniek bleek geschikt te zijn voor het onderscheiden van bostructuren (gerelateerd aan type en/of ontwikkelingsstadium).

Op basis van eenvoudige geometrische overwegingen en de veronderstelling dat het kronendak zich gedraagt als een ondoorzichtige isotrope volume–scatterer (bijvoorbeeld voor de X–band) kunnen grote deterministische patronen binnen homogeen veronderstelde gebieden worden geanalyseerd. De locale hellingen van het kronendakoppervlak kunnen nauwkeurig worden geschat en kunnen, indirect, in verband worden gebracht met andere factoren zoals locale groeiverschillen, etc.

De mogelijkheid om ruimtelijke informatie in statistische zin te verkrijgen middels een analyse van de speckle in ruwe SLAR data werd aangetoond. Gebruikmakend van een eenvoudig geometrisch model voor het kronendakoppervlak kon de rijafstand in bosplantages worden geschat binnen een nauwkeurigheid van enkele decimeters! In het algemeen kan gesteld worden dat de toepassing van deze techniek tweeledig zal zijn, namelijk (1) als ondersteuning van het onderzoek naar het microgolf backscattermechanisme op fundamenteel nieuwe wijze en (2) als een nieuwe fysische meetmethode in de remote sensing om bosstructuren op een kwantitatieve en fysisch goed gedefinieerde manier te bepalen (door middel van de autocorrelatie–functie).

Een voorlopige opsomming van potentiële toepassingsgebieden werd gegeven in paragraaf 6.6.2. De verwachting is dat het gebruik van de "kortere" golflengten (C– en X–band) geschikt is voor de volgende typen toepassingen:

(1) bosinventarisatie: areaalbepaling en bossoort en –type klassificatie,
(2) monitoring van fenologische ontwikkeling en fysiologische processen,
(3) detectie van ziekte en stress en
(4) monitoring van bosontwikkeling.

Vanwege de nog geringe ervaring is het veel moeilijker de potentiële toepassingsgebieden van de L–band, en de langere golflengten in het algemeen, aan te geven. In verband met de gebleken hoge mate van transparantie van het kronendak lijkt het echter waarschijnlijk dat deze langere golflengten unieke mogelijkheden voor bosinventarisatie en bosmonitoring kunnen bieden.

Voor het benutten van de volledige potentiële mogelijkheden van radar is nog veel achtergrondsonderzoek nodig. Met name de mogelijkheden van de lagere frequenties (de P–, L– en S–banden) en de potentie van radarpolarimetrie zijn nog nauwelijks bekend. Omdat deze belangrijke nieuwe potentiële mogelijkheden lijken te bieden, met name voor

bossen, is een systematische onderzoeksinspanning aan te bevelen.

Naast de noodzaak de empirische kennis te vergroten is het van groot belang om de backscatter modellen verder te ontwikkelen. Er werden verschillende benaderingswijzen genoemd. Het ligt in de verwachting dat deze modelvorming de ontwikkeling zal ondersteunen van technieken voor de schatting van (bio)fysische parameters en, indirect, voor de klassificatie en monitoring. Er werd opgemerkt dat interpretatieproblemen kunnen ontstaan. Het is bijvoorbeeld moeilijk om een eenduidige oplossing te vinden wanneer het aantal objectparameters in modellen het aantal (onafhankelijke) radarwaarnemingen overtreft. Een voor de hand liggende oplossing voor dit probleem is het gebruik van beschikbare (a priori) kennis, remote sensing producten van eerdere datum en/of additionele data van andere typen sensoren. Concepten voor de integratie van analyse technieken werden besproken. Deze aanpak blijkt zowel de efficiëntie van de analyse van radardata als de aanpak van het "inversieprobleem", de verhoging van de nauwkeurigheid en, in het algemeen, het vergroten van de potentiële toepassingsmogelijkheden van remote sensing ten goede te komen.

Ondanks het feit dat er nog veel achtergrondsonderzoek gedaan moet worden is nu reeds duidelijk dat radar een sleutelrol gaat vervullen in toekomstige remote sensing systemen. Aangezien de werking niet afhankelijk is van de belichting van de zon en radar vrijwel niet gehinderd wordt door atmosferische omstandigheden is het de enige betrouwbare oplossing, zowel voor (kleinschalige) inventarisaties van frequent bewolkte gebieden, als voor mondiale (satelliet–)monitoringsystemen. Vanwege deze eigenschappen en vanwege de eerder genoemde specifieke toepassingsmogelijkheden kan een belangrijke rol voor radar in de bosbouw worden voorzien.

Biography

Dirk Herman Hoekman was born in Zutphen, The Netherlands, on 16 July 1956. In 1975, he obtained the Atheneum–B diploma from the Nijmeegse Scholengemeenschap at Nijmegen. He received the degree of Ingenieur from the Department of Electrical Engineering of the Delft University of Technology in 1981. He enrolled in the Microwave Laboratory of this department in 1978, where he started his research in the field of microwave remote sensing with a study of backscatter modelling of agricultural crops.

Since 1981, he has been with the Department of Land Surveying and Remote Sensing of the Wageningen Agricultural University, where he lectures on microwave remote sensing and the physical backgrounds of remote sensing. His activities have focused on research in the field of microwave remote sensing, with particular emphasis on applications in agriculture and forestry. He was involved in several international radar remote sensing campaigns, such as the ESA/INPE Amazonian campaign (1986), the ESA/JRC Agriscatt campaign (1987 and 1988) and the ESA/JRC Maestro–1 campaign (1989). In 1990 he became a member of The Electromagnetics Academy.